

REPORT DOCUMENTATION PAGE				Form Approved OMB No. 0704-0188	
Public reporting burden for this collection of information is estimated to average 1 hour per response, including the time for reviewing instructions, searching existing data sources, gathering and maintaining the data needed, and completing and reviewing this collection of information. Send comments regarding this burden estimate or any other aspect of this collection of information, including suggestions for reducing this burden to Department of Defense, Washington Headquarters Services, Directorate for Information Operations and Reports (0704-0188), 1215 Jefferson Davis Highway, Suite 1204, Arlington, VA 22202-4302. Respondents should be aware that notwithstanding any other provision of law, no person shall be subject to any penalty for failing to comply with a collection of information if it does not display a currently valid OMB control number. PLEASE DO NOT RETURN YOUR FORM TO THE ABOVE ADDRESS.					
1. REPORT DATE (DD-MM-YYYY) 29-08-2012		2. REPORT TYPE Final Technical Report For FA9550-09-1-0452		3. DATES COVERED (From - To) From Sept 1 2009, to Aug 29, 20012	
A novel probabilistic multi-scale modeling and sensing framework for fatigue life prediction of aerospace structures and materials: DCT project				5a. CONTRACT NUMBER	
				5b. GRANT NUMBER FA9550-09-1-0452	
				5c. PROGRAM ELEMENT NUMBER	
6. AUTHOR(S) S. I. Rokhlin, S. Ghosh, H. Millwater				5d. PROJECT NUMBER	
				5e. TASK NUMBER	
				5f. WORK UNIT NUMBER Work Unit Number 95500910452	
7. PERFORMING ORGANIZATION NAME(S) AND ADDRESS(ES) 1) Materials Science and Engineering Department ,The Ohio State University, 1960 Kenny Road, Columbus, OH 43210-1016; 2) Civil and Mechanical Engineering Department, Johns Hopkins University, Baltimore, MD 21218; 3) Department of Mechanical Engineering University of Texas at San Antonio, San Antonio, TX				8. PERFORMING ORGANIZATION REPORT NUMBER	
9. SPONSORING / MONITORING AGENCY NAME(S) AND ADDRESS(ES) Air Force Office of Scientific Research Multi-Scale Structural Mechanics and Prognosis Program Program Director: Dr. David Stargel AF office of scientific research 875 N. Randolph St Room 3112, Arlington, VA 22203				10. SPONSOR/MONITOR'S ACRONYM(S)	
				11. SPONSOR/MONITOR'S REPORT NUMBER	
12. DISTRIBUTION / AVAILABILITY STATEMENT Approved for public release; distribution is unlimited.				AFRL-OSR-VA-TR-2012-1128	
13. SUPPLEMENTARY NOTES					
14. ABSTRACT This project entails three complementary tasks with the objective of integrating them into a unified platform for advancing a novel probabilistic multi-scale modeling and sensing framework for fatigue life prediction. In the <u>first task</u> (Ghosh, JHU), an integrated system of novel spatial-temporal multi-scale computational models for image based modeling of deformation and fatigue crack nucleation in polycrystalline titanium alloys is developed. A novel wavelet transformation based multi-time scaling algorithm and homogenized continuum anisotropic plasticity and probabilistic fatigue crack nucleation models are developed. In the <u>second task</u> (Rokhlin, OSU), a comprehensive experimental methodology and inverse models are developed for structural health monitoring and noninvasive assessment of fatigue sensitive microstructures in Ti alloys. The aim is to provide realistic data input for computational predictive models under development in this program. In the <u>third task</u> (Millwater, UTSA), the distribution of weakest-link type material properties for larger material volumes is predicted from evaluation of small microstructural models with Extreme Value Theory. A property distribution associated with a grain boundary is used to extrapolate the distribution for a grain which is then used to predict the property distribution for a volume of the polycrystalline material.					
15. SUBJECT TERMS					
16. SECURITY CLASSIFICATION OF:			17. LIMITATION OF ABSTRACT	18. NUMBER OF PAGES 170	19a. NAME OF RESPONSIBLE PERSON S.I. Rokhlin
a. REPORT	b. ABSTRACT	c. THIS PAGE			19b. TELEPHONE NUMBER (include area code) rokhlin.2@osu.edu (614) 292-7823

A Novel Probabilistic Multi-scale Modeling and Sensing Framework for Fatigue Life Prediction of Aerospace Structures and Materials: DCT Project

Sponsor: Air Force Office of Scientific Research
Multi-Scale Structural Mechanics and Prognosis Program

Grant No. FA-9550-09-1-045 2
Period of Performance: 2009-2012

Program Director: Dr. David Stargel

By

Somnath Ghosh

*Professor, Department of Civil Engineering and Mechanical Engineering
Johns Hopkins University, Baltimore, MD;*

Stanislav I. Rokhlin

*Professor, Department of Materials Science and Engineering
The Ohio State University, Columbus OH;*

Harry Millwater

*Professor, Department of Mechanical Engineering
University of Texas at San Antonio, San Antonio, TX*

August 25, 2012

Acknowledgments

The authors acknowledge the financial support provided by AFOSR Grant FA9550-09-1-0452, David Stargel, Program Manager. The authors also acknowledge Patrick Golden, Reji John, Mark Blodgett and Adam Pilchak of AFRL, Materials and Manufacturing Directorate for many insightful discussions, Mr. Kevin Maxwell of Texas A&M for the helpful conversations on finite element modeling, Professor Robert Brockman of UDRI for the helpful conversations on material modeling, and Mr. Chukwunonso Arinze of UTSA for assistance with the crystal elastic model and Professor Jim Williams from the OSU for helpful discussions of sample microstructures and sharing the OIM images.

Content

List of Figures.....	5
List of Tables.....	10
Abstract.....	12
Executive Summary.....	13
Task 1: Computational Multiscale Analysis Framework for Fatigue Crack Nucleation in Metallic Polycrystalline Microstructures.....	14
1.1 Image-Based Crystal-Plasticity FE Models for Deformation and Fatigue Crack Nucleation in Polycrystalline Aggregates.....	14
1.2 Multi-Time Scaling Crystal Plasticity FEM for Cyclic Deformation in Polycrystalline Materials: WATMUS Algorithm.....	15
1.3 Homogenized Constitutive and Fatigue Nucleation Models from Crystal Plasticity Simulations of Ti Alloys.....	17
1.4 Organization of Appendix A	17
Task 2: Development of Multi-Scale Sensing and Evaluation Framework for Fatigue Life Prediction.....	18
2.1 Dynamic load-lock-in processing for visualization of small fatigue crack initiation and Evolution.....	18
2.2 Imaging of damage precursors as anomalous plastic-microstrain: ultrasonic microtexture backscattering as strain markers.....	20
2.3 Experimental methodology and inverse models for ultrasonic volumetric assessment of fatigue sensitive microstructure.....	22
2.4 Organization of Appendix B.....	23
Task 3: Development of Localized Probabilistic Sensitivity Method to Determine Random Variable Region Importance.....	24
3.1 Homogenization-based Probabilistic Constitutive Model.....	24
3.1.1 Order Statistics and Extreme Value Theory.....	25
3.2 Homogenization-based Probabilistic Constitutive Model.....	25
3.2.1 MCS of small-scale model for response distribution.....	26
3.2.2 Estimate RVE response distribution with Extreme Value Theory and a Small-Model response distribution.....	26
3.2.2.1 Application of Order Statistics to determine the large-model property distribution from the small-model property distribution.....	26
3.3 Application of Homogenization Methodology to Plastic Slip Initiation Model.....	29
3.3.1 Model of Slip Initiation in Ti- α	29
3.3.2 Distributions predicted by 2-grain model.....	31
3.3.3 Distributions of larger SVEs	32
3.3.3.1 ~6-grain SVE.....	32
3.3.3.2 ~38-grain SVE.....	33
3.3.3.3 ~531-grain RVE.....	33
4. Conclusions.....	35
References.....	37
 Appendix A Computational Multiscale Analysis Framework for Fatigue Crack Nucleation in Metallic Polycrystalline Microstructures	 39
Abstract.....	39
Chapter 1 Relevant Information.....	40
1.1 Personnel Supported.....	40
1.2 Completed Ph.D. Dissertations/M.S. Theses.....	40
1.3 Books and Book Chapters.....	40
1.4 Refereed Journal Publications.....	40
1.5 Keynote Lectures.....	41
1.6 Invited Lectures at Conferences.....	42
Chapter 2 Introduction.....	43
2.1 Image-Based Crystal-Plasticity FE Models for Deformation and Fatigue Crack Nucleation	

in Polycrystalline Aggregates.....	43
2.2 Multi-Time Scaling Crystal Plasticity FEM for Cyclic Deformation in Polycrystalline Materials: WATMUS Algorithm.....	43
2.3 Homogenized Constitutive and Fatigue Nucleation Models from Crystal Plasticity Simulations of Ti Alloys.....	44
2.4 Organization of this Report.....	44
Chapter 3 Image-Based Crystal-Plasticity FEModels for Deformation and Fatigue Crack Nucleation in Polycrystalline Aggregates.....	45
3.1 Crystal Plasticity Finite Element (CPFE) Model for Dwell Fatigue.....	47
3.1.1 Crystal Plasticity Constitutive Relations.....	47
3.1.2 CPFE Simulations of Polycrystalline Ti-6242.....	48
3.2 Experimental Crack Observations in a Cyclic Dwell Test.....	50
3.2.1 Crack Nucleation Site for Dwell Loading.....	50
3.2.2 Detection and Monitoring Cracks in Mechanical Tests.....	52
3.3 Review and Evaluation of Some Microstructure-based Failure Models.....	52
3.3.1 Dislocation based Stroh-type Crack Nucleation Models.....	53
3.3.2 A Purely Stress based Nucleation Criterion.....	53
3.3.3 Energy based Approaches for Micro-crack Nucleation.....	53
3.3.4 Micro-void Growth Models for Prediction of Micro-crack Nucleation.....	54
3.4 A new Non-local Crack Nucleation Criterion from CPFE Variables.....	55
3.4.1 Model Description.....	55
3.4.2 Numerical Implementation of the Crack Nucleation Criterion.....	57
3.4.3 The Cottrell-Petch Fracture Model as a Limiting Case of the Nucleation Model.....	59
3.5 Parameter Calibration and Validation of the Crack Nucleation Criterion.....	61
3.5.1 Calibration of R_c for α/β Forged Ti-6242.....	61
3.5.2 Predicting Crack nucleation in Specimens 2 and 3.....	64
3.6 Conclusion.....	66
Chapter 4 Wavelet Transformation Induced Multi-Time Scaling in Crystal Plasticity FEM Simulations for Fatigue Crack Nucleation in Ti-6242 28.....	67
4.1 Introduction.....	67
4.2 Size and Rate Dependent Crystal Plasticity FE model for Ti-6242.....	68
4.3 Non-local Crack Nucleation Model for Near α Ti-alloys.....	70
4.4 Wavelet Transformation based Multi-time Scale (WATMUS) Method for Accelerated Cyclic CPFEM Simulations.....	71
4.4.1 A Slightly Modified WATMUS Scheme to Accommodate Larger Time Periods.....	77
4.5 Calibration and Validation of Critical Crack Nucleation Parameter R_c	79
4.5.1 Statistically Equivalent Microstructures.....	79
4.5.2 Evaluating Yield Strengths and Dwell Fatigue Simulations.....	80
4.6 Influence of Microstructural and Loading Characteristics on Crack Nucleation in Ti-6242.....	83
4.6.1 Sensitivity of Yield Strength to Grain Orientation and Size Distributions.....	84
4.6.2 Sensitivity of Crack Nucleation to Microstructural Features.....	85
4.6.3 Sensitivity of Crack Nucleation to Characteristics of Applied Loading.....	87
4.7 Conclusion.....	90
Chapter 5 Homogenized Constitutive and Fatigue Nucleation Models from Crystal Plasticity Simulations of Ti Alloys, Part 1: Macroscopic Anisotropic Yield Function.....	91
5.1 Introduction.....	91
5.2 Crystal Plasticity Finite Element (CPFE) Model for Micro-Scale Polycrystalline Simulations.....	92
5.3 Sensitivity Analysis with Respect to Microstructural Parameters.....	93
5.3.1 Parameters Representing Microstructural Characteristics.....	94
5.3.2 Sensitivity of Macroscopic Response to Microstructural Parameters.....	96
5.4 Development of Homogenization-based Anisotropic Plasticity Constitutive (HAPC) Model for Ti Alloys.....	99
5.4.1 Choice of a Suitable Framework for Yield Function.....	99
5.4.2 Suitability of the Cazacu-Barlat Framework for the HAPC Model of Ti Alloys.....	101

5.4.3 Evaluation of Microstructure Dependent Constitutive Parameters in the HAPC model.....	105
5.4.4 An Extension of the Homogenized Model to Account for Rate Dependency.....	107
5.5 Conclusion.....	109
5.6 Attachment A.....	110
5.7 Attachment B.....	111
Bibliography.....	113
Appendix B Multi-Scale Sensing & Evaluation Framework for Fatigue Life Prediction.....	119
Abstract.....	119
Chapter 1 Relevant Information.....	120
1.1 Personnel Supported.....	120
1.2 Refereed Journal Publications.....	120
1.3 Proceedings Publications.....	121
1.4 Invited Lectures at Conferences.....	121
Chapter 2 Introduction.....	122
2.1 Dynamic load-lock-in processing for visualisation of small fatigue crack initiation and Evolution.....	122
2.2 Imaging of damage precursors as anomalous plastic-microstrain: ultrasonic microtexture backscattering as strain markers.....	123
2.3 Experimental methodology and inverse models for ultrasonic volumetric assessment of fatigue sensitive microstructure.....	123
2.4 Organization of Appendix II.....	124
Chapter 3 Fatigue crack monitoring in engine-grade titanium alloy by dynamic subtraction of surface acoustic wave modulation.....	125
3.1 Introduction.....	125
3.2 Experiment.....	126
3.2.1 Samples.....	126
3.2.2 Experiment and data acquisition.....	126
3.3 Fatigue regime results: application to crack-sizing.....	128
3.3.1 The subtraction method.....	128
3.3.2 Discussion of fatigue regime results.....	129
3.3.3 Visualization of fatigue regime data.....	130
3.3.4 Crack evolution and ultrasonic signals.....	131
3.4 Modulation regime results and discussion.....	134
3.4.1 Modulation overview.....	134
3.4.2 Modulation and subtraction.....	135
3.5 Conclusion.....	138
Chapter 4 Imaging of damage precursors as anomalous plastic-microstrain: ultrasonic microtexture backscattering as strain markers.....	139
4.1 Background and method formulation.....	139
4.2 Approach and results.....	140
4.2.1 Samples and data acquisition.....	140
4.2.2 Results.....	140
4.3 Conclusion.....	141
Chapter 5 Inverse models and experimental methodology for ultrasonic volumetric assessment of fatigue sensitive microstructure.....	142
5.1 Introduction.....	142
5.2 Model with Duplex Microstructure.....	143
5.2.1 General model description.....	143
5.2.2 Effective elastic property of microtextured region (MTR).....	146
5.2.3 Attenuation in Duplex Microstructures.....	150
5.3 Ultrasonic measurements and comparison with the model.....	154
5.3.1 Near α -Ti sample.....	154
5.3.2 Attenuation and backscattering measurements.....	155
5.3.3 Measurement results.....	156

5.3.4 Comparison with the model and discussion.....	157
5.4. Further discussion and sensitivity to parameter uncertainty.....	158
5.4.1 Discussion and Sensitivity to Parameter Uncertainty.....	158
5.4.2 Orthotropic Crystallites and 3-D Texture.....	161
5.5. Conclusions.....	162
5.6. Attachment: Attenuation coefficients for hexagonal elongated grains.....	163
Bibliography.....	165

List of Figures

Figure 1: (a) CPFEM model of a polycrystalline microstructure undergoing creep deformation; (b) local stress distribution in grains with a hot-spot (green); (c) evolution of stress distribution with cycles along a line showing load-shedding behavior.....	15
Figure 2: (a) Decoupling fine and coarse time scale responses for cyclic loading: (a) fine scale solution, (b) stress contour at 10000 cycles created by the WATMUS based CPFEM simulation, (c) comparison of the evolution of volume averaged plastic strain by the WATMUS-based and fine time scale simulations, (d) evolution of local stresses with cycles for rate dependent crystal plasticity.....	16
Figure 3: The peak amplitude of the ultrasonic signal versus time (msec); vertical axis is cycle number. On the left, the data is before dynamic subtraction processing, signal is imbedded in the backscattering noise. On the right, the signal representation after subtraction clearly showing the fatigue crack initiation and evolution (bright strip pattern, showing crack location within the sample and its initiation at approximately 18,500 cycles. Signal-to-noise ratio was improved by 20x. Above the images are cycling fatigue load segments (on the left) with points indicating moments of ultrasonic data acquisition; on the right acquired ultrasonic signatures (acquired at the same load but at a different segment of the cyclic loading; those signatures are used for subtraction). Large reflected signal at the end is reference reflection.....	19
Figure 4: Ultrasonic crack detection in early stages of fatigue. Data shows crack detection in visualized the stress-cycle domain mode (a) fatigue cyclic data acquisition mode; (b) modulation mode of the data acquisition. Stress-cycle domain plots are useful in localizing the crack. Modulation can provide better information that the time traces alone.....	20
Figure 5: Local strain (gray pattern) along the sample length (scaled with time) with increase of number of fatigue cycles shown on the vertical axis (increase of pattern darkness represents increase of the local strain). High straining observed around the crack position as it initiates and grows. The persistent high local strain is observed at early stages of the experiment at the future crack location. This is an indication of excessive plastic strain in that part of the grain structure, increasing susceptibility to crack formation.....	21
Figure 6: (a) Schematic of ultrasonic backscattering measurement showing ultrasonic transducer and its beam and an ultrasonic backscatter volume. Also, the experimental time domain ultrasonic backscattering signal (noise) resulting from ultrasonic pulse propagation over the sample thickness is shown. (b) Spatial distribution map of the backscattering ultrasonic signal averaged over the sample thickness. Color variations of the map correspond to microtexture size variation in the direction of wave propagation.....	23
Figure 7: PMF of Number of Nearest Neighbors.....	27
Figure 8: Extreme Value Homogenization Strategy.....	28
Figure 9: Prismatic $\langle a \rangle$, Basal $\langle a \rangle$, First-Order Pyramidal $\langle a \rangle$, and First-Order Pyramidal $\langle c+a \rangle$ Slip System Families for H.C.P. Crystal Lattices.....	30
Figure 10: SVE Geometry.....	31
Figure 11: Comparison of Predicted Slip Initiation Strength Distributions.....	32
Figure 12: Comparison of 2-grain EVT predicted distribution and MCS distribution for 3 different volumes.....	33
Figure 13: Difference Between Predicted and Actual Slip Initiation Strength Distributions.....	34

Appendix A

Figure 3.1: OIM scan of the critical primary crack nucleation site in specimen 1 microstructure.....	49
Figure 3.2: (a) CPFEM model of the statistically equivalent microstructure of polycrystalline Ti-6242 at a critical location of specimen 1 depicting c -axis orientation distribution contour (radians), (b) contour plot of loading direction stress σ_{22}^P , and (c) contour plot of loading direction plastic strain ε_{22}^P	49
Figure 3.3: Distribution of local variables: (a) loading direction stress (σ_{22}^P), (b) local plastic strain along a section parallel to the x-axis at the end of 1000 seconds for a creep simulation on the two models of critical microstructure of specimen 1 with two different mesh densities.....	50

Figure 3.4:	Distribution of local variables from a simulation of the CPFE model of critical microstructure of specimen 1: (a) the loading direction stress (σ_{22}^P), and (b) the predominant prismatic Schmid factor along a section <i>AA</i> at the end of 1 and 300 dwell cycles.....	51
Figure 3.5:	Evolution of volume-averaged plastic strain with number of cycles for the three critical microstructures.....	51
Figure 3.6:	(a) Fractograph of a faceted nucleation site for a failed Ti-6242 dwell fatigue specimen, (b) crack length as a function of number of cycles for a secondary crack in specimen 2.....	52
Figure 3.7:	Evolution of fatigue damage with cycles: (a) calibration of the efficiency parameter f from critical microstructure of specimen 1, (b) prediction of number of cycles to micro-crack nucleation for three different microstructures.....	54
Figure 3.8:	Evolution of a void growth parameter V_g with cycle: (a) calibration of critical V_g for micro-crack nucleation in the critical microstructure of specimen 1, (b) prediction of the number of cycles for micro-crack nucleation for three other microstructures.....	55
Figure 3.9:	(a) A wedge crack with opening displacement of $4b$, produced by coalescence of four dislocations, (b) nucleation of a wedge crack in the hard grain resulting from a dislocation pile up in the soft grain.....	56
Figure 3.10:	Closure failure and crack opening displacement for (a) single pure edge dislocation, and (b) single pure screw dislocation.....	57
Figure 3.11:	(a) Wedge-crack in the hard grain as a result of dislocation pileup in adjacent soft grain, (b) distribution of the norm of Nye's dislocation tensor inside a representative soft grain.....	58
Figure 3.12:	A schematic diagram explaining of Cottrell-Petch fracture model.....	60
Figure 3.13:	(a) Evolution of the maximum R_1 over number of cycles for the FE model of critical microstructure of specimen 1, (b) evolution of the maximum R_2 over number of cycles for the FE model of critical microstructure of specimen 1.....	62
Figure 3.14:	Histograms of effective crack nucleation variables: (a) R_1 along a X-directed line passing through the hard-soft grain combination with the highest R_1 value, (b) R_2 along a X-directed line passing through the hard-soft grain combination with the highest R_2 value, for the critical microstructure of specimen 1 at 282 and 300 dwell cycles respectively.....	63
Figure 3.15:	(a) Evolution of the maximum R_1 over number of cycles for the FE model of non-critical microstructure of specimen 1, (b) evolution of the maximum R_2 over number of cycles for the FE model of non-critical microstructure of specimen 1.....	63
Figure 3.16:	Histograms of effective nucleation variables: (a) R_1 along a X-directed line passing through the hard-soft grain combination with the highest R_1 value, (b) R_2 along a X-directed line passing through the hard-soft grain combination with the highest R_2 value, corresponding to the non-critical microstructure of specimen 1 at 282 and 300 dwell cycles.....	64
Figure 3.17:	(a) Evolution of the maximum R_1 over number of cycles for the FE model of critical microstructure of specimen 2, (b) evolution of the maximum R_2 over number of cycles for the FE model of critical microstructure of specimen 2, (c) evolution of the maximum R_1 over number of cycles for the FE model of critical microstructure of specimen 3, (d) evolution of the maximum R_2 over number of cycles for the FE model of critical microstructure of specimen 3.....	65
Figure 4.1:	Schematic of a wedge micro crack formation resulting from dislocation pile-up in the soft grain near a hard soft grain boundary, where c is the micro crack length and $B = \ \mathbf{B}\ $ is the crack opening displacement due to dislocation pile-up.....	70
Figure 4.2:	FE model of a polycrystalline microstructure and loading conditions to demonstrate the accuracy and efficiency of the WATMUS method: (a) microstructure with $\langle c \rangle$ -axis orientation and mesh, (b) boundary conditions, and (c) cyclic loading profile.....	73
Figure 4.3:	Comparison of the evolution of the cycle-scale with averaged single time-scale internal variables at an integration point in the FE model of the polycrystalline microstructure for: (a) $F_{0,22}^P$, (b) g_0^α	73

Figure 4.4:	Relative error $e(N, \tau) = \frac{ \tilde{y}(N, \tau) - y(N, \tau) }{\ y(N, \tau)\ }$ of fine scale evolution of variables at 211 th cycle at an integration point in the FE model of the polycrystalline microstructure for: (a) F_{22}^P , (b) g^α , (c) σ_{22}	74
Figure 4.5:	Comparison of distribution of stress σ_{22} along a material line in the microstructure at $N = 211$ and $\tau = 1$ sec, by the WATMUS and single time-scale CPFEM simulations for: (a) σ_{22} (b) relative error in σ_{22}	75
Figure 4.6:	Evolution of $F_{0,22}^P$ with cycles by WATMUS-based CPFEM simulation: (a) volume averaged $F_{0,22}^P$, (b) distribution of $F_{0,22}^P$ at the 10, 000 th cycle, and (c) distribution of $F_{0,22}^P$ at the 300000 th cycle.....	76
Figure 4.7:	Evolution of fine time-scale σ_{22} at the 300, 000 th cycle by WATMUS-based CPFEM simulation: (a) applied load profile on the y -face of the microstructure, (b) distribution of σ_{22} at $\tau = 0$ sec, (c) distribution of σ_{22} at $\tau = 1$ sec.....	76
Figure 4.8:	Schematic of cyclic dwell loading: (a) dwell load profile applied on y -face of the polycrystalline microstructure (b) segments with different maximum resolution.....	77
Figure 4.9:	Evolution of cycle-scale internal variables at an integration point in the microstructure: (a) $F_{0,22}^P$ (b) one of the slip system resistances g_0^α	77
Figure 4.10:	Evolution of $F_{0,22}^P$ with cycles by the WATMUS based CPFEM simulations: (a) volume averaged $F_{0,22}^P$, (b) distribution of $F_{0,22}^P$ at the 21 st cycle, (c) distribution of $F_{0,22}^P$ at the 500 th cycle.....	78
Figure 4.11:	Evolution of loading direction stress component σ_{22} along a material line in the microstructure evaluated at cycles $N=21$ and $N=500$ and $\tau = 121$ sec.....	78
Figure 4.12:	Sub-surface crack propagation in specimen #2 obtained from ultrasonic experiments and corresponding number of cycles to nucleation [4].....	79
Figure 4.13:	Statistically equivalent image-based simulated polycrystalline microstructures and corresponding $\langle c \rangle$ -axis orientations for: (a) specimen 1 and (b) specimen 2.....	80
Figure 4.14:	(a) $\langle c \rangle$ -axis orientation distribution and (b) microtexture distribution for statistically equivalent specimen microstructures 1 and 2.....	80
Figure 4.15:	Volume averaged stress-strain plot of statistically equivalent microstructures obtained from constant strain rate CPFEM simulations. A yield stress of 915 MPa is obtained for 0.2% elastic strain.....	81
Figure 4.16:	Evolution of nodal R_α with cycles N in specimen 1 at the crack nucleation site under dwell loading, evaluated at $\tau = 121$ sec.....	82
Figure 4.17:	Evolution of maximum R_α with N in specimen 2 at a crack nucleation site under dwell cyclic loading, evaluated at $\tau = 121$ sec.....	82
Figure 4.18:	Contour plots of (a) $\langle c \rangle$ -axis orientation, (b) F_{22}^P and (c) σ_{22} on a section of specimen 2 containing the predicted crack nucleation site. The CPFEM variables are at $N=620$ and $\tau = 121$ sec.....	83
Figure 4.19:	Plastic Flow Index (PFI) distribution for specimens 1, 2 and 3.....	84
Figure 4.20:	Variation of slip system Schmid factors with $\langle c \rangle$ -axis orientation: (a) maximum basal $\langle a \rangle$ Schmid factor (b) maximum prismatic $\langle a \rangle$ Schmid factor.....	85
Figure 4.21:	Volume fraction distribution of hard grains and corresponding surface area fractions of surrounding soft grains ($S_{AFS\ SG}$) in specimens 1, 2 and 3.....	86
Figure 4.22:	Evolution of R at the predicted crack nucleation site for specimens 1, 2 and 3.....	87

Figure 4.23:	Comparison of number of cycles to crack nucleation for different volume fraction (VF) of hard grains with surface area fraction of surrounding soft grains (SAFSSG) between 0.9 to 1.....	87
Figure 4.24:	Evolution of R_a with cycles at the predicted crack nucleation site for specimen 3, under 4 different fatigue loading cases described in section 4.6.3.....	88
Figure 4.25:	Evolution of R_a with cycles at the crack nucleation site of specimen 3 for the fatigue loading cases A, C, E, F and G.....	89
Figure 4.26:	Number of cycles to crack nucleation in specimen 3 for different hold times.....	90
Figure 5.1:	Distribution functions of the three components of Schmid factor for a microstructure labeled MS1: (a) $S F_x$, (b) $S F_y$, (c) $S F_z$	94
Figure 5.2:	(a) A virtual microstructure of MS2 with 500 grains, discretized into 102697 tetrahedron elements; (b) Stress-strain curves for microstructures MS1 and MS2 corresponding to x and y-directed strain loadings.....	95
Figure 5.3:	Sensitivity of the stress-strain curve to the hardness H for constant $E = 117 GPa$, $YS = 936 MPa$	97
Figure 5.4:	Distribution of (a) MoDF represented by the misorientation angle, and (b) TDF represented by the texture index $T I$ for virtual specimens MS3 and MS4.....	97
Figure 5.5:	Distribution of (a) MoDF represented by the misorientation angle, and (b) TDF represented by the texture index $T I$ for virtual specimens MS5, MS6 and MS7.....	98
Figure 5.6:	(a) Distribution of grain size GSDF and (b) macroscopic stress-strain response for MS8 and MS9.....	99
Figure 5.7:	Macroscopic stress-strain curves in the y- and z- directions.....	100
Figure 5.8:	Homogenized response parameters plotted as a function of macroscopic plastic work: (a) flow Stress obtained from pure shear loading in the xz plane, (b) stress components for the biaxial tension loading $\varepsilon_{yy} : \varepsilon_{zz} 1 : 1$ under plane stress conditions ($\sigma_{xx} = 0$).....	102
Figure 5.9:	Yield loci for the microstructural RVE M10: (a) 3D yield locus at $W_p = 0.1 MPa$, (b) $\sigma_1 - \sigma_3$ yield locus at $W_p = 0.1 MPa$, compared with the numerical data obtained from CPFE simulations, (c) evolution of the yield locus with plastic work increase corresponding to $W_p = 0.1, 1.0, 4.0$ and $10.0 MPa$	104
Figure 5.10:	$\sigma_1 - \sigma_3$ yield loci for microstructure M10, corresponding to $W_p = 0.1 MPa$ (a) Comparison of the Cazacu-Barlat model with 17 parameters with Hill's anisotropic model, (b) Comparison of the 17 and 10 (reduced) parameter C-B models.....	105
Figure 5.11:	Calibration of viscoplastic parameters λ_0 and n	108

Appendix B

Figure 3.1:	(a) Setup for in-situ ultrasonic experiment during fatigue tests and (b) schematic of data acquisition and fatigue control system.....	127
Figure 3.2:	Structure of each fatigue test segment as a function of applied load versus time.....	128
Figure 3.3:	(a) A typical acquired reflected ultrasonic signal, showing the signal time from which are plotted: (b) the normalised peak amplitude against number of cycles; (c) the normalised peak amplitude against applied fatigue load and (d) the subtracted and normalised peak amplitude against number of cycles.....	129
Figure 3.4:	Reflected ultrasonic signal amplitude is plotted for a range of numbers of cycles in (a) the original form and (b) the subtracted form. The acquired reflected ultrasonic signal is plotted at 22000 cycles in (c) the original form and (d) the subtracted form.....	131
Figure 3.5:	The model of the crack within the specimen used in this work: (a) a top view; (b) an end view and (c) a side view.....	132
Figure 3.6:	(a) An example of the acquired ultrasonic crack signal showing peak shifting; (b) time difference due to peak shifting plotted against number of cycles and (c) plotted versus applied fatigue load.....	133
Figure 3.7:	Real time monitoring of small fatigue crack in Ti 6242: (a) the schematic of the sample and the ultrasonic transducer and reflector wedge arrangement and (b) an example of the	

	ultrasonic time trace of backscattering signal. It shows that prior to application of the signal subtraction algorithm the signal from an initiated small fatigue crack in Ti 6242 is completely embedded in the microstructure scattering noise.....	134
Figure 3.8:	(a) A typical frequency spectrum acquired from the modulation data in the modulation regime and (b) a typical plot of the amplitude of the first harmonic of modulation plotted versus signal time (to be compared to a typical acquired reflected ultrasonic signal in fig. 3(a)).....	136
Figure 3.9:	(a) The peak amplitude of the first harmonic of modulation plotted against number of cycles and (b) the modulation index plotted against number of cycles.....	136
Figure 3.10:	Modulation data of the ultrasonic signal amplitude reflected from the crack are plotted for a range of numbers of cycles in (a) the original form and (b) the subtracted form. The amplitude of the first harmonic of modulation is plotted against signal time at 22000 cycles in (c) the original form and (d) the subtracted form.....	137
Figure 4.1:	(a) Time shifting plotted versus signal time and (b) local strain plotted versus signal time..	140
Figure 5.1:	(a) Schematics of the model microstructure showing α – Ti crystallites as circles and ellipses which completely fill the material volume. Regions of the microstructure with a common crystallographic orientation of crystallites are called microtextural regions (MTR); those regions are approximated by ellipsoids as indicated by dashed ellipses. Those ellipsoidal shapes are preferentially oriented in the sample. The orientation of crystallites in the MTR is described by the orientation distribution function with the width varying from sample to sample. Arrows in the crystallites indicate their preferred (mean) crystallographic orientation of the anisotropy axis c ; those preferred crystallographic orientations in different MTRs are not correlated and the material is assumed to have elastic isotropy macroscopically. (b) Geometry of ellipsoidal grains with the axes a_x, a_y, a_z and wave propagation \mathbf{p} and scattering \mathbf{s} directions. The ellipsoid radii enter the formalism solely through the spatial correlation function Eq. (A1) that can be interpreted as the correlation lengths [5.10, 5.11]. The wave propagation direction is arbitrary to the preferred orientation of ellipsoids in (a).....	144
Figure 5.2:	Normalized Gaussian orientation distribution function [5.22] $\exp(\cos \theta / 2\sigma) / \exp(1/2\sigma)$ versus distribution angle θ for different texture parameters σ	149
Figure 5.3:	Effective elastic constants $C_{ij}(\sigma)$ (in the matrix form) of the MTRs for duplex microstructure verse microtexture parameter σ . At $\sigma = 0$ the effective elastic constants are equal to those of the α – Ti crystallites $C_{ij}(0) = c_{ij}$. As σ increase the material becomes isotropic with $2C_{44} = C_{11} - C_{12}$	149
Figure 5.4:	The total attenuation coefficients (solid lines) versus the texture parameter σ at three frequencies of 5, 10 and 15 MHz; longitudinal wave propagates in the z axis direction. Also shown for 15 MHz are the MTR and crystallite components of attenuation; α_{MTR} is dashed-dotted line and $\alpha_{Crystallites}$ is dashed line. The MTR radii are $a_x = 0.2$ mm , $a_y = 0.3$ mm and $a_z = 0.5$ mm and the radius of crystallites is 0.005mm.....	152
Figure 5.5:	The total attenuation for longitudinal wave versus frequency with three texture parameters σ of 0.01, 0.1 and 1.0 when wave propagates in the z axis direction. The MTR radii is $a_x = 0.16$ mm , $a_y = 0.19$ mm and $a_z = 0.29$ mm and the radius of crystallites is 0.005mm.....	153
Figure 5.6:	Longitudinal wave attenuation coefficients versus frequency in three orthogonal directions of titanium alloy sample. Dashed lines represent measurement and solid lines are analytical model; the texture parameter is $\sigma = 0.075$; the average MTR radii are as in Table 5.1. The orientation angle of the averaged MTR ellipsoid is $\theta = 73^\circ$ relative to the axial direction of the sample in the axial and hoop plane. The top dotted lines are provided for comparison; they are calculated for the same geometrical parameters of the MTR as the actual one except the MTR elastic properties are for a single α Ti (Table 5.1) crystal ($\sigma = 0$). The texture parameter $\sigma = 0.075$ is obtained by shift of the dotted curves to match the experimental data.....	155

Figure 5.7:	Backscattering coefficient for the MTRs versus frequency in the axial, radial and hoop directions. The irregular dashed lines are experimental data and solid lines are the theoretical model; the texture parameter is $\sigma = 0.075$; the average MTR radii and orientation as in Fig 5.6. The top dotted line is provided for comparison; it is for the backscattering amplitude in the radial direction for an artificial material with the same parameters as the actual one except the MTR elastic properties are for a single α Ti (Table 5.1) crystal ($\sigma = 0$).....	157
Figure 5.8:	Calculated backscattering amplitude (dotted lines) with 50% increase of average MTR ellipsoid radii; the texture parameter is also increased to $\sigma = 0.092$ to match the attenuation data (the MTR texture decreases with the texture parameter increase). The irregular dashed lines are measurements. The calculated backscattering curves for the original radii and texture parameters as in Fig 5.7 are also shown for comparison by solid lines.....	160
Figure 5.9:	The same as in Fig 5.7 where dashed lines represent backscattering measurement. Calculations are for the average MTR radii proportionally increased by 25% with the texture parameter $\sigma = 0.084$ (dotted lines) or decreased by 25% with the texture parameter $\sigma = 0.067$ (dashed-dotted lines); the parameters σ were obtained by match with the attenuation curves. The measured values are bounded between the calculations for the increased and decreased MTR radii.....	160

List of Tables

Table 1: Anisotropic Elastic Constants for Ti- α [GPa].....	29
Table 2: Critical Resolved Shear Stress for Slip System Families for Ti- α_p	30

Appendix A

Table 3.1: Primary crack nucleation data by ultrasonic monitoring in dwell fatigue experiments on Ti-6242.....	52
Table 3.2: Comparison of predicted cycles to crack nucleation with experimentally observed life.....	64
Table 3.3: Microstructural features of predicted location of crack nucleation site in dwell fatigue of Ti-6242.....	66
Table 4.1: Comparison of the number of cycles to crack nucleation predicted by the model with experimental results for specimen 2.....	83
Table 4.2: Crystallographic features of the crack nucleation site predicted by the model and experiments for specimens 1 and 2.....	83
Table 4.3: Microstructural features at the predicted crack nucleation site for specimen 3.....	86
Table 4.4: Comparison of number of cycles to crack nucleation in specimen 3 for different cyclic loadings.....	88
Table 4.5: Number of cycles to crack nucleation in specimen 3 for dwell cyclic load with different hold times.....	89
Table 5.1: Average Schmid factors and yield strengths of microstructural specimens MS1 and MS2 in the x, y and z directions.....	96
Table 5.2: Parameters reflecting the mechanical response (stress-strain response) and distribution of MoDF and TDF in the microstructures of the virtual specimens MS3 and MS4.....	97
Table 5.3: Parameters reflecting the mechanical response (stress-strain response) and distribution of MoDF and TDF in the microstructures of the virtual specimens MS5, MS6 and MS7.....	98
Table 5.4: Stress-strain curve parameters for microstructure MS10 in the y- and z- directions.....	99
Table 5.5: Calibrated values of anisotropic parameters of equation (5.20), corresponding to $W_p = 0.1MPa$ for microstructure M10.....	103
Table 5.6: Calibrated values of Hill's anisotropic parameters, corresponding to $W_p = 0.1MPa$ for microstructure M10.....	103
Table 5.7: Calibrated values of the reduced Cazacu-Barlat parameters at $W_p = 0.1MPa$ for the microstructure M10.....	105
Table 5.8: Microstructure descriptors for different RVEs used to develop the HAPC model.....	110
Table 5.9: Coefficients A_j^i in equation (5.27).....	111

Table 5.10: Coefficients B_j^i in equation (5.27).....	111
Table 5.11: Coefficients C_j^i in equation (5.27).....	111
Table 5.12: Various coefficients in equation (5.27).....	112

Appendix B

Table 5.1: Elastic constants for crystallites and effective elastic constants and radii of MTRs.....	152
--	-----

Abstract

This project entails three complementary tasks with the objective of integrating them into a unified platform for advancing a novel probabilistic multi-scale modeling and sensing framework for fatigue life prediction. In the first task (*Ghosh, JHU*), an integrated system of novel spatial-temporal multi-scale computational models for image based modeling of deformation and fatigue crack nucleation in polycrystalline titanium alloys is developed. A novel wavelet transformation based multi-time scaling algorithm and homogenized continuum anisotropic plasticity and probabilistic fatigue crack nucleation models are developed. In the second task (*Rokhlin, OSU*), a comprehensive experimental methodology and inverse models are developed for structural health monitoring and noninvasive assessment of fatigue sensitive microstructures in Ti alloys. The aim is to provide realistic data input for computational predictive models under development in this program. In the third task (*Millwater, UTSA*), the distribution of weakest-link type material properties for larger material volumes is predicted from evaluation of small microstructural models with Extreme Value Theory. A property distribution associated with a grain boundary is used to extrapolate the distribution for a grain which is then used to predict the property distribution for a volume of the polycrystalline material.

Executive Summary

This project entails three complementary tasks with the objective of integrating them into a unified platform for advancing a novel probabilistic multi-scale modeling and sensing framework for fatigue life prediction. In the *first task* (*Ghosh, JHU*), an integrated system of novel spatial-temporal multi-scale computational models for image based modeling of deformation and fatigue crack nucleation in polycrystalline titanium alloys is developed. A novel wavelet transformation based multi-time scaling algorithm and homogenized continuum anisotropic plasticity and probabilistic fatigue crack nucleation models are developed. In the *second task* (*Rokhlin, OSU*), a comprehensive experimental methodology and inverse models are developed for structural health monitoring and noninvasive assessment of fatigue sensitive microstructures in Ti alloys. The aim is to provide realistic data input for computational predictive models under development in this program. In the *third task* (*Millwater, UTSA*), the distribution of weakest-link type material properties for larger material volumes is predicted from evaluation of small microstructural models with Extreme Value Theory. A property distribution associated with a grain boundary is used to extrapolate the distribution for a grain which is then used to predict the property distribution for a volume of the polycrystalline material.

Task 1: Computational Multiscale Analysis Framework for Fatigue Crack Nucleation in Metallic Polycrystalline Microstructures

PI: Somnath Ghosh

Personnel supported: P. Chakraborty, Ph.D; J. Thomas, M.S. student; Masoud Anahid, Post-Doc.

Completed Ph.D. Dissertations/M.S. Theses:

1. P. Chakraborty, Ph.D. 2011, Dissertation Title: “Wavelet Transformation Based Multi-Time Scale Method for Fatigue Crack Initiation in Polycrystalline Alloys”.
2. D. S. Joseph, Ph.D. 2010, Dissertation Title: “Wavelet Decomposed Multi-Time Scale Algorithm for Crystal Plasticity FEM Based Analysis of Cyclic Deformation”.

The PI (S. Ghosh) and his coworkers have created an integrated system of novel spatial-temporal multi-scale computational models for image based modeling of deformation and fatigue crack nucleation in polycrystalline titanium alloys. A non-local energy based crack model has been developed in terms stress fields and dislocation pile-up from crystal plasticity FE simulations. To accommodate a large number of cycles to failure, a novel wavelet transformation based multi-time scaling algorithm is proposed for accelerated crystal plasticity finite element simulations. Homogenized continuum anisotropic plasticity and probabilistic fatigue crack nucleation models are developed for being incorporated in structural analysis codes to facilitate efficient analysis. This project has resulted in a number of published and forthcoming journal and proceeding publications. Significant research interaction with researchers at the Air Force Research Laboratories has developed as a consequence of this project. Some of the research conducted by the PI that is relevant to this grant is summarized below.

This work has developed a comprehensive computational micromechanical deformation and failure analysis framework to address the challenging issue of fatigue crack nucleation in polycrystalline microstructures of metals and alloys. It incorporates (i) computer simulation of polycrystalline microstructures from experimental data, (ii) image-based crystal plasticity finite element models for metals and alloys, (iii) fatigue crack nucleation models, and (iv) multi-time scale model for crystal plasticity without scale-separation requirements. The following sections summarize key developments of this task. The results of these activities have been or will be published in references [1-11] and are detailed in Appendix A.

1.1 Image-Based Crystal-Plasticity FE Models for Deformation and Fatigue Crack Nucleation in Polycrystalline Aggregates

Image-based micromechanical computational models of polycrystalline metals and alloys account for actual grain morphology and crystallographic orientations, as well as mechanisms that govern deformation and failure. Various slip and micro-twinning modes govern the deformation of crystalline, e.g. face centered cubic (*fcc*), body centered cubic (*bcc*) or hexagonal close-packed (*hcp*) materials. Image-based rate and size dependent crystal plasticity models for deformation and creep have been developed for in titanium alloys (*hcp*) and nickel-based superalloys (*fcc*). For example, α/β forged Ti-6242 consisting of colonies of transformed β -phase in a matrix of primary α -phase has been modeled. Evolution of slip system deformation resistance is controlled by both statistically stored dislocations corresponding to homogenous plastic deformation and geometrically necessary dislocations that accommodate the incompatibility of the plastic strain field. Material parameters for individual slip systems are calibrated from micro-strain experiments. figure 1(a) shows the stress contour plots in a deformed polycrystalline Ti6242 microstructure under creep loading. The corresponding grain to grain average stresses are depicted in figure 1(b). Under creep or dwell loading, favorably oriented microstructural regions undergo significant plastic straining due to slip on favorably oriented slip systems. Compatibility requirements result in a time-dependent rise in the

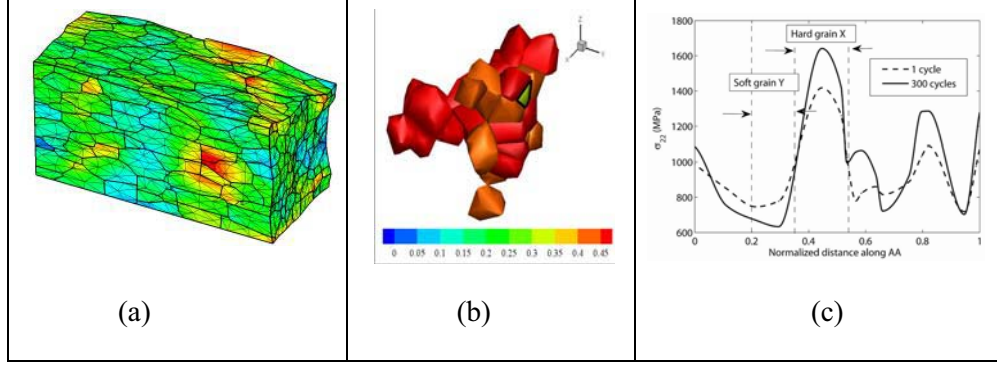


Figure 1: (a) CPFE model of a polycrystalline microstructure undergoing creep deformation; (b) local stress distribution in grains with a hot-spot (green); (c) evolution of stress distribution with cycles along a line showing load-shedding behavior.

local stress near the grain boundary in adjacent unfavorably oriented grains. This phenomenon is known as load shedding, in which time dependent local stress concentration near grain boundaries are caused by dislocation pileup in neighboring grains, as shown in figure 1(c). This local stress rise has been found to cause premature crack initiation in crystalline materials.

Premature fatigue failure in polycrystalline alloys, e.g. Ti alloys, under dwell loading conditions has been associated with low temperature creep induced early crack nucleation. Nucleation can dominate the fatigue process, occurring at 80-90% of the total life in these alloys. Thus, accurate assessment of the nucleation time is critical to predicting fatigue life. Experimental studies on crack evolution in Ti-6242 samples using quantitative tilt fractography and electron back scattered diffraction (EBSD) techniques in SEM show that crack initiates in a hard-orientation grain surrounded by soft-orientation grains undergoing creep deformation. We have developed a novel grain-level crack nucleation criterion utilizing evolving variables in crystal plasticity finite element simulations. The experimentally validated nucleation model is able to effectively predict the number of cycles as well as the crystallographic characteristics of the location.

The non-local crack nucleation model includes: (i) interaction of all active slip systems through plastic deformation gradients in the calculation of micro-crack opening, (ii) dislocation pile-up through the magnitude of plastic deformation gradient and the distance from grain boundary and (iii) mixed-mode cracking is considered.

1.2 Multi-Time Scaling Crystal Plasticity FEM for Cyclic Deformation in Polycrystalline Materials: WATMUS Algorithm

Fatigue life in metallic materials is typically of the order of thousands of cycles, depending on the material and loading conditions. A major shortcoming of CPFE simulations for fatigue life prediction is modeling the large number of cycles to complete failure or its nucleation. In single time-scale FE solutions using conventional time integration algorithms, each cycle is resolved into a number of time steps. In crystal plasticity calculations, this leads to exorbitant computational requirements. Consequently, 3D CPFE simulations for cyclic deformation have resorted to simulating a small number of cycles and subsequently extrapolating the results to thousands of cycles for making fatigue life predictions. Extrapolation or block integration methods can however lead to considerable error, particularly when it comes to the evolution of microstructural variables. The requirement of simulating a large number of cycles to reach the local states of crack nucleation and growth presents significant challenges due to the existence of different time scales, ranging from the scale of each load cycle to that of the component life. Methods of multi-scaling in the

temporal domain can avert some of these challenges. The method of direct separation of motions, based on locally periodic or nearly periodic assumptions in the temporal domain, cannot be extended to crystal plasticity solutions due to strong non-periodic response of evolving plastic variables and also due to localization in the spatial domain. In addition, they often invoke two-way coupling between time scales that requires solution of initial value problems at both time scales and does not provide any advantage over single time scale calculations. Asymptotic expansion based homogenization methods are also not suitable for CPFE simulations at or near fully reversed loading.

We have developed a multi-resolution wavelet transformation based multi-time scaling (WATMUS) algorithm for accelerated CPFE simulations to overcome the above deficiencies. The WATMUS methodology introduces wavelet decomposition of nodal displacements and all associated variables in the finite element formulation to decouple the response into a monotonic coarse cycle-scale behavior and oscillatory fine time scale behavior within each cycle. The wavelet decomposition naturally retains the high frequency response through the wavelet basis functions and transforms the low frequency material response into a “cycle scale” problem of coefficients undergoing monotonic evolution. No assumption of scale separation is needed with this method. Multi-resolution wavelet bases functions are effectively able to capture the rapidly varying fine scale response, which necessitates very small time steps in conventional single time scale FEM simulations. The number of wavelet coefficients can be optimally controlled through an adaptive control technique. The coarse cycle scale variables exhibit monotonic behavior that especially stabilizes with saturating hardness at higher levels of deformation. Relatively large increments, traversing several cycles at a time, can therefore be utilized in the numerical integration scheme with significantly enhanced efficiency. The WATMUS simulations exhibit approximately over 100 times speed-up, even with relatively low number of cycles. Subsequently, fine scale variations in temporal response at any point in a microstructural point can be recovered from values of wavelet coefficients and coarse scale state variables. As shown in figure 2(c), the WATMUS-based plastic strain evolution matches very well with the averaged fine scale CPFE simulations. Fine scale variations in temporal response at any point in a microstructural point can be recovered from values of the coarse scale state variables as shown in figure 2(d).

The novel framework introduced paves the way for a paradigm change in fatigue modeling of metals and alloys, consistent with the current thrust in integrated computational materials engineering or ICME.

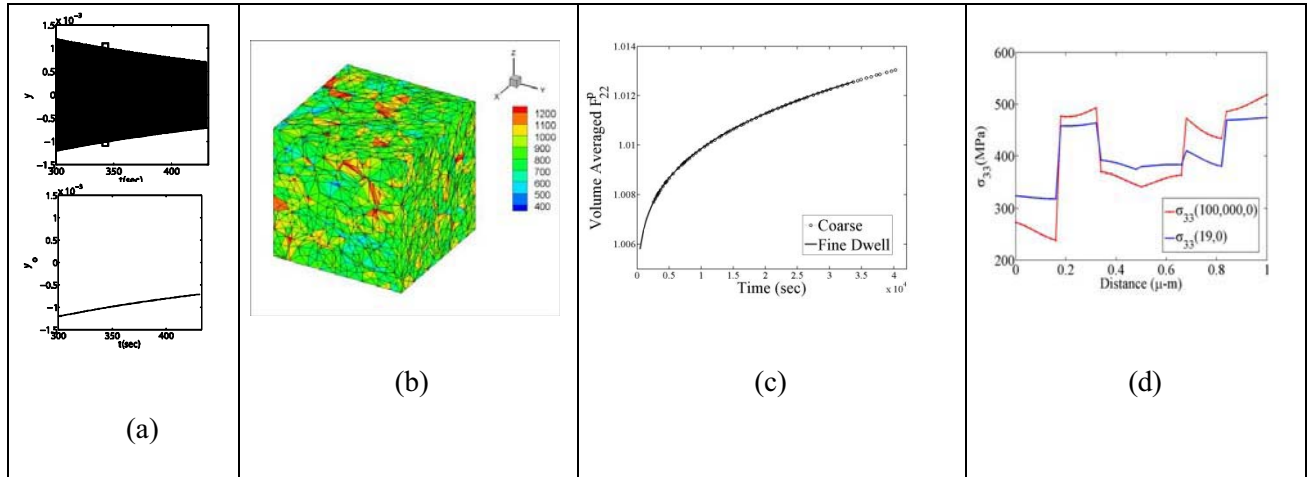


Figure 2: (a) Decoupling fine and coarse time scale responses for cyclic loading: (a) fine scale solution, (b) stress contour at 10000 cycles created by the WATMUS based CPFEM simulation, (c) comparison of the evolution of volume averaged plastic strain by the WATMUS-based and fine time scale simulations, (d) evolution of local stresses with cycles for rate dependent crystal plasticity.

1.3 Homogenized Constitutive and Fatigue Nucleation Models from Crystal Plasticity Simulations of Ti Alloys

Deformation and fatigue failure behavior of polycrystalline titanium alloys have strong dependence on the local microstructural characteristics. Reliable analysis of mechanical response and fatigue life in structures is contingent upon accurate description of material behavior using continuum-level constitutive models, with roots in the underlying microstructure. This work is aimed at developing continuum models of plastic deformation and fatigue crack nucleation in polycrystalline Ti alloys from detailed analysis of underlying polycrystalline microstructures. A homogenized, anisotropic plasticity constitutive (HAPC) model is developed from crystal plasticity finite element simulation results of microstructural representative volume elements. This model is able to capture important deformation characteristics of Ti-based alloys, which are pressure insensitivity, anisotropy, tension-compression asymmetry and kinematic hardening. The advantage of this model is that it avoids having to perform computationally expensive micromechanical analysis at each point in macroscopic simulations. An extension of this model is also introduced to account for the rate dependency observed in mechanical behavior of Ti alloys.

1.4 Organization of Appendix A

The details of Task 1 activities are described in Appendix A. It is divided into three subsequent chapters. In chapter 3, and image-based CPFE models for deformation and fatigue crack nucleation in polycrystalline titanium alloys is presented. A wavelet transformation induced multi-time scaling CPFEM for cyclic deformation (WATMUS) algorithm is developed in Chapter 4. Homogenized constitutive and fatigue nucleation models from CPFE simulations of Ti Alloys are developed in 5.

Task 2: Development of Multi-Scale Sensing and Evaluation Framework for Fatigue Life Prediction

PI: S. I. Rokhlin

Personnel supported: Jia Li , PhD student; George D Connolly, Post-Doc, L. Yang, Post-Doc

In this task the PI (S. I. Rokhlin) and his coworkers have developed a comprehensive experimental methodology and inverse models for structural health monitoring and noninvasive assessment of fatigue sensitive microstructures in Ti alloys. The aim is to provide realistic data input for computational predictive models under development in this project. *First* we describe the method for ultrasonically-monitored initiation and evolution of fatigue cracks in forged titanium alloy samples during fatigue testing. An in-situ surface wave acoustic method is applied during fatigue with an overlaid small low-frequency periodic loading, resulting in nonlinear modulation of the reflected ultrasonic pulses. The material is characterised by strong microstructure-induced ultrasonic scattering. To improve the signal-to-noise ratio a post-processing subtraction technique is introduced to enhance initiated crack detectability. The method is suitable for identification of small initiated and gradually-evolving fatigue crack features and is suitable for integration of microstructure-based fatigue life prognosis and multi-scale sensing. *Second* we describe a novel approach for ultrasonic imaging of damage precursors as anomalous plastic microstrain: ultrasonic microtexture backscattering as strain markers. It aims to detect anomalous local strain increase as fatigue crack precursors. The preliminary experimental data from fatigue experiments performed in this work on titanium samples have demonstrated and highlighted the precursors of crack initiation. The strain and the change in ultrasonic signals are linked dynamically as synchronized elasto-plastic strain variation due to fatigue loading. *Finally*, we describe experimental methodology and inverse models for ultrasonic volumetric assessment of fatigue sensitive microstructures in Ti alloys which are characterized by the presence of large microtextured regions (MTRs). A general model for elongated duplex microstructures is proposed for modeling scattering-induced ultrasonic longitudinal attenuation and backscattering in hexagonal polycrystals for application to titanium alloys. The material system consists of microtextured regions (MTRs) which are formed by much smaller α crystallites with preferred orientations. Their preferred orientation is represented by a modified Gaussian orientation distribution function. Scattering induced by MTRs and by crystallites is added to obtain ultrasonic attenuation in the medium. The effective elastic properties of MTRs are determined and used to obtain the scattering-induced MTR attenuation and backscattering. Crystallite attenuation is estimated by the untextured attenuation coefficient factored by a texture transition function. The total attenuation and backscattering are obtained by combining solutions for microtextured region attenuation and crystallite attenuation. Spectroscopic attenuation and backscattering measurements are performed on forged samples of titanium alloy. Reasonable agreement is found between experiment and the model predictions with a given texture parameter.

The results of these activities have been or will be published in references [12-21] and are detailed in Appendix B.

2.1 Dynamic Load-Lock-In Processing for Visualization of Small Fatigue Crack Initiation and Evolution

For practical application of robust fatigue analysis and structural health monitoring (SHM) methods leading to life prediction of aerospace materials and structures it is important to develop nondestructive capabilities in multi-scale sensing of damage evolution. A novel structural health monitoring (SHM) methodology is developed in this project, which utilize nonlinear-structural-load-modulated guided ultrasonic waves for real-time monitoring of damage initiation and evolution. The dynamic load-induced change of the crack opening/closure state modulates the sensor signature.

The difficulty of small crack detection and localization in Ti alloys is due to the presence of strong backscattering noise in titanium alloys as has been described in earlier studies. In contrast to the previous

work, the principal thrust of this study is tackling the difficulty in extracting meaningful information from the noise. This was achieved with the use of a novel subtraction technique applied to ultrasonic backscattering signatures that is dynamically synchronized with the applied cyclic load. Also, application of the dynamic subtraction method to data acquired during the modulation regime has resulted in a significant increase in crack SNR, improving crack detection and localization. It was shown to be effective in identifying just-formed fatigue cracks and as such, is particularly suited to online SHM for real-time monitoring.

The developed method for continuous ultrasonic monitoring of fatigue crack initiation, evolution and localization uses a novel multidimensional image representation of the large amounts of data collected in our methodology during fatigue testing. Image representation allows an extrapolation of identified patterns which is useful for distinguishing the crack from noise even at low signal-to-noise ratios. It has been shown that different cross-sections of the data representation provide continuous image patterns that facilitate the identification of reflected signals from the initiated damage. Measurement of the time differences between certain reflected signals can be used to quantify the evolution of the crack. Time domain subtraction at the same load level has been applied to improve the signal-to-noise ratio. Such a visualization approach allows greater understanding of crack initiation and evolution. As an example, figure 3 shows the effect of dynamic time domain subtraction with 20 times signal-to-noise ratio improvement.

In addition to the linear monitoring method the imaging modulation method has been developed and has been shown to allow earlier detection of the crack at early stages of the fatigue experiment, which is particularly relevant in health monitoring applications. This was achieved using a time domain subtraction method in conjunction with the modulation method, yielding great potential for improvements in early crack detection.

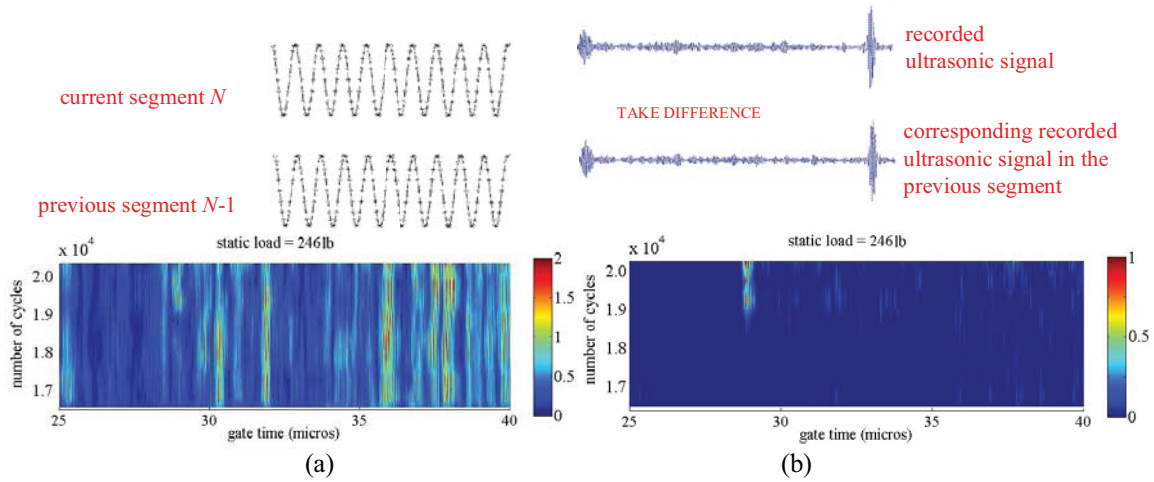


Figure 3: The peak amplitude of the ultrasonic signal versus time (mcsec); vertical axis is cycle number. On the left, the data is before dynamic subtraction processing, signal is imbedded in the backscattering noise. On the right, the signal representation after subtraction clearly showing the fatigue crack initiation and evolution (bright strip pattern, showing crack location within the sample and its initiation at approximately 18,500 cycles. Signal-to-noise ratio was improved by 20x. Above the images are cycling fatigue load segments (on the left) with points indicating moments of ultrasonic data acquisition; on the right acquired ultrasonic signatures (acquired at the same load but at a different segment of the cyclic loading; those signatures are used for subtraction). Large reflected signal at the end is reference reflection.

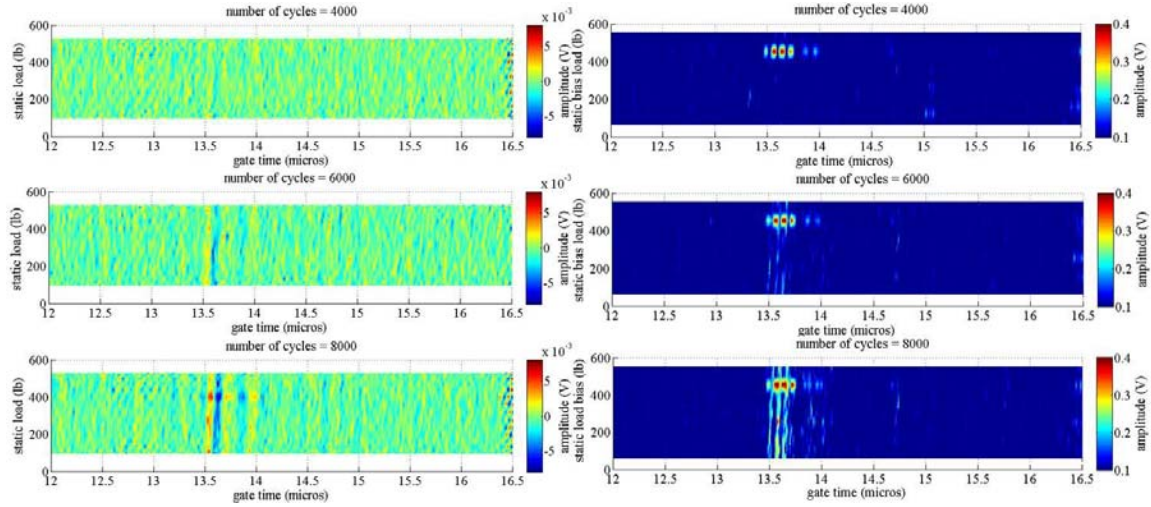


Figure 4: Ultrasonic crack detection in early stages of fatigue. Data shows crack detection in visualized the stress-cycle domain mode (a) fatigue cyclic data acquisition mode; (b) modulation mode of the data acquisition. Stress-cycle domain plots are useful in localizing the crack. Modulation can provide better information that the time traces alone.

2.2 Imaging of Damage Precursors as Anomalous Plastic-Microstrain: Ultrasonic Microtexture Backscattering as Strain Markers

Standard NDT or health monitoring techniques are able to detect fatigue cracks only in the latest stages of fatigue life of engine grade Ti alloys. The challenge of nondestructive detection of fatigue crack initiation, or more accurately small fatigue cracks, is addressed in item 2.1. An even more difficult problem, the solution of which is not available, is determination of fatigue damage precursors: i.e. such micro-regions of the sample where the initiation of a fatigue crack will occur with the highest probability. In this work we propose a method for dwell and cyclic fatigue damage precursor visualization based on backscatter signal (noise) variation with the applied fatigue load. We will illustrate this idea by preliminary experimental data, demonstrating such precursors appearing before and in the vicinity of the initiated fatigue crack in the titanium alloy sample studied.

To achieve the objective and the realization of the method to identify the damage precursors this work focused on the relative increase of plastic microstrains and thus dislocation build-up.

Recent research has shown that one main reason for early failure under dwell fatigue conditions in Ti alloys was the presence of large micro-textured regions (MTRs). In particular, it was shown that the crystallographic orientation and size of the MTRs are associated with facet-initiation sites of fatigue cracks. Physically, the MTRs are formed as regions of hexagonal α -phase crystallites with a common crystallographic orientation such that the combined MTR size noticeably outstrips the size of the primary α grains. Those MTRs can be considered as large grains with effective elastic properties that produce significant quantifiable ultrasonic scatter [18]. It was observed in this study that the scattering noise is significantly affected by fatigue loading not only for the results shown, but for a number of our earlier fatigue experiments for this alloy (those earlier digital ultrasonic data, that were analyzed in this study, were collected in our earlier fatigue experiments on Ti6242). The scattering amplitude variation is not systematic from sample to sample but the time stretching of the scattering signal is very consistent.

From our perspective, large local plastic deformations occur and accumulate prior to crack initiation. This local elasto-plastic strain variation is synchronized and associated with fatigue load, leading to excessive

grain size stretching and local variations of the ultrasonic scattering. At the frequencies studied, the random ultrasonic scattering signal is a result of interference of the scattering from grain boundaries of different grains. Large microplastic deformation changes this scatter interference and results in stretching of the backscatter signal in this microregion.

A peak-tracking (and, equally, trough-tracking) algorithm of ultrasonic backscatter noise evolution during fatigue cycling has been developed. It was applied to the shifts in the backscatter time signals in the data generated from fatigue experiments. This allows the measurement of the absolute time, and therefore of the time shift, of every backscatter signal peak and trough during the applied fatigue load cycles.

Fig. 5 shows the local strain plotted along the sample length (scaled with time) with increase of number of fatigue cycles (vertical axis). This figure clearly shows high straining around the crack position as it initiates and grows. The most important point from our objective is the persistent high local strain observed at early stages of the experiment at the future crack location. This, as we have discussed in the previous section, is an indication of excessive plastic strain in that part of the grain structure, increasing susceptibility to crack formation under cyclic loading.

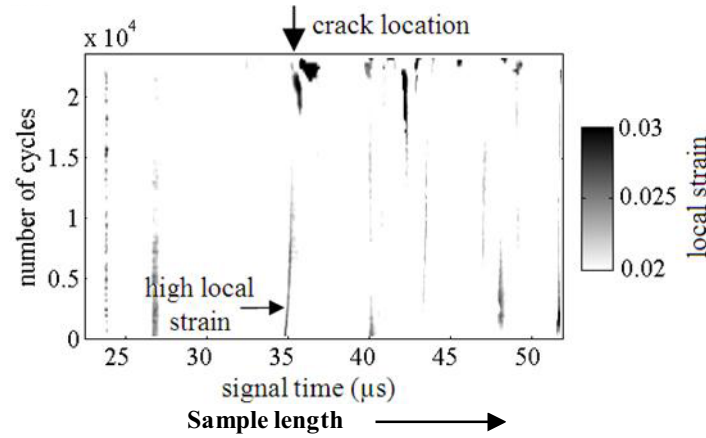


Figure 5: Local strain (gray pattern) along the sample length (scaled with time) with increase of number of fatigue cycles shown on the vertical axis (increase of pattern darkness represents increase of the local strain). High straining observed around the crack position as it initiates and grows. The persistent high local strain is observed at early stages of the experiment at the future crack location. This is an indication of excessive plastic strain in that part of the grain structure, increasing susceptibility to crack formation.

2.3 Experimental Methodology and Inverse Models for Ultrasonic Volumetric Assessment of Fatigue Sensitive Microstructure

Recent research in cyclic and dwell fatigue behavior of engine grade near-alpha titanium alloys have demonstrated that one of the main reasons for early fatigue damage initiation is the presence of large microtextured regions (MTRs) in these alloys. In general, MTRs (also known as macrozones) are formed as orientation clusters of a large number of small alpha crystallites with a common crystallographic orientation. Due to the detrimental effect of such microtextures on the dwell and cyclic fatigue properties it is highly desirable to determine the possible microtexture existence in manufactured parts and to characterize them nondestructively. Ultrasonic characterization using wave attenuation and backscattering may provide nondestructive methods to determine the presence of fatigue sensitive microtexture and its morphology [21, 15,18-20].

We have developed ultrasonic backscattering and attenuation models for scattering in Ti alloys to understand the relationship between ultrasonic scattering and the elongated microtextured microstructures. The microtexture is characterized by two size scales. The larger phase r is composed of elongated microtextured regions (MTRs) which by themselves are formed by smaller size hexagonal primary α crystallites (small phase α) with their preferred common orientation in the MTRs. The preferred orientation is not necessarily along the elongation direction of the MTRs. The model assumes that the directions of preferred orientation of crystallites in different MTRs are not correlated and their distribution is homogeneous; i.e. the medium is macroscopically isotropic (untextured). The material model explicitly describes the orientation distribution function of crystallites in MTRs with use of a modified Gaussian orientation distribution function. The ensemble elastic properties in MTRs are characterized by the effective stiffness using an average over the MTR region of the elastic properties of hexagonal crystallites with the specified orientation distribution function. The total attenuation and backscattering are considered as a sum of scattering by MTRs with effective elastic properties and additional scattering due to crystallites.

The experimental theoretical framework was developed to assess microstructural material characteristics using ultrasonic backscattering and for grading the size of microtexture from ultrasonic measurements. This was accomplished by developing an inverse experimental methodology for data processing usable by the inverse model developed in this research.

Ultrasonic attenuation and backscattering measurements on the forged Ti-6242 alloy samples were conducted and microtexture characteristics were obtained with the developed models. As an example of backscattering measurements is shown in figure 6.

Inverse experimental methodologies have been developed that have been applied together with our inverse models to assess microstructural material characteristics using ultrasonic backscattering and attenuation. We have determined that our effective model of the elastic properties and texture of the MTRs provides a consistent simulation framework to predict two independently measured ultrasonic characteristics of the same sample: attenuation and backscattering. We also have evaluated a sensitivity to microtexture parameters in the inversion model and have demonstrated the method's applicability for unique recovery of microtexture properties. Reasonable agreement was found between the experiment and the model predictions and direct comparison with orientation image microscopy (OIM) measurements of microtexture on the same samples

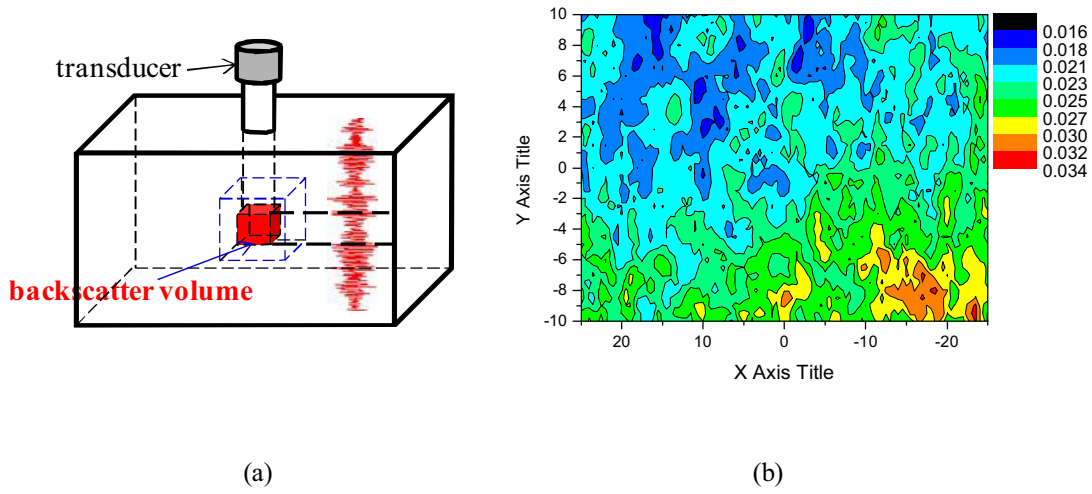


Figure 6: (a) Schematic of ultrasonic backscattering measurement showing ultrasonic transducer and its beam and an ultrasonic backscatter volume. Also, the experimental time domain ultrasonic backscattering signal (noise) resulting from ultrasonic pulse propagation over the sample thickness is shown. (b) Spatial distribution map of the backscattering ultrasonic signal averaged over the sample thickness. Color variations of the map correspond to microtexture size variation in the direction of wave propagation.

2.4 Organization of Appendix B

The details of Task 2 activities are described in Appendix I. It is divided into three subsequent chapters. In chapter 3, the developed methodology for dynamic load-lock-in processing for visualization of small fatigue crack initiation and evolution is described. Imaging of damage precursors based on ultrasonic microtexture backscattering is given in Chapter 4. Experimental methodology and inverse models for ultrasonic volumetric assessment of fatigue sensitive microstructure of Ti Alloys are provided in Chapter 5.

Task 3: Development of Localized Probabilistic Sensitivity Method to Determine Random Variable Region Importance

PI: H. Millwater

Personnel supported: G. Singh, Post-Doc,

Multi-scale modeling involves the computational modeling of materials at the microstructural level with the goal of improving the predictive performance of macroscopic material models. Difficulties in multi-scale modeling include properly addressing the inherent uncertainty in the microstructure and the corresponding material properties, bridging the gap between the microscopic and macroscopic length scales, and the computational expense of evaluating micro-scale models of the microstructure.

The methodology developed under this research was to explore a probabilistic framework to bridge the micro-macro gap for weakest-link types of material properties and to simplify the micro-scale model, greatly reducing the computational cost of multi-scale modeling.

A probabilistic framework for prediction of weakest-link type material property distributions from 2-grain models was proposed. Monte Carlo simulation and kernel density estimation were used to estimate the material property distribution of a grain boundary using a 2-grain model. Crystallographic orientation and grain boundary orientation were considered random variables. The non-asymptotic form of Extreme Value Theory was then employed to estimate the distribution of a grain with an uncertain number of neighboring grains. Non-asymptotic Extreme Value Theory was applied again to extrapolate the material property distribution to larger-volume microstructure models consisting of many grains. An example of the methodology is presented for identifying the applied uniaxial stress at which plastic slip initiates in a titanium alloy with a crystal elastic finite element model. The framework was verified by comparing the 2-grain Extreme Value Theory-predicted plastic slip initiation strength distribution with the obtained distribution from Monte Carlo simulation of larger scale finite element models (i.e. n -grain models, up to ~ 550 grain SVE). The methodology performs well for predicting the distributions of larger microstructure models but less so for smaller ones, for a much smaller computational cost. The results of these activities are being published in references [22] and are detailed below.

3.1 Homogenization-based Probabilistic Constitutive Model

The focus of much of the recent research in computational materials has been in digital representation of microstructures, constitutive relationships of different microstructural features, and multi-scale modeling [23]. An important aspect of multi-scale modeling is the development of a representative volume element (RVE), a volume of the microstructure of a large enough size that the distribution of the response of interest (i.e. yield strength) is in agreement with the distribution of the macroscopic material response. Determining the size of the RVE for a given response has been investigated [24]. Often the size of the RVE is too large to be computationally tractable for property identification. For this reason, statistical volume elements (SVEs) were developed. The SVE is smaller in general than the RVE and thus more computationally efficient to study, but is sampled many times to build up the statistics that would be captured by the RVE [25]. A natural question that arises concerning the SVE is: How small can an SVE be with minimal effect on the accuracy of the predicted macroscopic material property distribution? The smallest an SVE (measured in number of grains) could be is that of a single grain. This model would not include any effects on the response due to grain boundaries and as such is only suitable for modeling single crystals. The next simplest microstructure is that of 2 grains – a bicrystal. For some macroscopic material properties of interest, can a collection of 2-grain models be used to predict the macroscopic distributions? This work describes a probabilistic framework that attempts to obtain such macroscopic property distributions from small 2-grain models.

Certain material properties, such as elastic stiffness, are associated with volume-averaged behavior of the material, while other properties, such as crack initiation, depend on highly local physical processes. The local process-dependent properties typically involve a measure of some external or boundary condition such as life or strength/applied load such that when exceeded, a threshold at the local material point *and* the for the entire material has been reached. This type of behavior is called Weakest Link Theory (WLT) and has a long history of application in materials science. The statistics of WLT fall into the category of Extreme Value Theory (EVT), a subset of Order Statistics. Initially EVT was described by Weibull for characterizing the rupture of solids [26]; Batdorf revisited the concepts again for the strength of ceramics [27], and more recently Tryon and Cruse explored these concepts for fatigue life [28]. WLT is applied often in systems reliability analysis for series systems. The approach taken here in this work is to view the microstructure as a system of grains and grain boundaries, each of which has some probability distribution associated with the material property of interest.

3.1.1 Order Statistics and Extreme Value Theory

Order statistics is concerned with the distribution of the r^{th} smallest observation in a sample of n observations. For a given sample (X_1, X_2, \dots, X_n) , the observations may be sorted in increasing *order* and relabeled $(X_{1:n}, X_{2:n}, \dots, X_{n:n})$. The r^{th} order statistic is the r^{th} smallest value and labeled $X_{r:n}$. The extreme values, the minimum and maximum, are then $X_{1:n}$ and $X_{n:n}$.

If the sample is random, then uncertainty in X is described by its distribution $F_p(x)$. It is given the subscript “ P ” to identify it as the parent distribution that determines the distributions of $X_{1:n}, X_{2:n}, \dots, X_{n:n}$. The distribution of the r^{th} order statistic is then given in terms of $F_p(x)$ as

$$F_{r:n}(x) = \sum_{k=r}^n \binom{n}{k} (F_p(x))^k [1 - F_p(x)]^{n-k} = I_{F_p(x)}(r, n - r + 1) \quad (1)$$

With Extreme Value Theory, a subset of order statistics, the distribution [29] of the minimum for $r = 1$ reduces to a much simpler form as

$$F_{1:n}(x) = 1 - (1 - F_p(x))^n \quad (2)$$

The probability density function (PDF) is the derivative of the cumulative distribution function (CDF).

$$f_{1:n}(x) = n(1 - F_p(x))^{n-1} f_p(x) \quad (3)$$

3.2 Homogenization-based Probabilistic Constitutive Model

The probabilistic framework developed builds the distribution of the response of the macroscopic material from the distribution of the response of an SVE using order statistics. The key steps in the methodology are:

1. Sample the small-scale model with Monte Carlo simulation (MCS) to develop the distribution of the small-model response
2. Apply Extreme Value Theory and Order Statistics to estimate the distribution of the response of the large-scale model from the small-model distribution

Each of these steps is discussed in detail in the following subsections.

3.2.1 MCS of Small-Scale Model for Response Distribution

A small-scale microstructural model must be developed. This subsection discusses the issues involved with development of the small-scale model.

The extreme value methodology described in section 3.2.2 was developed for material properties associated with grain boundaries. As such, the small-scale model is a model of a grain boundary and consists of a 2-grain or bicrystal microstructure. Each grain must have a crystallographic orientation following the orientation distribution function (ODF) of the bulk material. Also the grain boundary physical orientation must be representative of the grain boundary physical orientation distribution of the bulk material.

A small volume is associated with the grain boundary. The boundary conditions applied to the small-scale model should be representative of the conditions experienced by the volumes about grain boundaries in the bulk material. In practice, this information is not readily available, and the mean stress or strain of the material is used instead.

Monte Carlo simulation (MCS) of the small-scale model involves sampling the distributions of the input variables: the crystallographic orientation of each grain, the orientation of the grain boundary (which is assumed planar), and the boundary conditions. The boundary conditions are given a deterministic value when their distribution is unknown.

The weakest link-type response of the small-scale model associated with the material property of interest (for example, crack initiation life) is collected from each evaluated realization of the model. With a large sample size, kernel density estimation may be used to obtain the distribution of the model response.

3.2.2 Estimate RVE Response Distribution with Extreme Value Theory and a Small-Model Response Distribution

Development of the large-model material property distribution is facilitated by the application of Extreme Value Theory and the small-model material property distribution.

The material property distribution for a 2-grain model was obtained in the previous step. This distribution was used as an approximation of the property distribution for an arbitrary pair of neighboring grains in the bulk material. The key assumption made in this methodology was that the small-model distribution is a good approximation of the distribution of the behavior of neighboring grains in the bulk material.

Based on this approximation, the small-model distribution was then used as the parent distribution with extreme value theory and order statistics to develop the distribution for the large-model. The parent distribution was denoted by its CDF, $F_p(\sigma_p)$.

The distributions for order statistics and EVT given in equations 1 and 2 are for the case where the n samples are independently and identically distributed. Applying these equations to the property distribution of different grains in an SVE will introduce some bias because the property distribution of one grain depends on the same factors that also affect other neighboring grains (i.e. orientation affects misorientation) and their distributions are not independent. The verification tests in section 3 indicate little bias is introduced by making the independence approximation.

3.2.2.1 Application of Order Statistics to determine the large-model property distribution from the small-model property distribution

Given the parent distribution for a grain boundary (i.e. the material property distribution CDF), $F_p(\sigma_p)$ and weakest link theory, the value of the property of a single grain with N adjacent grains is the minimum value of the N grain boundaries. Applying extreme value theory and modifying Eqn. 2.

$$F_{1:N}(\sigma_p) = 1 - (1 - F_p(\sigma_p))^N \quad (4)$$

The corresponding PDF is

$$f_{1:N}(\sigma_p) = N(1 - F_p(\sigma_p))^{N-1} f_p(\sigma_p) \quad (5)$$

Eqn. 4 assumes the value of N is deterministic. Selecting a grain at random in the material microstructure, the number of its neighboring grains, N is a random variable with a probability mass function [30]. An example is given in figure 7.

The uncertainty in N may be addressed with the total probability theorem [31]. The total probability theorem describes the probability of event A , considering all the conditional probabilities of event A given the probability of other events E_i .

$$P(A) = P(A|E_1)P(E_1) + \dots + P(A|E_N)P(E_N) = \sum_N P(A|E_i)P(E_i) \quad (6)$$

Eqn. 4 is modified with Eqn. 6 to account for the uncertainty in the number of neighboring grains of a randomly selected grain with

$$F_{1:N}(\sigma_p) = \sum_{N=1}^{\max N} [1 - (1 - F_p(\sigma_p))^N] P_N \quad (7)$$

where P_N is the probability that a grain will have N neighbors. This gives a model of the property distribution of a single grain.

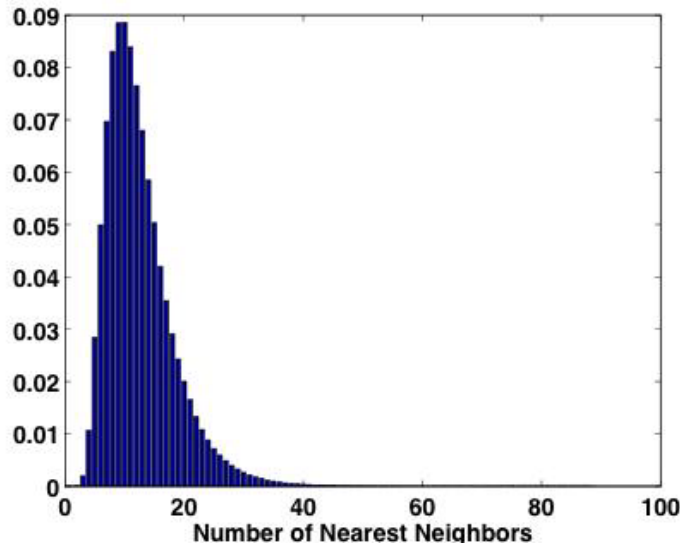


Figure 7: PMF of Number of Nearest Neighbors – Uncertainty in the number of neighboring grains for a given grain of interest can be accounted for with the total probability theorem.

To predict the property distribution considering multiple grains in a polycrystalline specimen, Equation 7 must be modified such that grain boundaries are not effectively counted twice. To do so, the number of neighbors N , in the exponent is divided by 2 in Equation 8.

$$F_{1:N}^*(\sigma_P) = \sum_{N=1}^{\max N} \left[1 - (1 - F_P(\sigma_P))^{N/2} \right] P_N \quad (8)$$

$$f_{1:N}^*(\sigma_P) = \sum_{N=1}^{\max N} \left[\frac{N}{2} (1 - F_P(\sigma_P))^{N/2-1} f_P(\sigma_P) \right] P_N \quad (9)$$

The weakest grain in an n grain model has the EVT predicted distribution in Equation 10

$$F_{1:n}(\sigma_P) = 1 - (1 - F_{1:N}^*(\sigma_P))^n \quad (10)$$

$$f_{1:n}(\sigma_P) = n (1 - F_{1:N}^*(\sigma_P))^{n-1} f_{1:N}^*(\sigma_P) \quad (11)$$

The Extreme Value Theory-based homogenization strategy is summarized in figure 8.

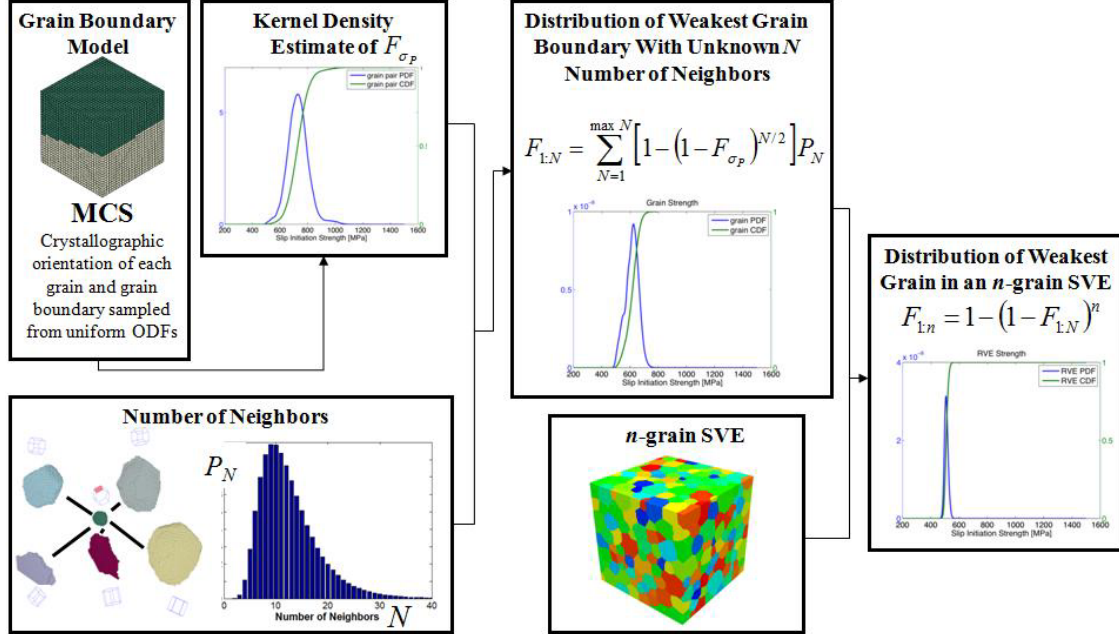


Figure 8: Extreme Value Homogenization Strategy – Monte Carlo simulation and kernel density estimation are used to develop the distribution for a grain boundary. Along with the distribution of the number of neighboring grains, extreme value theory is used to predict the distribution for a single grain based on the weakest grain boundary. The number of grains in a volume of interest is then used with extreme value theory to predict the distribution for a given volume based on the weakest grain.

3.3 Application of Homogenization Methodology to Plastic Slip Initiation Model

The methodology presented in section 3.2 is demonstrated using a model of plastic slip initiation. The distributions for the slip initiation strength predicted with the EVT framework for various size SVEs are presented and compared with results from MCS of SVE FE analyses.

3.3.1 Model of Slip Initiation in Ti- α

Titanium alloys are often used in aircraft structures and gas turbine engine components. Their high strength, low density, resistance to corrosion, and ability to withstand higher temperatures has lead to their widespread application [32]. Titanium alloys are generally classified into 3 categories α , $\alpha + \beta$, and β , depending on the relative presence of the α phase, which has a hexagonal close-packed (*hcp*) crystal structure, and the β phase, which is body-centered cubic (*bcc*). Examples of $\alpha + \beta$ alloys commonly used in aircraft include Ti-6Al-4V and Ti-6242. Depending on mechanical processing and heat treatment, they present microstructures ranging from fully lamellar to bi-modal to fully equiaxed, with varying volume fractions of α and β , though the α phase is the predominant phase. The specific microstructure studied here is fully equiaxed. The beta phase was not modeled, so the quantitative results of this study may only correspond to microstructures with very high volume fractions of the alpha phase. The microstructure modeled is a collection of equiaxed grains of Ti- α . Each grain has a different crystallographic orientation.

Each grain has the same elastic material properties in the form of a stiffness tensor, just rotated according to its crystallographic orientation. The *hcp* Ti- α_p phase is modeled as transversely isotropic. The elasticity tensor of transversely isotropic materials has 6 independent constants that describe the elastic response of the material. The elasticity tensor selected for this study was that given in [33].

The low symmetry of the *hcp* crystal structure and the elastic and plastic anisotropy of the α_p phase have important consequences for the yield strength and creep and fatigue life of titanium alloys. The deformation of titanium alloys is known to be sensitive to crystallographic texture [34] and microtexture [35]. The anisotropic stiffness and varying crystallographic orientations of each grain give rise to non-uniform stresses in the microstructure, even in the presence of uniform macroscopic loading [36]. These non-uniform stresses give rise to local plastic slip in the material. Observations of local deformation of Ti-6Al-4V with digital image correlation (DIC) show this strong inhomogeneity is established early in the loading of the material, and continues until failure [36].

The *hcp* crystal lattice has several slip system families. Slip in crystals generally occurs on planes in the lattice with relatively high close packing of atoms. These slip planes can be specified by the vector normal to the plane. For a given slip plane, dislocation glide (slip) occurs in a certain slip direction when the shear stress resolved on that plane in that direction exceeds the critical resolved shear stress τ_{CRSS} for that slip system. Slip systems that are identical under a rotation of the crystal lattice due to crystallographic symmetry are collected in a set called a family. The three slip system families for Ti- α_p in which plastic slip is most commonly observed are the prismatic, basal, and pyramidal. These slip systems for Ti- α_p are given in Miller-Bravais indices and presented in figure 9. Only the prismatic, basal, and first order pyramidal $\langle a \rangle$ direction, and first order pyramidal $\langle c+a \rangle$ direction slip systems were studied.

Table 1. Anisotropic Elastic Constants for Ti- α [GPa]

$C_{11} = C_{22}$	C_{33}	C_{12}	$C_{13} = C_{23}$	C_{44}	$C_{55} = C_{66}$
162.4	180.7	92.0	69.0	46.7	35.2

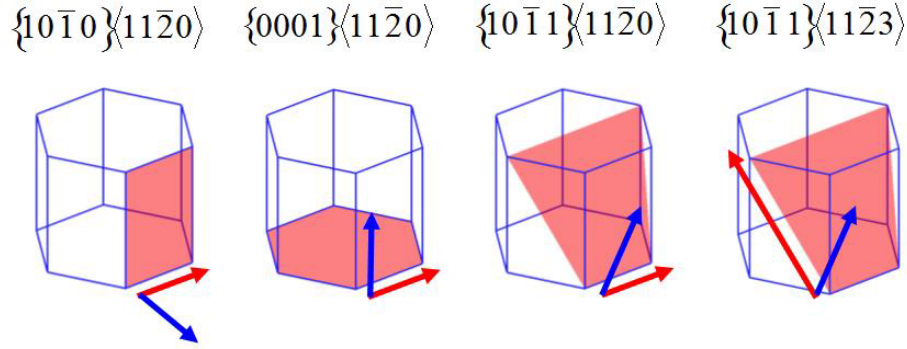


Figure 9: Prismatic $\langle a \rangle$, Basal $\langle a \rangle$, First-Order Pyramidal $\langle a \rangle$, and First-Order Pyramidal $\langle c+a \rangle$ Slip System Families for H.C.P. Crystal Lattices – The hexagonal unit cell is in blue. The slip planes are red with blue arrows normal to the plane. The slip directions are given by a red arrow. Note that of the slip systems modeled, only the pyramidal slip system provides for slip in the $\langle c \rangle$ direction.

Table 2. Critical Resolved Shear Stress for Slip System Families for Ti- α_p

Slip System Family	τ_{CRSS} [MPa]
Prismatic $\langle a \rangle$	384
Basal $\langle a \rangle$	444
Pyramidal I $\langle a \rangle$	404
Pyramidal I $\langle c+a \rangle$	536

For the α^{th} slip system, the resolved shear stress on the slip plane with unit normal \vec{n} and slip direction \vec{m} is found with

$$\tau_{RSS}^{\alpha} = m_i^{\alpha} \sigma_{ij} n_j^{\alpha} \quad (12)$$

The slip plane normal and slip direction vectors are found relative to the local material coordinate system. They must be transformed into the specimen coordinate system to be implemented with the stresses from ABAQUS in the above equation.

The critical resolved shear stress for each slip system family is given in table 2 above. There is a large variation in the values reported in the literature. Researchers tend to agree that the $\langle c+a \rangle$ slip systems have a higher resistance to slip than the $\langle a \rangle$ direction slip systems. The values used in [37] were selected for this study.

By comparing the critical resolved shear stress with the magnitude of the resolved shear stress given an applied uniaxial load, the applied uniaxial load necessary for plastic slip initiation may be extrapolated. The σ_p is the applied uniaxial load necessary to initiate plastic slip. A value for σ_p can be found for every location in the model and the location with the smallest value of σ_p limits the allowable uniaxial load that can be applied to the model without initiating slip. This weakest link behavior suggests application of extreme value theory.

3.3.2 Distributions predicted by 2-grain model

A small-scale microstructural finite element model was developed with the ABAQUS software. The model is a 2-grain or bicrystal microstructure. Each grain is modeled as half of a cube, and their shared face makes up their grain boundary. A perfect bond was assumed at the grain boundary. The model was meshed with a grid of 28x28x28 elements that each had dimensions 0.5x0.5x0.5 microns. The geometry is presented below in figure 10.

Monte Carlo simulation (MCS) was performed with the small-scale model and the distributions of the input variables: the crystallographic orientation of each grain and the orientation of the grain boundary (which is assumed planar). For equiaxed grains with no texture, a uniform orientation distribution for each crystallographic orientation and the grain boundary orientation was assumed. For each sample, a random rotation was applied to the material orientation of each grain to generate that grain's crystallographic orientation using unit quaternions [38]. The same was done for the grain boundary orientation.

A linear elastic finite element analysis was performed for each sample to obtain the stress state, σ_{ij} , at each integration point in the model. The stress tensor at the integration points in the model was used to calculate the resolved shear stress on each of the slip systems for primary alpha titanium. This was then compared with the critical resolved shear stress for each slip system.

The slip initiation strength was taken as the smallest uniaxial load necessary to activate any slip system at any integration point in the model. With a large sample size, kernel density estimation was then used to obtain the distribution of the slip initiation strength at a grain boundary.

The 2-grain model was exercised with Monte Carlo simulation for a sample size of 1000 realizations, varying the grain boundary and crystallographic orientations according to a uniform orientation distribution. A kernel density estimate based on this data was used to obtain $F_p(\sigma_p)$. It is assumed the 2-grain model is a good approximation of a pair of neighboring grains in a polycrystal. This “parent” distribution was used to predict the distribution for all of the boundaries associated with a random grain. The 2-grain parent distribution was then used in equation 6 with the distribution for the nearest neighbors given in figure 11 to obtain the distribution for the strength associated with the boundaries of a random grain. This child distribution is then used to predict the distribution for a polycrystal. The predicted grain strength distribution was then used as a parent distribution in 10 to obtain the distribution of the slip initiation strength of a polycrystal of 531 grains.

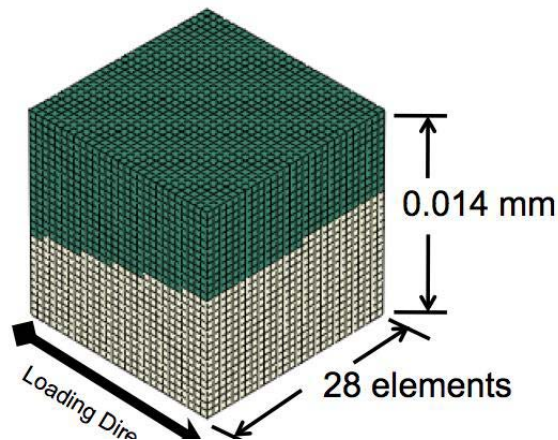


Figure 10: SVE Geometry – The anisotropic grains are green and gray. The size of the SVE is the size of the average grain in the material studied.

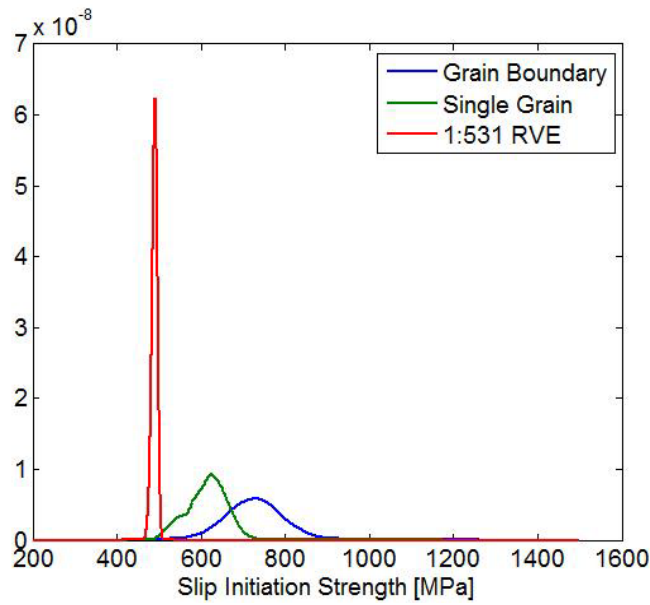


Figure 11: Comparison of Predicted Slip Initiation Strength Distributions – The mean and variance decrease for each successive level. The predicted RVE distribution is for a polycrystal of 531-grains.

All of the 2-grain model-predicted slip initiation strength distributions have a mean less than the macroscopic yield strength for titanium, as expected. A stronger verification of the framework was performed by running crystal elastic finite element analyses on large polycrystal models for comparison as described in the next section.

3.3.3 Distributions of larger SVEs

Verification tests with realizations of SVEs with more than 2 grains were performed with ABAQUS. Realizations of the statistically equivalent microstructures were generated in voxel form with DREAM.3D. Each realization was a sample of equiaxed grains with no crystallographic texture. A truncated log-normal grain size distribution was used, preventing simulation of excessively large grains [39]. The voxels were then used as brick elements in a finite element mesh for analysis with ABAQUS. Three different volumes were considered to assess the 2-grain model's prediction: 0.01x0.01x0.01 mm, 0.03x0.03x0.03 mm, and 0.09x0.09x0.09 mm.

3.3.3.1 ~6-grain SVE

The first verification example is shown in the upper left of figure 12. It was a cube with side of length 0.01mm. The number of realizations generated for the verification test was 1,234. The mean number of grains in each SVE was 5.6 grains and the standard deviation was 1.8 grains. A correlation of -0.35 was found between the extrapolated slip initiation strength and the number of grains in the SVE.

The obtained distribution of the slip initiation strength for the ~6-grain model from MCS is presented in the lower left of figure 12. The mean value was 681 MPa and the standard deviation was 59 MPa. The MCS distribution is compared to the predicted distribution from EVT. The predicted distribution has a mean of 575 MPa and standard deviation of 38 MPa. The predicted distribution differs significantly from the actual. The lower bounds of each are similar and the predicted distribution is conservative, but the means differ by 106 MPa and the EVT predicted variance is not conservative.

3.3.3.2 ~38-grain SVE

The second verification example is presented in the upper center of figure 12 and is a cube with side of length 0.03mm. The number of realizations generated for the verification test was 1,134. The mean number of grains in each SVE was 38 grains and the standard deviation was 5.1 grains. A negligible correlation of -0.114 was found between the extrapolated slip initiation strength and the number of grains in the SVE.

The obtained distribution of the slip initiation strength for the ~38-grain model from MCS and is presented in the lower center of figure 12. The mean value was 579 MPa and the standard deviation was 33 MPa. The predicted distribution has a mean of 524 MPa and standard deviation of 20 MPa. The predicted distribution differs slightly from the actual. The lower bounds of each are similar and the predicted distribution is conservative, and the means differ by 55 MPa. However, the EVT predicted variance is not conservative.

3.3.3.3 ~531-grain RVE

Due to the computational expense, only 10 full scale models were fully analyzed for slip initiation strength. An example of the equiaxed microstructure is shown in the upper right of figure 12. It is a cube with side of length 0.09mm. The mean number of grains in each realization was 531 and the standard deviation was 7.6 grains. The small sample size implies a larger prediction variance than the other size RVEs tested. The sample mean of the uniaxial stress necessary to initiate plastic slip was found to be 522 MPa and the sample standard deviation was 19 MPa, with slip occurring on the basal plane. The EVT predicted distribution has a mean of 494 MPa and a standard deviation of 8 MPa. The means differs by 28 MPa and the standard deviations differ by 11 MPa.

As discussed previously, it is expected that local, microscopic yielding will first take place at a lower applied uniaxial stress than that of macroscopic yielding. The range of the macroscopic yield strength of Ti-6Al-4V is ~800-1000 MPa, so the microscopic yielding results for the large model fall well below the upper limit imposed by the macroscopic yield strength.

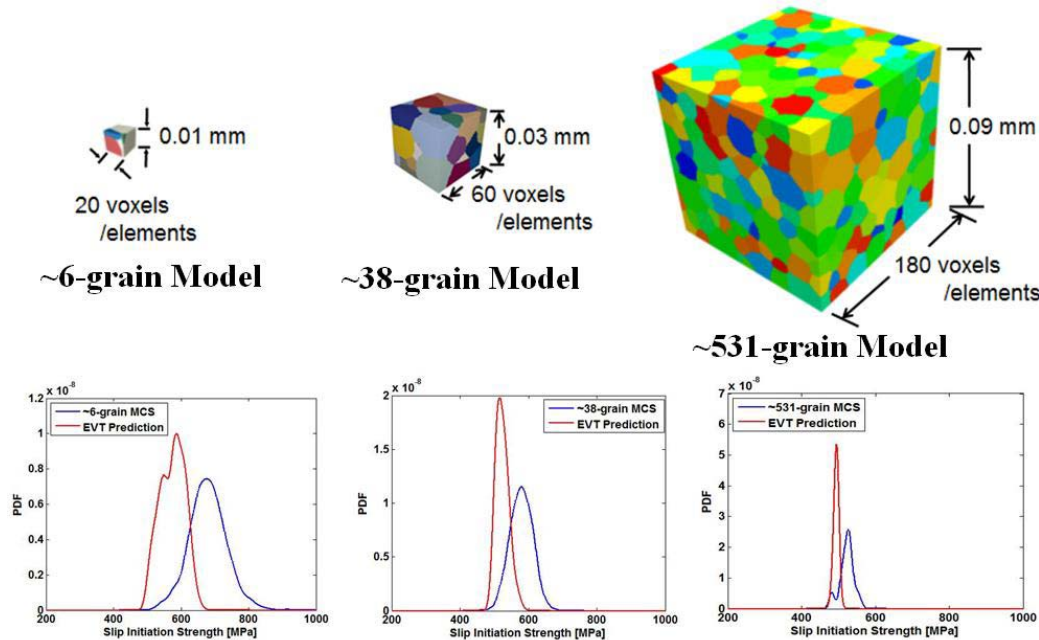


Figure 12: Comparison of 2-grain EVT predicted distribution and MCS distribution for 3 different volumes – The distributions shift to the left as the size of the model increases. The EVT predicted distribution agrees more closely with the MCS results as the size of the model increases.

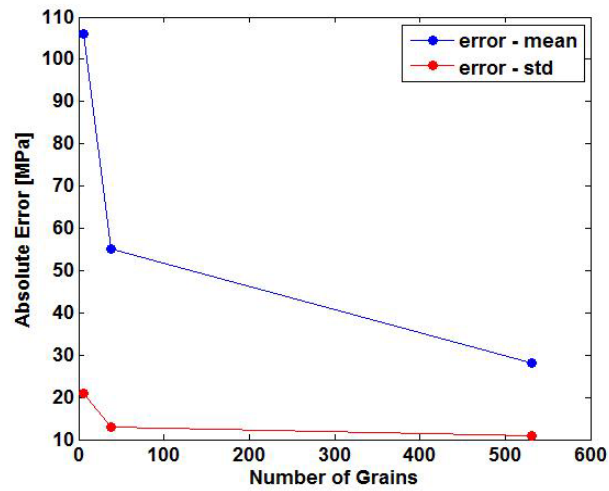


Figure 13: Difference Between Predicted and Actual Slip Initiation Strength Distributions – The difference between the Extreme Value Theory predicted polycrystalline slip initiation strength distribution and the “actual” distribution found from Monte Carlo simulation of polycrystalline synthetic microstructures is plotted. The error decreases as the size of the simulated model increases.

Figure 13 shows the decreasing difference between the 2-grain EVT predicted distribution and the actual MCS estimated distribution as the SVE size increases.

4. Conclusions

A novel grain-level crack nucleation criterion for dwell fatigue in polycrystalline titanium alloys is developed. The model utilizes evolving variables that are computed in crystal plasticity finite element (CPFE) simulations of polycrystalline microstructures to construct a criterion that is able to effectively predict the number of cycles to crack nucleation, as well as the characteristics of the local site. The basic idea behind this model is that dislocations piled up against the grain boundary in a soft grain can produce a wedge type micro-crack in an adjacent hard grain. Fatigue cracks are observed to nucleate with stress concentration caused by the load shedding phenomenon between adjacent hard and soft grains. The load shedding induced crack nucleation criterion depends on the local stresses in the hard grain as well as the non-local plastic strain gradients in adjacent soft grains. A direct approach is proposed in this work to evaluate the micro-crack length in the hard grain using the distribution of geometrically necessary dislocations inside a contiguous soft grain. The local effective stress required for crack nucleation is inversely related to the non-local plastic strain gradients in the neighboring soft grain. The proposed crack nucleation model can be reduced to a form similar to the Cottrell-Petch model in the limit, if only one slip plane of edge dislocations is considered. The critical parameter in the crack nucleation model is calibrated using experimental results of ultrasonic crack monitoring in dwell fatigue experiments and then validated against limited experimental data through predictions of the number of cycles to failure as well as the critical features of the failure site for dwell fatigue experiments. The general agreement with experiments is very satisfactory. In conclusion, the proposed model is adequate for identifying fatigue crack nucleation sites and the corresponding number of cycles in a polycrystalline aggregate.

The effects of critical morphological and crystallographic characteristics of the microstructure and loading conditions on grain-level crack nucleation in polycrystalline Ti-6242 microstructures are investigated. Crystal plasticity FEM simulations of statistically equivalent microstructures, in conjunction with a physically motivated crack nucleation model, are used to provide a mechanistic approach towards predicting this behavior. A non-local crack nucleation model in terms of the local stresses near the hard grain boundary and the piled-up dislocations in the adjacent soft grain is implemented to predict nucleation in the hard grain. The critical crack nucleation parameter value is calibrated using a combination of dwell fatigue experiments and CPFEM simulations performed on Ti-6242 specimens. Crack nucleation studies are performed for cyclic loads with the maximum applied stress levels at 90 – 95% of the macroscopic yield strength. Simulations with different cyclic load patterns suggest that fatigue crack nucleation in Ti-6242 strongly depends on the dwell cycle hold time at maximum stress. This is in compliance with experimental observations.

A homogenized, anisotropic plasticity constitutive (HAPC) model for Ti alloys is developed. In particular, this model includes an anisotropic yield function with a direct connection to the morphology and crystalline structure of the polycrystalline microstructure that can be incorporated in any macroscopic FEM code. The advantage of this model is that it avoids having to perform computationally expensive micromechanical analysis at each point in macroscopic simulations. It is able to capture important deformation characteristics of Ti-based alloys, which are pressure insensitivity, anisotropy, tension-compression asymmetry and kinematic hardening.

A systematic sensitivity analysis is conducted to establish the dependence of mechanical response on microstructural crystallographic and morphological parameters. This analysis concludes that average Schmid factors for three orthogonal directions and grain size distributions are important microstructural descriptors that should be incorporated in the homogenized yield functions. Parameters in the anisotropic yield function following the Cazacu-Barlat framework are calibrated from homogenization of CPFE results of polycrystalline microstructure simulations. The anisotropy parameters in the homogenized yield function are found to be functions of the microstructural descriptors, but evolve with plastic work. The functional forms of the parameters overcome limitations of constant anisotropy parameters that are conventionally assumed in anisotropic plasticity models. Comparison of the anisotropic HAPC model results with homogenized micromechanics results shows excellent agreement. The HAPC model has a significant efficiency advantage over the micromechanics models and is hence a very effective tool in making macroscopic deformation predictions with explicit reference to the microstructural composition.

An extreme value theory framework was developed for predicting polycrystalline model material property distributions from bicrystal model experiments. The methodology has some discrepancy in predicting the distribution of slip initiation strength of relatively small scale microstructure models, yet performs well for larger microstructure models. Potential causes of discrepancy between the EVT predicted distribution and the actual distribution may be due to non-local effects or the fact that grain size and shape were ignored in the 2-grain model. Incorporating their effects may improve the ability of the proposed framework to predict material property distributions. The successful demonstration of the proposed framework for the larger models indicates the methodology may serve as a useful technique for estimating the distribution of certain material properties at a much smaller computational cost than that of exercising full large scale models.

An investigation of the in-situ real-time ultrasonic monitoring of fatigue crack initiation and evolution on Ti-6242 specimens is performed. A novel multidimensional image representation of the large amounts of data collected during modulation fatigue testing has been introduced. It has been shown that different cross-sections of the data representation provide continuous image patterns that facilitate the identification of reflected signals. The measurement of the time differences between certain reflected signals can be used to quantify the evolution of the crack. Time domain subtraction has been applied to remove the initial pit reflection at the same given load level and it has been demonstrated that this removal is useful for pit dimensioning and detection of crack initiation. The extrapolation of identified patterns is useful for distinguishing the crack from noise even in low signal to noise ratios.

The modulation method has been developed to improve signal-to-noise ratio and to allow earlier fatigue crack detection. This method is particularly relevant in health monitoring applications. Time domain subtraction has been applied to the acquired time signal data from the fatigue regime and it has been demonstrated that an increase of crack SNR can be achieved in both the cyclic loading domain and the modulation domain. The space-cycle-loading imaging has been useful in visualising these improvements.

A new ultrasonic microstrain-gauging backscattering technique is proposed. It focuses on visualising excess localized plastic grain strain. The preliminary experimental data obtained during fatigue of titanium samples has demonstrated and highlighted the precursor of crack initiation. The strain and the change in ultrasonic signals are linked dynamically as synchronized elasto-plastic strain variation due to fatigue loading.

Due to the detrimental effect of microtextures on the fatigue properties in Ti alloys it is highly desirable to determine the possible microtexture existence in the engine components and to characterize them nondestructively. Ultrasonic backscattering and attenuation are dependent on the length scale of the grains therefore ultrasonic characterization may potentially provide nondestructive means to determine the microtexture presence and its morphology. Approximate attenuation and backscattering models are introduced for microstructures with elongated microtextured regions (MTRs) which are particularly applicable to forged Ti alloys. The MTRs are formed by a large number of small crystallites with a preferred orientation in the MTR. We approximate the crystallite ODF in the MTR by a Gaussian distribution function characterized by its width σ and determine the homogenized effective elastic properties of MTRs, which depend on σ . The resulting wave scattering model for MTR is quasi-static in the sense that the MTRs in the scattering model are considered as ellipsoidal single crystals with effective elastic properties and the scattering by crystallites, inside the MTRs, is considered separately as an additive attenuation term. Thus the total longitudinal attenuation coefficient is obtained by adding together both the MTR attenuation and crystallite attenuation. The results have shown that for strong microtexture (small σ) the MTR attenuation term is dominant, for relatively weak microtexture (large σ) the MTR scattering is small and the crystallite attenuation makes a major contribution even though it is significantly lower due to the smaller size of the crystallites.

Examples of attenuation and backscattering measurements are described and compared with the model. The average MTR sizes and crystallite elastic constants are obtained inversion of our directional backscattering measurements. Once the ODF parameter σ is selected the model predicts reasonably well both attenuation and backscattering in the different directions of the sample. This indicates the consistency of the model and the measurements.

References

1. S. Ghosh and D. Dimiduk (co-editors), *Computational Methods for Microstructure-Property Relations*, Springer NY, 1st Edition, 2011.
2. S. Ghosh and P. Chakraborty, "Wavelet Transformation Induced Multi-Time Scaling Crystal Plasticity FEM for Cyclic Deformation in Polycrystalline Materials" in *Scale Transition in Crystal Plasticity*, S. Bouvier, 209-243, 2011.
3. S. Ghosh, M. Anahid and P. Chakraborty, "Modeling Fatigue Crack Nucleation Using Crystal Plasticity Finite Element Simulations and Multi-time Scaling" in *Computational Methods for Microstructure-Property Relations*, S. Ghosh and D. Dimiduk (co-editors), 497-554, Springer NY, 2011.
4. M. Anahid and S. Ghosh, Constitutive and Fatigue Nucleation Models of Polycrystalline Ti Alloys from Homogenization of Crystal Plasticity FEM, Part 1: Macroscopic Anisotropic Constitutive Model, (submitted).
5. M. Anahid and S. Ghosh, Constitutive and Fatigue Nucleation Models of Polycrystalline Ti Alloys from Homogenization of Crystal Plasticity FEM, Part 2: Macroscopic Probabilistic Crack Nucleation Model, (submitted).
6. P. Chakraborty and S. Ghosh, Accelerating cyclic plasticity simulations using an adaptive wavelet transformation based multi-time scaling method, *Int. J. Numer. Meth. Eng.*, (in press).
7. S. Ghosh and P. Chakraborty, Microstructure and Load Sensitive Fatigue Crack Nucleation in Ti-6242 using Accelerated Crystal Plasticity FEM Simulations (submitted).
8. M. Anahid, M. Samal and S. Ghosh, Dwell fatigue crack nucleation model based on using crystal plasticity finite element simulations of polycrystalline Titanium alloys ", *J. Mech. Phys. Solids*, Vol. 59, pp. 2157-2176, August 2011.
9. P. Chakraborty, D. S. Joseph and S. Ghosh, Wavelet transformation based multi-time scale crystal plasticity FEM for cyclic deformation in titanium alloys under dwell load, *Fin. Elem. Ana. Des.*, 47 (6):610-618, 2011.
10. D. S. Joseph, P. Chakraborty and S. Ghosh, Wavelet transformation based multi-time scaling method for crystal plasticity FE simulations under cyclic loading, *Comput. Meth. Appl. Mech. and Eng.*, 199:2177-2194, 2010.
11. M. Anahid, P. Chakraborty, D. Joseph and S. Ghosh, A wavelet decomposed dual-time scale crystal plasticity FE model for analyzing crack nucleation in cyclic deformation, *Model. Simul. Mater. Sci. Eng.*, 17, 2009.
12. G. D. Connolly, J. Li and S. I. Rokhlin Fatigue crack monitoring in titanium alloy by dynamic subtraction of modulated surface acoustic wave, *NDT&E Int.* (submitted)
13. L. Yang and S. I. Rokhlin, Ultrasonic scattering in polycrystals with ellipsoidal orientation clusters of orthorhombic crystallites, *Wave Motion* (submitted).
14. L. Yang and S. I. Rokhlin "Ultrasonic backscattering in cubic polycrystals with ellipsoidal grains and texture" *J. Nondestruct. Eval.* (submitted).
15. O.I. Lobkis, L. Yang, J. Li and S. I. Rokhlin, Ultrasonic backscattering in polycrystals with elongated single phase and duplex microstructures, *Ultrasonics*, 52(6):694-705, 2012.
16. L. Yang, O. I. Lobkis and S. I. Rokhlin, Integrated model for ultrasonic wave propagation and scattering in polycrystalline medium with elongated hexagonal grains" *Wave Motion*, 49(5):544-560, 2012.
17. G. D. Connolly and S. I. Rokhlin, Enhancement of fatigue crack monitoring by surface acoustic wave reflection and modulation in a space-cycle-load domain: an imaging approach, *Struct. Health Monit.*, 11 (2):187-196, 2012.
18. L. Yang, J. Li, O. I. Lobkis, and S. I. Rokhlin, Ultrasonic propagation and scattering in duplex microstructures with application to titanium alloys, *J. Nondestruct. Eval.* 31(3):270-283, 2012.
19. L. Yang, O. I. Lobkis and S. I. Rokhlin, Shape effect of elongated grains on ultrasonic attenuation in polycrystalline materials, *Ultrasonics*, 51(6):697-708, 2011.
20. L. Yang, O. I. Lobkis and S. I. Rokhlin "Shape effect of elongated grains on ultrasonic attenuation in polycrystalline materials" *Ultrasonics*, 51(6):697-708, 2011.
21. O. I. Lobkis and S.I. Rokhlin "Characterization of polycrystals with elongated duplex microstructure by inversion of ultrasonic backscattering data" *Appl. Phys. Lett.*, 96(16):Arti.161905-1-3, 2010.

22. H.R. Millwater, G. Singh and M. Cortina, "Development of a Localized Probabilistic Sensitivity Method to Determine Random Variable Regional Importance," Reliability Engineering of System Safety.(in press).
23. D.L. McDowell, S. Ghosh, and S.R. Kalidindi, Representation and Computational Structure-Property Relations of Random Media, *Jour. Mat.* 63 (3):45-51, 2011.
24. T. Kanit, S. Forest, I. Galliet, V. Mounoury, and D. Juclin, Determination of the size of the representative volume element for random composites: statistical and numerical approach, *Inert. J. Sol. Struct.*, 40:3647-3679, 2011.
25. C.P. Przybyla, and D.L. McDowell, Simulated microstructure-sensitive extreme value probabilities for high cycle fatigue of duplex Ti-6Al-4V, *Int.l Jour. Plast.*, 2011
26. W. Weibull, A Statistical Theory of the Strength of Materials, *Ingeniorsvetenskapsakademiens Handlingar*, 151:1-45, 1939.
27. S.B. Batdorf, and J.G. Crose, A Statistical Theory for the Fracture of Brittle Structures Subjected to Nonuniform Polyaxial Stresses, *Jour. Appl. Mech.*, 41:459-464, 1974.
28. R.G. Tryon, and T.A. Cruse, A Reliability-Based Model to Predict Scatter in Fatigue Crack Nucleation Life, *Fatigue Fract. Eng. M*, 21:257-267, 1998.
29. E. Castillo, *Extreme Value Theory in Engineering*, Academic Press, INC., 1988.
30. M. Groeber, S. Ghosh, M.D. Uchic, and D.M. Dimiduk, A framework for automated analysis and simulation of 3D polycrystalline microstructures Part 1: Statistical characterization, *Acta Mater.*, 56:1257-1273, 2008.
31. A. H-S. Ang, and W.H. Tang, *Probability Concepts in Engineering Planning and Design* 2, NY: John Wiley & Sons, 1984.
32. G. Lutjering, and J.C. Williams, *Titanium 2nd ed. Engineering Materials and Processes*, NY: Springer Berlin Heidelberg, 2007.
33. J.R. Mayeur, and D.L. McDowell, A three-dimensional crystal plasticity model for duplex Ti-6Al-4V, *Int. Jour. Plast.*, 23:1457-1485, 2007.
34. V. Hasija, S. Ghosh, M. Mills, and D. Joseph, Deformation and creep modeling in polycrystalline Ti-6Al alloys, *Acta Mater.*, 51: 4533-4549, 2003.
35. M. R. Bache, W. J. Evans, V. Randle, and R. J. Wilson, Characterization of mechanical anisotropy in titanium alloys, *Mater. Sci. Eng.*, A257:139-144, 1998.
36. P. D. Littlewood, and A. J. Wilkinson, "Local deformation patterns in Ti-6Al-4V under tensile, fatigue and dwell fatigue loading," *Int. J. Fatigue*, <http://dx.doi.org/10.1016/j.ijfatigue.2012.03.001>, 2012.
37. I.P. Jones, and W.B. Hutchinson, "Stress-State Dependence of Slip in Titanium-6Al-4V and Other H.C.P. Metals," *Acta Metallurgica*, 29:951-968, 1981.
38. K. Shoemaker, "Uniform Random Rotations" in *Graphics Gems III. The graphics gems series*, Academic Press Professional, Inc., 1992.
39. J.C. Tucker, L.H. Chan, G.S. Rohrer, M.A. Groeber, and A.D. Rollet, Tail Departure of Log-Normal Grain Size Distributions in Synthetic Three-Dimensional Microstructures, *Metall. Mater. Trans. A*, 2011.

Appendix A

Task 1: Computational Multiscale Analysis Framework for Fatigue Crack Nucleation in Metallic Polycrystalline Microstructures

Abstract

The multi-scale computational modeling portion of this work under the direction of S. Ghosh has developed three major components contributing to the framework of multi-scale modeling of deformation and fatigue nucleation in polycrystalline titanium alloys. The first module develops a novel spatial-temporal multi-scale computational models from image-based microstructural models of polycrystalline titanium alloys to predict intra-/inter-granular crack initiation. A non-local energy based crack model has been developed in terms stress fields and dislocation pile-up in crystal plasticity simulations. The second module has developed a multi-resolution wavelet transformation based multi-time scaling (WATMUS) algorithm for accelerated CPFE simulations to accommodate a large number of cycles to failure. The WATMUS methodology introduces wavelet decomposition of nodal displacements and all associated variables in the finite element formulation to decouple the response into a monotonic coarse cycle-scale behavior and oscillatory fine time scale behavior within each cycle. The wavelet decomposition naturally retains the high frequency response through the wavelet basis functions and transforms the low frequency material response into a "cycle scale" problem of coefficients undergoing monotonic evolution. No assumption of scale separation is needed with this method. The third module develops a homogenized, anisotropic plasticity constitutive (HAPC) model from crystal plasticity finite element simulation results of microstructural representative volume elements. This model is able to capture important deformation characteristics of Ti-based alloys, which are pressure insensitivity, anisotropy, tension-compression asymmetry and kinematic hardening. The advantage of this model is that it avoids having to perform computationally expensive micromechanical analysis at each point in macroscopic simulations. An extension of this model is also introduced to account for the rate dependency observed in mechanical behavior of Ti alloys.

Chapter 1

Relevant Information

1.1 Personnel Supported

1. Somnath Ghosh, PI
2. Pritam Chakraborty, Ph.D. Student, Graduate Research Associate, 100%
Will join Idaho National Laboratories from September 2012
3. Masoud Anahid, Post-Doctoral Researcher, 50% Now at Scientific Forming Technologies Corporation

1.2 Completed Ph.D. Dissertations/M.S. Theses

1. P. Chakraborty, Ph.D. 2011, Dissertation Title: Wavelet Transformation Based Multi-Time Scale Method for Fatigue Crack Initiation in Polycrystalline Alloys.
2. D. S. Joseph, Ph.D. 2010, Dissertation Title: Wavelet Decomposed Multi-Time Scale Algorithm for Crystal Plasticity FEM Based Analysis of Cyclic Deformation.

1.3 Books and Book Chapters

1. Book: S. Ghosh and D. Dimiduk (co-editors), Computational Methods for Microstructure-Property Relations, Springer NY, 1st Edition, 2011, 790 pages. ISBN: 978-1-4419-0642-7
2. Book Chapter: S. Ghosh and P. Chakraborty, Wavelet Transformation Induced Multi-Time Scaling Crystal Plasticity FEM for Cyclic Deformation in Polycrystalline Materials in Scale Transition in Crystal Plasticity, S. Bouvier, P. Franciosi, O. Cazacu and I. Ionescu (editors), pp. 209-243, Wiley, August 2011.
3. Book Chapter: S. Ghosh, M. Anahid and P. Chakraborty, Modeling Fatigue Crack Nucleation Using Crystal Plasticity Finite Element Simulations and Multi-time Scaling in Computational Methods for Microstructure-Property Relations, S. Ghosh and D. Dimiduk (co-editors), pp. 497-554, Springer NY, January 2011.

1.4 Refereed Journal Publications

1. M. Anahid and S. Ghosh, Constitutive and Fatigue Nucleation Models of Polycrystalline Ti Alloys from Homogenization of Crystal Plasticity FEM, Part 1: Macroscopic Anisotropic Constitutive Model, (submitted).
2. M. Anahid and S. Ghosh, Constitutive and Fatigue Nucleation Models of Polycrystalline Ti Alloys from Homogenization of Crystal Plasticity FEM, Part 2: Macroscopic Probabilistic Crack Nucleation Model, (submitted).
3. P. Chakraborty and S. Ghosh, Accelerating cyclic plasticity simulations using an adaptive wavelet transformation based multi-time scaling method, International Journal for Numerical Methods in Engineering, (in press).

4. S. Ghosh and P. Chakraborty, Microstructure and Load Sensitive Fatigue Crack Nucleation in Ti-6242 using Accelerated Crystal Plasticity FEM Simulations (submitted).
5. M. Anahid, M. Samal and S. Ghosh, Dwell fatigue crack nucleation model based on using crystal plasticity finite element simulations of polycrystalline Titanium alloys ", Journal of the Mechanics and Physics of Solids, Vol. 59, pp. 2157-2176, August 2011.
6. P. Chakraborty, D. S. Joseph and S. Ghosh, Wavelet transformation based multi-time scale crystal plasticity FEM for cyclic deformation in titanium alloys under dwell load, Finite Elements in Analysis and Design, Vol. 47, No. 6, pp. 610-618, June 2011.
7. D. S. Joseph, P. Chakraborty and S. Ghosh, Wavelet transformation based multi-time scaling method for crystal plasticity FE simulations under cyclic loading, Computer Methods in Applied Mechanics and Engineering, Vol. 199, pp. 2177-2194, 2010.
8. M. Anahid, P. Chakraborty, D. Joseph and S. Ghosh, A wavelet decomposed dual-time scale crystal plasticity FE model for analyzing crack nucleation in cyclic deformation, Modeling and Simulation in Materials Science and Engineering, Vol. 17, 064009, September 2009.

1.5 Keynote Lectures

1. S. Ghosh, "Temporal Multi-Scaling in Crystal Plasticity FE Models of Polycrystalline Metals for Fatigue Crack Initiation", J.T. Oden 75th Birthday Symposium, University of Texas, Austin, TX, January 2012.
2. S. Ghosh, "Multi-Time Scaling Image Based Crystal Plasticity FE Models Dwell Fatigue Initiation in Polycrystalline Ti Alloys", Plasticity 2012, San Juan, Puerto Rico, January 2012.
3. S. Ghosh, "Multi-Scale Modeling of Deformation and Failure in Poly-phase and Polycrystalline Materials", 11th US National Congress of Computational Mechanics, Minneapolis, MN, July 2011.
4. S. Ghosh, "Computational Multi-scale Methods for Damage and Failure in Heterogeneous Materials", Air Force Workshop on High-rate Deformation Physics Of Heterogeneous Materials, Arlington, VA, July 2011.
5. S. Ghosh, "Multi-Time Scaling Based Crystal Plasticity FE Models of Dwell Fatigue Initiation in Polycrystalline Ti Alloys", 1st World Congress on Integrated Computational Materials Engineering, Seven Springs Mt Resort, PA, July 2011.
6. S. Ghosh, "Multi-Time Scaling Image Based Crystal Plasticity FE Models Dwell Fatigue Initiation in Polycrystalline Ti Alloys", Uncertainty Quantification and Multiscale Materials Modeling, Santa Fe, New Mexico, June 2011.
7. S. Ghosh, "Challenges in Computational Multiscale Materials Modeling", Joint ARO-AFOSR-NSF Workshop on Multiscale, Multiphysics Analysis and Design For Multifunctional Applications, Arlington, VA, May 2011.
8. S. Ghosh, "Temporal Multi-scaling in Image Based Crystal Plasticity FE Modeling of Dwell Fatigue in Ti Alloys Fatigue", IUTAM Symposium, Pensacola, Florida, April 2011.
9. S. Ghosh, "Crack Nucleation in Ti Alloys under Dwell Loading with Wavelet based Multi-Time Scale Approach", 9th World Congress of Computational Mechanics (WCCM/APCOM2010), Sydney, Australia, July 19-23, 2010.
10. S. Ghosh, "Dwell Fatigue Initiation in Polycrystalline Ti Alloys Using Multi-Time Scaling Crystal Plasticity FE Models", High Resolution Non-Invasive Damage Diagnostics & Predictive Modeling Workshop, London, England, June 1-3, 2010.
11. S. Ghosh, "Dwell Fatigue Initiation in Polycrystalline Ti Alloys Using Multi-Time Scaling Crystal Plasticity FE Models", Rolls-Royce Crystal Plasticity Modeling and Related Technology Workshop, Indianapolis, January 11-12, 2010.
12. S. Ghosh, D. Joseph, P. Chakraborty, "Dwell Fatigue Initiation in Polycrystalline Ti Alloys Using Multi-Time Scaling Crystal Plasticity FE Models", 16th International Symposium on Plasticity, St. Kitts, January 3-8, 2010.

1.6 Invited Lectures at Conferences

1. P. Chakraborty and S. Ghosh, "Wavelet Transformation Induced Multi-time Scale Crystal Plasticity FE Model for Predicting Crack Nucleation in Titanium Alloys", 11th US National Congress of Computational Mechanics, Minneapolis, MN, July 2011.
2. S. Ghosh and P. Chakraborty, "Modeling of dwell fatigue initiation in polycrystalline Ti alloys using multi-time scaling crystal plasticity FE models", 10th International Conference on Computational Plasticity, Barcelona, Spain, September 2009.

Chapter 2

Introduction

The PI (S. Ghosh) and his coworkers have created an integrated system of novel spatial-temporal multi-scale computational models for image based modeling of deformation and fatigue crack nucleation in polycrystalline titanium alloys. A non-local energy based crack model has been developed in terms stress fields and dislocation pile-up from crystal plasticity FE simulations. To accommodate a large number of cycles to failure, a novel wavelet transformation based multi-time scaling algorithm is proposed for accelerated crystal plasticity finite element simulations. Homogenized continuum anisotropic plasticity and probabilistic fatigue crack nucleation models are developed for being incorporated in structural analysis codes to facilitate efficient analysis. This project has resulted in a number of published and forthcoming journal and proceeding publications. Significant research interaction with researchers at the Air Force Research Laboratories has developed as a consequence of this project. Some of the research conducted by the PI that is relevant to this grant is summarized below.

2.1 Image-Based Crystal-Plasticity FE Models for Deformation and Fatigue Crack Nucleation in Polycrystalline Aggregates

Image-based micromechanical computational models of polycrystalline metals and alloys account for actual grain morphology and crystallographic orientations, as well as mechanisms that govern deformation and failure. Image-based rate and size dependent crystal plasticity models for deformation and creep have been developed for in titanium alloys (hcp). For example, alpha/beta forged Ti-6242 consisting of colonies of transformed beta-phase in a matrix of primary alpha-phase has been modeled. Compatibility requirements result in a time-dependent rise in the local stress near the grain boundary in adjacent unfavorably oriented grains. This phenomenon is known as load shedding, in which time dependent local stress concentration near grain boundaries are caused by dislocation pileup in neighboring grains. Premature fatigue failure in polycrystalline alloys, e.g. Ti alloys, under dwell loading conditions has been associated with low temperature creep induced early crack nucleation. Thus, accurate assessment of the nucleation time is critical to predicting fatigue life. We have developed a novel grain-level crack nucleation criterion utilizing evolving variables in crystal plasticity finite element simulations. The experimentally validated nucleation model is able to effectively predict the number of cycles as well as the crystallographic characteristics of the location. The non-local crack nucleation model includes: (i) interaction of all active slip systems, (ii) dislocation pile-up and (iii) mixed-mode cracking.

2.2 Multi-Time Scaling Crystal Plasticity FEM for Cyclic Deformation in Polycrystalline Materials: WATMUS Algorithm

Fatigue life in metallic materials is typically of the order of thousands of cycles, depending on the material and loading conditions. A major shortcoming of crystal plasticity FE simulations for fatigue life prediction is modeling the large number of cycles to complete failure or its nucleation. In single time-scale CPFE calculations, this leads to exorbitant computational requirements. Consequently, 3D CPFE simulations for cyclic deformation have resorted to simulating a small number of cycles and subsequently extrapolating the results to thousands of cycles for making fatigue life predictions. Extrapolation or block integration methods can however lead to considerable error, particularly when it comes to the evolution of microstructural variables. We have developed a multi-resolution wavelet transformation based multi-time scaling (WATMUS) algorithm for accelerated CPFE simulations to overcome the above deficiencies. The WATMUS

methodology introduces wavelet decomposition of nodal displacements and all associated variables in the finite element formulation to decouple the response into a monotonic coarse cycle-scale behavior and oscillatory fine time scale behavior within each cycle. The wavelet decomposition naturally retains the high frequency response through the wavelet basis functions and transforms the low frequency material response into a "cycle scale" problem of coefficients undergoing monotonic evolution. The coarse cycle scale variables exhibit monotonic behavior that especially stabilizes with saturating hardness at higher levels of deformation. Relatively large increments, traversing several cycles at a time, can therefore be utilized in the numerical integration scheme with significantly enhanced efficiency. The WATMUS simulations exhibit approximately over 100 times speed-up, even with relatively low number of cycles. Subsequently, fine scale variations in temporal response at any point in a microstructural point can be recovered from values of wavelet coefficients and coarse scale state variables.

2.3 Homogenized Constitutive and Fatigue Nucleation Models from Crystal Plasticity Simulations of Ti Alloys

Deformation and fatigue failure behavior of polycrystalline titanium alloys have strong dependence on the local microstructural characteristics. Reliable analysis of mechanical response and fatigue life in structures is contingent upon accurate description of material behavior using continuum-level constitutive models, with roots in the underlying microstructure. This work is aimed at developing continuum models of plastic deformation and fatigue crack nucleation in polycrystalline Ti alloys from detailed analysis of underlying polycrystalline microstructures. A homogenized, anisotropic plasticity constitutive (HAPC) model is developed from crystal plasticity finite element simulation results of microstructural representative volume elements. This model is able to capture important deformation characteristics of Ti-based alloys, which are pressure insensitivity, anisotropy, tension-compression asymmetry and kinematic hardening. The advantage of this model is that it avoids having to perform computationally expensive micromechanical analysis at each point in macroscopic simulations. An extension of this model is also introduced to account for the rate dependency observed in mechanical behavior of Ti alloys.

2.4 Organization of Appendix A

The Appendix is divided into three subsequent chapters. In chapter 3, and image-based CPFE models for deformation and fatigue crack nucleation in polycrystalline titanium alloys is presented. A wavelet transformation induced multi-time scaling CPFEM for cyclic deformation (WATMUS) algorithm is developed in Chapter 4. Homogenized constitutive and fatigue nucleation models from CPFE simulations of Ti Alloys are developed in 5. The report ends with a discussion.

Chapter 3

Image-Based Crystal-Plasticity FE Models for Deformation and Fatigue Crack Nucleation in Polycrystalline Aggregates

Titanium alloys with predominantly hexagonal close-packed (*hcp*) crystalline structure are used in various high performance automotive and aerospace propulsion applications due to their high strength ($\sim 700 - 1000 \text{ MPa}$), low density, high fracture toughness and corrosion resistance. However, the performance of Ti alloys is often hindered by time-dependent deformation at temperatures that are lower than those at which diffusion-mediated deformation, such as dislocation climb, occurs. This deformation characteristic leads to their premature fatigue failure under dwell loading service conditions [8]. Each dwell loading cycle is comprised of a loading phase followed by a hold phase, and subsequently an unloading phase. Crack nucleation under these conditions has been experimentally associated with grains that have their [0001] crystal orientations ($\langle c \rangle$ -axis) close to the deformation axis [100]. This early failure, in comparison with normal fatigue without any hold, has been attributed to local creep effects that occur during the hold period of dwell, e.g. in [57, 65, 66].

Plastic deformation in *hcp* Ti alloys has considerable dependence on the crystal orientation due to their low symmetries [52, 28, 117]. Slip behavior due to dislocation glide in hexagonal materials is highly anisotropic because of the difference in deformation resistances in different slip systems. The critical resolved shear strength (CRSS) for the $\langle c + a \rangle$ -slip on pyramidal planes is $\sim 3 - 4$ times larger than the CRSS for $\langle a \rangle$ -type slip on prism or basal planes. During the hold period, “soft” grains with favorably oriented $\langle a \rangle$ -type slip systems for dislocation glide ($\langle c \rangle$ -axis with nearly 45° orientation with respect to the deformation axis) undergo significant plastic straining. Contiguous “hard” grains with less-favorably oriented for $\langle a \rangle$ -type slip ($\langle c \rangle$ -axis parallel to the deformation direction), experience large local stress concentrations, especially near the shared grain boundary. This is a consequence of compatible, large elastic strains in the hard grains near the shared boundary. The phenomenon of rising stress-concentration with evolving creep strains in dwell cycles has been called load shedding in [52]. This rise in local stresses is found to cause early crack nucleation under dwell fatigue loading in [8].

Fatigue failure in metallic materials due to cyclic loading evolves in multiple stages [109]. These include micro-crack nucleation due to inhomogeneous plastic flow or grain boundary failure, followed by crack growth due to cyclic stresses, and finally coalescence of cracks to cause fast crack propagation. Depending on the material in question, and other factors like geometry, surface condition, stress/strain amplitude, strain rate, environment etc., the number of cycles to nucleation and the propagation can be quite different. For example, experimental investigations on dwell fatigue in Ti-6242 alloy in [94] using acoustic microscopy suggest that primary sub-surface crack nucleation occurs at $\sim 80 - 90\%$ of the total number of cycles to failure. These experiments show that nucleation can dominate the life limit of a metallic material. Consequently, fatigue crack nucleation has drawn considerable attention from the research community because of its role in catastrophic material failure.

A large body of literature exists on the prediction of fatigue life of metals. The phenomena of high cycle and low cycle fatigue have been traditionally characterized using macroscopic parameters like applied stresses, cyclic frequency, loading waveform, hold time etc., as well as statistical distributions of fatigue life and fatigue strength [109, 24, 68, 36, 51]. Fatigue analysis by total life approaches includes (i) the stress-life or S-N approach, where the stress amplitude versus life is de-

terminated, and (ii) the strain-life approach e.g. the Coffin-Manson rule, where the number of cycles to failure is determined as a function of plastic strain. However, predictions of these widely used models can suffer from significant scatter. This is primarily due to the absence of robust underlying physical mechanisms and information on the material microstructure in their representation. Morphological and crystallographic characteristics of the microstructure, e.g. crystal orientations, misorientations and grain size distribution, play significant roles in the mechanical behavior and fatigue failure response.

A number of models have also been proposed for fatigue crack nucleation. Some of the early models are based on the phenomenon of roughening of initially smooth surfaces with the application of cyclic stresses and strains in [35]. More recent work on fatigue in polycrystalline materials [63, 69, 54] postulates grain boundaries, which are critical to persistent slip bands in grains and free surfaces, as preferential sites of micro-crack nucleation and propagation. Inter-granular fatigue cracking has been investigated for the relation between grain boundary orientation and the direction of applied loading in [54]. Micro-crack nucleation due to grain boundary interaction with persistent slip bands has been studied in [126]. Inter-granular fatigue crack nucleation is predominant at sites with large misorientation between adjacent grains [64]. The nucleation of a fatigue crack has been attributed to random fluctuations in a metastable assembly of defect structures generated during cyclic deformation in [70]. A micro-crack nucleates when the Gibbs free energy changes due to the applied loading as well as other participating mechanisms, e.g. evolution of lattice defects overcomes the energy barrier for creating new surfaces. This model has been used in [124] to predict the number of cycles for micro-crack nucleation in steel and aluminum alloys. Another class of fatigue crack nucleation models based on the void growth in a plastically deforming matrix has been proposed [92]. Accumulated plastic strain has been used as a fatigue indicator parameter to predict fatigue crack nucleation site in materials which experience cracking within a band of intense slip. In [74], it is shown that the experimentally observed cracking in a polycrystalline Ni-base superalloy sample occurs in regions with the highest accumulated plastic strain predicted by the crystal plasticity simulations. A cleavage fracture criterion based on the stress normal to the basal plane has been introduced for Ti alloys to predict the features of crack formation site in [30, 74]. Using a crystal plasticity model along with this cleavage failure criterion, it has been shown that facets nucleate along the basal plane of a hard grain which has neighbouring grains with very specific orientations. This combination has been termed a rogue grain combination.

The recent years have seen a paradigm shift towards the use of material microstructure based detailed mechanistic models for predicting fatigue crack nucleation and propagation. The mechanistic models are promising alternatives to the empirical models. A review of some of the existing physics-based failure models is presented in [37]. Many of the microstructure based fatigue models seek accurate description of material behavior through crystal plasticity based finite element models. Crystal plasticity theories with explicit grain structures are effective in predicting localized cyclic plastic strains [76, 14, 23]. The mechanical behavior of aluminum alloys under cyclic loading has been studied using CPFE simulations of crystalline aggregates in [114, 27]. Crystal plasticity modeling with kinematic hardening for fatigue loading of Ti-6Al-4V has been presented in [78, 46, 45]. Crystal plasticity models for deformation and ratcheting fatigue of HSLA steels have been developed in [123, 98]. Ghosh et. al. have developed experimentally-validated, size dependent crystal plasticity FE models for titanium alloys in [52, 28, 117, 115], especially for modeling the load shedding phenomenon.

An early version of dwell fatigue crack nucleation model was developed in [65, 66] from CPFE simulations. This model capitalizes on the similarities between crack evolution at the tip of a crack and a dislocation pileup to derive a nonlocal crack nucleation criterion. However a limiting assumption made in this model is that dislocation pileup in neighboring soft grains follows the same distribution function as for single slip. However, the dislocation density distribution function per unit length is based on single slip activity, while the total dislocation density per unit area is a cumulative effect of slip on multiple slip systems. This inconsistency can lead to significant inaccuracies in the prediction of dwell fatigue crack nucleation.

The present work overcomes the limitations of the model in [65, 66] by avoiding the assumptions. It develops an experimentally validated, microstructure-based crack nucleation model for polycrystalline titanium alloys subject to cyclic dwell loading conditions. This nonlocal model accounts for the cumulative effect of slip on multiple slip systems, and involves evolving mixed mode stresses in the grain along with dislocation pileups in contiguous grains. The role of impurity inclusions on crack nucleation is ignored in this model. The chapter starts with a brief description of the crystal plasticity finite element model for load shedding in polycrystalline microstructures in section 5.2. Section 3.2 discusses experimental methods of fractography and acoustic microscopy used for crack monitoring in [94] and for validation of the nucleation model. A brief review of a few microstructure based failure models is given in section 3.3. Details of the computational procedure for evaluating the nucleation criterion are discussed in section 3.4. Material constants in this

criterion are calibrated using dwell fatigue simulation data at critical failure sites. Finally, the predictive capabilities of this model are demonstrated through a number of experimental validation tests in section 3.5.

3.1 Crystal Plasticity Finite Element (CPFE) Model for Dwell Fatigue

Ti alloys are often characterized by time-dependent “cold” creep deformation characteristics at temperatures lower than those, at which diffusion-mediated deformation such as dislocation climb is expected [57, 80, 52]. TEM studies, e.g. in [80] have shown that deformation actually proceeds via dislocation glide, and dislocations are inhomogeneously distributed into planar arrays. Significant creep strains can accumulate at applied stresses, even as low as 60% of the yield strength. This characteristic has been attributed to rate sensitivity effects in [57]. The α/β forged Ti-6242, is a biphasic polycrystalline alloy. It consists of colonies of transformed- β phase in a matrix of the primary α (*hcp*) phase. The primary α phase consists of equiaxed grains with an *hcp* structure, whereas the transformed- β colonies have alternating α (*hcp*) and β (*bcc*) laths. The alloy in this study consists of 70% primary α and 30% transformed- β grains. A size and time dependent large strain crystal plasticity based FE model has been developed and experimentally validated in [52, 28, 117, 115, 116]. For the transformed β -phase colony regions, a homogenized equivalent crystal model is developed in [28].

3.1.1 Crystal Plasticity Constitutive Relations

The stress-strain relation is written in terms of the second Piola-Kirchhoff stress \mathbf{S} and its work conjugate Lagrange-Green strain tensor \mathbf{E}^e as

$$\mathbf{S} = \mathbf{C} : \mathbf{E}^e, \quad \text{where } \mathbf{E}^e = \frac{1}{2} (\mathbf{F}^{eT} \mathbf{F}^e - \mathbf{I}) \quad (3.1)$$

\mathbf{C} is a fourth order anisotropic elasticity tensor and \mathbf{F}^e is the elastic component of the deformation gradient, obtained by multiplicative decomposition as:

$$\mathbf{F} = \mathbf{F}^e \mathbf{F}^p, \quad \det(\mathbf{F}^e) > 0 \quad (3.2)$$

where \mathbf{F} is the deformation gradient tensor and \mathbf{F}^p is its incompressible plastic component, i.e. $\det \mathbf{F}^p = 1$. The plastic part of the crystal plasticity equations involves a combined effect of slip on multiple slip systems. The flow rule, governing evolution of plastic deformation, is expressed in terms of the plastic velocity gradient \mathbf{L}^p as:

$$\mathbf{L}^p = \dot{\mathbf{F}}^p \mathbf{F}^{p-1} = \sum_{\alpha}^{nslip} \dot{\gamma}^{\alpha} \mathbf{s}^{\alpha} \quad (3.3)$$

where the Schmid tensor associated with α -th slip system \mathbf{s}^{α} is expressed in terms of the slip direction \mathbf{m}_0^{α} and slip plane normal \mathbf{n}_0^{α} in the reference configuration as $\mathbf{s}^{\alpha} = \mathbf{m}_0^{\alpha} \otimes \mathbf{n}_0^{\alpha}$. The plastic slip rate $\dot{\gamma}^{\alpha}$ on the α -th slip system has a power law dependence on the resolved shear stress (τ^{α}) and the slip system deformation resistance (g^{α}), given as

$$\dot{\gamma}^{\alpha} = \dot{\gamma} \left| \frac{\tau^{\alpha} - \chi^{\alpha}}{g^{\alpha}} \right|^{1/m} \text{sign}(\tau^{\alpha} - \chi^{\alpha}) \quad (3.4)$$

Here m is the material rate sensitivity parameter, $\dot{\gamma}$ is the reference plastic shearing rate and χ^{α} is the back stress that accounts for kinematic hardening in cyclic deformation [52].

The evolution of slip system deformation resistance is assumed to be controlled by two types of dislocations, viz. statistically stored dislocations (SSDs) and geometrically necessary dislocations (GNDs). SSD's correspond to homogeneous plastic deformation, while GND's accommodate incompatibility of the plastic strain field due to lattice curvature, especially near grain boundaries. The corresponding deformation resistance rate is expressed as:

$$\dot{g}^{\alpha} = \sum_{\beta} h^{\alpha\beta} |\dot{\gamma}^{\beta}| + \frac{k_0 \hat{\alpha}^2 G^2 b}{2(g^{\alpha} - g_0^{\alpha})} \sum_{\beta} \lambda^{\beta} |\dot{\gamma}^{\beta}| \quad (3.5)$$

The first term in equation (5.5) corresponds to SSDs. The modulus $h^{\alpha\beta} = q^{\alpha\beta} h^{\beta}$ (no sum on β) is the strain hardening rate due to self and latent hardening on the α -th slip system by slip on the β -th slip system respectively. Here, h^{β} is the self hardening coefficient and $q^{\alpha\beta}$ is a matrix describing latent hardening. The second term in equation (5.5) accounts for the effect of GNDs on work hardening [1]. Here, k_0 is a dimensionless material constant, G is the elastic shear modulus, b is the Burgers vector, g_0^{α} is the initial deformation resistance and $\hat{\alpha}$ is a non-dimensional constant. $\hat{\alpha}$ is taken to be $\frac{1}{3}$ in this

work following [7]. λ^β is a measure of slip plane lattice incompatibility, which can be expressed for each slip system as a function of slip plane normal \mathbf{n}^β and an incompatibility tensor Λ as:

$$\lambda^\beta = (\Lambda \mathbf{n}^\beta : \Lambda \mathbf{n}^\beta)^{\frac{1}{2}} \quad (3.6)$$

The dislocation density tensor Λ , introduced in [81] is a direct measure of the GND density. It can be expressed using the curl of plastic deformation gradient tensor \mathbf{F}^P . Since this crystal plasticity formulation does not explicitly incorporate a dislocation density tensor, it is indirectly extracted from the CPFE output data as:

$$\Lambda = \nabla^T \times \mathbf{F}^P \quad (3.7)$$

Grain size has a significant effect on the initial deformation resistance g_0^α . A Hall-Petch type relation with various slip direction-dependent characteristic length scales has been incorporated in the CPFE model in [115, 116]. Material properties for each constituent phase and individual slip system in the crystal plasticity model, as well as size effect parameters have been calibrated in [28, 117, 115]. Other parameters used in equation (5.5) include (i) shear modulus $G = 48 \text{ GPa}$, (ii) magnitude of Burgers vector $b = 0.30 \text{ nm}$, and (iii) $k_0 = 2$. Details of the microstructural morphology are also accounted for in the CPFE model through accurate phase volume fractions and orientation distributions. Extensive developments on polycrystalline microstructures that are statistically equivalent to those observed in OIM scans have been made in [40, 47, 48]. The statistically equivalent polycrystalline models are used in this study for simulating real microstructures.

3.1.2 CPFE Simulations of Polycrystalline Ti-6242

CPFE simulations of polycrystalline Ti-6242 under dwell loading conditions are conducted for evaluating stress and strain fields, required for predicting crack nucleation. Results from these simulations are used in section 3.5 to develop the proposed crack nucleation model. The crystal plasticity simulations follow dwell fatigue experiments in [94], which are to calibrate and validate the crack nucleation model. Experiments in [94] use three dog-bone specimens that are extracted from a Ti-6242 pancake forging provided by Ladish. The microstructure of these specimens have significant difference in crystallographic orientation, misorientation and micro-texture distribution. The dwell tests subject these specimens to cyclic loads with trapezoidal waveforms. Each load cycle has a maximum applied traction of 869 MPa ($\sim 95\%$ of the macroscopic yield stress for the overall material) at a hold time of 2 mins , and a loading/unloading time of 1 sec . The R -ratio, measured as the ratio of the minimum to maximum loading amplitudes, is zero.

Computer microstructures are reconstructed using methods developed in [40, 47, 48] from orientation imaging microscopy or OIM images at two sites in the material specimens. These are: (i) a critical microstructural region of a dwell fatigue crack tip and (ii) a non-critical region, where no cracks are observed microscopically. The OIM image for specimen 1 at the critical region is shown in figure 3.1. As discussed in [47, 48], statistical distribution functions of various microstructural parameters in the 2D OIM scan are generated and stereologically projected in the third dimension for creating the 3D statistics. The reconstructed 3D models have distributions of orientation, misorientation, microtexture, grain size and number of neighbors that are statistically equivalent to those observed experimentally in the OIM scans. Subsequently, CPFE models of the statistically equivalent microstructures are developed for analyzing the behavior of the critical and non-critical regions. A representative $65\mu\text{m} \times 65\mu\text{m} \times 65\mu\text{m}$ microstructural volume element of specimen 1 (critical region) consisting of 949 grains is shown in figure 3.2(a).

Prior to accepting a mesh for CPFE simulation leading to crack nucleation, a convergence study is conducted to examine mesh sensitivity. The critical microstructure of specimen 1 is simulated with finite element models of two different mesh densities. The first model consists of 78540 tetrahedron CST elements, while the second has 116040 elements, which is approximately 150% higher in mesh density. A creep simulation is performed for both these models for 1000 seconds at an applied load of 869 MPa in the Y-direction. The local stress component in the loading direction and the local plastic strain at the end of 1000 seconds are compared for various sections in the FE models. Plots comparing the distribution of these variables along a section parallel to the X-axis are shown in figures 3.3(a) and (b). The figures display excellent agreement between the two models with different mesh densities. It is concluded that the 78540-element mesh is a converged model for the loading considered and is used for the development of the crack initiation criterion. The CPFE models of specimens 1, 2 and 3 are run for 352, 663 and 447 cycles respectively, which correspond to the observed number of cycles to failure in the experiments.

Figures 3.2 and 3.4 depict the results of CPFE simulations for the model of specimen 1 located in the critical region. Figures 3.2(b) and (c) show the contour plots of the loading direction local stress (σ_{22}) and plastic strain ϵ_{22}^p respectively. Figure 3.4(a) plots the local stress σ_{22} after 1 cycle and 300 cycles respectively along a section AA shown in figure

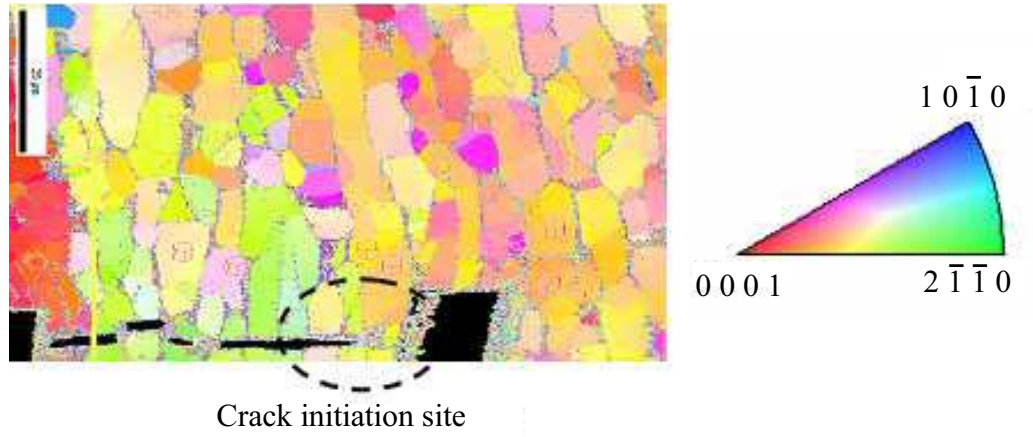


Figure 3.1: OIM scan of the critical primary crack nucleation site in specimen 1 microstructure

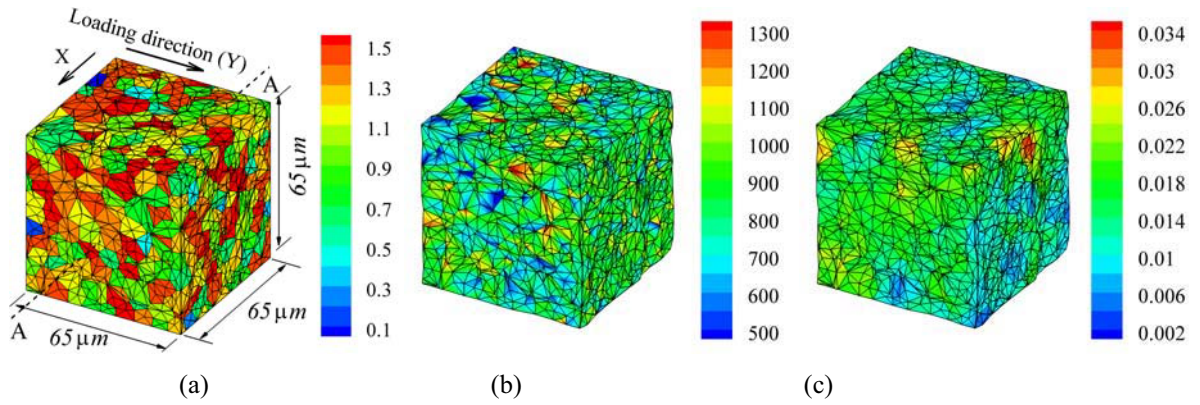


Figure 3.2: (a) CPFE model of the statistically equivalent microstructure of polycrystalline Ti-6242 at a critical location of specimen 1 depicting c -axis orientation distribution contour (radians), (b) contour plot of loading direction stress σ_{22} , and (c) contour plot of loading direction plastic strain ϵ_{22}^p .

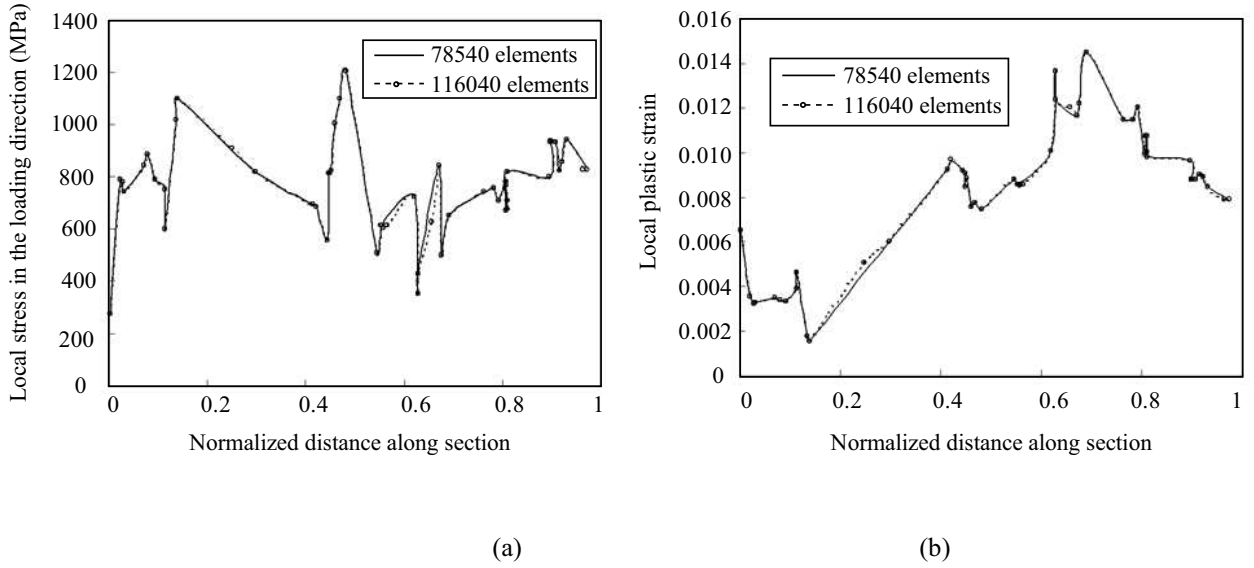


Figure 3.3: Distribution of local variables: (a) loading direction stress (σ_{22}), (b) local plastic strain along a section parallel to the x-axis at the end of 1000 seconds for a creep simulation on the two models of critical microstructure of specimen 1 with two different mesh densities.

3.2(a). This section AA passes through a hard-soft grain combination, as evidenced from the prismatic slip system Schmid factor (SF) plot in figure 3.4(b). A stress peak is seen in the grain X and a stress valley in the grain Y in figure 3.4(a). The stress peak at X after the 300 cycles is considerably higher than that after the first cycle. Also, this magnitude is much higher than the applied stress of 869 MPa. The peak stress increases with the number of cycles or time, while the valley keeps dropping with time. This is the consequence of load shedding from the grains adjacent to X , which undergo significant time-dependent plastic strain or creep. Figure 3.4(b) shows that the hard oriented grain X has a much lower SF (~ 0.11) than its neighboring soft oriented grain Y , which has a high SF (~ 0.49). This large mismatch in SF is responsible for load shedding from the soft grain at Y onto the hard grain at X . Similar observations have also been made in [52, 28, 117, 115, 116]. This load shedding induced stress concentration in the hard grains provides a foundation for developing the grain-level crack nucleation in a polycrystalline Ti alloy microstructure. Volume-averaged plastic strains (ϵ_{22}^p) in the loading direction are plotted as functions of the number of cycles, for the critical microstructures of the three specimens, in figure 3.5. The microstructure of specimen 3 shows the maximum plastic strain, while that of specimen 1 shows the least.

3.2 Experimental Crack Observations in a Cyclic Dwell Test

3.2.1 Crack Nucleation Site for Dwell Loading

Extensive experimental studies on the relation between crack evolution and crystallographic orientations in samples of Ti-6242 have been conducted in [100] using quantitative tilt fractography and Electron Back Scattered Diffraction (EBSD) techniques in SEM. Figure 3.6(a) shows the fractograph of a small region of crack nucleation site for a failed Ti-6242 specimen in dwell fatigue. Failure sites are found to be predominantly at those locations where the basal plane is nearly orthogonal to the principal loading direction [100, 8]. These sites consist of facets that form on the basal plane of the primary α grains. In [103], the angle θ_c between the loading axis and the crystallographic c -axis at the failure site has been found to be quite small ($\sim 0^\circ - 30^\circ$). Furthermore, the failure site shows a low prism activity with the Schmid factor $SF \sim 0 - 0.1$ and a moderate basal activity with $SF \sim 0.3 - 0.45$. However, the region surrounding the failure site has a high prismatic and basal activity with $SF \sim 0.5$. The overall inference from these observations is that while crack nucleation occurs in a region that is unfavorably oriented for slip (hard grain), it is surrounded by grains that are favorably oriented for slip (soft grain). These observations also suggest, time-dependent accumulation of stress in the hard oriented grains due to load shedding with increasing plastic deformation in the surrounding soft grains. This is responsible for crack nucleation in Ti alloys under creep and dwell loading.

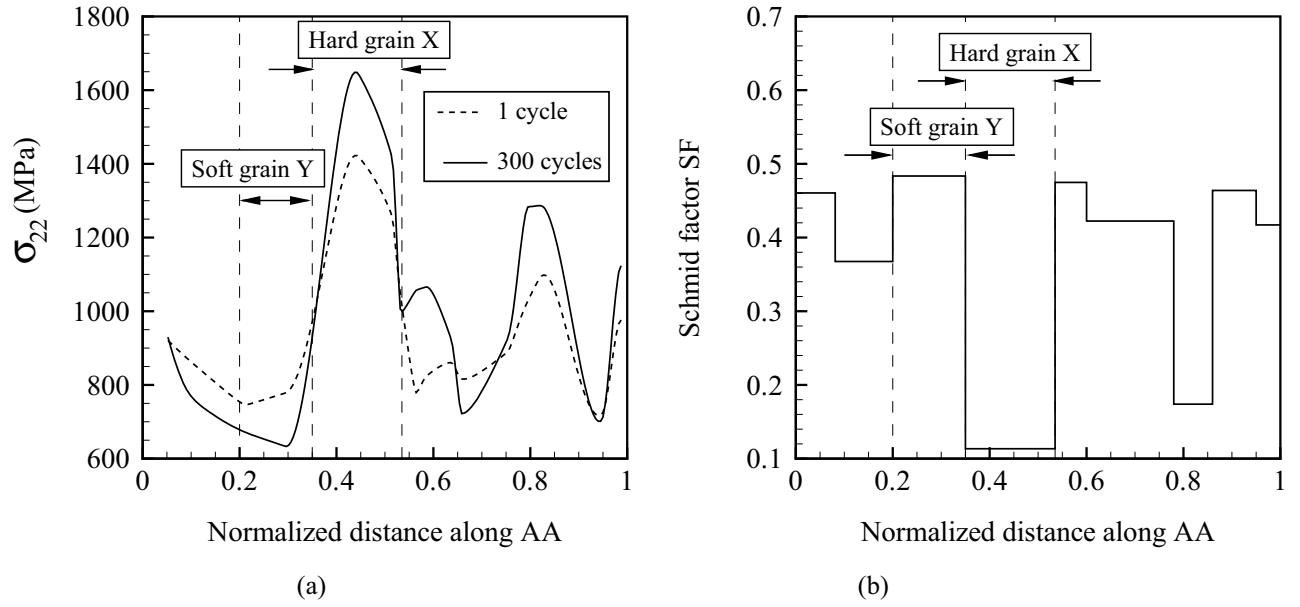


Figure 3.4: Distribution of local variables from a simulation of the CPFEE model of critical microstructure of specimen 1: (a) the loading direction stress (σ_{22}), and (b) the predominant prismatic Schmid factor along a section AA at the end of 1 and 300 dwell cycles.

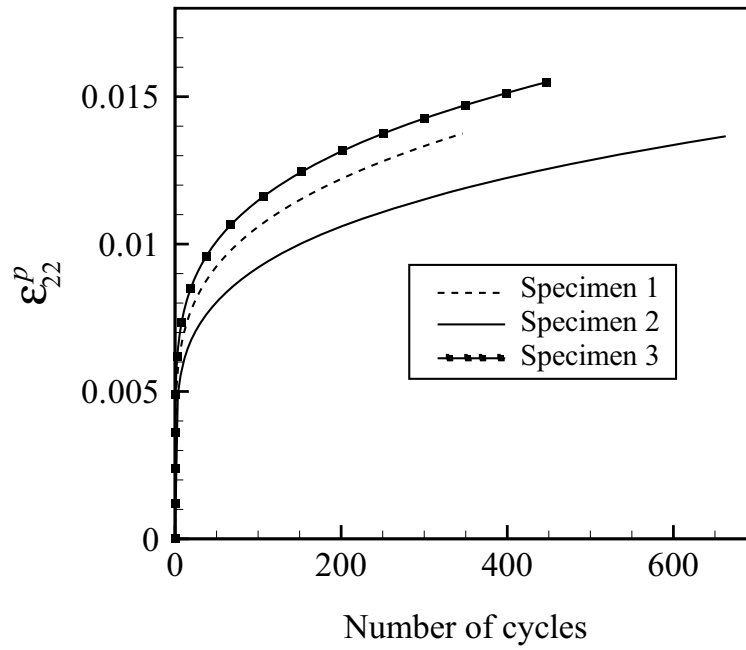
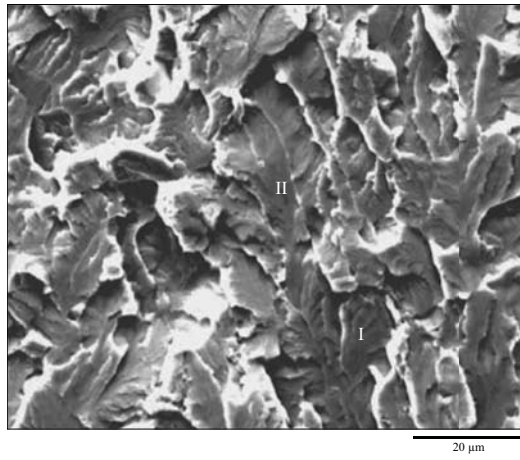
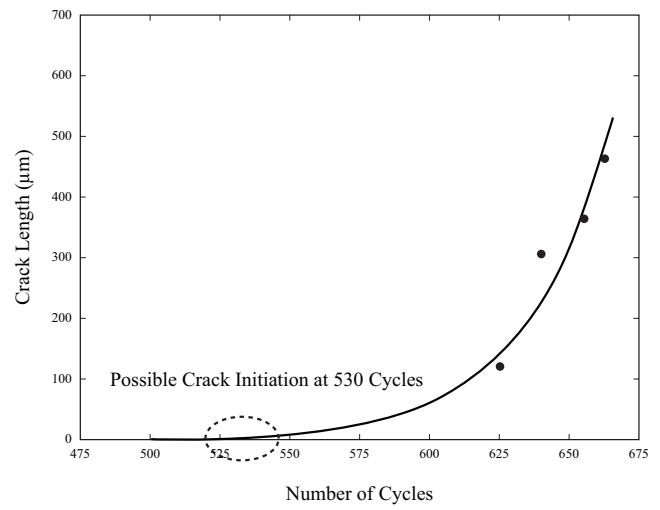


Figure 3.5: Evolution of volume-averaged plastic strain with number of cycles for the three critical microstructures.



(a)



(b)

Figure 3.6: (a) Fractograph of a faceted nucleation site for a failed Ti-6242 dwell fatigue specimen, (b) crack length as a function of number of cycles for a secondary crack in specimen 2.

3.2.2 Detection and Monitoring Cracks in Mechanical Tests

Ultrasonic techniques, such as in-situ surface acoustic wave techniques have been developed for monitoring subsurface crack nucleation in high micro-texture α/β forged Ti-6242 specimens for dwell fatigue and creep experiments in [94]. The experiments monitor crack nucleation and growth in real time, making estimation of the time for crack nucleation possible. Dwell fatigue experiments are conducted with the three microstructural specimens mentioned in section 3.1.2. The specimens 1, 2 and 3 fail after 352, 663 and 447 cycles, respectively. In [94, 121] crack growth in specimens 2 and 3 is monitored through micro-radiographic images taken by interrupting the experiment every 15 cycles. Figure 3.6(b) is a representative plot of the observed crack length as a function of the number of cycles for a secondary crack in specimen 2. This crack is of length 125 μm at 625 cycles, while at 663 cycles, it is of length 470 μm . In figure 3.6(b), the plot is extrapolated backwards to zero length to estimate the number of cycles to crack nucleation. For this specimen, crack nucleation is estimated to be approximately at 530 cycles. The number of cycles to crack nucleation, obtained by extrapolating plots for primary cracks that grew to cause final failure, are given in table 3.1. The primary crack initiated at 83% life (550 cycles) for specimen 2, while it nucleated at 85% life (380 cycles) for specimen 3. The results generally suggest that primary crack nucleation in dwell fatigue occurs in the range 80 - 90% of the total number of cycles to failure.

Specimen #	Test type	Specimen life (cycles)	Cycles to crack nucleation	% Life at primary crack nucleation
1	2-min dwell load	352	—	—
2	2-min dwell load (with modulation)	663	550	83%
3	2-min dwell load (with modulation)	447	380	85%

Table 3.1: Primary crack nucleation data by ultrasonic monitoring in dwell fatigue experiments on Ti-6242.

3.3 Review and Evaluation of Some Microstructure-based Failure Models

A few existing microstructure-based failure models are examined for dwell fatigue crack nucleation in polycrystalline Ti alloys in this section. Results of the CPFE simulations in section 3.1.2 are used as inputs to these models. The failure

predictions by these models are compared with the experimental observations of section 3.2.

3.3.1 Dislocation based Stroh-type Crack Nucleation Models

Stress concentration induced mode-I crack nucleation at the grain boundary of a crystalline solid has been modeled in [108] using a dislocation pileup model. The model proposes that a crack is nucleated under the condition that:

$$n\sigma_0 \geq 12\alpha G \quad (3.8)$$

where n is the number of dislocations in the pile up, σ_0 is the applied stress on the slip plane, G is the shear modulus and $\alpha = \frac{\gamma_s}{bG}$ is a material constant in terms of γ_s , the surface energy and b the Burgers vector.

Crack nucleation by dislocation pileups has also been studied in [105, 104], where it was proposed that a dislocation pile up leads to a mode-II crack by dislocation coalescence. Dislocation pileup is represented from equilibrium consideration in a grain of size d , yielding a cleavage fracture criterion as:

$$\sigma_E \geq \left(\frac{2\gamma_s G}{\pi(1-\nu)d} \right)^{0.5} \quad (3.9)$$

In this model, the stress σ_E required to fracture a grain is inversely related to the square root of the grain size. While the functional forms are different, both models assume that the crack nucleates at the hard-soft grain boundary as a consequence of stress concentration caused by dislocation pileup in the soft grain.

However, these early local models of metal fracture have some serious limitations with respect to failure prediction in Ti alloys. They lack the combined effect of multi-axial (normal and shear) stresses on crack nucleation. Furthermore, only one slip system in one slip plane is considered, and the interaction of different slip systems are not accounted for.

3.3.2 A Purely Stress based Nucleation Criterion

A purely stress-based criterion has been tested in [65]. In this model, a crack is nucleated when an effective mixed-mode stress exceeds a critical value, i.e. $T_{eff} \geq T_{crit}$. Results of CPFE simulations show that the rate of change of T_{eff} per cycle is very low at higher cycles, with saturation in hardness (increases only by 3.7% in the last 250 cycles). For a constant T_{crit} , even a small variation in T_{crit} will cause the predicted life to change by hundreds of cycles. For example, a 3.5% change in T_{crit} from 1660 MPa to 1724 MPa results in a 150% change in the predicted life from 100 cycles to 352 cycles. This is not an observed phenomenon and requires an ammendment with the incorporation of other evolving variables.

3.3.3 Energy based Approaches for Micro-crack Nucleation

An approach for predicting micro-crack nucleation, based on the Gibbs free energy change due to the nucleation of a micro-crack from a metastable assembly of defect structures during cyclic deformation, has been proposed in [70, 124]. An energy barrier must be overcome during the formation of a fatigue crack due to the energy required to create new surfaces. A fatigue crack spontaneously nucleates when the energy accumulated in slip bands reaches a critical value, given by a maximum in the plot of Gibbs free energy change versus the number of cycles. Prior to nucleation, the accumulated damage is in the form of increased lattice defects. The area of the stress-plastic strain hysteresis loop is a measure of the total mechanical energy spent during the cycling loading process. Most of the irreversible energy is converted to heat and only a small portion of this irreversible energy is stored as defects, which is taken care of through an efficiency parameter f in this model.

A particular form of this class of models, developed in [15], is tested for Ti alloys. By assuming the nucleation of a penny-shaped crack of length a^* , the fatigue damage accumulated in each cycle is derived in [15] as:

$$f_d = \int_N \frac{\pi E f t \Delta \sigma \Delta \epsilon_p}{\pi E \gamma_s - 4 \sigma^2 a^* (1 - \nu^2)} dN \quad (3.10)$$

where E is Young's modulus of elasticity, ν is Poison's ratio, t is the thickness of the region around the micro-crack that is drained of defects when the crack forms, σ is maximum stress in the cycle, $\Delta \sigma$ and $\Delta \epsilon_p$ are stress and plastic strain ranges in the cycle, and γ_s is the surface energy per unit area for formation of new crack surfaces.

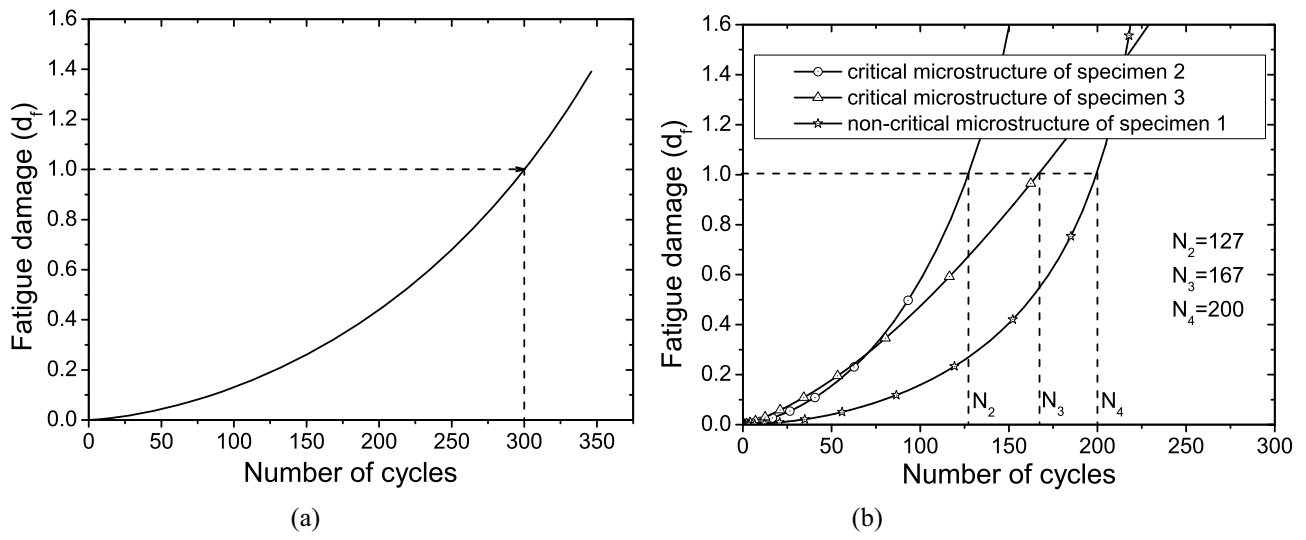


Figure 3.7: Evolution of fatigue damage with cycles: (a) calibration of the efficiency parameter f from critical microstructure of specimen 1, (b) prediction of number of cycles to micro-crack nucleation for three different microstructures.

In examining this model for Ti alloys, γ_s is taken as 5 N/m , $E = 128 \text{ GPa}$ and $\nu = 0.33$. Equation (3.10) is integrated over the cycles to calculate the cumulative fatigue damage parameter d_f at each Gauss point in the finite element mesh. For the material in consideration, the critical size of penny-shaped micro-crack a^* is assumed to be 50 nm . The size of the region is assumed to be $t = 40 \text{ nm}$, which is of the same order as the size of nucleation zone in [124]. The efficiency parameter f is calibrated from the experimental data for number of cycles for nucleation of micro-crack in Ti-6242. The number of cycles for the three microstructural specimens are given in tables 3.1 and 3.2. Crack nucleation in the specimen 1 is assumed at 85% of the total life, viz. 300 cycles. The cumulative fatigue damage d_f evolution with number of cycles for this microstructure is shown in figure 3.7(a). Micro-crack nucleation occurs when the parameter d_f reaches 1. From this figure, the efficiency parameter f is calibrated as 0.0125. The other specimens 2 and 3 are similarly analyzed using $f = 0.0125$ and the evolution of cumulative fatigue damage d_f with cycles are plotted in figure 3.7(b). The predicted number of cycles for micro-crack nucleation are 127 and 167 for critical microstructures of specimens 2 and 3 respectively. However, the corresponding experimental values are 530 and 380 respectively. Also, for a non-critical microstructure of specimen 1, where no crack was experimentally observed, this model predicts crack nucleation at 200 cycles. This energy based approach is thus not suitable for predicting fatigue crack nucleation in these Ti alloys.

3.3.4 Micro-void Growth Models for Prediction of Micro-crack Nucleation

Some micro-crack nucleation criteria in the literature have used micro-void growth models, e.g. in [92], which consider the effect of stress multi-axiality and plastic strain evolution. A void-growth parameter V_g is expressed in these models as:

$$V_g = \int_{\epsilon_{eq}^p} c_1 \exp \frac{3}{2} \frac{\sigma_m}{\sigma_{eq}} d\epsilon_{eq}^p \quad (3.11)$$

where σ_m is the hydrostatic stress, σ_{eq} is the von Mises stress and ϵ_{eq}^p is the equivalent plastic strain. The constant c_1 has been given as 0.283 in [92]. For using this model in predicting crack nucleation, a critical value of V_g is calibrated from CPFE simulations of the critical microstructure of specimen 1. The evolution of V_g is shown in figure 3.8(a) for this microstructure. Knowing the experimental value of the number of cycles to micro-crack nucleation as ~ 300 , the critical void growth parameter is calibrated from figure 3.8(a) as 0.016755. This value is subsequently used to predict the number of cycles for micro-crack nucleation in the critical microstructures of specimens 2 and 3 as well as in the non-critical microstructure of specimen 1. Figure 3.8(b) shows the evolution of V_g . The number of cycles for micro-crack nucleation are predicted as 6, 6 and 107 for the critical microstructures of specimens 2 and 3 and the non-critical microstructure of specimen 1 respectively. This predicted cycles to failure do not match with experimental data in table 3.2. Again, these type of models are not suitable for accurate life prediction for titanium alloys considered in this work.

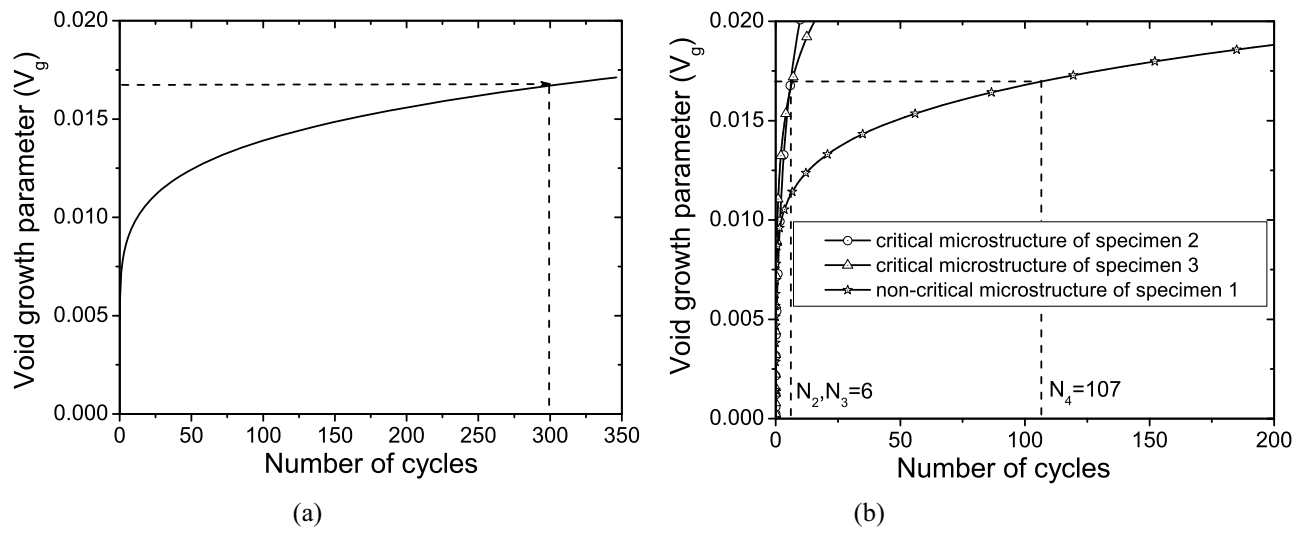


Figure 3.8: Evolution of a void growth parameter V_g with cycle: (a) calibration of critical V_g for micro-crack nucleation in the critical microstructure of specimen 1, (b) prediction of the number of cycles for micro-crack nucleation for three other microstructures.

3.4 A new Non-local Crack Nucleation Criterion from CPFE Variables

3.4.1 Model Description

The inter-granular crack nucleation model is built on the premise that a wedge crack nucleates in the neighboring grain as a dislocation approaches the grain boundary. An edge dislocation, which is an extra half plane of atoms wedged between two complete planes, is equivalent to a micro-crack with opening displacement of one atomic spacing b . As more dislocations are piled up, the opening displacement increases in size as shown in figure 3.9(a). The crack opening displacement corresponds to the closure failure along a circuit, surrounding the piled-up dislocations. If n edge dislocations of Burger's vector b , contribute to the formation of a micro-crack, a wedge with opening displacement $B = nb$ is produced. It should be noted that while the dislocations are piled up at the grain boundary of a soft grain, the wedge crack initiates in the adjacent hard grain as shown in figure 3.9(b).

The micro-crack length c in figure 3.9(a) can be considered as the length after which, the disturbance in the lattice structure of the hard grain subsides. This disturbance is caused by extra half-planes of atoms in the soft grain. This micro-crack length c may be related to crack opening displacement B using two different formulae as:

- (i) With a 90° intercept definition suggested in [91],

$$c_1 = B/2 \quad (3.12)$$

This formula is commonly used to infer crack opening displacements in FE analyses of cracks [6].

- (ii) The equilibrium length of a wedge crack with an opening displacement B is related to the elastic properties and surface energy in [108] as:

$$c_2 = \frac{G}{8\pi(1-\nu)\gamma_s} B^2 \quad (3.13)$$

where ν is the Poisson's ratio and G is the shear modulus.

The suitability of c_1 or c_2 as crack length in the crack nucleation criterion is decided based on their relative accuracy, when compared with experiments in section 3.5.

The wedge crack is initially stable. As more dislocations enter the crack, the crack opening size increases, causing the crack length to grow. Additionally, the stress in the hard grain across the micro-crack also aids in the opening up of the crack. The multi-axial stress acting on the micro-crack surface is a combination of normal and shear stresses as shown in figure 3.9(b). It is assumed that cracks nucleate (grow) from the tip, when the mixed mode stress intensity factor K_{mix}

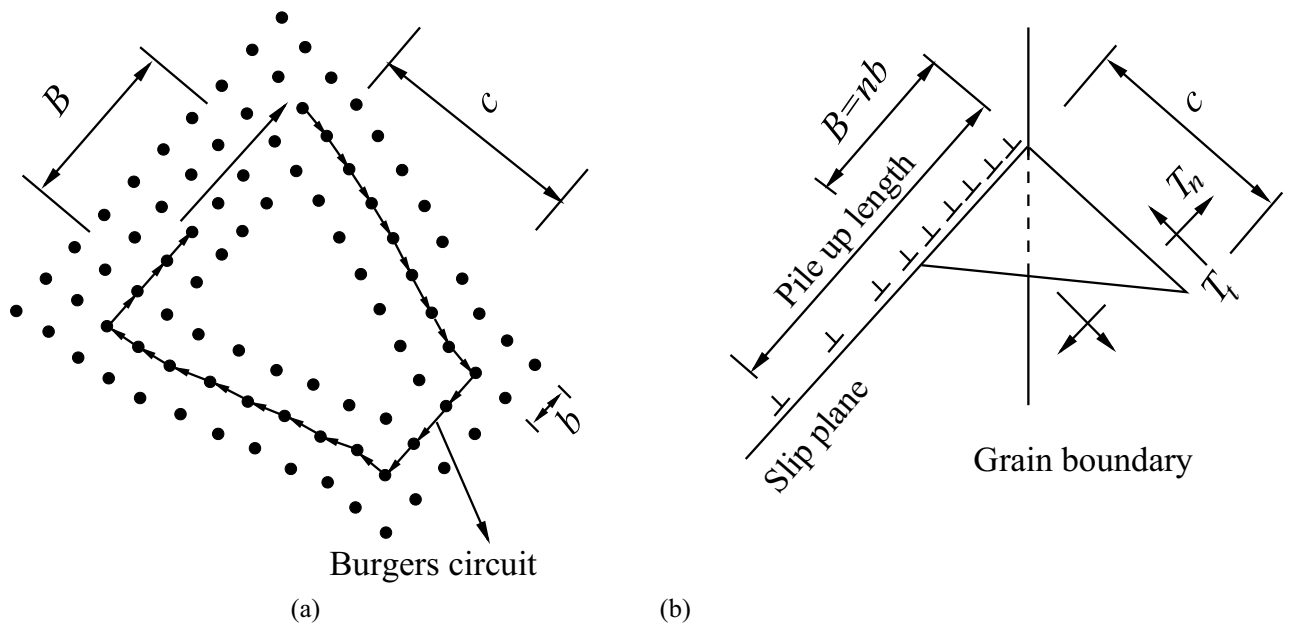


Figure 3.9: (a) A wedge crack with opening displacement of $4b$, produced by coalescence of four dislocations, (b) nucleation of a wedge crack in the hard grain resulting from a dislocation pile up in the soft grain.

exceeds a critical value, K_c . K_{mix} is expressed in terms of normal stress intensity factor, K_n and shear stress intensity factor K_t as:

$$K_{mix}^2 = K_n^2 + \beta K_t^2 \quad (3.14)$$

where β is a shear stress factor, which is used to assign different weights to the normal and shear traction components for mixed mode. In [95], β is defined as the ratio of the shear to normal fracture toughness of the material, i.e. $\beta \approx K_{nc}/K_{tc}$. A value of $\beta = 0.7071$ is suggested for Ti-64 alloys in [86], and is used in this study. Using the definitions for stress intensity factors $K_n = \langle T_n \rangle \sqrt{\pi c}$ and $K_t = T_t \sqrt{\pi c}$ and noting that the micro-crack grows when $K_{mix} \geq K_c$, the hard grain crack nucleation criterion, ahead of dislocation pile-ups in adjacent soft grain is stated as:

$$T_{eff} = \sqrt{\langle T_n \rangle^2 + \beta T_t^2} \geq \frac{K_c}{\sqrt{\pi c}} \quad (3.15)$$

or equivalently

$$R = T_{eff} \sqrt{c} \geq R_c, \quad \text{where } R_c = \frac{K_c}{\sqrt{\pi}} \quad (3.16)$$

T_{eff} is an effective stress for mixed mode crack nucleation. It is expressed in terms of the stress component normal to the crack surface $T_n = \sigma_{ij} n_i^b n_j^b$ and the tangential stress component $T_t = \|\mathbf{T} - T_n \mathbf{n}^b\|$. Here \mathbf{T} is the stress vector on the crack surface, σ_{ij} is the Cauchy stress tensor and n_i^b are the components of unit outward normal to the crack surface. Only the tensile normal stress $\langle T_n \rangle$, represented by the McCauley bracket $\langle \rangle$, contributes to the effective stress responsible for crack opening. Sensitivity analysis with different values of β indicate that T_{eff} is not very sensitive to β for $\langle c + a \rangle$ oriented hard grains, since $T_n \gg T_t$. It is worth noting that the stress components in (4.12) are remote applied stresses. However, since the typical values of c that cause unstable cracking are of the order of nanometers, while the typical grain size is of the order of microns, it is reasonable to consider the maximum stress at the hard grain boundary as the remote stress. As more dislocations are added to the pile-up with time, the wedge crack opening displacement and length increase. This implies that a smaller T_{eff} is needed to initiate a crack with increasing plastic deformation and pile-up. This contributes to the non-locality aspect of the crack nucleation criterion.

The parameter R_c in equation (3.16) depends on the elastic properties as well as on the critical strain energy release rate G_c . It has the units of stress intensity factor ($MPa \sqrt{\mu m}$). It is calibrated from crack nucleation data extracted from a combination of experiments and simulations on a single microstructure.

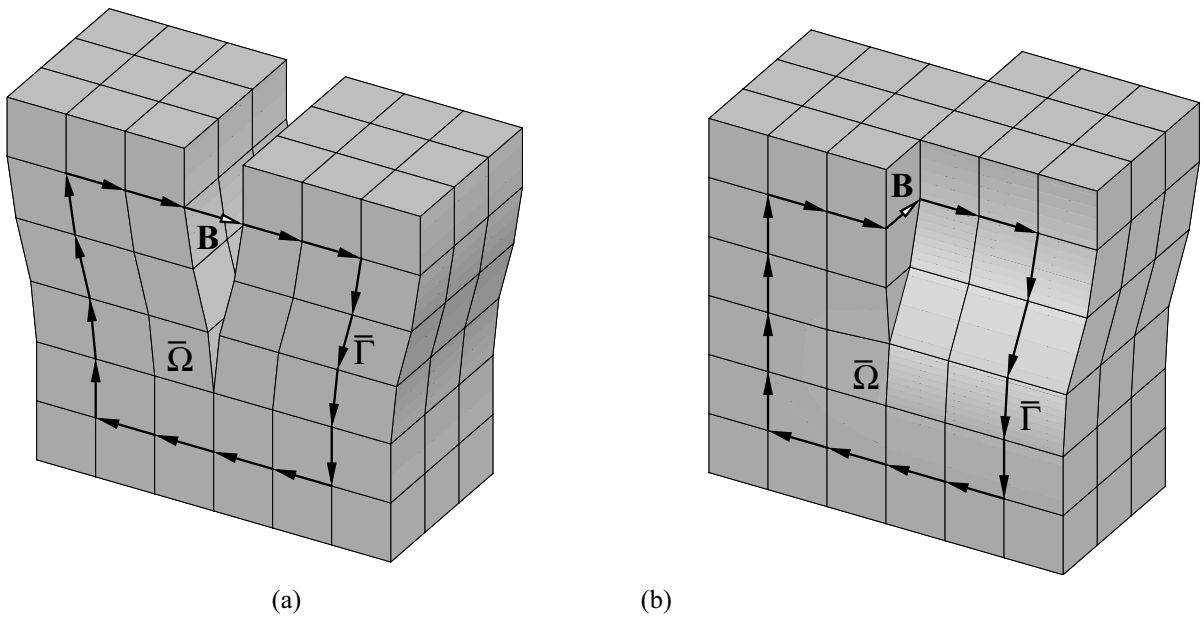


Figure 3.10: Closure failure and crack opening displacement for (a) single pure edge dislocation, and (b) single pure screw dislocation.

3.4.2 Numerical Implementation of the Crack Nucleation Criterion

This section describes a method for calculating micro-crack opening displacement B , required in equations (3.12) or (3.13) to estimate the micro-crack length. Crack nucleation is examined on different planes in the hard grain of the polycrystalline microstructure.

For estimating B , it is necessary to know the distribution of dislocations inside the soft grain. The crystal plasticity model discussed in section 5.2 does not explicitly have dislocation density as a state variable. Hence the plastic strains and their gradients that are available from the results of the CPFE simulations are used to estimate the micro-crack opening displacement B . The wedge opening displacement in figure 3.9(a) is equal to the closure failure along a circuit surrounding the piled-up edge dislocations on one slip plane. This can be extended to a generalized 3D representation of dislocations for multiple slip systems. The corresponding closure failure, which is manifested as the crack opening displacement, is a vector quantity. In the dislocation glide model, the lattice incompatibility can be measured by the closure failure of a line integral along a Burgers circuit $\bar{\Gamma}$ in the intermediate configuration. Closure failure is equivalent to the net Burgers vector \mathbf{B} of all dislocations passing through the region $\bar{\Omega}$, bounded by the circuit. The Burgers vector can be mapped to a line integral along a referential circuit, Γ using the plastic deformation gradient \mathbf{F}^p . Using Stoke's theorem, the closure failure is related to the surface integral of the curl of \mathbf{F}^p over a referential surface Ω as:

$$\mathbf{B} = \oint_{\bar{\Gamma}} d\bar{\mathbf{x}} = \oint_{\Gamma} \mathbf{F}^p d\mathbf{X} = \int_{\Omega} \boldsymbol{\Lambda} \cdot \mathbf{n} d\Omega \quad (3.17)$$

where \mathbf{n} is the unit normal to the surface Ω and $\boldsymbol{\Lambda}$ is the Nye's dislocation tensor given in equation (5.7). Components of $\boldsymbol{\Lambda}$ are evaluated at each quadrature point using shape function based interpolation of nodal values of \mathbf{F}^p , as described in [3].

The closure failure obtained from equation (3.17) can make any arbitrary angle with respect to the surface, depending on the type of dislocations passing through Ω . It also depends on the angle between dislocation line and the surface. For pure edge dislocation with the dislocation line perpendicular to Ω , the closure failure, \mathbf{B} lies in the plane, as shown in figure 3.10(a). If the dislocation line is not perpendicular to Ω , the closure failure does not lie in the plane. For pure screw dislocation with a dislocation line perpendicular to Ω , \mathbf{B} is also perpendicular to the plane, as shown in figure 3.10(b). For a mixed type of dislocation with edge and screw components, \mathbf{B} is neither perpendicular nor parallel to Ω .

Consider a point A on the hard-soft grain boundary, shown in figure 3.11(a), which impedes dislocations generated from a source in the soft grain. There are different planes with different normal vectors which contain point A . The closure failure caused by dislocations piercing each of these planes depends on the normal, \mathbf{n} based on equation (3.17). The stresses on each of the resulting micro-cracks are also different. Consequently, there are different possible competing

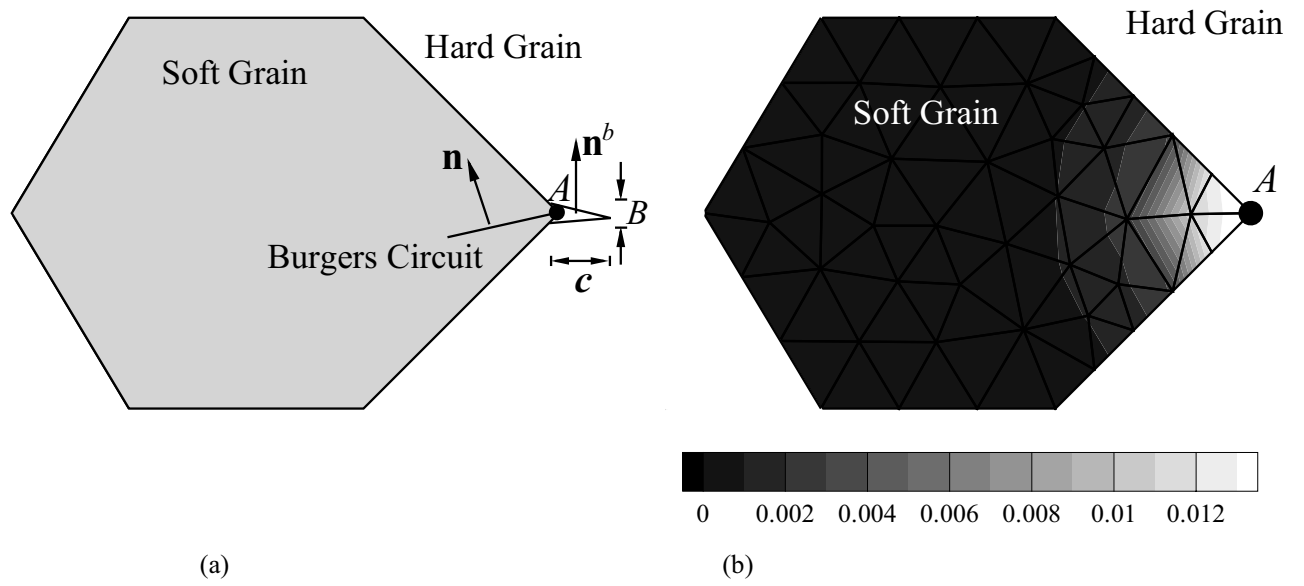


Figure 3.11: (a) Wedge-crack in the hard grain as a result of dislocation pileup in adjacent soft grain, (b) distribution of the norm of Nye's dislocation tensor inside a representative soft grain.

micro-cracks with dissimilar stress intensity factors at point A . The crack with the highest mixed-mode stress intensity factor is considered as the critical one. If the unit normal to the unit area surrounded by a Burgers circuit containing point A in figure 3.11(a) is denoted by \mathbf{n} , the size of crack opening displacement B is calculated using equation (3.17) as:

$$B = \|\Lambda \cdot \mathbf{n}\| \quad (3.18)$$

This is used in either equation (3.12) or (3.13) to estimate the crack length c . Neglecting the effect of screw dislocations on the wedge crack opening, the unit normal to the wedge crack surface is obtained as:

$$\mathbf{n}^b = \frac{\Lambda \cdot \mathbf{n}}{B} \quad (3.19)$$

The effective stress T_{eff} on the wedge crack surface is measured using the procedure described in section 3.4.1. The mixed mode stress intensity factor that corresponds to the wedge crack produced by dislocations passing through the unit area surface with unit normal of \mathbf{n} is obtained as:

$$K_{mix} = T_{eff} \sqrt{\pi c} \quad (3.20)$$

This procedure is executed for all possible \mathbf{n} vectors in 3D space. The vector \mathbf{n}_{cr} , which yields the highest stress intensity factor, is considered as the critical normal vector. The critical crack opening displacement at the hard-soft grain boundary is then obtained as $\mathbf{B}_{cr} = \Lambda \cdot \mathbf{n}_{cr}$. This relation is true when all dislocations are concentrated in a very small portion of the soft grain, surrounding the point A . However, dislocations are distributed in the entire soft grain. Figure 3.11(b) shows the contour of the norm of Nye's dislocation tensor inside a representative soft grain. The maximum value occurs at the hard-soft grain boundary (point A), and the values decrease with increasing distances from the grain boundary. Λ is available at the Gauss point of all the tetrahedron elements within the soft grain from the CPFE simulations. Each element I contains its own dislocations quantified by Nye's dislocation tensor Λ_I at that element. Dislocations associated with element I produce a crack opening displacement as:

$$\mathbf{B}_I = W_I A_I \Lambda_I \cdot \mathbf{n}_{cr} \quad (3.21)$$

Here A_I is the surface area associated with element I , into which the dislocations penetrate. It is estimated through the assumption of an equivalent spherical domain that has the same volume as the element. The center of this sphere is assumed to coincide with the element integration point. Assuming that the plane containing the Burgers circuit in the element I passes through the integration point, A_I is equal to the circular cross-sectional area passing through the center of

sphere, expressed as:

$$A_I = \pi R_I^2 = 1.77(V_I)^{\frac{2}{3}} \quad \text{where} \quad R_I = \sqrt[3]{\frac{3}{4\pi}V_I}, \quad (3.22)$$

V_I is the element volume and R_I is sphere's radius. A weighting parameter W_I is introduced to \mathbf{B}_I to account for the diminishing effect of a dislocation on the crack opening displacement with distance. A formula $W_I = \exp(-r_I^2/2l^2)$, where r_I is the distance from the point with maximum dislocation density (A in figure 3.11(b)) has been proposed in [31]. This expression is used for the I -th element integration point. $W_I \rightarrow 0$ beyond a critical distance l and $W_I = 1$ when $r_I = 0$. Thus the crack opening displacement B , accounting for the contribution of all elements in the soft grain on the hard grain crack, is stated as:

$$B = \|\mathbf{B}\| = \left\| \sum_I \mathbf{B}_I \right\| = \left\| \sum_I W_I A_I \Lambda_I \cdot \mathbf{n}_{cr} \right\| \quad (3.23)$$

Defining an effective dislocation tensor as:

$$\mathbf{D}_{eff} = \sum_I W_I A_I \Lambda_I \quad (3.24)$$

equation (3.23) can be rewritten as:

$$B = \|\mathbf{D}_{eff} \cdot \mathbf{n}_{cr}\| \quad (3.25)$$

Using the 90° intercept, defined in section 3.4.1, to estimate the micro-crack length, c is obtained using equations (3.25) and (3.12) as:

$$c_1 = \frac{1}{2} \|\mathbf{D}_{eff} \cdot \mathbf{n}_{cr}\| \quad (3.26)$$

If equation (3.13) is used to relate the micro-crack length to the crack opening displacement, c is estimated as

$$c_2 = \frac{G}{8\pi(1-\nu)\gamma_s} \|\mathbf{D}_{eff} \cdot \mathbf{n}_{cr}\|^2 \quad (3.27)$$

With material properties set to $G = 48GPa$, $\nu = \frac{1}{3}$ and $\gamma_s = 5N/m$, this equation is written as

$$c_2 = 573 \times 10^6 \|\mathbf{D}_{eff} \cdot \mathbf{n}_{cr}\|^2 \quad (\text{in m}) \quad (3.28)$$

The unit normal to the wedge crack surface in the hard grain is

$$\mathbf{n}^b = \frac{\mathbf{D}_{eff} \cdot \mathbf{n}_{cr}}{\|\mathbf{D}_{eff} \cdot \mathbf{n}_{cr}\|} \quad (3.29)$$

The effective traction T_{eff} is updated using the procedure described in section 3.4.1 and \mathbf{n}^b from equation (3.29). Finally, T_{eff} and c are used in equation (3.16) to calculate the effective nucleation variable R . R is checked for every grain pair in the CPFEM model at the post-processing stage. The condition posed in equation (3.16) is nonlocal, since the stress required to initiate a crack at a point in the hard grain depends on the gradient of plastic strain in the neighboring soft grains.

3.4.3 The Cottrell-Petch Fracture Model as a Limiting Case of the Nucleation Model

A schematic diagram explaining the Cottrell-Petch fracture model [25, 88] is shown in figure 3.12. It shows a pileup of n positive edge dislocations on a single slip plane, impeded by the grain boundary. If it is assumed that all the dislocations coalesce and form a wedge type micro-crack normal to the applied tensile stress σ_f , the fracture stress is given as [25, 88]:

$$\sigma_f = \frac{2\gamma_s}{nb} \quad (3.30)$$

The proposed crack nucleation model is shown to reduce to the Cottrell-Petch model in the limiting case of one active slip system in which only edge dislocations slip on a single plane.

To derive this limiting case, the origin of the Cartesian coordinate system is fixed on the leading dislocation with X and Y axes oriented along the slip direction and slip plane normal respectively, as shown in figure 3.12. The Z axis points out of page. For a single active slip system, the plastic slip rate $\dot{\gamma}^\alpha$ on slip systems other than the active one is zero. Slip direction and normal vectors \mathbf{m}_0 and \mathbf{n}_0 are equal to the unit vectors along X and Y directions respectively. Equation (5.3) can be rewritten in terms of the plastic slip on the active system γ , as:

$$\mathbf{L}^p = \dot{\mathbf{F}}^p \mathbf{F}^{p-1} = \dot{\gamma} \mathbf{m}_0 \otimes \mathbf{n}_0 \quad (3.31)$$

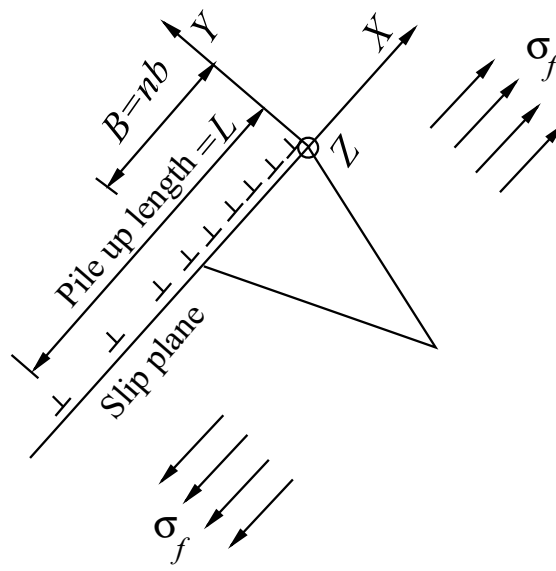


Figure 3.12: A schematic diagram explaining of Cottrell-Petch fracture model

The only non-zero component of the plastic velocity gradient tensor is $\mathbf{L}_{12}^p = \dot{\gamma}$. The corresponding plastic deformation gradient and the Nye's dislocation tensor in matrix form are:

$$\mathbf{F}^p = \begin{bmatrix} 1 & \gamma & 0 \\ 0 & 1 & 0 \\ 0 & 0 & 1 \end{bmatrix} \quad \Lambda = \begin{bmatrix} -\frac{\partial \gamma}{\partial Z} & 0 & \frac{\partial \gamma}{\partial X} \\ 0 & 0 & 0 \\ 0 & 0 & 0 \end{bmatrix} \quad (3.32)$$

The Nye's dislocation tensor is zero for any point outside the slip plane. For any point on the slip plane it can be obtained from equation (3.32). Substituting Λ in equation (3.32) in equation (3.17), the closure failure is obtained to be always along the slip direction (X -axis) for any arbitrary \mathbf{n} vector. The closure failure caused by dislocations passing through a unit area on the plane normal to X -axis is equal to $-\partial \gamma / \partial Z$. These dislocations are of screw type, parallel to the slip direction. If no screw dislocation is present, $-\partial \gamma / \partial Z = 0$. Therefore the Nye's dislocation tensor can be reduced to:

$$\Lambda = \begin{bmatrix} 0 & 0 & \frac{\partial \gamma}{\partial X} \\ 0 & 0 & 0 \\ 0 & 0 & 0 \end{bmatrix} \quad (3.33)$$

Following the procedure outlined in section 3.4.2, \mathbf{n}_{cr} is obtained as the unit vector along the Z direction. In the Cottrell-Petch model, all dislocations in the pileup have the same contribution to the crack opening displacement, and hence the weighting parameter in equation (3.24) is 1 for all dislocations. Equation (3.24) may be written in a continuous form as

$$\mathbf{D}_{eff} = \int_{\Omega} \Lambda d\Omega \quad (3.34)$$

where Ω is an area surrounding the dislocation pileup. If ρ is the dislocation density per unit length, it can be shown that $\frac{\partial \gamma}{\partial X} d\Omega = \rho b dX$ at any point A on the dislocation pileup, where $d\Omega$ is an infinitesimal area around point A . Thus,

$$\int_{\Omega} \frac{\partial \gamma}{\partial X} d\Omega = \int_0^L \rho b dX = nb \quad (3.35)$$

L and n denote the dislocation pileup length and number of dislocations in the pileup respectively. Using equations (3.33), (3.34) and (3.35) the effective dislocation tensor \mathbf{D}_{eff} is obtained as:

$$\mathbf{D}_{eff} = \begin{bmatrix} 0 & 0 & nb \\ 0 & 0 & 0 \\ 0 & 0 & 0 \end{bmatrix} \quad (3.36)$$

This expression is used in equation (3.27) to calculate the wedge crack length c as

$$c = \frac{Gn^2b^2}{8\pi(1-\nu)\gamma_s} \quad (3.37)$$

In the Cottrell-Petch model, the traction on the wedge crack has the normal component only, and hence $T_{eff} = T_n$ in equation (4.12). Also the mixed mode fracture toughness, K_c should be replaced by the normal fracture toughness K_{nc} , which equals to

$$K_c = K_{nc} = \sqrt{\frac{4G\gamma_s}{1-\nu}} \quad (3.38)$$

Using equations (3.16), (3.37) and (3.38), the crack nucleation criterion is simplified to

$$T_n nb \geq 4\sqrt{2}\gamma_s \quad (3.39)$$

In other words, the local fracture stress based on the proposed crack nucleation model is

$$T_n = \frac{4\sqrt{2}\gamma_s}{nb} \quad (3.40)$$

From this equation, the tensile stress required for crack nucleation is deduced to be $2\sqrt{2}$ times the fracture stress proposed by Cottrell-Petch model in equation (3.30). The reason for this difference is that the stress in equation (3.40) is the local stress, while equation (3.30) is based on the applied stress. The CPFE simulations in section 3.5 shows that the local effective stress T_{eff} at failure site is generally $\sim 2 - 3$ times larger than the applied stress, which is consistent with the difference between equations (3.30) and (3.40).

3.5 Parameter Calibration and Validation of the Crack Nucleation Criterion

Experimental data from section 3.2.2 are used again for calibrating and validating the proposed crack nucleation model in section 3.4. The number of cycles to major crack nucleation under dwell loading for the three microstructural specimens are given in tables 3.1 and 3.2. Based on the observations made in the experiments, crack nucleation in the critical microstructure of specimen 1 is assumed at two different percentages of the total life, viz. 80% and 85%. This corresponds to 282 and 300 cycles respectively. This data is used for calibrating the parameter R_c in equation (3.16). As a validation exercise, the calibrated value of R_c is used to predict the number of cycles to crack nucleation in specimens 2 and 3. It is expected that the nucleation criterion will be met at some locations in the CPFE models of the critical microstructures, but will not be satisfied for the non-critical microstructure.

3.5.1 Calibration of R_c for α/β Forged Ti-6242

The crack nucleation parameter R_c in equation (3.16) is calibrated from results of 2-minute dwell fatigue CPFE simulations of a critical microstructure of specimen 1. Crack nucleation is assumed at 282 and 300 cycles, corresponding to 80% and 85% of the total life of ~ 352 cycles respectively. The variable R in the LHS of equation (3.16) is determined for all grain pairs at the end of 282 and 300 cycles respectively, as follows:

- For each grain pair in the microstructure, a constituent grain is designated as hard or soft based on the amount of plasticity and stress concentration.
- For each grain in the pair, elements with a common triangular edge on the shared boundary are determined. The nodes of these triangles are the common nodes between the two grains.
- For each common node on the shared boundary, the procedure in section 3.4.2 is implemented to obtain the critical normal vector \mathbf{n}_{cr} and the stress intensity factor associated with this normal vector. The Nye's dislocation tensor at each common node, which is required to estimate c , is obtained from the integration points in the surrounding elements inside the soft grain. A weighted averaging scheme, described in [3], is used for this purpose. Correspondingly, the nodal values of stress components are calculated from the integration points in the surrounding elements inside the hard grain.
- The common node with the highest stress intensity factor is chosen. This corresponds to the point A in section 3.4.2. Consequently, the variable R is obtained for the grain pair using equations (3.22)-(3.29).

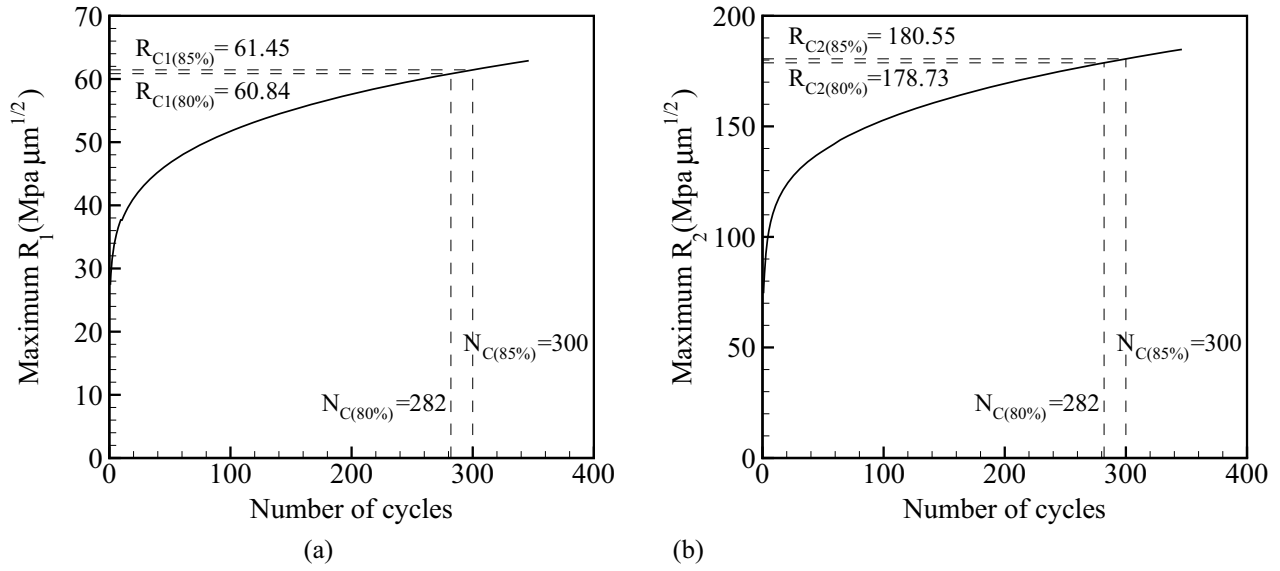


Figure 3.13: (a) Evolution of the maximum R_1 over number of cycles for the FE model of critical microstructure of specimen 1, (b) evolution of the maximum R_2 over number of cycles for the FE model of critical microstructure of specimen 1

It should be noted that the R value depends on the equation used to estimate micro-crack length c . If equation (3.26) is used to calculate c , the resulting R value is denoted by R_1 . Otherwise, if equation (3.28) is used to determine c , the R value is denoted by R_2 . The hard grain with the maximum value of R_1 is identified and the evolution of this maximum R_1 with number of cycles is plotted in figure 3.13(a). Two limiting values of R_c are determined from the values of R_1 at 282 and 300 cycles respectively. They are:

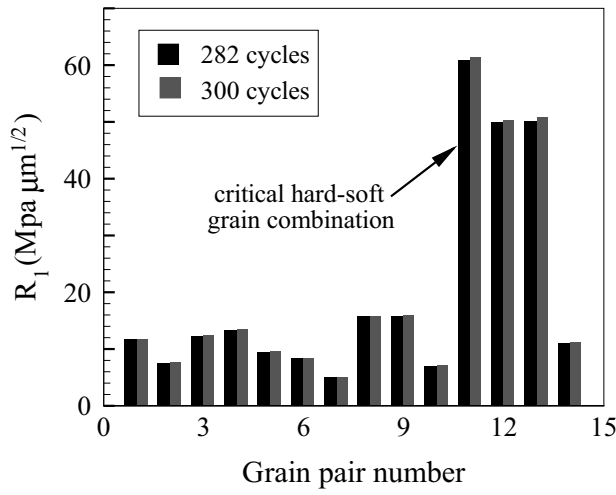
- $R_{c1(80\%)} = 60.84 \text{ MPa } \mu\text{m}^{1/2}$
- $R_{c1(85\%)} = 61.45 \text{ MPa } \mu\text{m}^{1/2}$

Histograms of R_1 at 282 and 300 cycles respectively, are shown in figure 3.14(a) along a X-directed line passing through the hard-soft grain combination with the highest R_1 value. This line intersects 14 grain boundaries. Also the evolution of maximum R_2 with number of cycles is plotted in figure 3.13(b), and the critical R_c values are obtained from the values of R_2 at 282 and 300 cycles as:

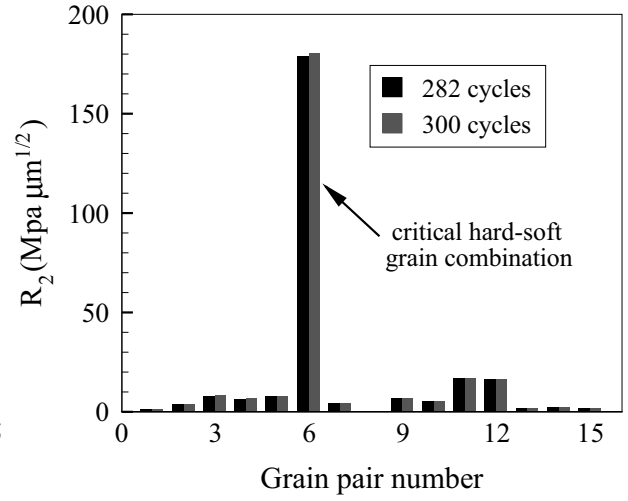
- $R_{c2(80\%)} = 178.73 \text{ MPa } \mu\text{m}^{1/2}$
- $R_{c2(85\%)} = 180.55 \text{ MPa } \mu\text{m}^{1/2}$

Figure 3.14(b) shows the histograms of R_2 at 282 and 300 cycles respectively along a X-directed line passing through the hard-soft grain combination with the highest R_2 value. This line intersects 15 grain boundaries. The calibrated values of R_c are subsequently used for predicting crack nucleation in other specimens.

Results of the CPFE simulation for the non-critical microstructure of specimen 1, described in section 3.1.2, are post-processed to evaluate the values of R_1 and R_2 for all grain-pairs. Figures 3.15(a) and (b) plot the evolution of maximum R_1 and maximum R_2 as a function of cycles respectively. The maximum R_1 reached at the end of 352 cycles is $44 \text{ MPa } \mu\text{m}^{1/2}$. This is less than both critical values $R_{c1(80\%)}$ and $R_{c1(85\%)}$ for both limiting cases. Also the maximum R_2 reached at the end of 352 cycles is only $95 \text{ MPa } \mu\text{m}^{1/2}$. This is also far less than the limiting values of R_{c2} . Thus the criterion predicts no crack nucleation for the polycrystalline crystal plasticity microstructure, constructed for the non-critical region. This is consistent with experimental observations. In this microstructure the hard-soft grain combination with the highest value of R_1 is the same as that with the highest value of R_2 . Histograms of R_1 and R_2 along a X-directed line passing through this grain pair at 282 and 300 cycles are shown in figures 3.16(a) and (b).

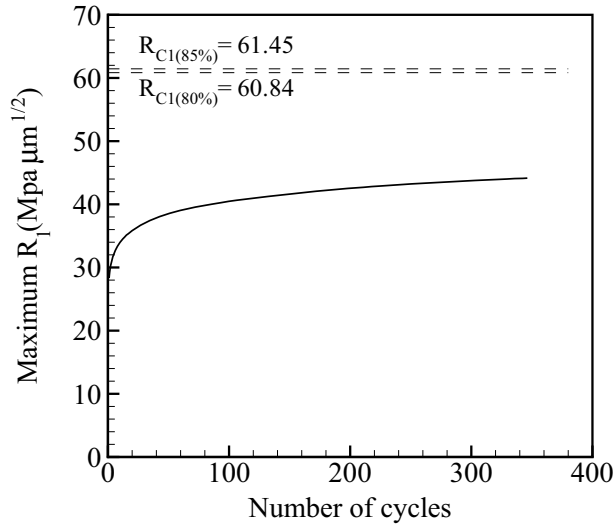


(a)

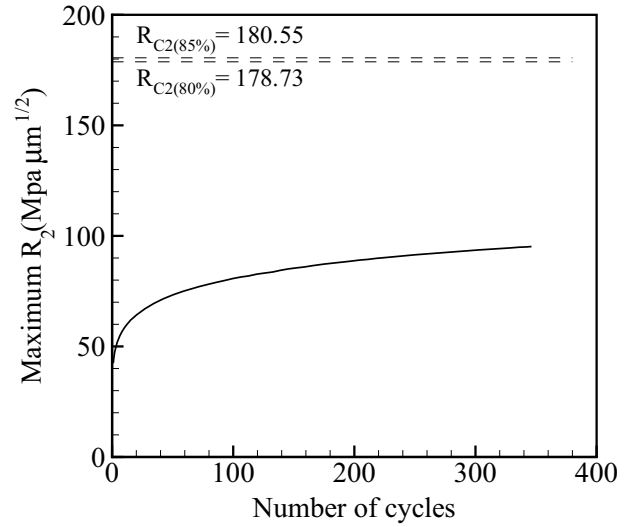


(b)

Figure 3.14: Histograms of effective crack nucleation variables: (a) R_1 along a X-directed line passing through the hard-soft grain combination with the highest R_1 value, (b) R_2 along a X-directed line passing through the hard-soft grain combination with the highest R_2 value, for the critical microstructure of specimen 1 at 282 and 300 dwell cycles respectively.



(a)



(b)

Figure 3.15: (a) Evolution of the maximum R_1 over number of cycles for the FE model of non-critical microstructure of specimen 1, (b) evolution of the maximum R_2 over number of cycles for the FE model of non-critical microstructure of specimen 1.

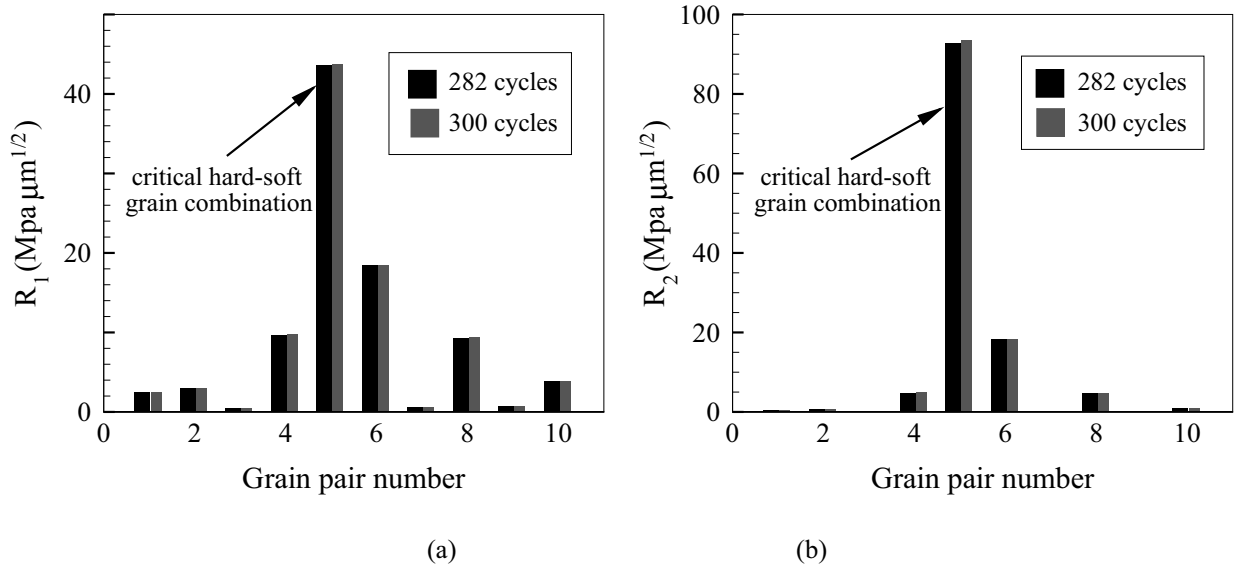


Figure 3.16: Histograms of effective nucleation variables: (a) R_1 along a X-directed line passing through the hard-soft grain combination with the highest R_1 value, (b) R_2 along a X-directed line passing through the hard-soft grain combination with the highest R_2 value, corresponding to the non-critical microstructure of specimen 1 at 282 and 300 dwell cycles.

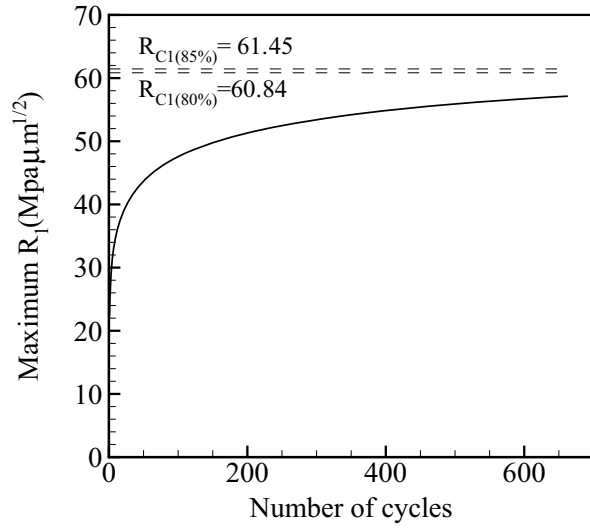
Microstructure label	Cycles to crack nucleation (experiment)	Cycles to crack nucleation (predicted)		% Relative error	
		80% of life	85% of life	80% of life	85% of life
Specimen 2	530	534	567	+0.72	+6.93
Specimen 3	380	385	405	+1.35	+6.49

Table 3.2: Comparison of predicted cycles to crack nucleation with experimentally observed life.

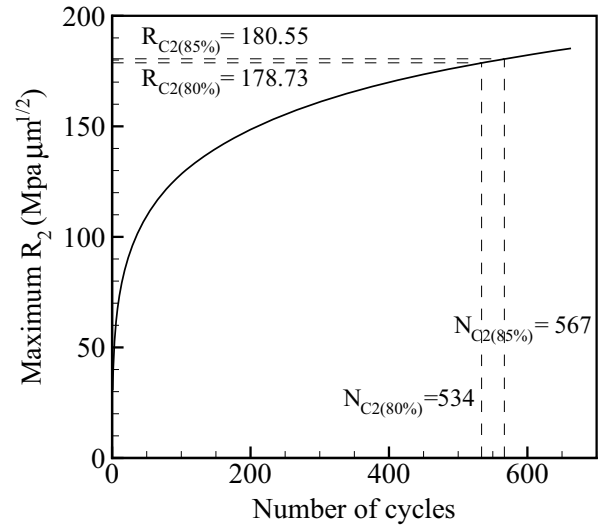
3.5.2 Predicting Crack nucleation in Specimens 2 and 3

Statistically equivalent CPFE models of the critical microstructure of specimens 2 and 3 are generated from orientation imaging microscopy scans surrounding primary and secondary cracks in the failed specimens. For specimen 2, crack nucleation is experimentally determined to occur at 530 cycles in section 3.2.2. The 2-min CPFE simulation is performed for 663 cycles using loading conditions described in [94]. Figure 3.17(a) shows the evolution of the maximum R_1 with cycles, where equation (3.26) is used to estimate c . In this figure the R_1 curve does not intersect the critical values of R_{c1} . Therefore no crack nucleation is predicted within the 663 cycles if equation (3.26) is used. However if equation (3.28) is used to estimate c , the number of cycles to nucleation are predicted as $N_{c2(80\%)} = 534$ and $N_{c2(85\%)} = 567$. These correspond to the locations where the R_2 curve in figure 3.17(b) intersects the critical values of $R_{c2(80\%)}$ and $R_{c2(85\%)}$ respectively. The difference with the experimentally determined value of 530 cycles is 0.72% for 80% of life and 6.93% for 85% of life. This agreement is considered to be excellent.

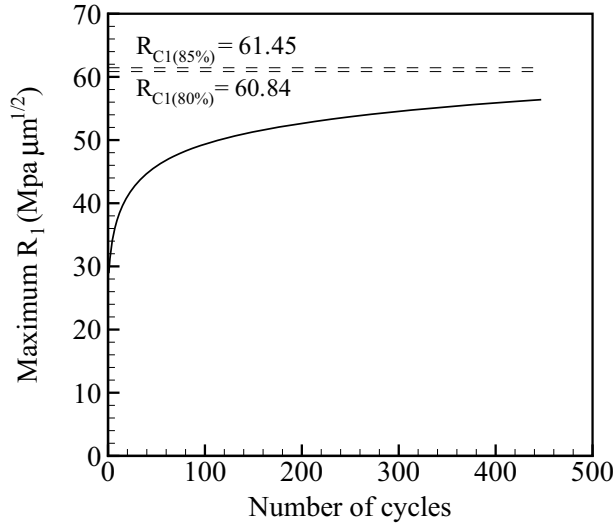
Finally, the 2-min. dwell fatigue problem is simulated for 447 cycles for the critical microstructure of specimen 3. Evolution of the maximum R_1 with the crack length c_1 is plotted in figure 3.17(c). The criterion is not able to predict a crack nucleation for specimen 3 within the 447 cycles, if equation (3.26) is used. However, the evolution of the maximum R_2 using the crack length c_2 in equation (3.28) is plotted in figure 3.17(d). The number of cycles to nucleation are predicted to be $N_{c2(80\%)} = 385$ and $N_{c2(85\%)} = 405$. From table 3.1, experimentally this crack is seen to initiate at 380 cycles. The differences in the simulated and experimental results are 1.35% for 80% of life and 6.49% for 85% of life. From these results, it is evident that using equation (3.28) for the crack length results in excellent agreement of the predicted number of cycles to crack nucleation and experimental observations. Results of crack nucleation from the evolution of R_2 are summarized in Table 3.2. Alternatively, if R_{c2} is calibrated from results on specimen 2, the calibrated value is found to be $R_{c2} = 178.51 \text{ MPa } \mu\text{m}^{1/2}$. Correspondingly, the number of cycles to nucleation for specimen 3 is found to be $N_{c2} = 383$.



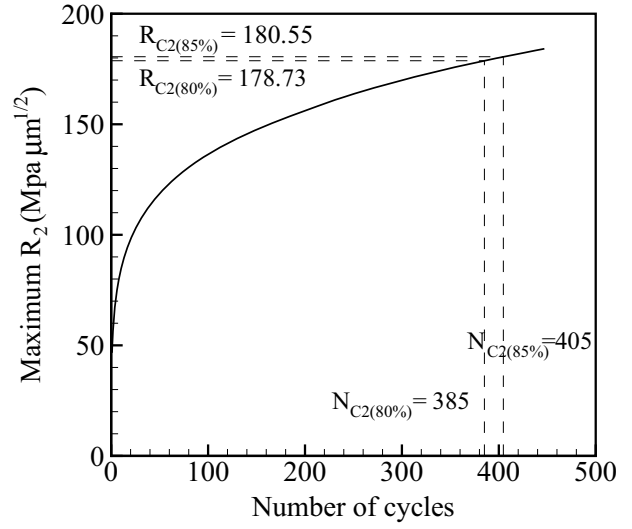
(a)



(b)



(c)



(d)

Figure 3.17: (a) Evolution of the maximum R_1 over number of cycles for the FE model of critical microstructure of specimen 2, (b) evolution of the maximum R_2 over number of cycles for the FE model of critical microstructure of specimen 2, (c) evolution of the maximum R_1 over number of cycles for the FE model of critical microstructure of specimen 3, (d) evolution of the maximum R_2 over number of cycles for the FE model of critical microstructure of specimen 3.

Microstructural parameters	Experiments	Specimen 1	Specimen 2	Specimen 3
θ_c	$\sim 0 - 30^\circ$	14.5°	36.7°	23.8°
Prismatic Schmid factor	$\sim 0.0 - 0.1$	0.03	0.16	0.08
Basal Schmid factor	$\sim 0.3 - 0.45$	0.24	0.47	0.34

Table 3.3: Microstructural features of predicted location of crack nucleation site in dwell fatigue of Ti-6242

This corresponds to only a 0.7% difference from the experimentally determined value of 380 cycles.

As an additional validation measure, characteristics of the local microstructure are identified at the crack nucleation sites in the CPFE domain and compared with the corresponding experimental observations made in [103]. Results computed with the crack length c_2 and the effective nucleation parameter R_2 are given in table 3.3. Specifically, three dominant microstructural characteristics contributing to the crack nucleation process are compared. These are the c axis orientation (θ_c) and the Schmid factors of the prismatic and basal planes for the hard grain. The simulated predictions are very consistent with the experimental observations in [103]. These results prove convincingly the predictive capability of the crack nucleation criterion both in terms of the overall life and location of cracks.

3.6 Conclusion

This work develops a novel grain-level crack nucleation criterion for dwell fatigue in polycrystalline titanium alloys. The model utilizes evolving variables that are computed in crystal plasticity finite element (CPFE) simulations of polycrystalline microstructures to construct a criterion that is able to effectively predict the number of cycles to crack nucleation, as well as the characteristics of the local site. The basic idea behind this model is that dislocations piled up against the grain boundary in a soft grain can produce a wedge type micro-crack in an adjacent hard grain. The crack nucleation model include some of the following features:

- Interaction of all active slip systems are accounted for through plastic deformation gradients in the calculation of micro-crack opening;
- Dislocations in the pile-up contribute to the wedge crack opening, through the magnitude of plastic deformation gradient and the distance from grain boundary;
- Mixed-mode cracking is considered;
- It is non-local, accounting for stress concentration in the hard grain as well as dislocation pile-up in adjacent soft grain;
- Location and direction of the micro-crack are calculated.

A necessary ingredient for this nucleation model is an experimentally validated, rate and size dependent, crystal plasticity FE model for computational modeling of the mechanical response at the level of individual grains. The 3D CPFE models utilize polycrystalline microstructures that have equivalent statistics of morphological and crystallographic characteristics. The computer models are created from failure sites (critical region) and non-failure sites (non-critical regions) of the specimens. Fatigue cracks are observed to nucleate with stress concentration caused by the load shedding phenomenon between adjacent hard and soft grains. The load shedding induced crack nucleation criterion depends on the local stresses in the hard grain as well as the non-local plastic strain gradients in adjacent soft grains. A direct approach is proposed in this work to evaluate the micro-crack length in the hard grain using the distribution of geometrically necessary dislocations inside a contiguous soft grain. The local effective stress required for crack nucleation is inversely related to the non-local plastic strain gradients in the neighboring soft grain. The proposed crack nucleation model can be reduced to a form similar to the Cottrell-Petch model in the limit, if only one slip plane of edge dislocations is considered.

The critical parameter in the crack nucleation model is calibrated using experimental results of ultrasonic crack monitoring in dwell fatigue experiments. The model is then validated against limited experimental data through predictions of the number of cycles to failure as well as the critical features of the failure site for dwell fatigue experiments. The general agreement with experiments is very satisfactory. In conclusion, the proposed model is adequate for identifying fatigue crack nucleation sites and the corresponding number of cycles in a polycrystalline aggregate. Evolving the cracks for life prediction is still a considerable challenge since appropriate fracture models must be incorporated to propagate the cracks.

Chapter 4

Wavelet Transformation Induced Multi-Time Scaling in Crystal Plasticity FEM Simulations for Fatigue Crack Nucleation in Ti-6242

4.1 Introduction

The fatigue life and number of cycles to crack nucleation in commercially used titanium alloys, such as Ti-6242, exhibit considerable variation at room temperature [98]. This is due to the influence of heterogeneities in the underlying microstructure on deformation and fatigue characteristics [9, 10, 99]. Mechanistic approaches, implementing crystal plasticity-based finite element (CPFE) simulations of polycrystalline microstructures, have been pursued in the literature [98, 44, 96, 18, 76, 73] to develop fatigue life models. These mechanistic approaches are more accurate than conventional lifing methods, where the microstructural influence on fatigue life is accommodated through phenomenological models obtained from extensive testing of specimens [109, 68, 36, 51, 24, 85].

At room temperature, inelastic deformation in Ti-6242 commences predominantly by slip on different slip systems in individual grains of the microstructure [9, 10, 99]. The number of slip systems and their resistance to slip depends on the morphological and crystallographic characteristics. For instance in the *hcp* phase of Ti-6242, the 3 basal and prismatic $\langle a \rangle$ slip systems have much lower slip resistances in comparison with the 6 $\langle a \rangle$ pyramidal, 12 $\langle c + a \rangle$ first order pyramidal and 6 $\langle c + a \rangle$ second order pyramidal slip systems [53, 29]. Consequently, grains with orientations that induce higher resolved shear stresses on the basal or prismatic systems have more plastic deformation than those activating the pyramidal systems. This material anisotropy due to the large difference in critical resolved shear stress in different slip systems results in large heterogeneity in the plastic deformation in polycrystalline aggregates. It leads to significant load-shedding induced stress concentration at grain boundaries. This is perceived to be the primary driver of microstructure-dependent crack nucleation [9, 71].

The present work uses a size and rate-dependent CPFE model of Ti-6242 developed in [53, 29, 119] to capture this load-shedding induced stress rise in the microstructure leading to crack nucleation. Particularly vulnerable are boundaries between grains having large time-dependent plastic deformation (soft grain) and those with little or no plasticity (hard grain) owing to their orientation with respect to the loading direction. Morphological and crystallographic features of the polycrystalline alloy are statistically represented in the CPFE models using methods developed in [49, 50]. The use of such a statistical description not only reduces the number of grains in the FE simulations but also captures the key features of the microstructure that affect its macroscopic and microscopic response. A non-local crack nucleation model has been developed in [4] to study early crack nucleation in polycrystalline Ti-alloys under dwell fatigue cyclic loading. The crack nucleation criterion is functionally dependent on stress concentration and dislocation pile-up at grain boundaries. These variables are obtained from CPFEM simulations. A combination of CPFE simulations and ultrasonic testing of dwell fatigue Ti-6242 samples has been used in [4] for calibrating and validating the nucleation model. This model is extended in the present work to study microstructure and load dependent crack nucleation in Ti-6242.

Although CPFE simulations accurately capture the deformation behavior of polycrystalline alloys, they require very

small time steps when conventional time integration schemes are used to march forward in time. In cyclic loading and deformation, small time steps in every cycle of the loading process leads to prohibitively large computations, when analysis is performed for a large number of cycles to fatigue failure. To overcome this limitation, fatigue life predictions have been performed in [13, 98, 113] by extrapolating the results based on CPFEM simulations performed for few cycles. However extrapolation can lead to considerable error in the evolution of *local* microstructural variables and cause inaccurate fatigue life prediction. Accurate life prediction requires cycle-by-cycle evolution of all microstructural variables in cyclic CPFEM simulations till the failure event.

Evolution of CPFE variables under cyclic loading has two distinct time scales, viz. (i) fine time scale corresponding to the high frequency oscillations of the applied loading and (ii) coarse time scale corresponding to the low frequency evolution of material relaxation. Multi-time scaling methods may be devised to decouple this dual-time behavior and perform time integration only for the coarse time-scale problem with the lower frequency response. The *wavelet transformation induced multi-time scaling* or WATMUS method, developed in [59, 22], has shown significant computational benefits in rapidly traversing a high number of cycles. The WATMUS method is distinctly advantageous over other multi-time scale schemes such as the method of separation of motions [16, 111], asymptotic expansion based methods [125, 72] or almost periodic temporal homogenization operator based method [84, 83], where inherent scale separation and local periodicity or almost periodicity in temporal evolution are assumed. Such assumptions are invalid for crystal plasticity variables, which show strong non-periodic evolution and spatio-temporal localization. The WATMUS method does not make these assumptions and is used in the present work to perform accelerated cyclic CPFEM simulations.

This work is intended to understand the effects of microstructure and cyclic loading conditions on grain-level crack nucleation. The WATMUS method based cyclic CPFE simulations of polycrystalline Ti-6242 microstructures are used to accomplish this mechanistic approach. An overview of the CPFE model is presented in section 4.2. The crack nucleation model developed in [4] is discussed in section 4.3. The WATMUS method is described in section 4.4 along with some examples to demonstrate its efficiency and accuracy. Calibration and validation of the crack nucleation model parameters for dwell fatigue using CPFEM simulations and experiments are conducted in section 4.5. A detailed numerical study of the different factors affecting fatigue crack nucleation in Ti-6242 is executed in section 4.6. In section 4.6.2, relations between crystallographic features and cycles to crack nucleation are developed. The dependence on the number of cycles to crack nucleation on characteristics of the applied load is studied in section 4.6.3.

4.2 Size and Rate Dependent Crystal Plasticity FE model for Ti-6242

The rate and size dependent crystal plasticity constitutive laws governing deformation in polycrystalline, bi-phasic Ti-6242 alloys have been developed in detail in [53, 29, 119, 118]. The total deformation gradient is assumed to be multiplicatively split into an elastic and plastic part [60, 5] as:

$$\mathbf{F} = \mathbf{F}^e \mathbf{F}^p \quad (4.1)$$

The elastic part of the deformation gradient \mathbf{F}^e captures the stretching and rotation of the lattice, whereas the plastic deformation is due to crystallographic slip on different slip systems. It is expressed from the relation

$$\dot{\mathbf{F}}^p \mathbf{F}^{p-1} = \sum_{\alpha} \dot{\gamma}^{\alpha} \mathbf{S}_0^{\alpha} \quad (4.2)$$

where $\dot{\gamma}^{\alpha}$ is the slip rate on different slip systems and \mathbf{S}_0^{α} is the Schmid tensor expressed in terms of the slip direction \mathbf{m}_0^{α} and slip plane normal \mathbf{n}_0^{α} in an intermediate configuration. A power law model described in [5, 12] is used to determine the slip-rate on different slip systems as:

$$\dot{\gamma}^{\alpha} = \dot{\alpha} \left| \frac{\tau^{\alpha} - \chi^{\alpha}}{g^{\alpha}} \right|^{\frac{1}{m}} \text{sign}(\tau^{\alpha} - \chi^{\alpha}) \quad (4.3)$$

where $\dot{\alpha}$ is a reference slip rate, τ^{α} is the resolved shear stress on the slip system, χ^{α} is a back stress, g^{α} is the slip system resistance and m is the power law exponent. The resolved shear stress on a slip system is obtained from

$$\tau^{\alpha} = \mathbf{F}^{eT} \mathbf{F}^e \mathbf{T}^* : \frac{1}{2} (\mathbf{S}_0^{\alpha} + \mathbf{S}_0^{\alpha T}) \quad (4.4)$$

where \mathbf{T}^* is the 2nd Piola-Kirchoff (PK2) stress. A hyper-elastic law is used to obtain the PK2 stress from the work conjugate Lagrange-Green strain tensor $\mathbf{E}^e (= \frac{1}{2}(\mathbf{F}^{eT} \mathbf{F}^e - \mathbf{I}))$ as:

$$\mathbf{T}^* = \mathbf{C} : \mathbf{E}^e \quad (4.5)$$

where \mathbf{C} is the elastic stiffness tensor. The back stress evolution on a slip system follows the law:

$$\dot{\chi}^\alpha = c\dot{\gamma}^\alpha - d\chi^\alpha |\dot{\gamma}^\alpha| \quad (4.6)$$

where c and d are the direct hardening and dynamic recovery coefficients respectively [79]. Slip system resistance evolution follows the relation:

$$\dot{g}^\alpha = \sum_{\beta} q^{\alpha\beta} h^\beta |\dot{\gamma}^\beta| \quad (4.7)$$

where h^β is the self hardening parameter and $q^{\alpha\beta}$ is a matrix describing latent hardening. The microstructure of Ti-6242 consists of primary α grains and transformed β colonies. The primary α grains have a *hcp* crystal lattice structure, while the transformed β colonies consist of alternate laths of *hcp* lattice and symmetric *bcc* lattice. Different self hardening relationships are used for modeling the α and β phases [29]. The evolution of self hardening for the α phase is modeled as:

$$\begin{aligned} h^\alpha &= h_0^\alpha \left| 1 - \frac{g^\alpha}{g_s^\alpha} \right|^r \text{sign} \left(1 - \frac{g^\alpha}{g_s^\alpha} \right) \\ g_s^\alpha &= \tilde{g} \left| \frac{\dot{\gamma}^\alpha}{\dot{a}} \right|^c \end{aligned} \quad (4.8)$$

where h_0^α is a reference self hardening parameter and g_s^α is the saturation value of slip system resistance. Self hardening rate of the β phase is given as:

$$\begin{aligned} h^\alpha &= h_s^\alpha + \text{sech}^2 \left[\frac{h_0^\alpha - h_s^\alpha}{\tau_s^\alpha - \tau_0^\beta} \gamma^{acc} \right] (h_0^\alpha - h_s^\alpha) \\ \gamma^{acc} &= \int_0^t \sum_{\alpha} |\dot{\gamma}^\alpha| dt \end{aligned} \quad (4.9)$$

h_0^α and h_s^α are the initial and asymptotic hardening rates, τ_s^α represents the saturation value of shear stress when $h_s^\alpha = 0$, and γ^{acc} is the accumulated plastic slip on the slip system.

To avoid explicit modeling of the alternating lath structure of transformed β colonies in the CPFEM simulations of polycrystalline Ti-6242, an equivalent homogenized model has been proposed in [29]. It is based on a mixture rule, where the individual phases at a material point are subject to a homogeneous deformation gradient \mathbf{F} , giving rise to different stresses and plastic variables in each of the phases. The homogenized stress is obtained from the weighted sum of the stresses based on volume fractions of individual phases in the colony as:

$$\sigma = w_\alpha \sigma_\alpha + w_\beta \sigma_\beta \quad (4.10)$$

The weights w_α and w_β correspond to the volume fractions of individual phases of these alloys.

The effect of grain size and lath thickness on the slip system resistance is also considered in the crystal plasticity model in [119]. A Hall Petch type relation is used to modify the initial slip system resistances $g^\alpha(t = 0)$ to capture size effect according to the relation:

$$g^\alpha(t = 0) = g_0^\alpha + \frac{K^\alpha}{\sqrt{D^\alpha}} \quad (4.11)$$

where g_0^α is the homogeneous slip system resistance, D^α is a characteristic length parameter that corresponds to the mean-free path of the dislocations in a grain. For globular α grains, the transmission of dislocations to adjacent grains is resisted by grain boundaries and hence grain diameter is considered as characteristic length in equation (4.11). For transformed β colonies, dislocation motions can be impeded either by the colony boundary or lath boundary depending on the Burger's orientation relation between α and β laths [53, 29]. Hence either colony size or lath thickness is used for D^α in equation (4.11) for slip system resistances of the transformed β colonies. K^α is a constant that depends on the Poisson's ratio, shear modulus, Burgers vector and barrier strength. The different parameters in the model have been calibrated from experiments on single crystal Ti-6Al and Ti-6242 in [53, 29, 119].

Analysis of the microstructural influence on deformation and creep behavior requires statistically equivalent polycrystalline microstructures in CPFEM simulations. Statistically equivalent microstructures of polycrystalline alloys have been constructed from distributions of grain size, shape, orientation, misorientation, and microtexture in [49, 50]. Simulations in [4, 119] have demonstrated that hard grains surrounded by soft regions develop large stresses near their boundaries, which keep increasing with time due to rate effects.

4.3 Non-local Crack Nucleation Model for Near α Ti-alloys

A crack nucleation model, developed in [4], is used in this work to model grain-level nucleation in a polycrystalline ensemble. The model has been motivated from experimental observations of failed Ti-6242 samples under room temperature dwell-fatigue loading with a maximum stress of 90-95% of yield strength, and stress ratio $\sigma_{min}/\sigma_{max} = 0$ [102, 101]. Experimentally extracted crystallographical features of grains at failure sites suggest that regions of hard grains surrounded by soft grains are susceptible to initiate a crack [101, 4]. During the hold period of the loading, soft grains with favorably oriented $\langle a \rangle$ -type slip systems for dislocation glide undergo significant plastic straining. Contiguous hard grains with less-favorably oriented for $\langle a \rangle$ -type slip ($\langle c \rangle$ -axis parallel to the deformation direction), experience large local stress concentrations, especially near the shared grain boundary. This is a consequence of compatible, large elastic strains in the hard grains near the shared boundary. The phenomenon of rising stress-concentration with evolving creep strains in dwell cycles has been called load shedding [53, 4]. The hard grain crack nucleation criterion, ahead of dislocation pile-ups in adjacent soft grain has been derived to be [4]:

$$T_{eff} = \sqrt{\langle T_n \rangle^2 + \beta T_t^2} \geq \frac{K_c}{\sqrt{\pi c}} \quad (4.12)$$

or equivalently

$$R = T_{eff} \cdot \sqrt{c} \geq R_c, \quad \text{where } R_c = \frac{K_c}{\sqrt{\pi}} \quad (4.13)$$

In equations (4.12) and (4.13), T_{eff} is an effective traction on the hard grain basal plane for mixed mode crack nucleation. It is expressed in terms of the stress component normal to the crack surface $T_n = \sigma_{ij}n_i^b n_j^b$ and the tangential stress component $T_t = \|\mathbf{T} - T_n \mathbf{n}^b\|$. Here \mathbf{T} is the stress vector on the crack surface, σ_{ij} is the Cauchy stress tensor and n_i^b are the components of unit outward normal to the crack surface. Only the tensile normal stress $\langle T_n \rangle$, represented by the McCauley bracket $\langle \rangle$, contributes to the effective stress responsible for crack opening. K_c is the critical mixed-mode stress intensity factor and $\beta \approx K_{nc}/K_{tc}$ is a shear stress factor used to assign different weights to the normal and shear traction components for mixed-mode. A value of $\beta = 0.7071$ is used for Ti-64 alloys in this study. c is the length of a wedge micro-defect or crack on the basal plane of the hard grain caused by dislocation pile-up in the adjacent soft grain. A schematic of a micro-crack of length c on the basal plane of a hard grain, the corresponding dislocation pile-up \mathbf{B} in the adjacent soft grain and the local effective traction T_n, T_t at the crack nucleation site is shown in figure 4.1. The critical crack nucleation parameter R_c in equation (4.13) is a material property, which is calibrated from experiments.

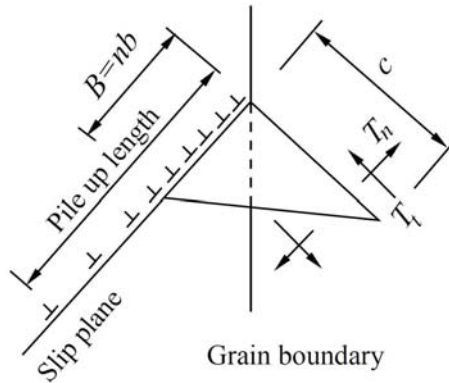


Figure 4.1: Schematic of a wedge micro crack formation resulting from dislocation pile-up in the soft grain near a hard soft grain boundary, where c is the micro crack length and $B = \|\mathbf{B}\|$ is the crack opening displacement due to dislocation pile-up.

The micro-crack length c in equation (4.13) is obtained from the relation proposed in [107] as:

$$c = \frac{G}{8\pi(1-\nu)\gamma_s} B^2 \quad (4.14)$$

where B is the crack opening displacement, G is the shear modulus, ν is the Poisson's ratio and γ_s is the surface energy. The crack opening displacement $B = \|\mathbf{B}\|$ is a non-local variable that is evaluated from the equation:

$$\mathbf{B} = \int_{\Omega} \mathbf{\Lambda} \cdot \mathbf{n} d\Omega = \int_{\Omega} (\nabla^T \times \mathbf{F}^p) \cdot \mathbf{n} d\Omega \quad (4.15)$$

Here \mathbf{n} is normal to surface Ω in which the Burgers circuit is considered, $\mathbf{\Lambda}$ is Nye's dislocation tensor and ∇ is the curl operator. The numerical procedure to evaluate the evolving crack nucleation parameter (R_α) at a node α on the grain boundary is described in [4].

4.4 Wavelet Transformation based Multi-time Scale (WATMUS) Method for Accelerated Cyclic CPFEM Simulations

Fatigue life predictions in polycrystalline metallic microstructures involve cyclic crystal plasticity FEM simulations till crack nucleation. Depending on the microstructure and load profile, this may involve simulations for large number of cycles. Such simulations may become computationally prohibitive using conventional time integration schemes in FEM codes. In [59, 22], a wavelet transformation based multi-time scale or WATMUS method has been developed to reduce the problem to a set of low frequency, coarse time-scale governing equations. In the WATMUS scheme, any time dependent variable $v^\zeta(t)$ is expressed as:

$$v^\zeta(t) = v(N, \tau) = \sum_{k=1}^n v_k(N) \psi_k(\tau) \quad \forall \quad \tau \in [0, T] \quad (4.16)$$

The superscript ζ corresponds to the dependence of the variable on the two time-scales, which for this problem correspond to a cycle scale N and an intra-cycle fine time-scale τ . $\psi_k(\tau)$ are wavelet basis functions that capture the high frequency response within each cycle, n is the number of basis functions required for accurate representation of the waveform. Compact support, multi-resolution and orthogonality properties of the wavelet basis functions [120, 106] allow significant reduction in the number of basis functions required for accurate representation of arbitrary waveforms in different evolving variables. The compact or finite support of the wavelet basis functions also eliminates spurious oscillations that may arise with truncation of terms in infinitely supported basis functions such as the spectral basis functions. $v_k(N)$ are the associated coefficients that evolve monotonically in the cycle (N)-scale. Using orthogonality property, they may be expressed as:

$$v_k(N) = \frac{1}{T} \int_0^T v(N, \tau) \psi_k(\tau) d\tau \quad (4.17)$$

where T is time period of the applied load. Wavelet transformation facilitates numerical integration of the CPFEM equations in the cycle-scale traversing several cycles in each step. This leads to significant efficiency gain.

The cycle-scale weak form for the FEM micromechanics problem of the polycrystalline microstructure, in the absence of inertia terms, is obtained by substituting equation (4.16) in the semi-discrete system of equations. The resulting transformed system of equations to be solved for the wavelet coefficients at each node α is given as:

$$\begin{aligned} R_{i,k}^\alpha(N) &= \frac{1}{T} \int_0^T R_i^\alpha(N, \tau) \psi_k d\tau \\ &= \sum_e \int_{V_{0,e}} \frac{1}{T} \int_0^T \frac{\partial P^\alpha}{\partial x_j} \sigma_{ji} J_e \psi_k d\tau dV_{0,e} - \sum_{S_\tau} \int_{S_0} \frac{1}{T} \int_0^T P^\alpha t_i J_A \psi_k d\tau dS_0 = 0 \end{aligned} \quad (4.18)$$

where P^α are the FE shape functions in every element e , S_τ are the surfaces on which tractions are applied, α are the nodes of the discretized domain, $V_{0,e}$ and S_0 are the element volumes and surfaces in the reference configuration respectively and σ_{ji} are the stresses at integration points in the spatially discretized domain. The transformed weak form (4.18) is solved at discrete cyclic increments using a Quasi-Newton iterative scheme for the wavelet coefficients of nodal displacements $C_{i,k}^\alpha$:

$$C_{i,k}^\alpha(N) = \frac{1}{T} \int_0^T u_i^\alpha(N, \tau) \psi_k(\tau) d\tau \quad (4.19)$$

u_i^α are the nodal displacement degrees of freedom in the finite element model. The oscillatory stress response $\sigma_{ji}(N, \tau)$ in equation (4.18) depends on the oscillatory deformation gradient $F_{ij}(N, \tau)$ and internal variables $y_m(N, \tau)$. $F_{ij}(N, \tau)$ at each integration point in any cycle is obtained from the coefficients of nodal displacements $C_{i,k}^\alpha(N)$ using the relation:

$$F_{ij}(N, \tau) = \delta_{ij} + \frac{\partial P^\alpha}{\partial X_j} \sum_{k=1}^n C_{i,k}^\alpha(N) \psi_k(\tau) \quad (4.20)$$

In crystal plasticity, the evolution of internal variables is governed by first order rate equations of the type

$$\dot{y}_m^\zeta(t) = f_m(y_m^\zeta, F_{ij}^\zeta, t) \quad (4.21)$$

Here y_m^ζ are internal variables represented in a single time-scale t and f_m are non-linear functions. The oscillatory evolution of the dual-scale variable $y_m(N, \tau)$ in any cycle may be obtained from the fine-scale time integration as:

$$y_m(N, \tau) = y_{m0}(N) + \int_0^\tau f_m(y_m, F_{ij}, N, \tau) d\tau \quad (4.22)$$

where $y_{m0}(N) = y_m(N, \tau = 0)$ are values of internal variables at the beginning of a cycle. This forms a new cycle-scale variable, corresponding to the initial values of internal variables y_{m0} , which have a monotonic evolution in the cycle-scale. Cycle-scale rate equations are numerically defined for y_{m0} as [59]:

$$\frac{\partial y_{m0}}{\partial N} = y_{m0}(N+1) - y_{m0}(N) = y_m(N, T) - y_{m0}(N) \quad (4.23)$$

where

$$y_m(N, T) = y_{m0}(N) + \int_0^T f_m(y_m, F_{ij}, N, \tau) d\tau \quad (4.24)$$

Since f_m are non-linear functions, numerical time-integration using the backward Euler scheme is performed on equation (4.24). The cycle-scale internal variables are integrated using a 2^{nd} order backward difference formula, expressed as:

$$\begin{aligned} y_{m0}(N) &= \beta_1 y_{m0}(N - \Delta N) - \beta_2 y_{m0}(N - \Delta N - \Delta N_p) + \beta_3 \left. \frac{\partial y_{m0}}{\partial N} \right|_N \Delta N \\ \text{where } \beta_1 &= \frac{(r+1)^2}{(r+1)^2 - 1} \quad \beta_2 = \frac{1}{(r+1)^2 - 1} \quad \beta_3 = \frac{(r+1)^2 - (r+1)}{(r+1)^2 - 1} \\ \text{and } r &= \frac{\Delta N_p}{\Delta N} \end{aligned} \quad (4.25)$$

The Newton-Raphson iterative scheme is used to solve equation (4.25).

Adaptive methodologies have been developed in [59] to improve the efficiency and reduce the number of degrees of freedom in the WATMUS method. Only those wavelet coefficients of nodal displacements that evolve, are selected and retained in the function representations. Subsequently, the optimal set of equations are solved in a cyclic increment using the cycle-scale weak form of equation (4.18). Additionally an optimal cycle-stepping condition is derived for improving computational efficiency. Optimal cycle-steps are predicted from an upper bound of the truncation error in the 2^{nd} order backward difference formula used to integrate the cycle scale internal variables. The use of these adaptive criteria significantly enhances the performance of WATMUS method for cyclic CPFEM simulations.

The accuracy of the WATMUS method is demonstrated by comparing the evolution of crystal plasticity variables obtained from (i) single time-scale, and (ii) WATMUS method-enhanced dual time-scale simulations of a statistically equivalent virtual polycrystalline Ti-6242 microstructure [49, 50]. In figure 4.2, the microstructure is subjected to a triangular cyclic load on the y -face with a maximum and minimum normal traction of 869 MPa and 0 MPa respectively, and a time period of 2 secs.

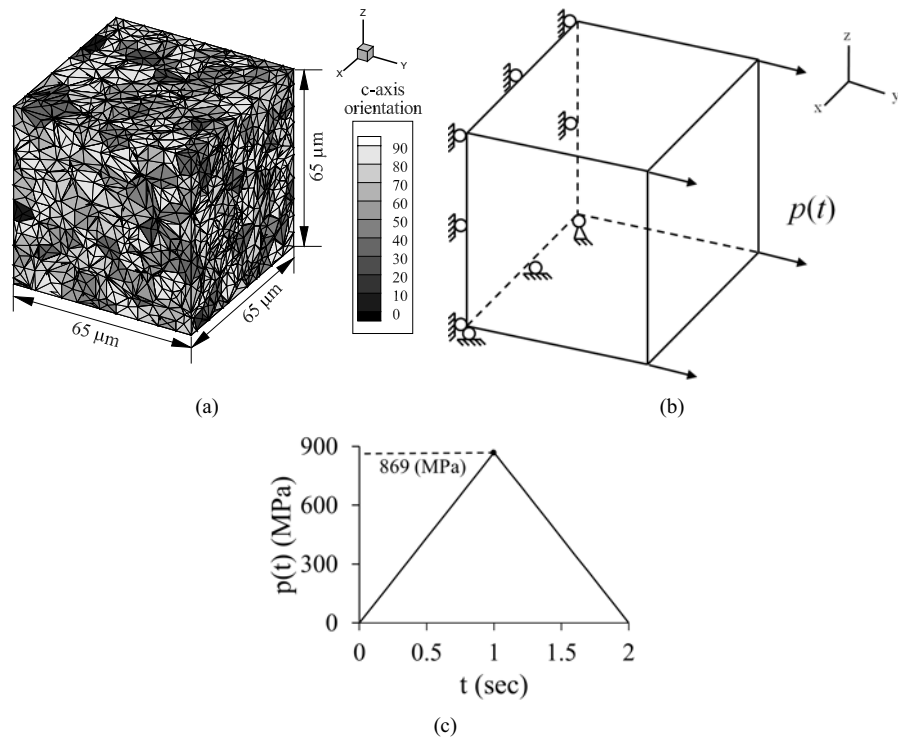


Figure 4.2: FE model of a polycrystalline microstructure and loading conditions to demonstrate the accuracy and efficiency of the WATMUS method: (a) microstructure with $\langle c \rangle$ -axis orientation and mesh, (b) boundary conditions, and (c) cyclic loading profile.

The WATMUS method-enhanced CPFEM simulation is performed for 300,000 cycles and the evolutionary variables, e.g. set of wavelet coefficients of nodal displacements $C_{i,k}^\alpha$ and the history of coarse scale internal variables $\mathbf{y}_0^{\alpha/\beta} = \{F_{ij,0}^p, g_0^\alpha, \chi_0^\alpha\}$ are compared with a single time-scale simulation. The single time-scale simulation suffers from a large computational overhead, and the simulation is performed for 215 cycles only. A comparison of the evolution of coarse internal variables at an integration point in the microstructure is shown in figure 4.3.

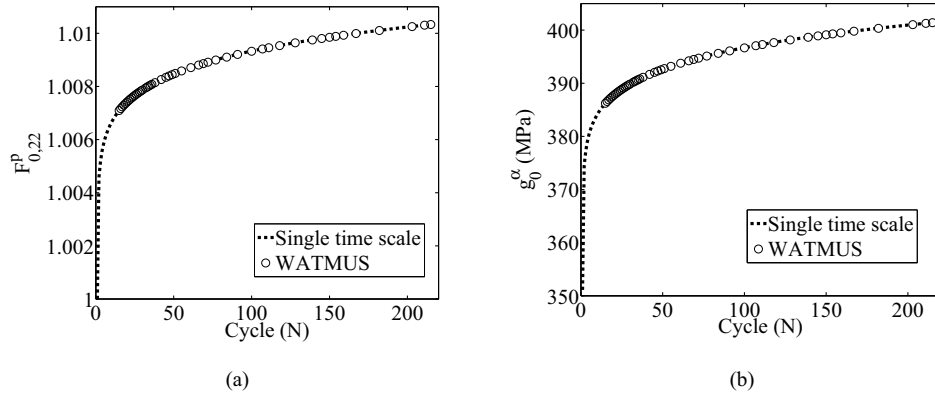


Figure 4.3: Comparison of the evolution of the cycle-scale with averaged single time-scale internal variables at an integration point in the FE model of the polycrystalline microstructure for: (a) $F_{0,22}^p$, (b) g_0^α .

Highly resolved fine time-scale response within any cycle can be reconstructed from the cycle-scale variables obtained from WATMUS-based CPFEM simulations using the wavelet basis in equation (4.16). The relative error in the reconstructed fine time-scale evolution of internal variables with respect to the single time scale results is defined as

$e(N, \tau) = \frac{|\tilde{y}(N, \tau) - y(N, \tau)|}{\|\tilde{y}(N, \tau)\|}$, where $\tilde{y}(N, \tau)$ is reconstructed from the cycle-scale variables using the wavelet basis and $y(N, \tau)$ is the single time-scale solution. The relative error for different variables at an element integration point in the microstructure in the 211th cycle is depicted in figure 4.4.

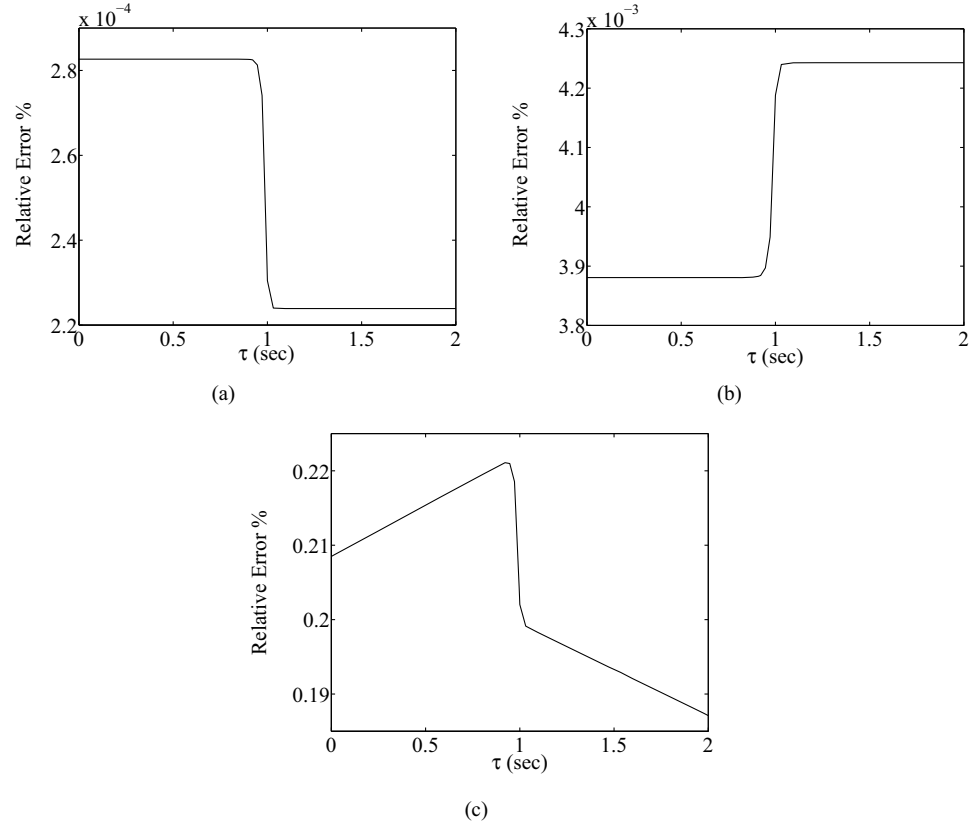
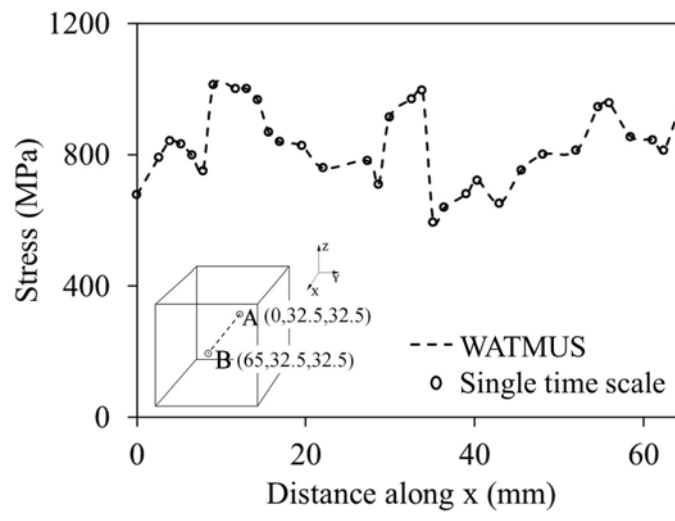
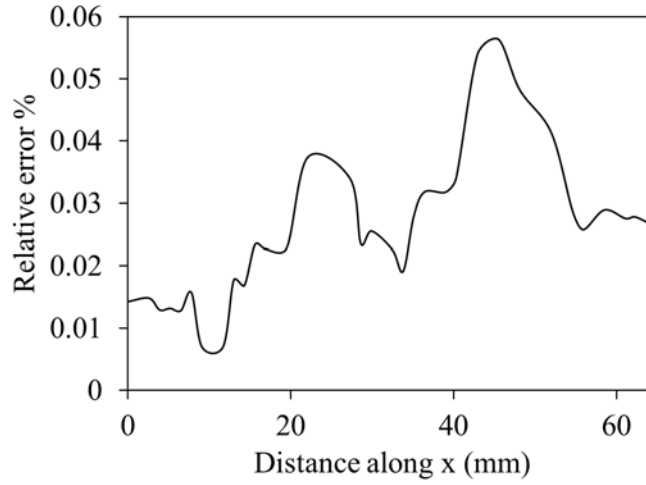


Figure 4.4: Relative error $e(N, \tau) = \frac{|\tilde{y}(N, \tau) - y(N, \tau)|}{\|\tilde{y}(N, \tau)\|}$ of fine scale evolution of variables at 211th cycle at an integration point in the FE model of the polycrystalline microstructure for: (a) F_{22}^p , (b) g^α , (c) σ_{22} .

The distribution of the loading direction stress σ_{22} along a specified material line in the microstructure, as obtained by the WATMUS and single time scale simulations is compared in the figure 4.5.



(a)



(b)

Figure 4.5: Comparison of distribution of stress σ_{22} along a material line in the microstructure at $N = 211$ and $\tau = 1$ sec, by the WATMUS and single time-scale CPFEM simulations for: (a) σ_{22} (b) relative error in σ_{22} .

These comparisons conclusively show that the WATMUS method is able to capture the evolution of the local microstructural variables very accurately. Finally to demonstrate the power of the WATMUS method in traversing a large number of cycles, the evolution of plastic deformation gradient $F_{0,22}^p$ with advancing cycles are shown in figure 4.6 for up to 300,000 cycles.

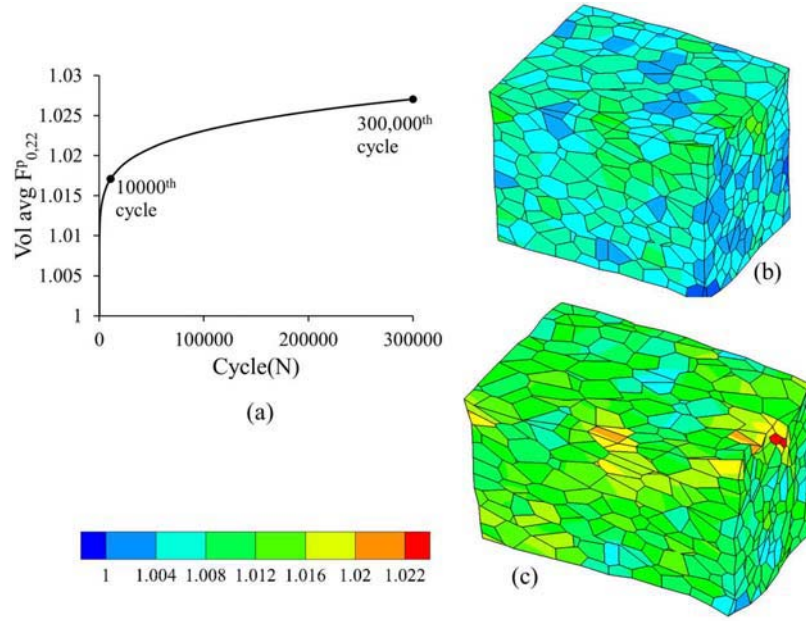


Figure 4.6: Evolution of $F_{0,22}^p$ with cycles by WATMUS-based CPFEM simulation: (a) volume averaged $F_{0,22}^p$, (b) distribution of $F_{0,22}^p$ at the 10,000th cycle, and (c) distribution of $F_{0,22}^p$ at the 300,000th cycle.

The corresponding evolution of stress σ_{22} in the 300,000th cycle at the fine time-scale $\tau = 0$ and $\tau = 1$ sec are shown in figure 4.7.

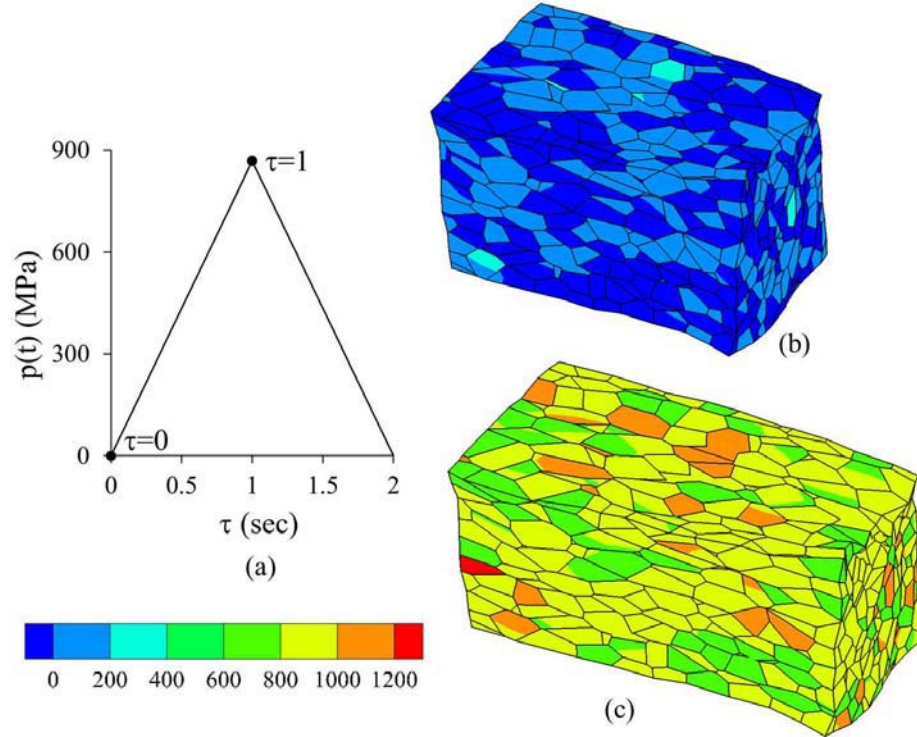


Figure 4.7: Evolution of fine time-scale σ_{22} at the 300,000th cycle by WATMUS-based CPFEM simulation: (a) applied load profile on the y -face of the microstructure, (b) distribution of σ_{22} at $\tau = 0$ sec, (c) distribution of σ_{22} at $\tau = 1$ sec.

To evaluate the computational efficiency, the CPU time to perform 215 cycles for the single time-scale CPFEM simu-

lation is extrapolated to 300,000 cycles and compared with the CPU time taken to perform 300,000 cycles of WATMUS simulation. A computational speedup of ~ 100 times is obtained for this problem.

4.4.1 A Slightly Modified WATMUS Scheme to Accommodate Larger Time Periods

The WATMUS algorithm proposed in [59] is suitable for problems where the time period of applied load is relatively small. This is due to the fact that the entire oscillatory response over a cycle is represented by a single set of multi-resolution wavelet basis functions. This deteriorates the resolution when large time periods are involved, often encountered in dwell fatigue simulations. To alleviate this shortcoming, the total time period is divided into smaller segments with different maximum resolutions. The maximum resolution in every segment is determined from the first few cycles of a single time-scale simulation. This structure is not altered in the cycle-scale simulation. The use of different maximum resolutions drastically reduces the total number of wavelet coefficients that needs to be stored and also expedites the fine time-scale integration to obtain the cycle-scale rate equations of internal variables y_{m0} .

To demonstrate the advantage of this modification in handling large time periods, a dwell fatigue simulation using the WATMUS method is performed for the polycrystalline microstructure in figure 4.2. A schematic of the dwell load with 2 min hold and the corresponding segments are shown in figures 4.8(a) and 4.8(b) respectively.

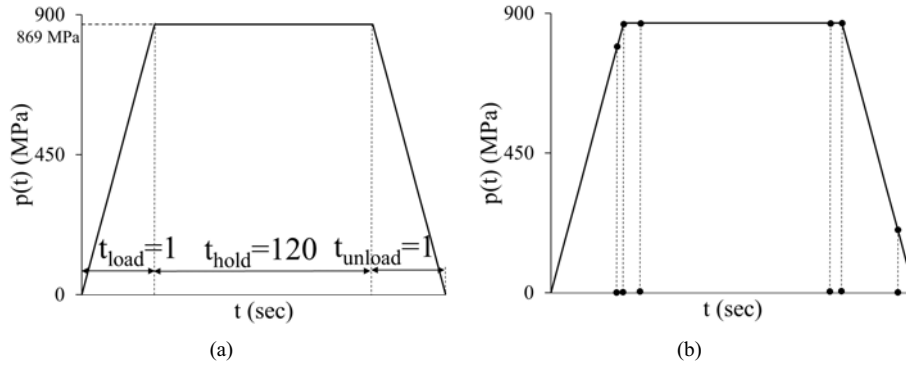


Figure 4.8: Schematic of cyclic dwell loading: (a) dwell load profile applied on y -face of the polycrystalline microstructure (b) segments with different maximum resolution.

The cycle-scale evolution of $F_{0,22}^p$ and g_0^α for a slip system at an integration point in the microstructure by the WATMUS method-enhanced CPFEM simulation is shown in figure 4.9.

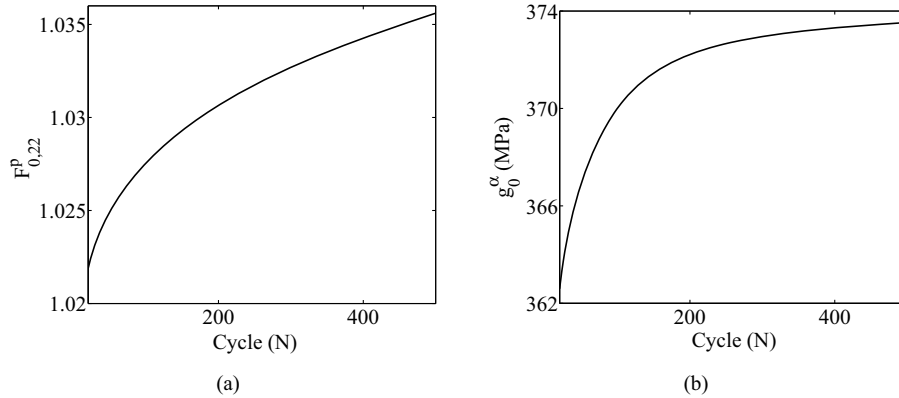


Figure 4.9: Evolution of cycle-scale internal variables at an integration point in the microstructure: (a) $F_{0,22}^p$ (b) one of the slip system resistances g_0^α .

The monotonic evolution of $F_{0,22}^p$ and contour plots of its distribution are shown in figure 4.10.

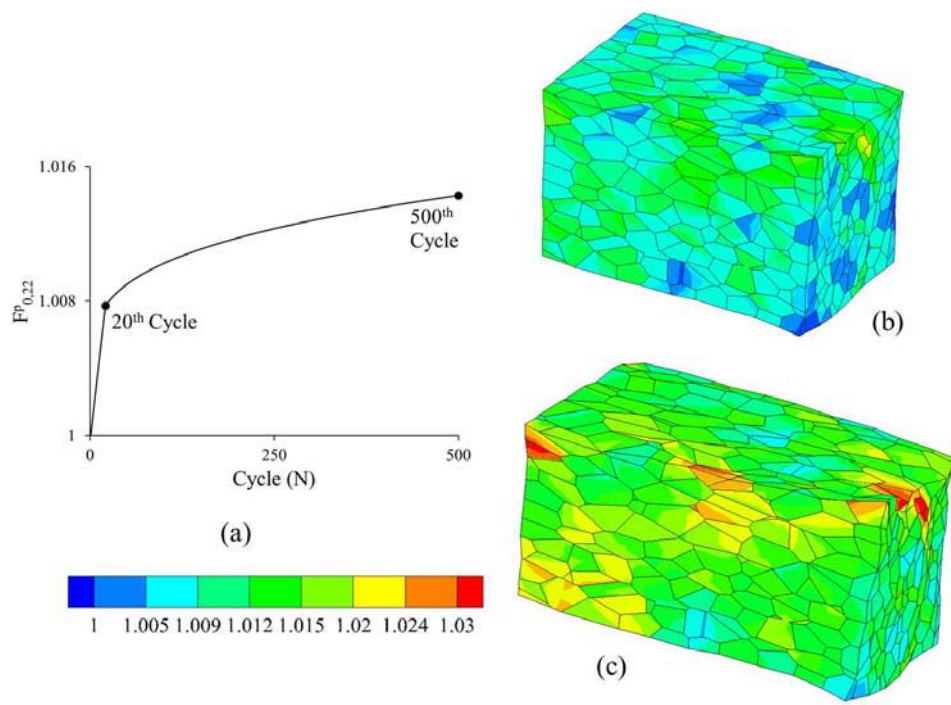


Figure 4.10: Evolution of $F_{0,22}^p$ with cycles by the WATMUS based CPFEM simulations: (a) volume averaged $F_{0,22}^p$, (b) distribution of $F_{0,22}^p$ at the 21st cycle, (c) distribution of $F_{0,22}^p$ at the 500th cycle.

The evolution of σ_{22} along a material line in the microstructure is evaluated for the cycles 21 and 500, at $\tau = 121$ sec, and is depicted in figure 4.11. Large stresses develop in the hard grains adjacent to soft grains due to anisotropy, leading to orientation dependent rate of plastic deformation and load-shedding. The stress peak rises with advancing cycles of the load, thus enhancing the probability of crack nucleation in these hard grains.

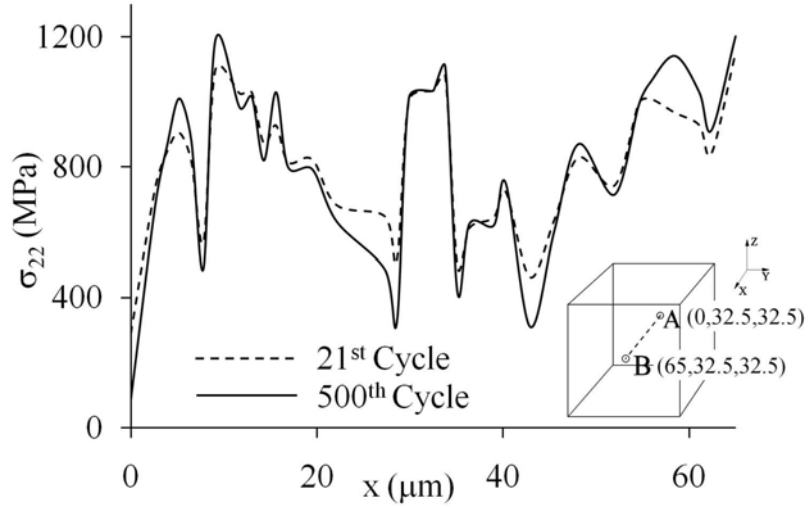


Figure 4.11: Evolution of loading direction stress component σ_{22} along a material line in the microstructure evaluated at cycles N=21 and N=500 and $\tau = 121$ sec.

The WATMUS method-enhanced CPFE simulations is used in conjunction with the crack nucleation model in section 4.3 to study the fatigue nucleation behavior of Ti-alloys.

4.5 Calibration and Validation of Critical Crack Nucleation Parameter R_c

The critical crack nucleation parameter R_c should be calibrated prior to conducting crack nucleation sensitivity analyses using CPFEM simulations. Subsequent validation studies are performed using 2 different specimens of the Ti-6242 alloy, subject to dwell fatigue load with a hold time of 2 min, and loading and unloading time of 1 sec each. The maximum stress in a loading cycle is 869 MPa, which is 95% of the yield strength, while the minimum stress is 0 MPa. Subsurface crack propagation has been monitored by using micro-radiographic images from interrupted experiments in [93]. The lengths of the dominant cracks are progressively recorded and plotted as shown in figure 4.12. The number of cycles to initiate a crack is estimated by extrapolating the curve to zero crack length. From dwell fatigue experiments on Ti-6242 specimens, it has been observed in [93] that crack nucleation occurs at 80 – 85% of the total number of cycles to failure N_f . The evolution of a crack with cycles for the specimen 2, along with the extrapolated functional fit, are shown in figure 4.12.

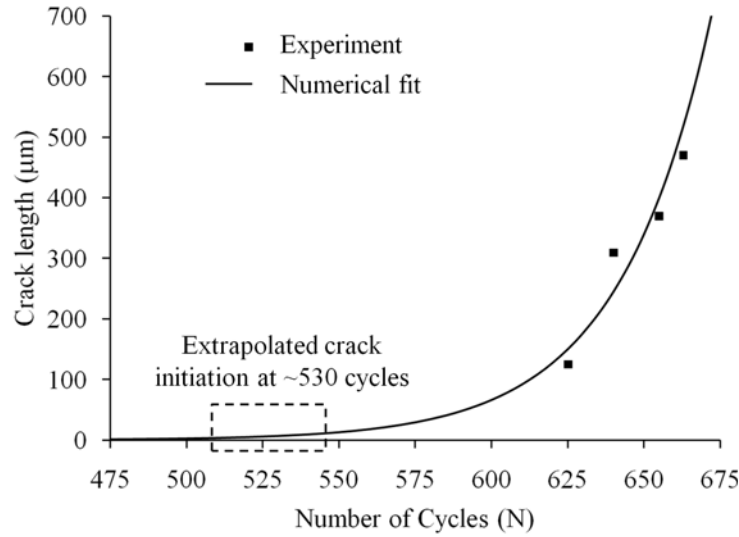


Figure 4.12: Sub-surface crack propagation in specimen #2 obtained from ultrasonic experiments and corresponding number of cycles to nucleation [4].

4.5.1 Statistically Equivalent Microstructures

CPFEM simulation specimens of statistically equivalent polycrystalline microstructures are generated from orientation imaging microscopy (OIM) scans of the Ti-6242 microstructure. Following developments in [49, 50, 39], distribution and correlation functions of various crystallographic and morphological parameters, e.g. orientation, misorientation, microtexture, grain size etc. from OIM scans of material specimens are used to generate statistically equivalent image based microstructures. The resulting microstructures for specimens 1 and 2 are shown in figure 4.13. Their c -axis orientation distribution and microtexture are shown in figure 4.14.

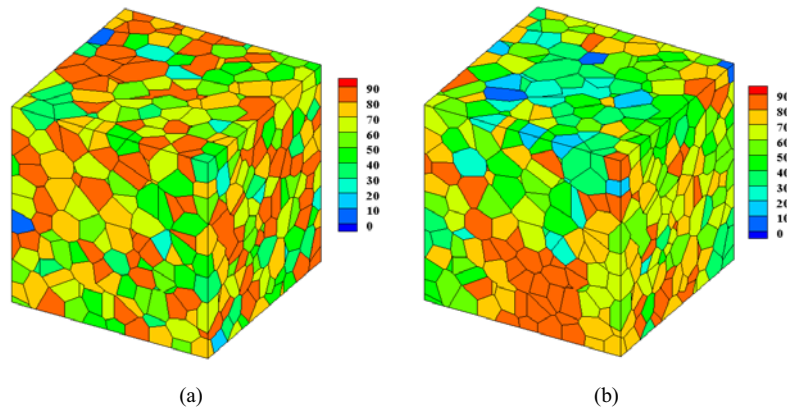


Figure 4.13: Statistically equivalent image-based simulated polycrystalline microstructures and corresponding $\langle c \rangle$ -axis orientations for: (a) specimen 1 and (b) specimen 2.

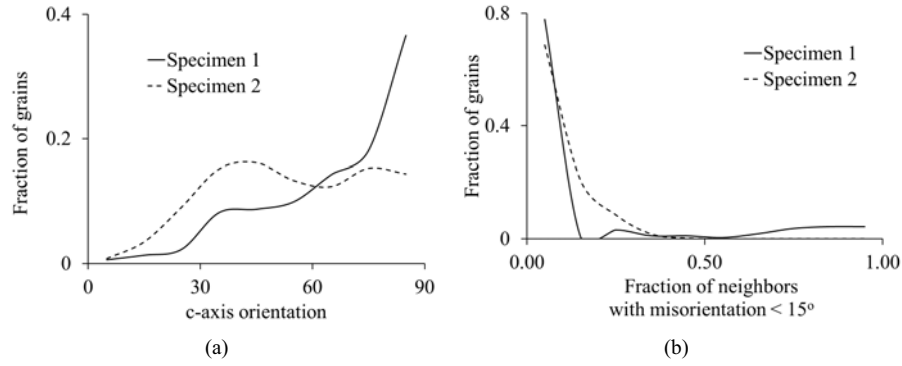


Figure 4.14: (a) $\langle c \rangle$ -axis orientation distribution and (b) microtexture distribution for statistically equivalent specimen microstructures 1 and 2.

4.5.2 Evaluating Yield Strengths and Dwell Fatigue Simulations

The overall yield strengths of the specimens 1 and 2 in the loading direction are evaluated from constant strain rate simulations prior to dwell fatigue simulations. These values are required for applied load control at 95% of the yield strength in dwell-fatigue tests. The evolution of volume averaged stress-true strain in the loading direction σ_{22} - ϵ_{22} are shown in figure 4.15. Corresponding to 0.2% elastic strain, an yield strength value of ~ 915 MPa is assessed for these specimens.

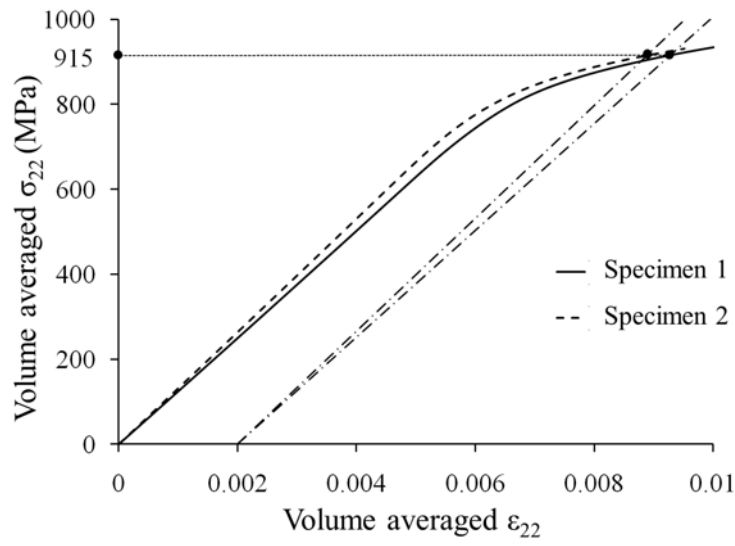


Figure 4.15: Volume averaged stress-strain plot of statistically equivalent microstructures obtained from constant strain rate CPFEM simulations. A yield stress of 915 MPa is obtained for 0.2% elastic strain.

The WATMUS method-enhanced CPFEM simulations are performed under dwell loading for validating the crack nucleation model. Consistent with experimental procedures, a maximum applied stress of 869 MPa, which corresponds to 95% of the yield stress, and a stress ratio $\sigma_R = \sigma_{min}/\sigma_{max} = 0$ is applied. Following the procedure described in [4], the crack nucleation parameter R_α at every node on grain interfaces is evaluated at $\tau = 121$ secs in each cycle for the 2-minute dwell.

Experimental results of specimen 1, which fails after 352 cycles, are used to calibrate R_c . From the conclusions of experimental studies in [93], the minimum and maximum number of cycles to crack nucleation for the specimen 1 is estimated as $N_{c(80\%)} = 282$ (80% of N_f) and $N_{c(85\%)} = 300$ (85% of N_f). The evolution of the nodal R_α at the grain boundaries is obtained from CPFEM simulations of specimen 1. The maximum R_α values at $N_{c(80\%)} = 282$ and $N_{c(80\%)} = 300$ are considered as the lower and upper limits of R_c respectively.

$$\begin{aligned} R_{c(80\%)} &= \max_{\alpha} R_{\alpha}(N = 282, \tau = 121 \text{ sec}) = 6.54 \text{ MPa } \sqrt{\mu\text{m}} \\ R_{c(85\%)} &= \max_{\alpha} R_{\alpha}(N = 300, \tau = 121 \text{ sec}) = 6.80 \text{ MPa } \sqrt{\mu\text{m}} \end{aligned} \quad (4.26)$$

The evolution of $R_{\alpha}(N, \tau = 121 \text{ sec})$ with cycles at the predicted crack nucleation site is shown in figure 4.16.

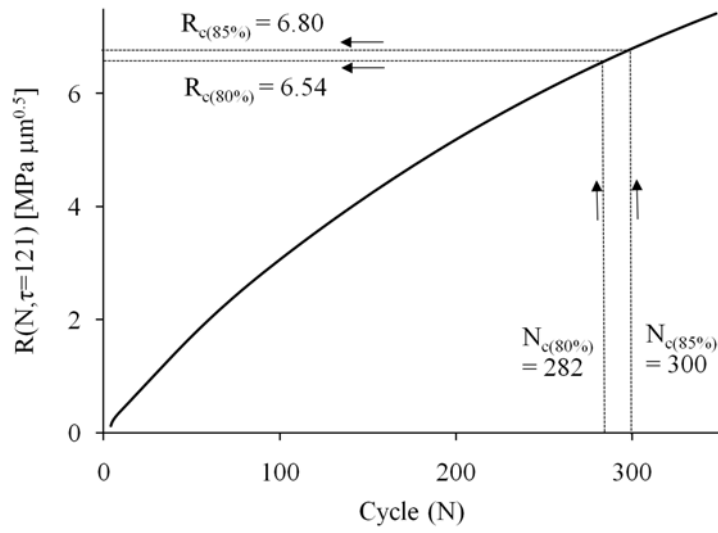


Figure 4.16: Evolution of nodal R_α with cycles N in specimen 1 at the crack nucleation site under dwell loading, evaluated at $\tau = 121$ sec.

Experimental results of specimen 2 are used to validate the crack nucleation model for the calibrated R_c value. The number of cycles to crack nucleation from interrupted dwell fatigue experiments is 550 cycles. From the CPFE simulations, the number of cycles to crack nucleation is predicted for 80% and 85% respectively of the total life as:

$$\begin{aligned} N_{c(80\%)} : \max_{\alpha} R_{\alpha}(N, \tau = 121 \text{ sec}) &= R_{c(80\%)} \Rightarrow N_{c(80\%)} = 620 \\ N_{c(85\%)} : \max_{\alpha} R_{\alpha}(N, \tau = 121 \text{ sec}) &= R_{c(85\%)} \Rightarrow N_{c(85\%)} = 694 \end{aligned} \quad (4.27)$$

The evolution of maximum R_α at a grain boundary node with crack nucleation is shown in figure 4.17.

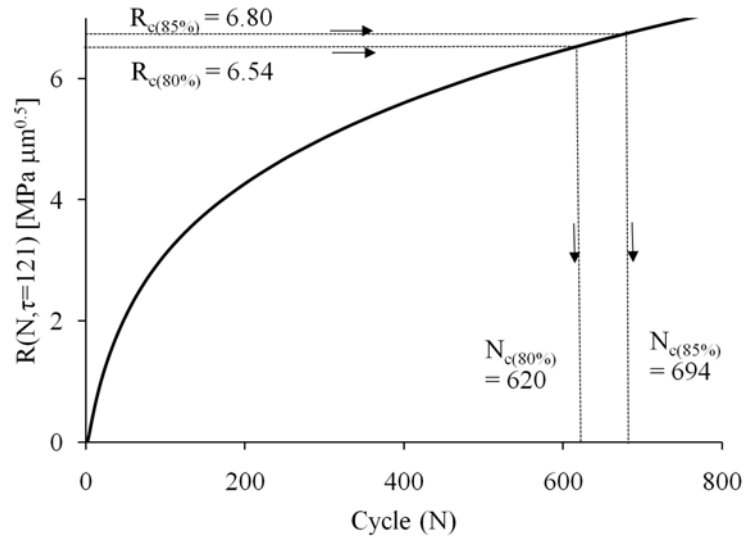


Figure 4.17: Evolution of maximum R_α with N in specimen 2 at a crack nucleation site under dwell cyclic loading, evaluated at $\tau = 121$ sec.

The predicted number of cycles to crack nucleation for specimen 2 along with the associated error are summarized in table 4.1. The crystallographic features of the predicted crack nucleation site for both the specimens are compared with experimentally observed characteristics in table 4.2.

Cycles to crack nucleation (Experiment)	Cycles to crack nucleation (Predicted)		% Relative error	
	80% of life	85% of life	80% of life	85% of life
550	620	694	12.7	25.4

Table 4.1: Comparison of the number of cycles to crack nucleation predicted by the model with experimental results for specimen 2.

Microstructural parameters	Experiments	Specimen 1	Specimen 2
θ_c	$0 - 30^\circ$	38.5°	25.2°
Prismatic Schmid factor	$0.0 - 0.1$	0.17	0.09
Basal Schmid factor	$0.3 - 0.45$	0.48	0.38

Table 4.2: Crystallographic features of the crack nucleation site predicted by the model and experiments for specimens 1 and 2.

Contour plots of σ_{22} , F_{22}^p and the $\langle c \rangle$ -axis orientation on a microstructural section of specimen 2, containing a crack nucleation site are shown in figure 4.18. The variables are evaluated for cycle $N = 620$ and intra-cycle time $\tau = 121$ sec. Crack nucleation is predicted near the triple point of grains 1, 2 and 3, shown in figure 4.18(a). From the distribution of $\langle c \rangle$ -axis orientation θ_c at the crack nucleation site (CNS) in figure 4.18(a), it is observed that the grain labeled 1 has $\theta_c < 30^\circ$ and is hence the hard grain. As seen in figure 4.18(b), this grain undergoes reduced plastic deformation in comparison with the surrounding soft grains, for which $\theta_c > 40^\circ$ in figure 4.18(a). The presence of large soft grains surrounding grain 1 cause large stresses develop in the hard grain as seen in figure 4.18(c). This causes nucleation of a crack at its interface with grains 2 and 3.

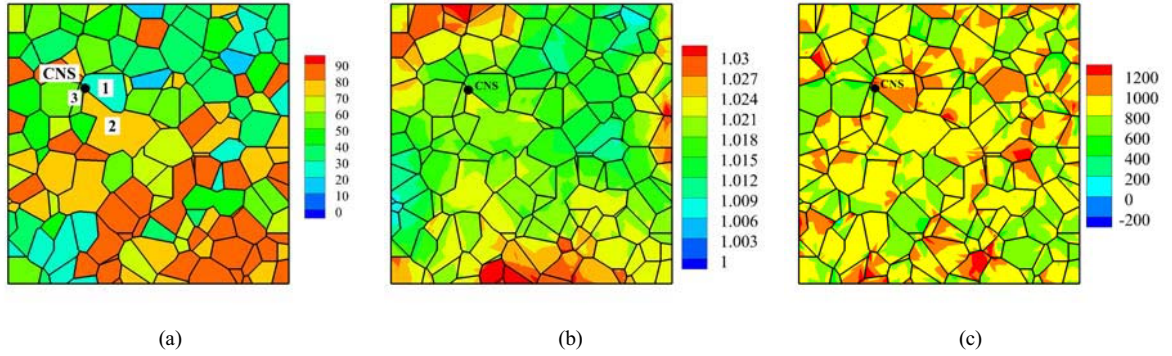


Figure 4.18: Contour plots of (a) $\langle c \rangle$ -axis orientation, (b) F_{22}^p and (c) σ_{22} on a section of specimen 2 containing the predicted crack nucleation site. The CPFEM variables are at $N=620$ and $\tau=121$ sec.

Two important inferences can be made from figure 4.18. The first is that the $\langle c \rangle$ -axis orientation has a strong influence on the local evolution of crystal plasticity variables, and can be used to distinguish between hard and soft grains. The second is that the local hard-soft grain arrangements can be used to examine the sensitivity of crack nucleation life on the microstructure.

4.6 Influence of Microstructural and Loading Characteristics on Crack Nucleation in Ti-6242

Quantitative correlation of microstructural and loading characteristics to the fatigue life using computational models can improve life prediction capabilities as well as provide tools for microstructure design [82, 2]. Experimental studies have been performed by various authors to identify different factors that influence the fatigue life of Ti-alloys. The effect of colony structure on room temperature low cycle fatigue behavior of β -processed and β -annealed Ti-alloys has been

investigated in [33]. Selected area electron channeling has been used in [26] to identify the crystallography of flat facets on the fracture surfaces of α/β Ti-alloys under fatigue loading. Near basal facet orientation has been observed at the crack nucleation site in [99, 101, 102]. Similar studies have been performed in [11, 9, 10, 32] to relate microstructure, texture and operating conditions to room temperature fatigue life of α/β Ti-alloys. The fatigue life varies significantly with applied load characteristics and underlying microstructure. This section is aimed at studying the sensitivities of room temperature crack nucleation in Ti-6242 to microstructural features and loading profile under cyclic loading using the WATMUS method-enhanced CPFE simulations.

4.6.1 Sensitivity of Yield Strength to Grain Orientation and Size Distributions

The yield strength of a polycrystalline alloy depends on the plastic flow behavior of the individual grains. Room temperature plastic deformation in Ti-6242 is primarily due to slip in individual grains. Consequently, factors affecting initiation of slip are used to study the sensitivity of yield strength to the underlying microstructure. Functional relations between microstructural characteristics such as grain orientation and size distribution and the yield strength have been established in [29, 118]. From equation (4.3), the initiation of slip is directly related to the resolved shear stress τ^α and inversely related to the slip system resistance g^α . The resolved shear stress, in turn depends on the orientation of the grain with respect to the direction along which yield strength is measured. The slip system resistance g_0^α depends on the type of slip system, i.e. $\langle a \rangle$ -basal, $\langle a \rangle$ -prismatic, $\langle a \rangle$ -pyramidal, $\langle c + a \rangle$ pyramidal and the grain size from equation (4.11).

Plastic deformation in a grain of a given size and orientation with the loading direction, is represented by a parameter termed as the *Plastic Flow Index* or *PFI*, defined as:

$$PFI = \max_{\alpha} \left(\frac{|\cos \theta_n^\alpha \cos \theta_m^\alpha|}{0.5} \right) \left(\frac{g_0^{\text{prismatic}}}{g^\alpha} \right) \quad (4.28)$$

where θ_n^α and θ_m^α are the angles made by the slip plane normals and the corresponding slip directions with the loading direction. $g_0^{\text{prismatic}}$ is the slip system resistance of the prismatic $\langle a \rangle$ slip system in equation (4.11) and its value is taken from [119]. The calibrated value of g_0 in [119] is the smallest for the prismatic $\langle a \rangle$ slip system. Hence, it is considered as a reference in equation (4.28) since it implies least resistance to slip. A crystal oriented with the maximum Schmid factor 0.5 along the prismatic $\langle a \rangle$ slip system has the minimum yield strength and maximum plastic flow, compared to any other grain orientation. Thus the *PFI* is considered to provide an effective measure of plastic flow in the grain. It also depends on the loading direction or Schmid factor of individual slip systems in the grain. For a grain, the value of *PFI* can vary between 0 and 1, i.e. $0 \leq PFI < 1$. A higher value of *PFI*, i.e. $PFI \rightarrow 1$ indicates higher plastic flow and lower strength for the grain. The yield strengths of specimens 1 and 2 in the y-direction are related to the underlying grain sizes and orientations by considering the *PFI* distribution of individual grains in the microstructure. The distributions are compared in figure 4.19.

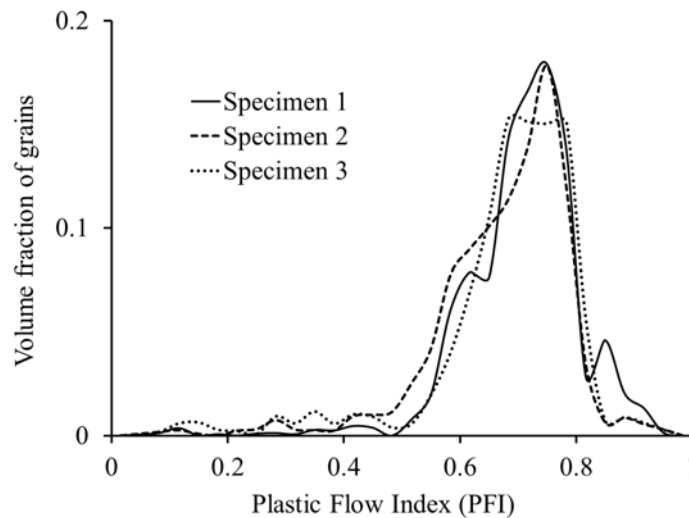


Figure 4.19: Plastic Flow Index (*PFI*) distribution for specimens 1, 2 and 3.

The distributions show that both specimens 1 and 2 have similar high volume fractions ($VF \approx 0.2$) in the range $0.7 \leq PFI < 0.8$. Constant strain-rate CPFE simulation results in figure 4.15 also show similar yield strengths in the y-direction for these specimens. The *PFI* distribution provides an effective metric in relating the yield strength to the underlying grain sizes and orientations. To validate this postulate, a third virtual microstructure (specimen 3) is constructed by randomly assigning orientations to grains in the FE model of figure 4.2(a). The orientations are chosen from the set of orientations in specimen 1. The grain sizes of specimen 3 are the same as for specimen 1. The *PFI* distribution for specimen 3 is compared with those for specimens 1 and 2 in figure 4.19. This has a lower volume fraction in the range $0.7 \leq PFI < 0.8$. Correspondingly, specimen 3 is expected to have a higher yield strength. This is corroborated by constant strain-rate CPFE simulation results, for which the yield strength is 940 MPa. Since $\cos \theta_n^\alpha \cos \theta_m^\alpha$ in equation (4.28) depends on the direction of loading, the *PFI* distributions for different loading directions capture the anisotropy in the macroscopic response as well.

4.6.2 Sensitivity of Crack Nucleation to Microstructural Features

Macroscopic descriptors such as the *Plastic Flow Index* distribution are unable to capture the local variations in grain orientations and sizes. Hence, they are not suitable for relating variations in microstructural features to the fatigue nucleation life. Crystallographic features at the crack nucleation site, obtained from fatigue experiments on Ti-6242 in [101, 102] are reported in table 4.2. This data can be used to capture the effect of local variations in microstructural features on the number of cycles to fatigue crack nucleation. Grains are distinguished as hard or soft, based on their $\langle c \rangle$ -axis orientation with respect to the loading axis. Orientations between 0° and 30° ensures that the maximum prismatic and basal $\langle a \rangle$ Schmid factors are in the range 0.0 – 0.1 and 0.3 – 0.45 respectively, as shown in figure 4.20.

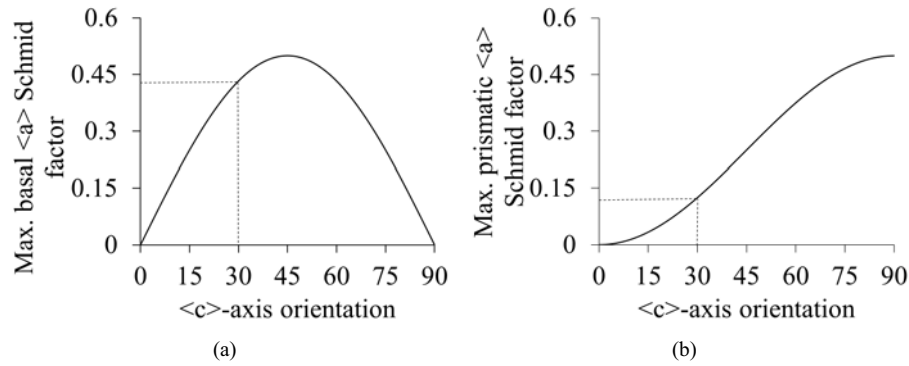


Figure 4.20: Variation of slip system Schmid factors with $\langle c \rangle$ -axis orientation: (a) maximum basal $\langle a \rangle$ Schmid factor (b) maximum prismatic $\langle a \rangle$ Schmid factor.

The $\langle c \rangle$ -axis orientation at the crack nucleation site for specimen 1 is predicted to be 38.5° by the crack nucleation model. Consequently, a $\langle c \rangle$ -axis orientation range of $0 - 40^\circ$ is used here to identify hard and soft grains. A grain is assumed to be hard when its $\langle c \rangle$ -axis orientation with respect to the loading direction is less than 40° . Since hard grains surrounded by soft grains are more susceptible to crack nucleation, the surface area fraction of soft grains surrounding each hard grain or *SAFSSG* is examined as a potential metric. The distribution of *SAFSSG* for specimens 1, 2 and 3 is shown in figure 4.21.

Microstructural parameters	Experiments	Specimen 3
θ_c	0 – 30°	5.6
Prismatic Schmid factor	0.0 – 0.1	0.005
Basal Schmid factor	0.3 – 0.45	0.01

Table 4.3: Microstructural features at the predicted crack nucleation site for specimen 3.

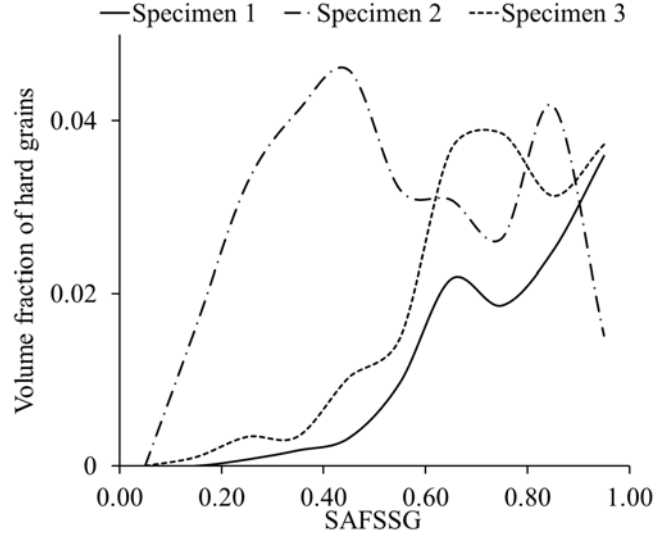


Figure 4.21: Volume fraction distribution of hard grains and corresponding surface area fractions of surrounding soft grains (*SAFSSG*) in specimens 1, 2 and 3.

The number of cycles to crack nucleation depends on the extreme values of the distribution in figure 4.21. This implies that a microstructure with a higher volume fraction of hard grains with high *SAFSSG* is likely to nucleate cracks earlier. Figure 4.21 illustrates that specimen 2 should have the longest nucleation life and specimen 3 should have the shortest life. This observation is supported by dwell fatigue simulations and experiments for specimens 1 and 2.

To consolidate this observation, dwell fatigue simulations are performed on specimen 3 with a maximum applied stress of 894 MPa, corresponding to 95% of its macroscopic yield stress of 940 MPa. The crack nucleation parameter R_α is evaluated at all nodes at grain interfaces in every cycle N for $\tau = 121$ sec. Crack nucleation is considered to happen when $R_\alpha(N, \tau = 121 \text{ sec})$ at any node exceeds a critical value R_c . The predicted number of cycles to crack nucleation, corresponding to nucleation at 80% or 85% of total life, are $N_{c(80\%)} = 167$ and $N_{c(85\%)} = 177$ respectively. The microstructural features observed at the predicted crack nucleation site for specimen 3 are shown in table 4.3. The evolution of R_α at the predicted crack nucleation site for the 3 different microstructures are compared in figure 4.22.

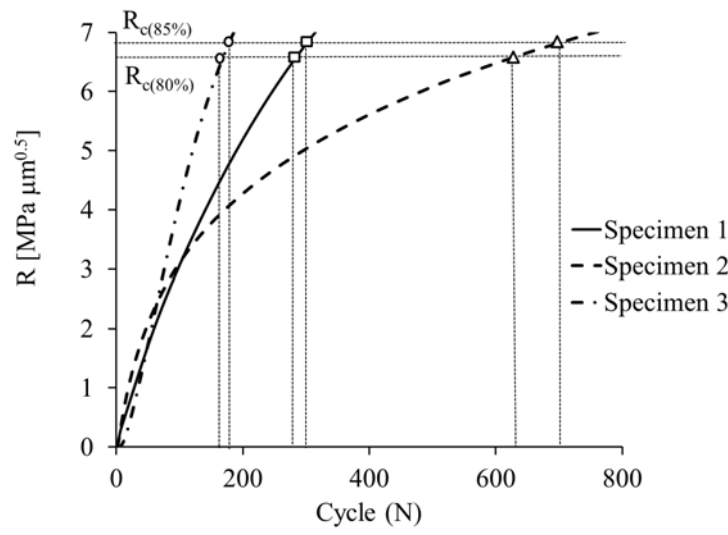


Figure 4.22: Evolution of R at the predicted crack nucleation site for specimens 1, 2 and 3.

A comparison of cycles to crack nucleation for different volume fraction (VF) of hard grains with increasing surface area fraction $SAFSSG$ between 0.9 to 1 is shown in figure 4.23.

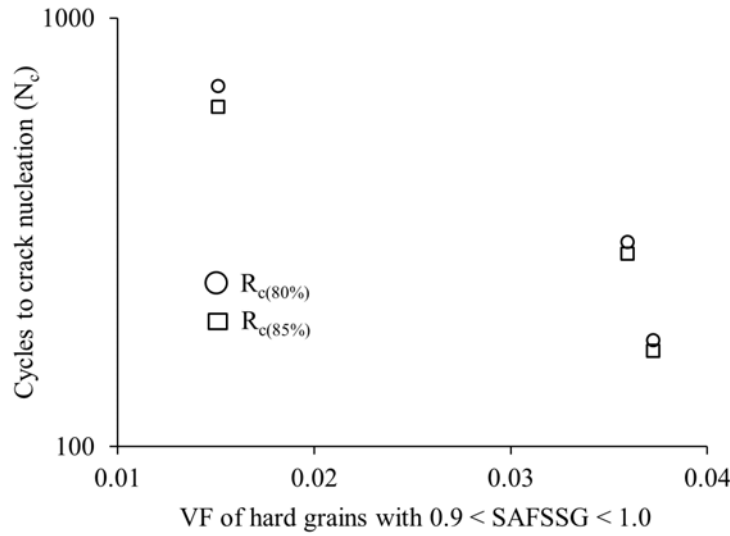


Figure 4.23: Comparison of number of cycles to crack nucleation for different volume fraction (VF) of hard grains with surface area fraction of surrounding soft grains (SAFSSG) between 0.9 to 1.

4.6.3 Sensitivity of Crack Nucleation to Characteristics of Applied Loading

Specimen 3 is subjected to 4 different loading cases for this sensitivity study, viz.:

- Case A: $\sigma_{max}=894$ MPa, $\sigma_r = 0$, $T_{load} = T_{unload} = 1sec$ and $T_{hold} = 120sec$
- Case B: $\sigma_{max}=847$ MPa, $\sigma_r = 0$, $T_{load} = T_{unload} = 1sec$ and $T_{hold} = 120sec$
- Case C: $\sigma_{max}=894$ MPa, $\sigma_r = 0$, $T_{load} = T_{unload} = 61sec$ and $T_{hold} = 0sec$
- Case D: $\sigma_{max}=894$ MPa, $\sigma_r = 0$, $T_{load} = T_{unload} = 1sec$ and $T_{hold} = 0sec$

The maximum applied stress σ_{max} is 95% of yield strength for cases A, C and D, while it is 90% for case B. Dwell load with 2 min hold is applied in cases A and B. Triangular loading with time periods $T = 122$ secs and $T = 2$ secs are

Case No.	Cycles to crack nucleation	
	80% of life	85% of life
A	167	177
B	2945	3172
C	9191	9734
D	51997	55195

Table 4.4: Comparison of number of cycles to crack nucleation in specimen 3 for different cyclic loadings.

respectively applied for cases C and D. The WATMUS method is used to perform cyclic CPFEM simulations and the crack nucleation parameter R_α is evaluated at nodes on the grain boundaries. Within a cycle, R_α is evaluated at the beginning of unloading. This corresponds to $\tau = 121$ sec for cases A and B, $\tau = 61$ sec for case C and $\tau = 1$ sec for case D. The evolution of R_α at the node, where crack nucleation is predicted, is shown in figure 4.24.

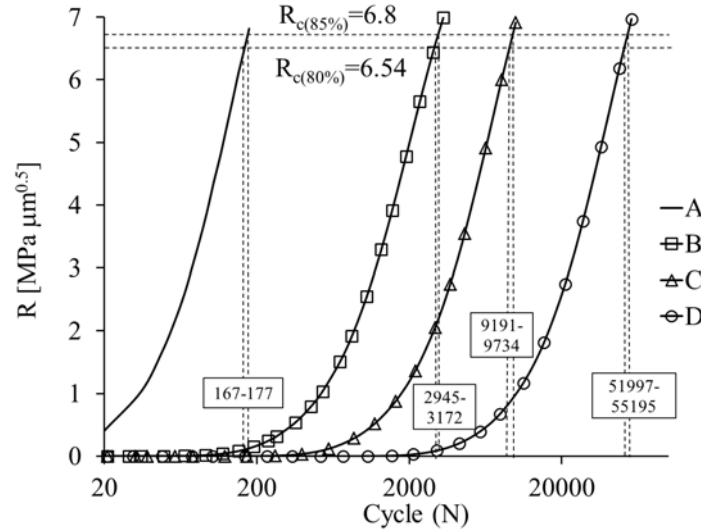


Figure 4.24: Evolution of R_α with cycles at the predicted crack nucleation site for specimen 3, under 4 different fatigue loading cases described in section 4.6.3.

The predicted number of cycles to crack nucleation based on the calibrated R_c values are summarized in table 4.4. The microstructure has a shorter life when subjected to dwell loading cases A and B in comparison with normal cyclic loading cases C and D. For the latter cases, a decrease in loading frequency reduces life. The number of cycles to crack nucleation for dwell case A and normal fatigue case D at 95% of yield strength shows the same trend as observed experimentally in [9, 10, 99].

In every dwell cycle, the microstructure is held at the maximum stress level for a longer period of time than in the normal cyclic loading. This results in a larger inelastic deformation and strain accumulation in the microstructure within each dwell cycle. Similar observations have been made from experiments on Ti-6242 in [99] and Timetal 685 in [9]. Stress concentration and micro-crack growth at the hard soft grain interface are more pronounced in every cycle for the dwell loading. This explains the reduction in life to crack nucleation under dwell load of case A when compared to normal cyclic load of case D. A reduction in the maximum applied stress in dwell loading for case B reduces the cyclic strain accumulation and the accompanying stress rise. Consequently, it shows a longer life than case A. When the frequency of normal cyclic loading is reduced in case C, ramping to the maximum applied stress in every cycle happens slowly. This results in increased plastic strain accumulation and stress rise, compared to the higher frequency case D. Thus, frequency reduction for the same maximum stress level decreases the nucleation life of the microstructure.

The number of cycles to crack nucleation for specimen 3 for different hold, loading and unloading times in dwell cyclic loading are also compared. The applied stress levels are kept at $\sigma_{max}=894$ MPa and $\sigma_{min}=0$ MPa, while the total period of loading is $T = 122$ sec. The WATMUS based CPFEM simulations are performed for three different cases, viz.:

Case No.	Cycles to crack nucleation	
	80% of life	85% of life
E	247	261
F	364	394
G	690	755

Table 4.5: Number of cycles to crack nucleation in specimen 3 for dwell cyclic load with different hold times.

- Case E: $T_{load} = T_{unload} = 16sec$ and $T_{hold} = 90sec$
- Case F: $T_{load} = T_{unload} = 31sec$ and $T_{hold} = 60sec$
- Case G: $T_{load} = T_{unload} = 46sec$ and $T_{hold} = 30sec$

The number of cycles to nucleate a crack is evaluated and the nodal R_α at the predicted crack nucleation site is evaluated at $\tau=106$ secs, 91 secs and 76 secs respectively within the cyclic increments. This is shown in figure 4.25.

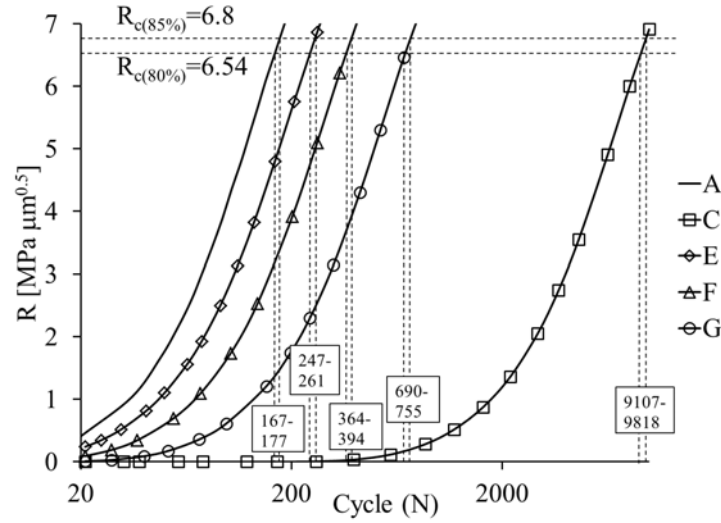


Figure 4.25: Evolution of R_α with cycles at the crack nucleation site of specimen 3 for the fatigue loading cases A, C, E, F and G.

The number of cycles to crack nucleation for cases E,F and G are summarized in table 4.5. With increasing hold time, the dislocation pile-up length at the hard-soft grain boundaries and stress-peak in the hard grains has a larger increase in every load cycle, resulting in shorter life to initiation. A comparison of the number of cycles to crack nucleation for different hold times is shown in figure 4.26.

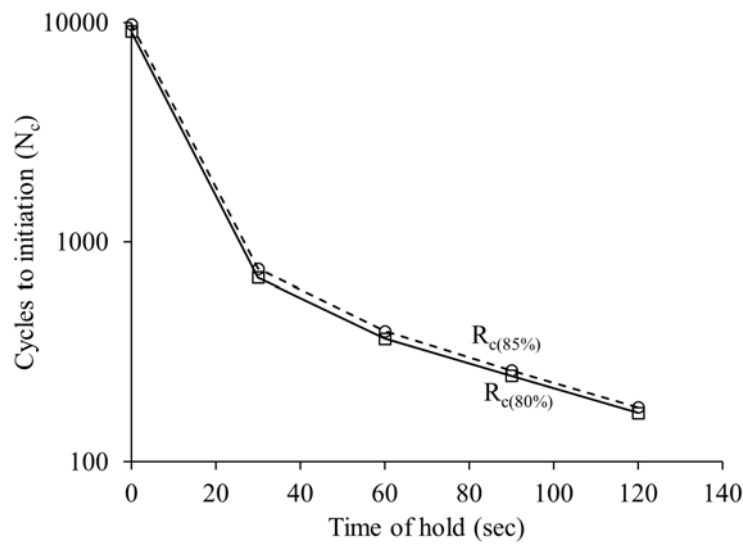


Figure 4.26: Number of cycles to crack nucleation in specimen 3 for different hold times.

4.7 Conclusion

This work investigates the effects of critical morphological and crystallographic characteristics of the microstructure and loading conditions on grain-level crack nucleation in polycrystalline Ti-6242 microstructures. Crystal plasticity FEM simulations of statistically equivalent microstructures, in conjunction with a physically motivated crack nucleation model, are used to provide a mechanistic approach towards predicting this behavior. A non-local crack nucleation model in terms of the local stresses near the hard grain boundary and the piled-up dislocations in the adjacent soft grain is implemented to predict nucleation in the hard grain. Crack nucleates when a parameter R at any node on hard soft grain interfaces exceeds a critical value R_c for the material. This critical parameter value is calibrated using a combination of dwell fatigue experiments and CPFEM simulations performed on Ti-6242 specimens. It is practically impossible to conduct CPFEM simulations till the incidence of crack nucleation for many microstructures and load cases, using conventional single time-scale simulation methods. A necessary ingredient of these simulations is the wavelet transformation induced multi-time scaling or WATMUS algorithm for accelerated cyclic CPFEM simulations.

Crack nucleation studies are performed for cyclic loads with the maximum applied stress levels at 90 – 95% of the macroscopic yield strength. To understand the effect of microstructural characteristics on the fatigue crack nucleation behavior, the dependence of yield strength on the underlying grain orientations and sizes is developed through the introduction of an effective microstructural parameter *Plastic Flow Index* or *PFI*. The *PFI* distribution is found to provide a good measure of the yield strength for a microstructure. However, this distribution is not suitable to undermine the effects of the microstructure on crack nucleation, since it is a *local* event. Hence a local microstructural variable is defined in terms of the neighborhood of the hard grains. Specifically the surface area fraction of soft grains surrounding each hard grain or *SAFSSG* is used to establish the microstructural sensitivity of cycles to crack nucleation. The WATMUS-based CPFEM simulations of 3 representative microstructures are performed under cyclic dwell loading and the cycles to crack nucleation are predicted. The results confirm the effectiveness of the *SAFSSG* in capturing the influence of microstructure on cycles to crack nucleation. Furthermore, simulations with different cyclic load patterns suggest that fatigue crack nucleation in Ti-6242 strongly depends on the dwell cycle hold time at maximum stress. This is in compliance with experimental observations.

Chapter 5

Homogenized Constitutive and Fatigue Nucleation Models from Crystal Plasticity Simulations of Ti Alloys, Part 1: Macroscopic Anisotropic Yield Function

5.1 Introduction

Titanium alloys find important utilization in various defense and commercial applications due to their high strength, low density, high fracture toughness and corrosion resistance. Plastic deformation in these predominantly hexagonal close-packed or *hcp* alloys has considerable dependence on the underlying microstructure, e.g. crystal orientation due to their low symmetries [52, 28, 117] and grain size [119]. Slip behavior due to dislocation glide in hexagonal materials is highly anisotropic because of the difference in deformation resistances for different slip systems. The critical resolved shear strength (CRSS) for $\langle c + a \rangle$ -slip on the pyramidal planes is $\sim 3 - 4$ times larger than the CRSS for $\langle a \rangle$ -type slip on the prism or basal planes [52]. Under creep conditions “soft” grains with favorably oriented $\langle a \rangle$ -type slip systems for dislocation glide ($\langle c \rangle$ -axis with nearly 45° orientation with respect to the deformation axis) undergo significant plastic straining. Contiguous “hard” grains with less-favorably oriented for $\langle a \rangle$ -type slip ($\langle c \rangle$ -axis parallel to the deformation direction), experience large local stress concentrations, especially near the shared grain boundary.

Prediction of deformation behavior and fatigue life in polycrystalline Ti alloys has received considerable attention within the materials research community in the recent times. Significant research has been conducted to develop continuum plasticity models for titanium alloys, e.g. in [75, 97, 62, 61]. Based on phenomenological approaches, these macroscopic constitutive models introduce internal scalar or tensor variables that are typically determined from experimental observations. While these models have been undoubtedly very useful in structural scale analyses using computational methods like the finite element method, a shortcoming sometimes encountered is that they do not explicitly account for microstructural characteristics and evolving deformation mechanisms. Lack of adequate information on microstructural morphology and underlying physical mechanisms often result in limited predictive capabilities for general material and load classes. To compensate for this, some models have incorporated a large number of parameters in their expressions without direct physical relevance. Similarly, conventional fatigue analysis methods by, e.g., the stress-life or strain-life approaches, or damage tolerant approaches [109] exhibit scatter in their predictions due to lack of underlying physics based mechanisms and information about the actual material microstructure. Material microstructure-based mechanistic models of deformation and fatigue failure is seen as a promising alternative to such empiricism. Crystal plasticity finite element (CPFE) models with explicit grain structures in polycrystalline aggregates have been developed for predicting localized stresses and plastic strains e.g. in [77, 43, 52, 28, 117? ? ?]. These explicit microstructure-based CPFE models have been extended to model fatigue failure in [4, 99, 8, 96, 18, 73]. It is however prohibitive to conduct computational modeling of the entire structure at the scale of the microstructure with explicit representation grains, especially for large domains.

Multi-scale computational homogenization theories have been proposed for estimating averaged material properties of heterogeneous materials [110, 67, 42, 34]. For crystal plasticity, this class of multi-scale finite element models for predicting anisotropy and texture evolution, assign a polycrystalline microstructure to each element integration point, whose texture evolves with time. In [122], a uniform deformation gradient is enforced in all constituent grains of the poly-

crystalline microstructure according to Taylor's assumption, to predict anisotropic stress-strain response in high purity α Ti alloys. A polycrystalline model with self-consistent homogenization scheme is implemented in an explicit FE code in [112] to simulate the mechanical response of textured zirconium, deforming under four-point bend conditions. These approaches however can be computationally intractable for large structural problems, since detailed micromechanical analyses should be conducted for every integration point of macroscopic elements in a finite element model.

To overcome the shortcomings of simultaneous macro-micro modeling, different techniques have been suggested to reduce prohibitive numerical efforts required for CPFE simulations. A special "texture-component crystal plasticity finite element" has been proposed in [89, 90] where the initial orientation distribution function (ODF) is approximated in the form of discrete localized spherical texture components at integration points of the FE mesh. Each preferred orientation is assigned a scatter and amplitude. While this scattering of discrete orientations prevents overestimation of the overall anisotropy, the local anisotropy is still overestimated [17]. A promising alternative to incorporating crystal plasticity models in multi-scale finite element codes is to develop texture-based anisotropic yield surface models at the macroscopic level, e.g. in [19, 20]. Yield functions are expressed in terms of some polynomials whose coefficients are functions of microstructural properties. Selection of an appropriate yield function, which can capture important deformation characteristics is essential to get a dependable distribution of local stress/strains and reliable life prediction. For multi-phase materials undergoing damage and failure, Ghosh et. al. have developed computationally efficient, anisotropic homogenization based continuum plasticity-damage (HCPD) in ductile-elastic-plastic materials [38] and homogenization based continuum damage mechanics (HCDM) in brittle-elastic composites [58]. These reduced order models are constructed from rigorous homogenization of micromechanical analyses results of representative volume elements (RVE), following the Hill-Mandel postulate. These homogenized, reduced order models modify conventional phenomenological models to account for the presence of heterogeneities and their interactions in the microstructure. These aspects give rise to strong anisotropy in the constitutive relations that evolve with increasing plasticity and damage.

This work is aimed at developing homogenization-based macroscopic constitutive and crack nucleation models from detailed micromechanical crystal plasticity FE analysis of polycrystalline microstructures. The first part develops a homogenized, anisotropic plasticity constitutive model, specifically an yield function, for Ti alloys in a vein similar to developments in [38, 58]. This model can be incorporated in general purpose FEM codes for macroscopic analysis, thus avoiding computationally expensive polycrystalline micromechanical analysis at each integration point in a finite element mesh. The yield function proposed by [19, 20] possesses desired properties for modeling the anisotropic behavior of textured titanium alloys. It can also capture the tension-compression asymmetry inherent to these materials. This framework is adopted for the homogenized plasticity constitutive model for Ti alloys. The model is further extended to accommodate rate-dependent behavior observed in these alloys.

In this work, the crystal plasticity finite element model (CPFEM) for micro-level simulations is presented in section 5.2. Section 5.3 provides a detailed discussion on sensitivity analysis, required for determining microstructural parameters that should be incorporated in the homogenized model. Homogenization of the crystal plasticity simulation results is performed in section 5.4 to develop the continuum anisotropic constitutive models. Different anisotropic yield functions are discussed in this section for describing the mechanical behavior of Ti alloys. An extension to incorporate the rate sensitivity is discussed in subsection 5.4.4.

5.2 Crystal Plasticity Finite Element (CPFE) Model for Micro-Scale Polycrystalline Simulations

Ti alloys are characterized by time-dependent "cold" creep deformation characteristics at temperatures lower than those, at which diffusion-mediated deformation such as dislocation climb is expected [57, 80, 52]. TEM studies [80] have shown that deformation actually proceeds via dislocation glide, and dislocations are inhomogeneously distributed into planar arrays. Significant creep strains can accumulate at applied stresses, even as low as 60% of the yield strength. This characteristic has been attributed to rate effects in [57]. The material studied in this work is single-phase α -Ti-6Al which has a *hcp* crystal structure. The *hcp* crystals consist of 5 different families of slip systems, namely the basal $\langle a \rangle$, prismatic $\langle a \rangle$, pyramidal $\langle a \rangle$, first order pyramidal $\langle c + a \rangle$ and second order pyramidal $\langle c + a \rangle$ with a total of 30 slip systems. Size and time dependent, finite strain CPFE models have been developed by Ghosh et. al. in [52, 28, 117? ?].

In the CPFE model, crystal deformation results from a combination of the elastic stretching and rotation of the crystal lattice and plastic slip on the different slip systems. The stress-strain relation is written in terms of the second Piola-Kirchhoff stress \mathbf{S} and its work conjugate Lagrange-Green strain tensor \mathbf{E}^e as

$$\mathbf{S} = \mathbf{C} : \mathbf{E}^e, \quad \text{where } \mathbf{E}^e = \frac{1}{2} (\mathbf{F}^{eT} \mathbf{F}^e - \mathbf{I}) \quad (5.1)$$

\mathbf{C} is a fourth order anisotropic elasticity tensor and \mathbf{F}^e is the elastic component of the deformation gradient, obtained by multiplicative decomposition as:

$$\mathbf{F} = \mathbf{F}^e \mathbf{F}^p, \quad \det(\mathbf{F}^e) > 0 \quad (5.2)$$

where \mathbf{F} is the deformation gradient tensor and \mathbf{F}^p is its incompressible plastic component, i.e. $\det \mathbf{F}^p = 1$. The plastic part of the crystal plasticity equations involves a combined effect of slip on multiple slip systems. The flow rule, governing evolution of plastic deformation, is expressed in terms of the plastic velocity gradient \mathbf{L}^p as:

$$\mathbf{L}^p = \dot{\mathbf{F}}^p \mathbf{F}^{p-1} = \sum_{\alpha}^{nslip} \dot{\gamma}^{\alpha} \mathbf{s}^{\alpha} \quad (5.3)$$

where the Schmid tensor associated with α -th slip system \mathbf{s}^{α} is expressed in terms of the slip direction \mathbf{m}_0^{α} and slip plane normal \mathbf{n}_0^{α} in the reference configuration as $\mathbf{s}^{\alpha} = \mathbf{m}_0^{\alpha} \otimes \mathbf{n}_0^{\alpha}$. The plastic slip rate $\dot{\gamma}^{\alpha}$ on the α -th slip system has a power law dependence on the resolved shear stress (τ^{α}) and the slip system deformation resistance (g^{α}), given as

$$\dot{\gamma}^{\alpha} = \dot{\gamma} \left| \frac{\tau^{\alpha} - \chi^{\alpha}}{g^{\alpha}} \right|^{1/m} \text{sign}(\tau^{\alpha} - \chi^{\alpha}) \quad (5.4)$$

Here m is the material rate sensitivity parameter, $\dot{\gamma}$ is the reference plastic shearing rate and χ^{α} is the back stress that accounts for kinematic hardening in cyclic deformation [52].

The evolution of slip system deformation resistance is assumed to be controlled by two types of dislocations, viz. statistically stored dislocations (SSDs) and geometrically necessary dislocations (GNDs). SSD's correspond to homogeneous plastic deformation, while GND's accommodate incompatibility of the plastic strain field due to lattice curvature, especially near grain boundaries. The corresponding deformation resistance rate is expressed as:

$$\dot{g}^{\alpha} = \sum_{\beta} h^{\alpha\beta} |\dot{\gamma}^{\beta}| + \frac{k_0 \hat{\alpha}^2 G^2 b}{2(g^{\alpha} - g_0^{\alpha})} \sum_{\beta} \lambda^{\beta} |\dot{\gamma}^{\beta}| \quad (5.5)$$

The first term in equation (5.5) corresponds to SSDs. The modulus $h^{\alpha\beta} = q^{\alpha\beta} h^{\beta}$ (no sum on β) is the strain hardening rate due to self and latent hardening on the α -th slip system by slip on the β -th slip system respectively. Here, h^{β} is the self hardening coefficient and $q^{\alpha\beta}$ is a matrix describing latent hardening. The second term in equation (5.5) accounts for the effect of GNDs on work hardening [1]. Here, k_0 is a dimensionless material constant, G is the elastic shear modulus, b is the Burgers vector, g_0^{α} is the initial deformation resistance and $\hat{\alpha}$ is a non-dimensional constant. $\hat{\alpha}$ is taken to be $\frac{1}{3}$ in this work following [7]. λ^{β} is a measure of slip plane lattice incompatibility, which can be expressed for each slip system as a function of slip plane normal \mathbf{n}^{β} and an incompatibility tensor Λ as:

$$\lambda^{\beta} = (\Lambda \mathbf{n}^{\beta} : \Lambda \mathbf{n}^{\beta})^{\frac{1}{2}} \quad (5.6)$$

The dislocation density tensor Λ , introduced in [81] is a direct measure of the GND density. It can be expressed using the curl of plastic deformation gradient tensor \mathbf{F}^p . Since this crystal plasticity formulation does not explicitly incorporate a dislocation density tensor, it is indirectly extracted from the CPFE output data as:

$$\Lambda = \nabla^T \times \mathbf{F}^p \quad (5.7)$$

Grain size has a significant effect on the initial deformation resistance g_0^{α} . A Hall-Petch type relation with various slip direction-dependent characteristic length scales has been incorporated in the CPFE model in [? ?]. Material properties for each individual slip system in the crystal plasticity model, as well as size effect parameters have been calibrated in [52, 28, 117?]. Other parameters used in equation (5.5) include (i) shear modulus $G = 48 \text{ GPa}$, (ii) magnitude of Burgers vector $b = 0.30 \text{ nm}$, and (iii) $k_0 = 2$. Details of the morphological and crystallographic features of the microstructures are also accounted for in the CPFE model through accurate grain size and orientation distributions. Extensive developments on polycrystalline microstructures that are statistically equivalent to those observed in OIM scans have been made in [40, 47, 48].

5.3 Sensitivity Analysis with Respect to Microstructural Parameters

Prior to developing a microstructure-dependent, macroscopic constitutive model for the Ti alloy α -Ti-6Al, sensitivity analysis is conducted to assess the dependence of material response on important features pertaining to the underlying microstructure. The macroscopic response is established by homogenizing the CPFE simulation results for the polycrystalline microstructural representative volume elements (RVEs). It is also essential to establish critical parameters that adequately characterize the polycrystalline microstructure, which can be incorporated in the model.

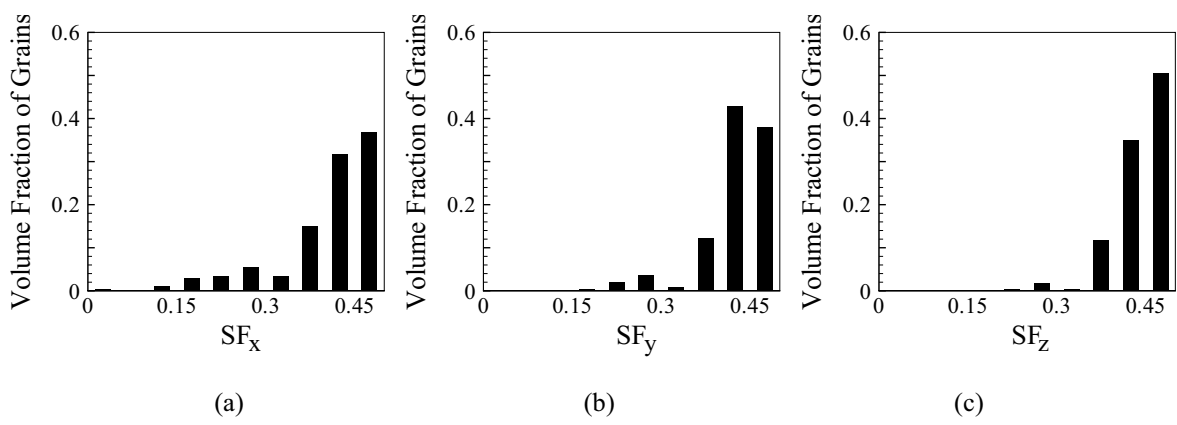


Figure 5.1: Distribution functions of the three components of Schmid factor for a microstructure labeled MS1: (a) SF_x , (b) SF_y , (c) SF_z .

5.3.1 Parameters Representing Microstructural Characteristics

Four different parameters, which represent crystallographic and morphological characteristics of the microstructure are considered for the sensitivity analysis. These are delineated in the following sub-sections.

Orientation Distribution Function (ODF)

Plastic deformation in *hcp* crystalline Ti alloys has considerable dependence on the crystal orientation due to their low symmetries. The deformation resistance g^α for the $\langle c + a \rangle$ slip on pyramidal planes is $\sim 3 - 4$ times larger than that for $\langle a \rangle$ -type slip on prism or basal planes [52]. This implies that plastic deformation in polycrystalline Ti alloys is primarily the result of slip activity on the basal and prismatic slip system in grains with the highest value of the critical resolved shear stress τ^α . The Schmid factor (SF), for a slip system α depends on the loading axis and is defined as:

$$SF = \cos\phi\cos\lambda \quad (5.8)$$

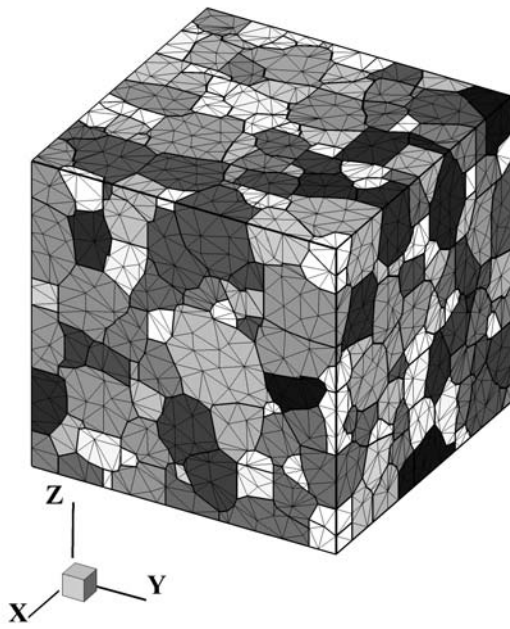
where ϕ is the angle between the loading axis and the slip plane normal \mathbf{n}^α , and λ is the angle between loading axis and the slip direction \mathbf{m}^α in the reference configuration. The SF transforms the applied stress to the resolved shear stress on a given slip system. Therefore, corresponding to equation (5.4), the SF of each slip system in a grain has a direct effect on the plastic behavior of that grain, and consequently on the overall plastic response of the microstructure. In this study the SF for each grain will henceforth correspond to the highest Schmid factor among basal and prism slip systems in the grain. A grain with considerable plastic deformation is termed as a "soft" grain. Softer grains in a microstructure have higher values of SF in comparison with other grains. To represent the orientation of slip systems in each grain with respect to the three orthogonal reference axes x , y , z , three Schmid factor components labeled as SF_x , SF_y and SF_z are defined for x , y and z directed loadings, respectively. The distribution of SF_x , SF_y and SF_z is considered as a good representation of the orientation of a polycrystalline microstructure. The average values of each of these distributions for each component, are considered as scalar measures of the orientation that can be incorporated in the constitutive relation. Figure 5.1 shows the distribution of SF_x , SF_y and SF_z for a sample microstructure containing 600 grains labeled as MS1. The average values of these component parameters are $\overline{SF}_x = 0.405$, $\overline{SF}_y = 0.425$ and $\overline{SF}_z = 0.441$.

Misorientation Distribution Function (MoDF)

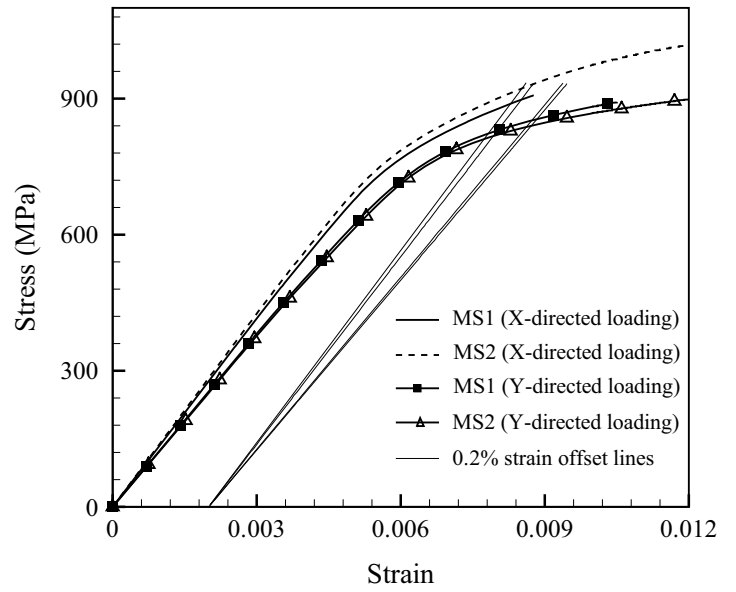
The misorientation between two neighboring grains 1 and 2 is measured in terms of a rotation axis vector \mathbf{n} and a misorientation angle θ_{mis} [28]. The axis \mathbf{n} represents a common slip direction for both crystallographic lattice systems. The misorientation angle θ_{mis} between two neighboring grains is the rotation about \mathbf{n} , required to bring the two crystal lattices into coincidence, and is expressed as:

$$\theta_{mis} = \min \left| \cos^{-1} \left[\frac{\text{tr}(\mathbf{g}_1 \mathbf{g}_2^{-1} \mathbf{O} - \mathbf{I})}{2} \right] \right| \quad (5.9)$$

where \mathbf{g}_1 and \mathbf{g}_2 represent orientation matrices of grain 1 and 2, respectively and \mathbf{O} is a crystal symmetry operator defined in [28]. Three scalar parameters are used to represent the misorientation distribution (MoDF) in macroscopic constitutive



(a)



(b)

Figure 5.2: (a) A virtual microstructure of MS2 with 500 grains, discretized into 102697 tetrahedron elements; (b) Stress-strain curves for microstructures MS1 and MS2 corresponding to x and y-directed strain loadings.

relations, viz. (i) mean (μ_{MoDF}), (ii) standard deviation (σ_{MoDF}), and (iii) percentage of grain pairs with misorientation less than 20° (R_{MoDF}).

Texture Distribution Function (TDF)

A parameter, termed as "texture index" or TI is defined for each grain as the volume fraction of its neighboring grains with similar orientation. A neighbor is considered to have similar orientation as the central grain, if the misorientation angle between the two grains is less than 15° . The parameter TI values range from 0 to 1. For all grains in the microstructure having the same orientation, the TI is 1 for all grains. On the other hand, $TI \rightarrow 0$ for all grains, in a purely random microstructure. It should be noted that the orientation of a textured region also affects the material macroscopic response. For example, a microstructure containing a large number of "hard" grains has a higher yield strength in comparison with that containing "soft" textured grains. To account for this, a modified texture index \hat{TI} is defined as $TI \times SF$, where SF is the Schmid factor of that grain. \hat{TI} ranges from 0 to 0.5. The distribution function of \hat{TI} is considered as a representative of texturing and is denoted as TDF . Three scalar parameters are used to represent the texture distribution (TDF) in macroscopic constitutive relations, viz. (i) mean (μ_{TDF}), (ii) standard deviation (σ_{TDF}), and (iii) percentage of grains with $\hat{TI} \geq 0.25$ (R_{TDF}).

Grain Size Distribution Function (GSDF)

The mechanical behavior of polycrystalline Ti alloys, in particular strength, has a strong dependence on grain size [?]. The strengthening effect is primarily due to dislocation pile-up at the grain boundary. The slip system deformation resistance is strongly affected by the mean free path traversed by dislocations. In [?], size effect is incorporated in the rate-dependent crystal plasticity constitutive model through insertion of characteristic length scales in the expression for deformation resistance of individual slip systems. For primary α grains, the characteristic length scale corresponds to the grain size, that is represented by the diameter of an equivalent sphere with the same volume as the grain. The grain size distribution in Ti alloys is found to follow a log-normal distribution, and hence the GSDF is assumed to be a log-normal function. This distribution function is defined by specifying the mean (μ_{GSDF}) and the standard deviation (σ_{GSDF}), which represent grain size distribution in the macroscopic constitutive relations.

Adequacy of the microstructural characteristic functions with respect to key mechanical properties

The four microstructural parameters and their distributions described in the previous sections should in general be sufficient to unambiguously represent the material response, at least with respect to key mechanical properties. Only then, can these be incorporated in the constitutive relations with confidence. To test this condition, two different specimen virtual microstructures, labeled as MS1 and MS2, are generated using identical statistical distributions of the four parameters. MS1 consists of 600 grains, discretized into a FE mesh containing 124820 tetrahedron elements, while MS2 has 500 grains with 102697 tetrahedron elements, as shown in figure 5.2(a). Crystal plasticity FE simulations of the two microstructures are conducted by applying a tensile constant strain-rate of $10^{-4} s^{-1}$ in the x , y and z directions. The volume-averaged stress-strain response in these directions are respectively plotted in figure 5.2(b). The yield strength in each direction is obtained by applying the 0.2% offset rule on the resulting stress-strain curve as shown in figure 5.2(b). Table 5.1 summarizes the average Schmid factors and the evaluated yield strengths in the three directions for the two microstructures. The yield strength along the z direction is smaller in comparison with the other two directions, which is consistent with the observation that lower average value of Schmid factors correspond to higher yield strength. For the same loading conditions, the maximum difference in yield strength between the two microstructures with same statistics is found to be 2.7%. This small difference in response establishes the conjecture that the four parameters adequately represent the key material response.

Table 5.1: Average Schmid factors and yield strengths of microstructural specimens MS1 and MS2 in the x , y and z directions.

Average Schmid Factors	\overline{SF}_x	\overline{SF}_y	\overline{SF}_z
	0.405	0.425	0.441
Microstructure	Yield Stress (MPa)		
	x -direction loading	y -direction loading	z -direction loading
MS1	897	852	826
MS2	922	840	812

5.3.2 Sensitivity of Macroscopic Response to Microstructural Parameters

Sensitivity of the macroscopic stress-strain response to the microstructural parameters discussed in section 5.3.1 is now analyzed. The macroscopic response is assumed to be characterized by three quantities, viz. (i) elastic stiffness E corresponding to the slope of the elastic portion; (ii) yield strength YS corresponding to 0.2% offset rule; and (iii) hardness H corresponding to the slope of stress-strain curve in the plasticity region. The difference in macroscopic responses of the two microstructures MS1 and MS2 is assumed to be negligible if the difference in E and YS are less than 4%, and the difference in H is less than 20% for the two microstructures. A higher tolerance is allowed for H to accommodate for its relatively small value in comparison with E . To substantiate this, figure 5.3 depicts the different stress-strain curves for the same values of yield strength ($YS = 936 MPa$) and elastic stiffness ($E = 117 GPa$), but different values of H . The 20% difference in H does not make a significant difference in the stress-strain curve.

Sensitivity of macroscopic response to TDF and MoDF

Two sets of virtual microstructures, containing $7 \times 7 \times 7$ cubic grains of equal size $7.5 \mu m$ each, are generated for this sensitivity analysis. The first set contains microstructures labeled MS3 and MS4, which have the same average Schmid factors ($\overline{SF}_x = 0.417$, $\overline{SF}_y = 0.434$ and $\overline{SF}_z = 0.452$). The virtual specimens are subjected to a tensile constant strain-rate of $10^{-4} s^{-1}$ in the y direction. The distributions of MoDF and TDF for MS3 and MS4 are presented in figures 5.4. The ordinates correspond to the grain contact area and volume fractions respectively, while the abscissae correspond to the misorientation angle and the texture index respectively. The distributions for the two microstructures are quite different. The values of the statistical metrics μ_{MoDF} , σ_{MoDF} , R_{MoDF} , and μ_{TDF} , σ_{TDF} and R_{TDF} are summarized in table 5.2. The corresponding values of YS , H and E are also compared in this table. The percentage difference between the values of YS , H and E is 3.5, 5.8 and 0.5 respectively, which are all less than the tolerances assigned.

The second set of virtual microstructures considers three specimens labeled MS5, MS6 and MS7, all of which have the same average Schmid factors $\overline{SF}_x = 0.434$, $\overline{SF}_y = 0.418$ and $\overline{SF}_z = 0.428$. The corresponding TDF and MoDF plots are shown in figure 5.5. The values of the statistical metrics μ_{MoDF} , σ_{MoDF} , R_{MoDF} , μ_{TDF} , σ_{TDF} and R_{TDF} , along with the

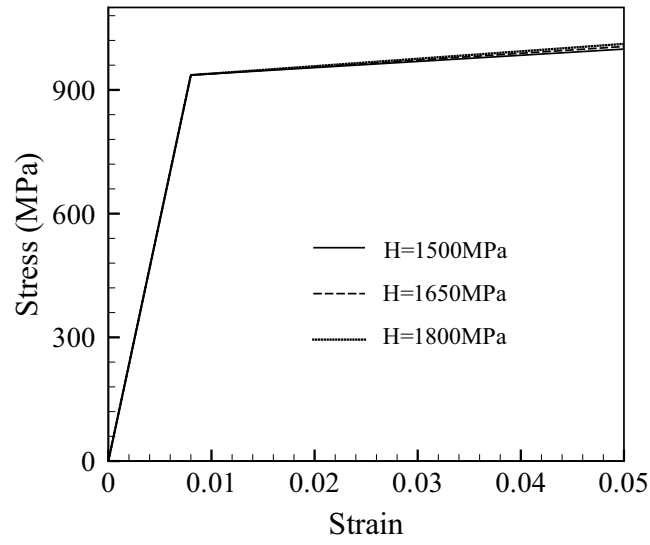


Figure 5.3: Sensitivity of the stress-strain curve to the hardness H for constant $E = 117 \text{ GPa}$, $YS = 936 \text{ MPa}$.

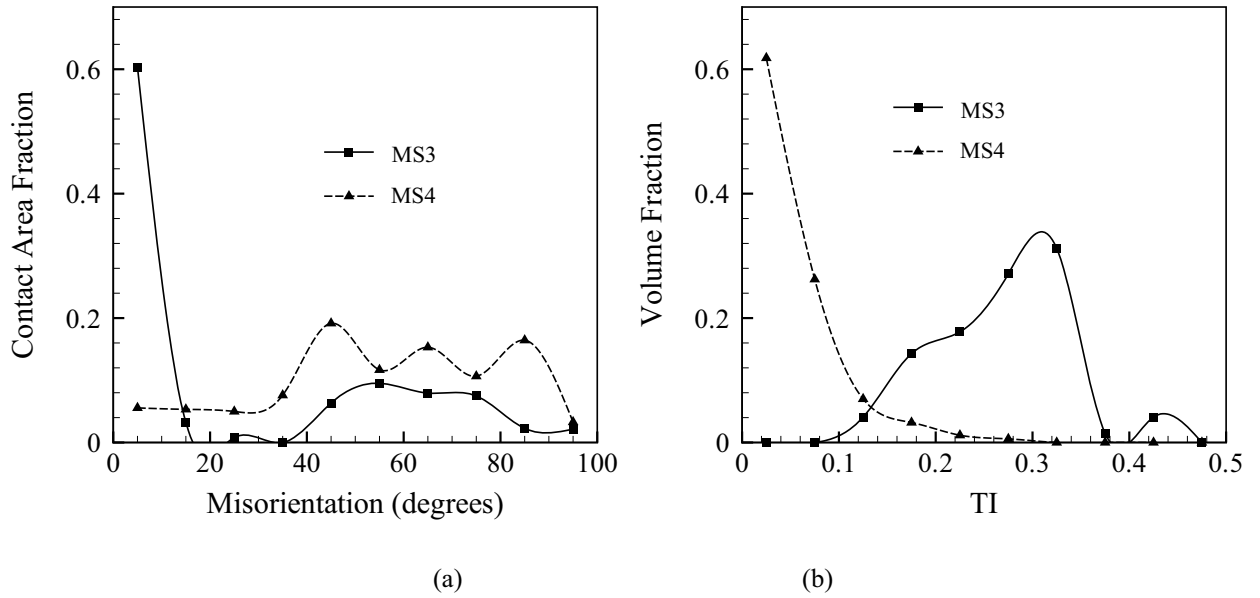


Figure 5.4: Distribution of (a) MoDF represented by the misorientation angle, and (b) TDF represented by the texture index TI for virtual specimens MS3 and MS4.

Table 5.2: Parameters reflecting the mechanical response (stress-strain response) and distribution of MoDF and TDF in the microstructures of the virtual specimens MS3 and MS4.

	E (MPa)	YS (MPa)	H (GPa)	MoDF			TDF		
				μ_{MoDF}	σ_{MoDF}	R_{MoDF}	μ_{TDF}	σ_{TDF}	R_{TDF}
MS3	117	824	979	25.05	30.52	0.63	0.27	0.06	0.64
MS4	118	854	1038	54.92	24.17	0.11	0.04	0.06	0.01
Diff (%)	0.5	3.5	5.8						

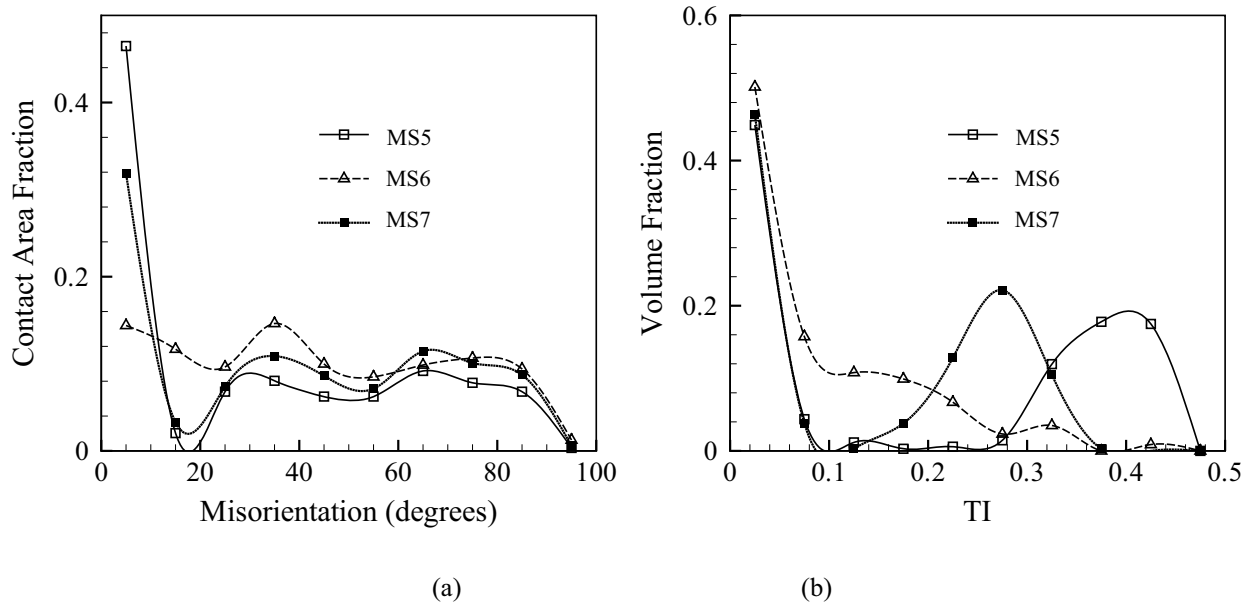


Figure 5.5: Distribution of (a) MoDF represented by the misorientation angle, and (b) TDF represented by the texture index TI for virtual specimens MS5, MS6 and MS7.

values of E , YS and H are summarized in table 5.3. Again, the difference between the values of YS , H and E are less than the tolerances. Therefore TDF and MoDF are inferred to have little effect on the macroscopic response. Moreover these parameters are considered to cause stress and strain redistribution between grains in the microstructure and are important in local phenomena like crack nucleation. The misorientation and texture parameters are consequently not included in the macroscopic constitutive model.

Table 5.3: Parameters reflecting the mechanical response (stress-strain response) and distribution of MoDF and TDF in the microstructures of the virtual specimens MS5, MS6 and MS7.

	E (MPa)	YS (MPa)	H (GPa)	MoDF			TDF		
				μ_{MoDF}	σ_{MoDF}	R_{MoDF}	μ_{TDF}	σ_{TDF}	R_{TDF}
MS5	115	855	1065	30.45	29.99	0.49	0.19	0.18	0.49
MS6	115	861	1121	42.74	26.77	0.26	0.08	0.10	0.07
MS7	115	858	996	37.20	30.51	0.35	0.14	0.14	0.33
Max. Diff (%)	0.2	0.6	11.8						

Sensitivity to the grain size distribution GSDF

A log-normal distribution of the GSDF is characterized by its mean μ_{GSDF} and standard deviation σ_{GSDF} . For sensitivity analysis of the macroscopic response to σ_{GSDF} , two virtual microstructures labeled MS8 and MS9 are generated with the same average Schmid factor in all directions. The microstructures have the same average grain size i.e. $\mu_{GSDF} = 1$, but different standard deviations, viz. 0.486 for MS8 and 0.2 for MS9. Figure 5.6(a) shows the GSDF for MS8 and MS9. Crystal plasticity FE simulations are conducted on the microstructures by applying a tensile constant strain rate of $10^{-4} s^{-1}$ in the y direction. The simulated macroscopic stress-strain curves are shown in figure 5.6(b). The corresponding yield strengths are $YS = 838.5 MPa$ for MS8 and $YS = 892.9 MPa$ for MS9. The difference in the two yield strengths is 6.1%, which is larger than the assumed tolerance of 4%. This difference can be explained as follows. Though both microstructures have the same average grain size, MS9 with higher σ_{GSDF} has a few number of very large grains. While the number fraction of these grains is small, the volume fraction of these grains is appreciable. Because the macroscopic response is obtained using volume averaging, the effect of these grains is important. The volume average of grain sizes for specimens MS8 and MS9 are $5.16 \mu m$ and $2.55 \mu m$ respectively. Consequently the parameter to be incorporated in constitutive relations is changed to the average of grain size distribution GSDF based on the volume fraction of grains. This is denoted by D .

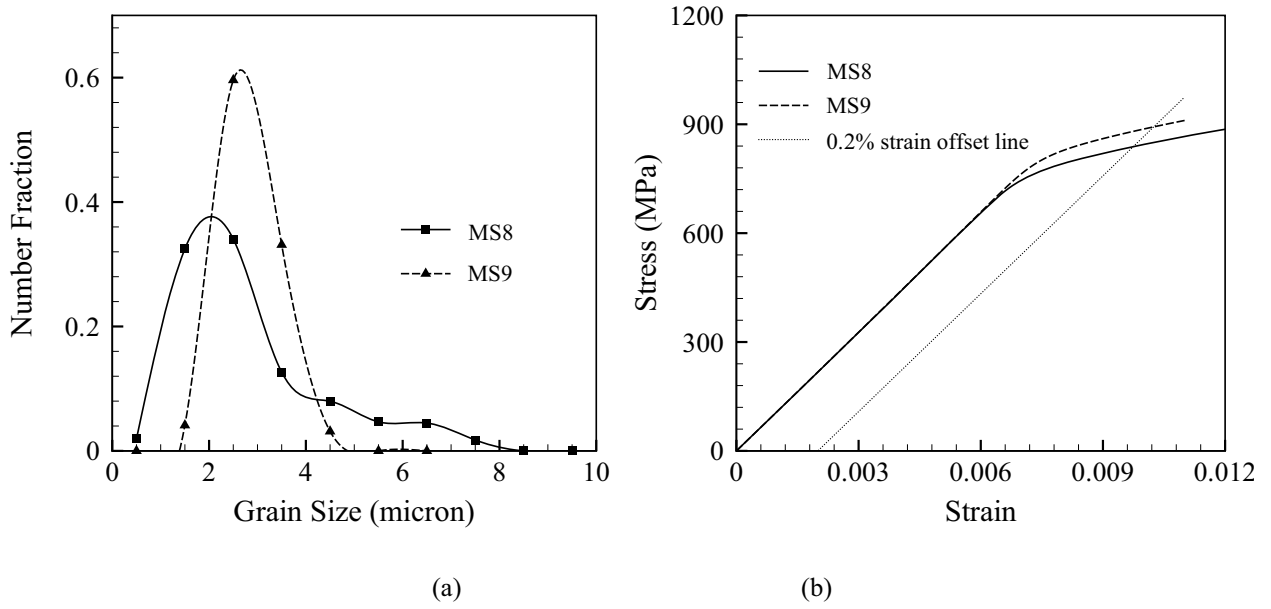


Figure 5.6: (a) Distribution of grain size GSD and (b) macroscopic stress-strain response for MS8 and MS9.

Sensitivity of macroscopic response to ODF

Finally, the sensitivity of macroscopic response to the average Schmid factor is studied through CPFE simulations of a microstructure labeled MS10 that is soft in the y direction ($\overline{SF}_y = 0.47$) and hard in the z direction ($\overline{SF}_z = 0.15$). Two CPFE simulations are conducted with: (i) a tensile constant strain rate of $10^{-4} s^{-1}$ applied in the y -direction, and (ii) a tensile constant strain rate of $10^{-4} s^{-1}$ applied in the z -direction. Figure 5.7 shows the macroscopic stress-strain curves for the y and z -direction loadings. The values of E , YS and H for these two directions are given in table 5.4. The values in the y - and z - directions differ considerably, requiring the insertion of the average Schmid factors in the constitutive models.

Table 5.4: Stress-strain curve parameters for microstructure MS10 in the y - and z - directions.

	Schmid Factor	$E(GPa)$	$YS(MPa)$	$H(MPa)$
y -direction loading	0.47	106	718	918
z -direction loading	0.15	148	1332	702
Diff(%)		33.1	59.9	26.7

5.4 Development of Homogenization-based Anisotropic Plasticity Constitutive (HAPC) Model for Ti Alloys

The homogenization based continuum anisotropic plasticity or HAPC model is developed from micromechanical analysis of polycrystalline microstructures discussed previously. Specifically an appropriate yield function for the HAPC model is determined to capture the characteristics observed in mechanical behavior of Ti alloys.

5.4.1 Choice of a Suitable Framework for Yield Function

A few key features are necessary for selecting the suitable continuum yield criterion. These are: (i) pressure insensitivity, (ii) anisotropy, (iii) tension-compression asymmetry and (iv) kinematic hardening. A few candidate anisotropic yield criteria are considered for this purpose. The quadratic anisotropic yield criterion for plastic deformation, described in [55], has a functional form in terms of the principal stress components as:

$$F(\sigma_1 - \sigma_2)^2 + G(\sigma_1 - \sigma_3)^2 + H(\sigma_2 - \sigma_3)^2 - Y_f^2 = 0 \quad (5.10)$$

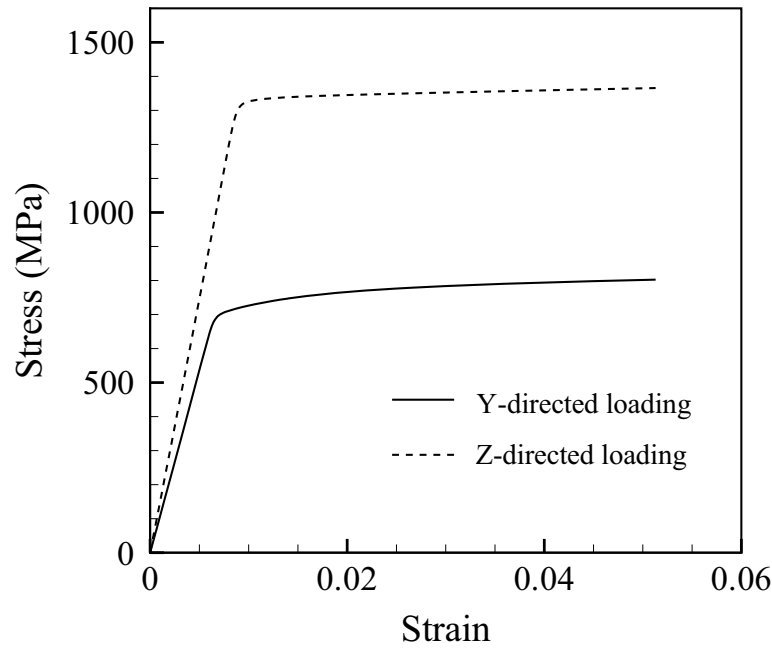


Figure 5.7: Macroscopic stress-strain curves in the y - and z - directions.

where F , G and H are anisotropic parameters and Y_f is the flow stress. This model has been utilized mostly to model cubic metals that do not exhibit tension-compression asymmetry. Thus it is not suitable criterion for modeling Ti alloys with *hcp* crystalline structure. This yield function has been modified in [56] to account for tension-compression asymmetry by adding linear stress terms as:

$$F(\sigma_1 - \sigma_2)^2 + G(\sigma_1 - \sigma_3)^2 + H(\sigma_2 - \sigma_3)^2 + L\sigma_1 + M\sigma_2 - (L + M)\sigma_3 - Y_f^2 = 0 \quad (5.11)$$

This function corresponds to a low eccentricity elliptical yield locus that can model the kinematic hardening as well. However, this criterion is not suitable for modeling the highly anisotropic behavior of Ti alloys, which requires including higher order stress terms. A robust model for yielding and plastic deformation of anisotropic *hcp* materials has been proposed in [19, 20, 21]. The yield criterion is of the form:

$$(J_2^0)^{\frac{3}{2}} - J_3^0 - Y_f^3 = 0 \quad (5.12)$$

where Y_f is the yield stress in shear. J_2^0 is a generalization of the 2^{nd} invariant of the deviatoric stress tensor J_2 for orthotropy that is expressed as:

$$J_2^0 = \frac{a_1}{6}(\sigma_{xx} - \sigma_{yy})^2 + \frac{a_2}{6}(\sigma_{xx} - \sigma_{zz})^2 + \frac{a_3}{6}(\sigma_{yy} - \sigma_{zz})^2 + a_4\sigma_{xy}^2 + a_5\sigma_{xz}^2 + a_6\sigma_{yz}^2 \quad (5.13)$$

J_3^0 is a generalization of the 3^{rd} invariant of the deviatoric stress tensor J_3 for orthotropy that is expressed as:

$$\begin{aligned} J_3^0 &= \frac{1}{27}(b_1 + b_2)\sigma_{xx}^3 + \frac{1}{27}(b_3 + b_4)\sigma_{yy}^3 + \frac{1}{27}[2(b_1 + b_4) - (b_2 + b_3)]\sigma_{zz}^3 \\ &+ \frac{2}{9}(b_1 + b_4)\sigma_{xx}\sigma_{yy}\sigma_{zz} - \frac{1}{9}(b_1\sigma_{yy} + b_2\sigma_{zz})\sigma_{xx}^2 - \frac{1}{9}(b_3\sigma_{zz} + b_4\sigma_{xx})\sigma_{yy}^2 \\ &- \frac{1}{9}[(b_1 - b_2 + b_4)\sigma_{xx} + (b_1 - b_3 + b_4)\sigma_{yy}]\sigma_{zz}^2 + 2b_{11}\sigma_{xy}\sigma_{xz}\sigma_{yz} \\ &- \frac{1}{3}\sigma_{yz}^2[(b_6 + b_7)\sigma_{xx} - b_6\sigma_{yy} - b_7\sigma_{zz}] \\ &- \frac{1}{3}\sigma_{xz}^2[2b_9\sigma_{yy} - b_8\sigma_{zz} - (2b_9 - b_8)\sigma_{xx}] \\ &- \frac{1}{3}\sigma_{xy}^2[2b_{10}\sigma_{zz} - b_5\sigma_{yy} - (2b_{10} - b_5)\sigma_{xx}] \end{aligned} \quad (5.14)$$

The number of anisotropic parameters in equation (5.12) is 17, which includes $a_i (i = 1, 2, \dots, 6)$ and $b_i (i = 1, 2, \dots, 11)$. If all coefficients $b_i (i = 1, 2, \dots, 11)$ are set to zero, the Cazacu-Barlat or *C-B* criterion reduces to the Hill's model. J_3^0 with stress terms of odd exponents are added to account for the tension-compression asymmetry. For isotropic conditions $a_i = a_j (i, j = 1, 2, \dots, 6)$ and $b_i = b_j (i, j = 1, 2, \dots, 11)$. Both J_2^0 and J_3^0 do not depend on the hydrostatic stress, thus making the model pressure-insensitive. This model framework with higher order stress terms is examined for its suitability in representing the highly anisotropic behavior of Ti alloys.

5.4.2 Suitability of the Cazacu-Barlat Framework for the HAPC Model of Ti Alloys

The sensitivity analysis in section 5.3.2 concluded that four microstructural descriptor-based parameters, viz. the three orientation-related parameters (\overline{SF}_x , \overline{SF}_y and \overline{SF}_z) and the volume averaged grain size D , should be incorporated in the three-dimensional HAPC model. The HAPC model for Ti alloys adopts the framework of the anisotropic yield function in [19, 20, 21] with 17 anisotropic parameters in equations (5.12) - (5.14). The model parameters are calibrated by homogenization of CPFE micromechanical analyses conducted on representative volume elements (RVE) of the microstructure with different microstructural features. They are naturally functions of the microstructure descriptors, and may evolve with increasing plastic flow as deduced in section 5.4.3. The homogenized flow stress in shear in equation (5.12) is a function of the microstructural descriptors as well as the macroscopic plastic work. The material principal coordinate system introduced in [38] is accounted for by representing RVEs in terms of orientation-dependent descriptors \overline{SF}_x , \overline{SF}_y and \overline{SF}_z .

To examine the suitability of the *C-B* yield criterion in capturing the anisotropic behavior of Ti alloys, numerical simulations are conducted for the RVE labeled M10 with a strong micro-texture, characterized by the distribution descriptors $\overline{SF}_x = 0.471$, $\overline{SF}_y = 0.470$, $\overline{SF}_z = 0.146$ and $D = 7.5 \mu m$. M10 consists of $7 \times 7 \times 7$ cubic grains, discretized into a FE mesh of 16464 tetrahedron elements. The RVE is subjected to 19 loading conditions delineated below.

- Three uniaxial tension tests along x , y and z directions
- Three pure shear tests on xy , xz and yz planes
- Three uniaxial compression tests along x , y and z directions
- Three biaxial tension tests ($\epsilon_{xx} : \epsilon_{yy} = 1 : 1$ with $\sigma_{zz} = 0$; $\epsilon_{zz} : \epsilon_{xx} = 1 : 1$ with $\sigma_{yy} = 0$; and $\epsilon_{yy} : \epsilon_{zz} = 1 : 1$ with $\sigma_{xx} = 0$)
- Three biaxial compression tests ($\epsilon_{xx} : \epsilon_{yy} = -1 : -1$ with $\sigma_{zz} = 0$; $\epsilon_{zz} : \epsilon_{xx} = -1 : -1$ with $\sigma_{yy} = 0$; and $\epsilon_{yy} : \epsilon_{zz} = -1 : -1$ with $\sigma_{xx} = 0$)
- Four tension tests with constrained transverse strain ($\epsilon_{xx} : \epsilon_{zz} = 1 : 0$ with $\sigma_{yy} = 0$; $\epsilon_{xx} : \epsilon_{yy} = 1 : 0$ with $\sigma_{zz} = 0$; $\epsilon_{yy} : \epsilon_{zz} = 1 : 0$ with $\sigma_{xx} = 0$; and $\epsilon_{xx} : \epsilon_{zz} = 0 : 0 : 1$ with $\sigma_{yy} = 0$)

Since Y_f is the homogenized flow stress in shear, CPFE simulation of simple shear test in the xy plane is used to calculate Y_f . Micromechanical analysis is followed by homogenization. The macroscopic plastic work W_p and Cauchy stress components σ_{ij} are evaluated from the microstructural variables using the relations:

$$W_p = \frac{1}{V} \sum_{I=1}^{N^e} W_p^I V^I \quad \text{and} \quad \sigma_{ij} = \frac{1}{V} \sum_{I=1}^{N^e} \sigma_{ij}^I V^I \quad (5.15)$$

where W_p^I and σ_{ij}^I are the plastic work and stress components at integration points of the tetrahedral element I , V^I is the volume of the I^{th} element and V is the total volume of the microstructure. For pure shear loading in the xy plane, the only nonzero macroscopic stress component is σ_{xy} . Therefore equations (5.12) - (5.14) reduce to

$$(a_4)^{\frac{3}{2}} \sigma_{xy}^3 - Y_f^3 = 0 \quad (5.16)$$

Parameter a_4 is set to 1 to make $Y_f(W_p) = \sigma_{xy}$. The flow stress Y_f is plotted as a function of W_p in figure 5.8(a).

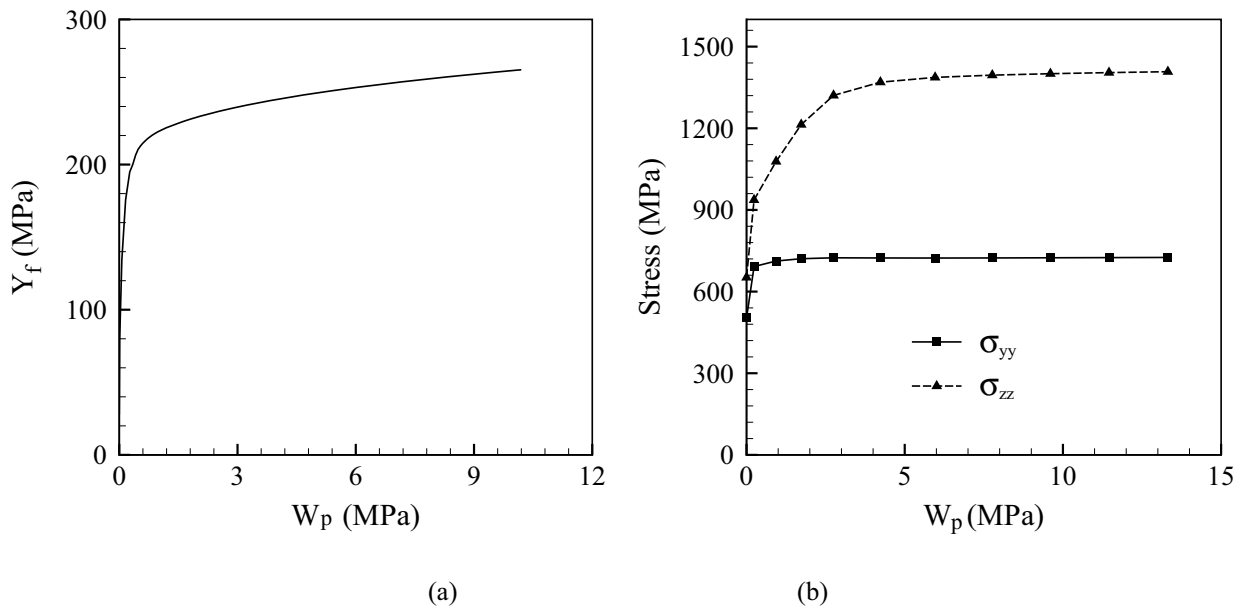


Figure 5.8: Homogenized response parameters plotted as a function of macroscopic plastic work: (a) flow stress obtained from pure shear loading in the xz plane, (b) stress components for the biaxial tension loading $\epsilon_{yy} : \epsilon_{zz} 1 : 1$ under plane stress conditions ($\sigma_{xx} = 0$).

Yield surface with calibrated parameters in the C-B Model Framework

To calibrate the anisotropic parameters $a_i (i = 1, 2, 3, 5, 6)$ and $b_i (i = 1, 2, \dots, 11)$, CPFE simulations are performed for RVE-M10 under the 19 loading conditions, followed by homogenization. All loading conditions are prescribed for a constant strain-rate of $10^{-4} s^{-1}$. At the end of each strain increment in the CPFE analyses, macroscopic stresses and plastic work are obtained from equation (5.15). The stress components are plotted as functions of W_p in figure 5.8(b), for one of the biaxial tension loadings $\epsilon_{yy} : \epsilon_{zz} 1 : 1$ under plane stress conditions ($\sigma_{xx} = 0$). The macroscopic normal stress σ_{yy} is much less than σ_{zz} due to anisotropy of this microstructure. For a given value of W_p , the stress components are obtained from plots such as in figure 5.8(b). This is done for all the loading conditions. The anisotropic parameters are then evaluated by least square minimization of function in equation (5.12) as:

$$\min_{a_i (i=1, \dots, 6), b_i (i=1, \dots, 11)} \sum_{I=1}^{19} [(J_2^0)^{3/2} - (J_3^0)_I - Y_f^3]^2 \quad (5.17)$$

Here

$$(J_2^0)_I = \frac{a_1}{6} (\sigma_{xx}^I - \sigma_{yy}^I)^2 + \frac{a_2}{6} (\sigma_{xx}^I - \sigma_{zz}^I)^2 + \frac{a_3}{6} (\sigma_{yy}^I - \sigma_{zz}^I)^2 + a_4 (\sigma_{xy}^I)^2 + a_5 (\sigma_{xz}^I)^2 + a_6 (\sigma_{yz}^I)^2 \quad (5.18)$$

and

$$\begin{aligned} (J_3^0)_I &= \frac{1}{27} (b_1 + b_2) (\sigma_{xx}^I)^3 + \frac{1}{27} (b_3 + b_4) (\sigma_{yy}^I)^3 + \frac{1}{27} [2(b_1 + b_4) - (b_2 + b_3)] (\sigma_{zz}^I)^3 \\ &+ \frac{2}{9} (b_1 + b_4) \sigma_{xx}^I \sigma_{yy}^I \sigma_{zz}^I - \frac{1}{9} (b_1 \sigma_{yy}^I + b_2 \sigma_{zz}^I) (\sigma_{xx}^I)^2 - \frac{1}{9} (b_3 \sigma_{zz}^I + b_4 \sigma_{xx}^I) (\sigma_{yy}^I)^2 \\ &- \frac{1}{9} [(b_1 - b_2 + b_4) \sigma_{xx}^I + (b_1 - b_3 + b_4) \sigma_{yy}^I] (\sigma_{zz}^I)^2 + 2b_{11} \sigma_{xy}^I \sigma_{xz}^I \sigma_{yz}^I \\ &- \frac{1}{3} (\sigma_{yz}^I)^2 [(b_6 + b_7) \sigma_{xx}^I - b_6 \sigma_{yy}^I - b_7 \sigma_{zz}^I] \\ &- \frac{1}{3} (\sigma_{xz}^I)^2 [2b_9 \sigma_{yy}^I - b_8 \sigma_{zz}^I - (2b_9 - b_8) \sigma_{xx}^I] \\ &- \frac{1}{3} (\sigma_{xy}^I)^2 [2b_{10} \sigma_{zz}^I - b_5 \sigma_{yy}^I - (2b_{10} - b_5) \sigma_{xx}^I] \end{aligned} \quad (5.19)$$

In equations (5.18) and (5.19), σ_{ij}^I are the macroscopic stress components for the loading case number I at a given value of W_p . After evaluating the anisotropic parameters for a given value of W_p , the 3D yield locus in the principal coordinate

system can be obtained from equations (5.12) - (5.14) by setting the shear stress components to zero. This results in:

$$\begin{aligned}
& \left[\frac{a_1}{6}(\sigma_1 - \sigma_2)^2 + \frac{a_2}{6}(\sigma_1 - \sigma_3)^2 + \frac{a_3}{6}(\sigma_2 - \sigma_3)^2 \right]^{\frac{3}{2}} \\
& - \left\{ \frac{1}{27}(b_1 + b_2)\sigma_1^3 + \frac{1}{27}(b_3 + b_4)\sigma_2^3 + \frac{1}{27}[2(b_1 + b_4) - (b_2 + b_3)]\sigma_3^3 \right. \\
& + \frac{2}{9}(b_1 + b_4)\sigma_1\sigma_2\sigma_3 - \frac{1}{9}(b_1\sigma_2 + b_2\sigma_3)\sigma_1^2 - \frac{1}{9}(b_3\sigma_3 + b_4\sigma_1)\sigma_2^2 \\
& \left. - \frac{1}{9}[(b_1 - b_2 + b_4)\sigma_1 + (b_1 - b_3 + b_4)\sigma_2]\sigma_3^2 \right\} - Y_f^3 = 0
\end{aligned} \tag{5.20}$$

where σ_1 , σ_2 and σ_3 are the principal stresses. The 3D yield locus for the microstructure M10 at $W_p = 0.1 \text{ MPa}$ is shown in figure 5.9(a). The projection of this yield surface on the $\sigma_1 - \sigma_3$ plane is compared with numerical data obtained from CPFE simulations in figure 5.9(b). Good agreement is observed between the *C-B* yield locus and the stress data-points obtained from CPFE simulations. Evolution of the yield locus with increase in plastic work ($W_p = 0.1, 1.0, 4.0$ and 10.0 MPa) is shown in figure 5.9(c). Values of the anisotropic parameters in equation (5.20), corresponding to $W_p = 0.1 \text{ MPa}$ are summarized in table 5.5. The values of b_i are smaller than those of a_i . This is observed in other microstructures as well. Consequently, some of the b_i parameters in the *C-B* yield criterion are set to zero to reduce the number of coefficients that requires calibration.

In the first iteration, all b_i parameters are set to zero. This reduces the *C-B* criterion to the Hill's model with only 6 anisotropic parameters. The process of calibrating the anisotropic parameters is repeated by least square minimization of this function:

$$\min_{a_i(i=1,\dots,6)} \sum_{I=1}^{19} [(J_2^0)_I^{3/2} - Y_f^3]^2 \tag{5.21}$$

where $(J_2^0)_I$ is obtained from equation (5.18). The calibrated parameters in the Hill's model, corresponding to $W_p = 0.1 \text{ MPa}$, are summarized in table 5.6. The resulting Hill's yield surface at $W_p = 0.1 \text{ MPa}$, projected on the $\sigma_1 - \sigma_3$ plane, is shown in figure 5.10(a). Comparing this yield locus with the *C-B* yield locus in figure 5.10(a) shows reasonable difference.

Table 5.5: Calibrated values of anisotropic parameters of equation (5.20), corresponding to $W_p = 0.1 \text{ MPa}$ for microstructure M10.

a_1	a_2	a_3	a_4	a_5	a_6	b_1	b_2	b_3	b_4
0.364	0.060	0.108	1	0.542	0.547	-0.048	0.026	-0.072	0.023

Table 5.6: Calibrated values of Hill's anisotropic parameters, corresponding to $W_p = 0.1 \text{ MPa}$ for microstructure M10.

a_1	a_2	a_3	a_4	a_5	a_6
0.359	0.055	0.105	1	0.542	0.547

In the second iteration, the parameters $b_i (i = 5, 6, \dots, 11)$ are set to zero. This removes the shear terms from J_3^0 , and the number of parameters, which require calibration, reduces to 10. In this case only 15 loading conditions are considered for homogenization and calibration purposes, which are:

- Three uniaxial tension tests in the x , y and z directions
- Three pure shear tests in xy , xz and yz planes
- Three uniaxial compression tests in the x , y and z directions
- Three biaxial tension tests ($\epsilon_{xx} : \epsilon_{yy} = 1 : 1$ with $\sigma_{zz} = 0$; $\epsilon_{zz} : \epsilon_{xx} = 1 : 1$ with $\sigma_{yy} = 0$; and $\epsilon_{yy} : \epsilon_{zz} = 1 : 1$ with $\sigma_{xx} = 0$)
- Three biaxial compression tests ($\epsilon_{xx} : \epsilon_{yy} = -1 : -1$ with $\sigma_{zz} = 0$; $\epsilon_{zz} : \epsilon_{xx} = -1 : -1$ with $\sigma_{yy} = 0$; and $\epsilon_{yy} : \epsilon_{zz} = -1 : -1$ with $\sigma_{xx} = 0$)

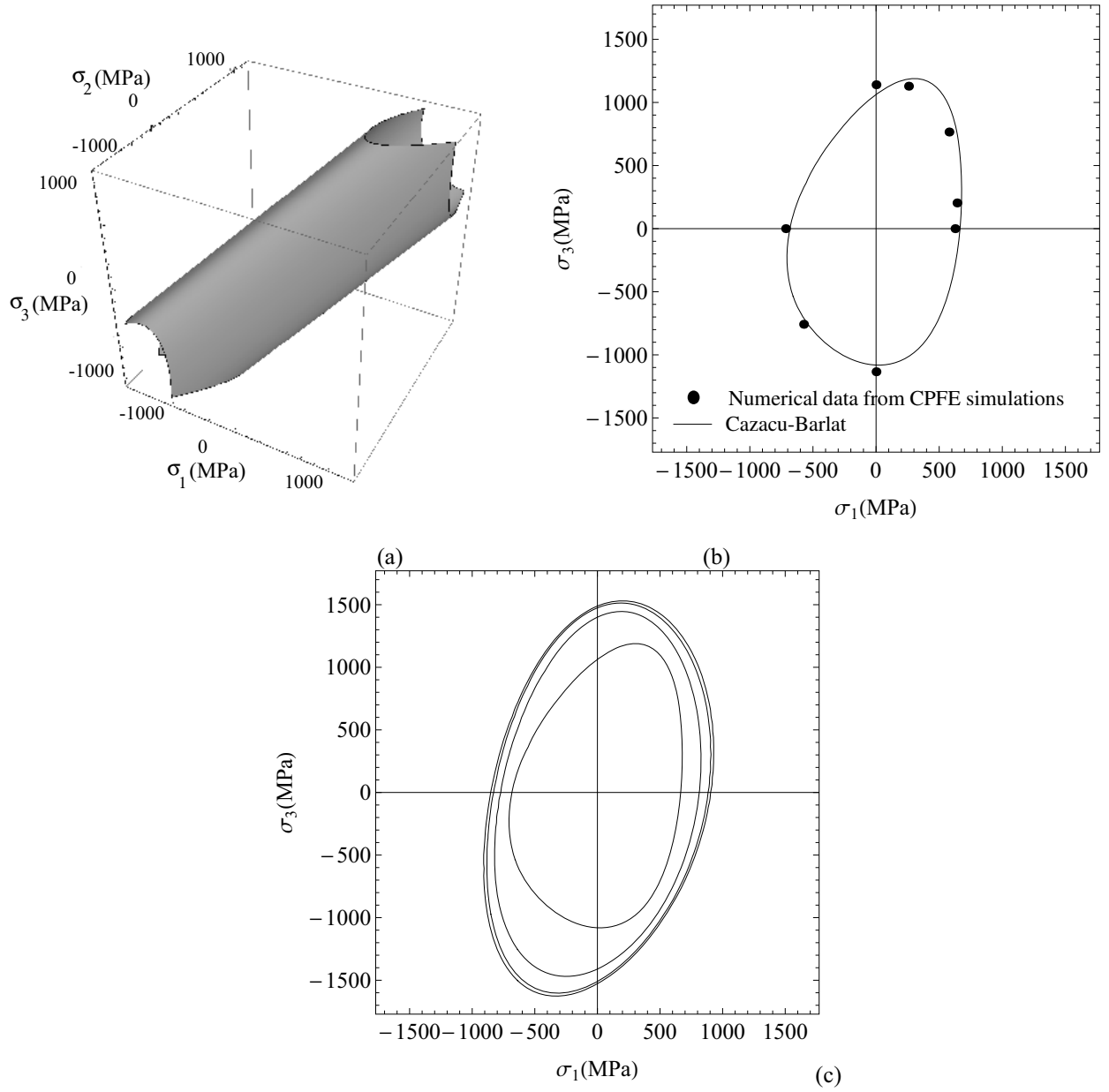


Figure 5.9: Yield loci for the microstructural RVE M10: (a) 3D yield locus at $W_p = 0.1 \text{ MPa}$, (b) $\sigma_1 - \sigma_3$ yield locus at $W_p = 0.1 \text{ MPa}$, compared with the numerical data obtained from CPFE simulations, (c) evolution of the yield locus with plastic work increase corresponding to $W_p = 0.1, 1.0, 4.0$ and 10.0 MPa .

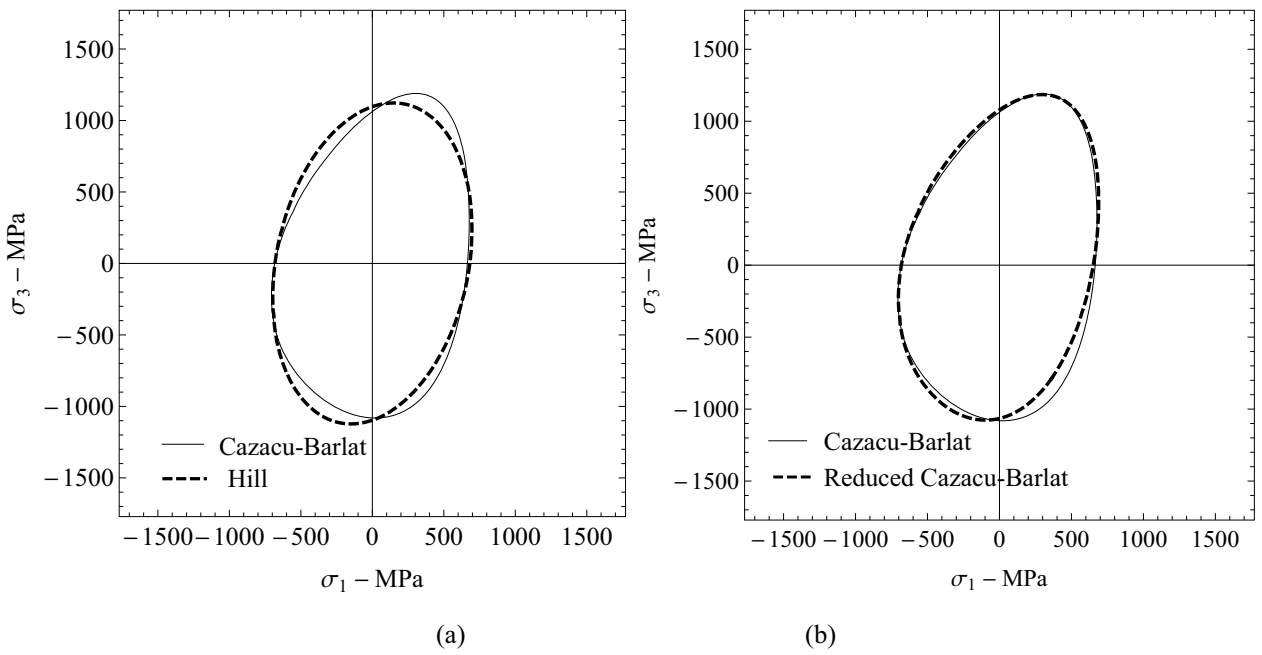


Figure 5.10: $\sigma_1 - \sigma_3$ yield loci for microstructure M10, corresponding to $W_p = 0.1 \text{ MPa}$ (a) Comparison of the Cazacu-Barlat model with 17 parameters with Hill's anisotropic model, (b) Comparison of the 17 and 10 (reduced) parameter $C-B$ models.

The parameters $a_i (i = 1, \dots, 6)$ and $b_i (i = 1, \dots, 4)$ are calibrated by least square minimization of this function:

$$\min_{a_i(i=1,\dots,6), b_i(i=1,\dots,4)} \sum_{I=1}^{15} [(J_2^0)^{3/2}_I - (J_3^*)_I - Y_f^3]^2 \quad (5.22)$$

where $(J_3^*)_I$ is the reduced form of $(J_3^0)_I$ as:

$$\begin{aligned} (J_3^*)_I &= \frac{1}{27}(b_1 + b_2)(\sigma_{xx}^I)^3 + \frac{1}{27}(b_3 + b_4)(\sigma_{yy}^I)^3 + \frac{1}{27}[2(b_1 + b_4) - (b_2 + b_3)](\sigma_{zz}^I)^3 \\ &+ \frac{2}{9}(b_1 + b_4)\sigma_{xx}^I\sigma_{yy}^I\sigma_{zz}^I - \frac{1}{9}(b_1\sigma_{yy}^I + b_2\sigma_{zz}^I)(\sigma_{xx}^I)^2 - \frac{1}{9}(b_3\sigma_{zz}^I + b_4\sigma_{xx}^I)(\sigma_{yy}^I)^2 \\ &- \frac{1}{9}[(b_1 - b_2 + b_4)\sigma_{xx}^I + (b_1 - b_3 + b_4)\sigma_{yy}^I](\sigma_{zz}^I)^2 \end{aligned} \quad (5.23)$$

It should be noted that the reduced $C-B$ criterion, $(J_2^0)^{3/2} - J_3^* - Y_f^3 = 0$, still satisfies the required characteristics for an acceptable yield criterion, viz. pressure-insensitivity, anisotropy and tension-compression asymmetry. The calibrated parameters corresponding to $W_p = 0.1 \text{ MPa}$ are summarized in table 5.7. The resulting yield surface at $W_p = 0.1 \text{ MPa}$, projected on the $\sigma_1 - \sigma_3$ plane, is shown in figure 5.10(b). This yield locus, when compared with the one obtained from $C-B$ model with all 17 parameters shows no significant difference. Thus the $C-B$ yield model with reduced number of parameters will be used to develop the macroscopic HAPC constitutive model for Ti alloys.

Table 5.7: Calibrated values of the reduced Cazacu-Barlat parameters at $W_p = 0.1 \text{ MPa}$ for the microstructure M10.

a_1	a_2	a_3	a_4	a_5	a_6	b_1	b_2	b_3	b_4
0.359	0.074	0.093	1	0.542	0.547	-0.032	-0.004	-0.057	0.003

5.4.3 Evaluation of Microstructure Dependent Constitutive Parameters in the HAPC model

The anisotropic parameters $a_i (i = 1, \dots, 6)$, $b_i (i = 1, \dots, 4)$ and the flow stress (Y_f) in the reduced $C-B$ model are microstructure-dependent. To adequately account for microstructural variations, 70 different polycrystalline RVEs with different microstructure descriptors are considered. The characteristics of these microstructures are summarized in table 5.8 in the

Attachment A. Each RVE consists of $7 \times 7 \times 7$ cubic grains. The volume averages of Schmid factors \overline{SF}_x , \overline{SF}_y and \overline{SF}_z vary between 0.146 and 0.498 in the microstructures. Three values, viz. 7.5, 15 and 40 μm are considered for the average grain size D .

For each RVE, CPFE simulations are conducted under 12 different loading conditions, viz.:

- Three uniaxial tension tests in the x , y and z directions
- Three pure shear tests in xy , xz and yz planes
- Three uniaxial compression tests in the x , y and z directions
- Three biaxial tension tests ($\epsilon_{xx} : \epsilon_{yy} = 1 : 1$ with $\sigma_{zz} = 0$; $\epsilon_{zz} : \epsilon_{xx} = 1 : 1$ with $\sigma_{yy} = 0$; and $\epsilon_{yy} : \epsilon_{zz} = 1 : 1$ with $\sigma_{xx} = 0$)

For each microstructure, the flow stress Y_f is obtained at different values of W_p and the anisotropic parameters for each microstructure are evaluated at different values of W_p by least square minimization of the function:

$$\min_{a_i(i=1,...,6), b_i(i=1,...,4)} \sum_{I=1}^{12} [(J_2^0)^{3/2} - (J_3^*)_I - Y_f^3]^2 \quad (5.24)$$

The procedure in section 5.4.2 is used to calibrate a_i ($i = 1, \dots, 6$) and b_i ($i = 1, \dots, 4$). A few key observations are made from the homogenization studies.

- Anisotropic yield parameters for each microstructure evolves with averaged plastic work W_p .
- The flow stress for each microstructure evolves with increase in plastic work W_p .
- The flow stress for a given value of W_p decreases with increase in the average grain size, D .
- If $\overline{SF}_i > \overline{SF}_j > \overline{SF}_k$ then $a_i > a_m > a_n$, where a_i, a_m, a_n are the anisotropic parameters associated with the normal stress components in the J_2^0 part of the yield criterion, i.e.

$$J_2^0 = \frac{a_i}{6}(\sigma_i - \sigma_j)^2 + \frac{a_m}{6}(\sigma_i - \sigma_k)^2 + \frac{a_n}{6}(\sigma_j - \sigma_k)^2 + a_4\sigma_{xy}^2 + a_5\sigma_{xz}^2 + a_6\sigma_{yz}^2 \quad (5.25)$$

- Higher Schmid factors in x and y directions result in lower flow stress Y_f .

The calibrated values of the anisotropic parameters a_i and b_i and the flow stress Y_f for different RVEs are used to derive a functional forms of parameters in the HAPC model in terms of microstructural descriptor statistics \overline{SF}_x , \overline{SF}_y , \overline{SF}_z and D , as well as the evolving plastic work W_p . Power law functional forms are assumed for the parameters as:

$$\begin{aligned} a_i &= (A_1^i + A_2^i \overline{SF}_x^{\alpha_i})(A_3^i + A_4^i \overline{SF}_y^{\beta_i})(A_5^i + A_6^i \overline{SF}_z^{\gamma_i})(A_7^i + A_8^i D^{\eta_i}) \\ &\quad (A_9^i + A_{10}^i W_p^{\kappa_i}) \quad i = 1, \dots, 6 \\ b_i &= (B_1^i + B_2^i \overline{SF}_x^{\chi_i})(B_3^i + B_4^i \overline{SF}_y^{\delta_i})(B_5^i + B_6^i \overline{SF}_z^{\epsilon_i})(B_7^i + B_8^i D^{\phi_i}) \\ &\quad (B_9^i + B_{10}^i W_p^{\varphi_i}) \quad i = 1, \dots, 4 \\ Y_f &= (C_1^i + C_2^i \overline{SF}_x^{\lambda})(C_3^i + C_4^i \overline{SF}_y^{\mu})(C_5^i + C_6^i \overline{SF}_z^{\nu})(C_7^i + C_8^i D^{\theta}) \\ &\quad (C_9^i + C_{10}^i W_p^{\psi}) \end{aligned} \quad (5.26)$$

The coefficients A_j^i , B_j^i , C_i , β_i , γ_i , η_i , κ_i , χ_i , δ_i , ϵ_i , ϕ_i , φ_i , λ , μ , ν , θ and ψ are obtained from a least square fit of the data for RVEs in table 5.8. The resulting values of the coefficients are given in tables 5.9, 5.10, 5.11 and 5.12 in Attachment B. The strength of the dependencies are generally indicated by the exponents. For example, a weak dependence is signaled

by a near-zero exponent. The corresponding values of a_i , b_i and Y_f are given below.

$$\begin{aligned}
a_1 &= 0.1(0.9 + 15.6\overline{SF}_x^{1.9})(0.3 + 5.9\overline{SF}_y^{1.8})(0.01 - 6.6\overline{SF}_z^{10.6})(66.6 + 0.4D^{0.5}) \\
a_2 &= 0.0 \\
a_3 &= 0.0 \\
a_4 &= 1.0 \\
a_5 &= 3.0(0.2 + 3.4\overline{SF}_x^{-0.01})(0.05 - 0.07\overline{SF}_y^{1.4})(0.05 + 0.2\overline{SF}_z^{1.9})(36.4 - 1.3D^{0.1}) \\
a_6 &= (-3.9 + 4.2\overline{SF}_x^{-0.1})(-0.1 + 0.8\overline{SF}_y^{7.8})(0.2 + 0.9\overline{SF}_z^{1.1}) \\
&\quad (-5.2 + 0.002D^{1.0})(6.1 - 0.006W_p^{0.7}) \\
b_1 &= -5.4(0.01 + 0.6\overline{SF}_x^{3.4})(0.5 + 0.1\overline{SF}_y^{2.8})\overline{SF}_z^{3.7}(22.1 + 0.1D^{0.8})(0.2 + 0.3W_p^{0.3}) \\
b_2 &= (1.6 - 1.8\overline{SF}_x^{0.1})(1.5 - 2.1\overline{SF}_y^{0.7})(1.6 - 2.6\overline{SF}_z^{1.1})(42.6 + 0.3D^{0.8})(-2.0 + 2.0W_p^{0.01}) \\
b_3 &= (0.8 + 2.4\overline{SF}_x^{2.7})(-0.8 + 5.7\overline{SF}_y^{1.7})(-0.002 - 0.03\overline{SF}_z^{3.8}) \\
&\quad (24.7 + 0.1D^{1.0})(0.2 + 1.0W_p^{0.2}) \\
b_4 &= 0.0 \\
Y_f &= 0.2(3.7 - 39.1\overline{SF}_x^{7.6})(0.7 - 40.4\overline{SF}_y^{9.8})(16.2 + 17.7\overline{SF}_z^{1.0})(40.5 - 12.9D^{0.1})
\end{aligned} \tag{5.27}$$

It is clear from these expressions that the macroscopic constitutive parameters and consequently the yield function not only depend on morphological and crystallographic features of the polycrystalline microstructure, but also on the evolution of internal variables during the deformation process.

5.4.4 An Extension of the Homogenized Model to Account for Rate Dependency

A rate-dependent viscoplastic extension of the HAPC model is proposed in this section. The rate-dependent framework follows an over-stress viscoplastic model [87] with anisotropy introduced through the yield functions developed in section 5.4.3. In this model, the viscoplastic strain rate is expressed in terms of a function $\phi(F)$ of the over-stress F as:

$$\dot{\epsilon}^P = \lambda_0 \phi(F) \frac{\partial F / \partial \sigma}{\|\partial F / \partial \sigma\|} \tag{5.28}$$

where λ_0 is a temperature dependent viscosity coefficient. The viscoplastic strain rate in equation (5.28) follows the associated flow rule and hence satisfies normality and incompressibility conditions. In [87] and [41] a power law expression, i.e. $\phi(F) = \langle F \rangle^n$ has been discussed to adequately represent the behavior of most metals. $\langle \cdot \rangle$ is the McCauley operator corresponding to the positive sign of the argument. The over-stress F corresponds to a measure of the excess equivalent flow stress σ_{eq} over the rate-independent yield stress Y_f , i.e.

$$F = \sigma_{eq} - Y_f \tag{5.29}$$

where

$$\begin{aligned}
\sigma_{eq}^3 &= (J_2^0)^{3/2} - J_3^* \\
&= \left[\frac{a_1}{6}(\sigma_{xx} - \sigma_{yy})^2 + \sigma_{xy}^2 + a_5\sigma_{xz}^2 + a_6\sigma_{yz}^2 \right]^{\frac{3}{2}} \\
&\quad - \left[\frac{1}{27}(b_1 + b_2)\sigma_{xx}^3 + \frac{1}{27}b_3\sigma_{yy}^3 + \frac{1}{27}[2b_1 - (b_2 + b_3)]\sigma_{zz}^3 \right. \\
&\quad + \frac{2}{9}b_1\sigma_{xx}\sigma_{yy}\sigma_{zz} - \frac{1}{9}(b_1\sigma_{yy} + b_2\sigma_{zz})\sigma_{xx}^2 - \frac{1}{9}b_3\sigma_{zz}\sigma_{yy}^2 \\
&\quad \left. - \frac{1}{9}[(b_1 - b_2)\sigma_{xx} + (b_1 - b_3)\sigma_{yy}]\sigma_{zz}^2 \right]
\end{aligned} \tag{5.30}$$

The anisotropy parameters a_i and b_i , as well as the rate-independent yield stress Y_f in equation (5.29) are given in equations (5.27). These parameters evolve with plastic work.

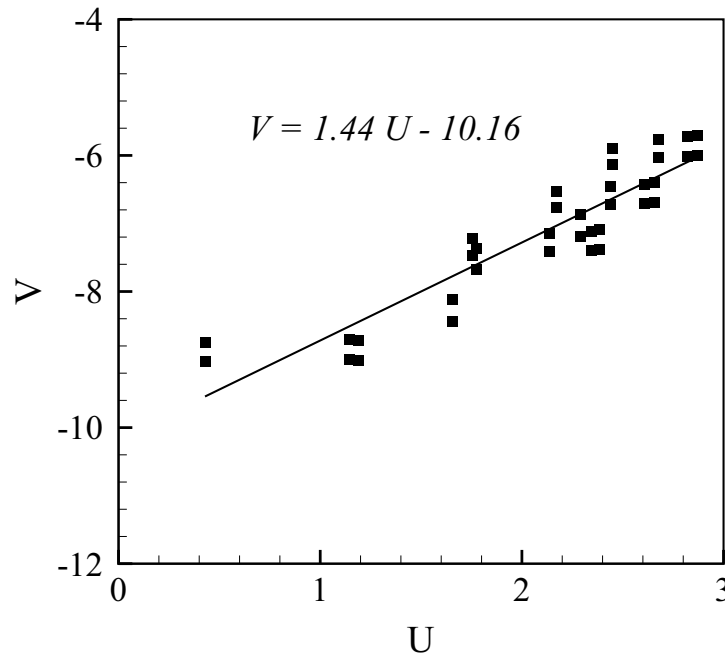


Figure 5.11: Calibration of viscoplastic parameters λ_0 and n

The homogenized viscosity coefficient λ_0 and exponent n in equation (5.28) are calibrated from a set of loading conditions combining N different imposed *strain ratios* and M different applied *strain-rates*. In each increment, the stress tensor σ , the plastic strain rate tensor $\dot{\epsilon}^p$, and the plastic work W_p are computed from CPFE simulation results. The corresponding yield stress $Y_f(W_p)$ and anisotropy coefficients a_i and b_i are evaluated using equations (5.27). The overstress F is obtained at each time increment from equations (5.29) and (5.30) and its derivative with respect to σ_{ij} is evaluated as:

$$\frac{\partial F}{\partial \sigma_{ij}} = \frac{\partial \sigma_{eq}}{\partial \sigma_{ij}} = \frac{1}{3} \left[(J_2^0)^{3/2} - J_3^* \right]^{-2/3} \left[\frac{3}{2} (J_2^0)^{1/2} \frac{\partial J_2^0}{\partial \sigma_{ij}} - \frac{\partial J_3^*}{\partial \sigma_{ij}} \right] \quad (5.31)$$

To determine λ_0 and n , equation (5.28) is rewritten by taking the logarithm of both sides as:

$$\begin{aligned} \ln(\dot{\epsilon}_{ij}^p) &= \ln(\lambda_0) + n \ln\langle F \rangle + \ln\left(\frac{\partial F / \partial \sigma_{ij}}{\|\partial F / \partial \sigma\|}\right) \\ \text{or} \\ \ln\left[\frac{\dot{\epsilon}_{ij}^p \|\partial F / \partial \sigma\|}{\partial F / \partial \sigma_{ij}}\right] &= \ln(\lambda_0) + n \ln\langle F \rangle \end{aligned} \quad (5.32)$$

Equation (5.32) is a linear relation between $U (= \ln\langle F \rangle)$ and $V (= \ln\left[\frac{\dot{\epsilon}_{ij}^p \|\partial F / \partial \sigma\|}{\partial F / \partial \sigma_{ij}}\right])$. Consequently, a plot of V versus U yields a straight line with slope equal to n and the intercept equal to $\ln(\lambda_0)$. The viscoplastic parameters λ_0 and n are consequently obtained by finding the best linear fit to the measured data (U, V) corresponding to different stress components for different loading conditions at different time increments. Four different strain rates under uniaxial tension are applied to calibrate these parameters, corresponding to $N = 1$ and $M = 4$. The applied strain rates are: $\dot{\epsilon}_{xx}^{(1)} = 0.0001 \text{ s}^{-1}$, $\dot{\epsilon}_{xx}^{(2)} = 0.0005 \text{ s}^{-1}$, $\dot{\epsilon}_{xx}^{(3)} = 0.001 \text{ s}^{-1}$ and $\dot{\epsilon}_{xx}^{(4)} = 0.002 \text{ s}^{-1}$. Figure 5.11 shows the best linear fit to the measured data at different time increments considering only $\dot{\epsilon}_{xx}^p$ and $\dot{\epsilon}_{yy}^p$. The corresponding viscoplastic parameters are evaluated as:

$$\lambda_0 = e^{-10.16} = 3.9 \times 10^{-5} \quad \text{and} \quad n = 1.44 \quad (5.33)$$

The methodology discussed in this section provides a path for extending the rate-independent continuum anisotropic plasticity model derived from homogenization of polycrystalline crystal plasticity finite element simulation results into a rate-dependent model.

5.5 Conclusion

This work is aimed at developing a homogenized, anisotropic plasticity constitutive (HAPC) model for Ti alloys. In particular, this model develops an anisotropic yield function with a direct connection to the morphology and crystalline structure of the polycrystalline microstructure that can be incorporated in any macroscopic FEM code. The advantage of this model is that it avoids having to perform computationally expensive micromechanical analysis at each point in macroscopic simulations. It is able to capture important deformation characteristics of Ti-based alloys, which are pressure insensitivity, anisotropy, tension-compression asymmetry and kinematic hardening. The overall framework of the HAPC model follows the structure of the anisotropic Cazacu-Barlat yield function that possesses the desired attributes of anisotropy and tension-compression asymmetry inherent to polycrystalline metals. This framework is further extended to accommodate rate-dependent behavior observed in mechanical behavior of Ti alloys. Parameters in the HAPC model are calibrated from results of homogenization of microstructural CPFEM analysis variables of the polycrystalline RVEs with varying orientation distributions and grain sizes.

A systematic sensitivity analysis is conducted to establish the dependence of mechanical response on microstructural crystallographic and morphological parameters. This analysis concludes that average Schmid factors for three orthogonal directions and grain size distributions are important microstructural descriptors that should be incorporated in the homogenized yield functions. Parameters in the anisotropic yield function following the Cazacu-Barlat framework are calibrated from homogenization of CPFE results of polycrystalline microstructure simulations. The anisotropy parameters in the homogenized yield function are found to be functions of the microstructural descriptors, but evolve with plastic work. The functional forms of the parameters overcome limitations of constant anisotropy parameters that are conventionally assumed in anisotropic plasticity models. Comparison of the anisotropic HAPC model results with homogenized micromechanics results shows excellent agreement. The HAPC model has a significant efficiency advantage over the micromechanics models and is hence a very effective tool in making macroscopic deformation predictions with explicit reference to the microstructural composition. The second part of this two-part paper will develop a probabilistic crack nucleation model for structural scale analysis of polycrystalline Ti alloys from grain-level crack nucleation results.

5.6 Attachment A

Table 5.8: Microstructure descriptors for different RVEs used to develop the HAPC model.

RVE	\overline{SF}_x	\overline{SF}_y	\overline{SF}_z	D	RVE	\overline{SF}_x	\overline{SF}_y	\overline{SF}_z	D
M10	0.471	0.47	0.146	7.5	M130	0.437	0.268	0.47	7.5
M11	0.471	0.47	0.146	15	M131	0.437	0.268	0.47	15
M12	0.471	0.47	0.146	40	M132	0.437	0.268	0.47	40
M20	0.445	0.446	0.36	7.5	M140	0.47	0.473	0.428	7.5
M21	0.445	0.446	0.36	15	M141	0.47	0.473	0.428	15
M22	0.445	0.446	0.36	40	M142	0.47	0.473	0.428	40
M30	0.445	0.446	0.496	7.5	M150	0.323	0.448	0.382	7.5
M31	0.445	0.446	0.496	15	M151	0.323	0.448	0.382	15
M32	0.445	0.446	0.496	40	M152	0.323	0.448	0.382	40
M40	0.43	0.435	0.401	7.5	M160	0.482	0.498	0.483	7.5
M41	0.43	0.435	0.401	15	M161	0.482	0.498	0.483	15
M42	0.43	0.435	0.401	40	M162	0.482	0.498	0.483	40
M50	0.47	0.437	0.268	7.5	M171	0.146	0.471	0.47	15
M51	0.47	0.437	0.268	15	M172	0.146	0.471	0.47	40
M52	0.47	0.437	0.268	40	M180	0.36	0.445	0.446	7.5
M60	0.428	0.47	0.473	7.5	M181	0.36	0.445	0.446	15
M61	0.428	0.47	0.473	15	M182	0.36	0.445	0.446	40
M62	0.428	0.47	0.473	40	M190	0.496	0.445	0.446	7.5
M70	0.382	0.323	0.448	7.5	M191	0.496	0.445	0.446	15
M71	0.382	0.323	0.448	15	M192	0.496	0.445	0.446	40
M72	0.382	0.323	0.448	40	M200	0.401	0.43	0.435	7.5
M80	0.483	0.482	0.498	7.5	M201	0.401	0.43	0.435	15
M81	0.483	0.482	0.498	15	M202	0.401	0.43	0.435	40
M82	0.483	0.482	0.498	40	M210	0.268	0.47	0.437	7.5
M91	0.47	0.146	0.471	15	M211	0.268	0.47	0.437	15
M92	0.47	0.146	0.471	40	M212	0.268	0.47	0.437	40
M100	0.446	0.36	0.445	7.5	M220	0.473	0.428	0.47	7.5
M101	0.446	0.36	0.445	15	M221	0.473	0.428	0.47	15
M102	0.446	0.36	0.445	40	M222	0.473	0.428	0.47	40
M110	0.446	0.496	0.445	7.5	M230	0.448	0.382	0.323	7.5
M111	0.446	0.496	0.445	15	M231	0.448	0.382	0.323	15
M112	0.446	0.496	0.445	40	M232	0.448	0.382	0.323	40
M120	0.435	0.401	0.43	7.5	M240	0.498	0.483	0.482	7.5
M121	0.435	0.401	0.43	15	M241	0.498	0.483	0.482	15
M122	0.435	0.401	0.43	40	M242	0.498	0.483	0.482	40

5.7 Attachment B

Table 5.9: Coefficients A_j^i in equation (5.27).

i/j	j=1	j=2	j=3	j=4	j=5	j=6	j=7	j=8	j=9	j=10
i=1	0.9	15.6	0.3	5.9	0.01	-6.6	66.6	0.4	-2.2	2.3
i=2	1.6	14.2	0.4	1.1	0.04	2.4	40.0	0.1	0.8	0.8
i=3	1.6	-3.2	0.4	4.7	0.08	4.8	33.8	0.03	-1.2	1.2
i=4	1.0	0.0	1.0	0.0	1.0	0.0	1.0	0.0	1.0	0.0
i=5	0.2	3.4	0.05	-0.07	0.05	0.2	36.4	1.3	-3.0	6×10^{-7}
i=6	3.9	4.2	-0.1	0.8	0.2	0.9	-5.2	0.002	6.1	-0.006

Table 5.10: Coefficients B_j^i in equation (5.27).

i/j	j=1	j=2	j=3	j=4	j=5	j=6	j=7	j=8	j=9	j=10
i=1	0.01	0.6	0.5	0.1	2×10^{-4}	5.4	22.1	0.1	0.2	0.3
i=2	1.6	-1.8	1.5	-2.1	1.6	-2.6	42.6	0.3	-2.0	2.0
i=3	0.8	2.4	-0.8	5.7	0.002	0.03	24.7	0.1	0.2	1.0
i=4	1.8	2.0	1.8	-2.0	1.9	-3.6	34.5	0.1	1.4	-1.4

Table 5.11: Coefficients C_j^i in equation (5.27).

i/j	j=1	j=2	j=3	j=4	j=5	j=6	j=7	j=8	j=9	j=10
i=1	3.7	39.1	0.7	-40.4	16.2	17.7	40.5	-12.9	-3.3	3.5

Table 5.12: Various coefficients in equation (5.27).

	α_i	β_i	γ_i	η_i	κ_i	χ_i	δ_i	ϵ_i	ϕ_i	φ_i	λ	μ	ν	θ	ψ
i=1	1.9	1.8	10.6	0.5	0.002	3.4	2.8	3.7	0.8	0.3	7.6	9.8	1.0	0.1	0.005
i=2	2.1	2.2	2.5	0.4	0.003	0.1	0.7	1.1	0.8	0.01					
i=3	1.8	2.6	2.0	0.8	0.001	2.7	1.7	3.8	1.0	0.2					
i=4	-	-	-	-	-	0.2	0.6	1.9	1.0	0.03					
i=5	-0.01	1.4	1.9	0.1	4.5										
i=6	-0.1	7.8	1.1	1.0	0.7										

Bibliography

- [1] A. Acharya and A. J. Beaudoin. Grain-size effect in viscoplastic polycrystals at moderate strains. *Jour. Mech. Physics Solids*, 48:2213–2230, 2000.
- [2] B. L. Adams, A. Henrie, B. Henrie, M. Lyon, S. R. Kalidindi, and H. Garmestani. Micorstructure-sensitive design of a compliant beam. *J. Mech. Phys. Solids*, 49:1639–1663, 2001.
- [3] M. Anahid, P. Chakraborty, D. S. Joseph, and S. Ghosh. Wavelet decomposed dual-time scale crystal plasticity FE model for analyzing cyclic deformation induced crack nucleation in polycrystals. *Model. Simul. Mater. Sci. Engng.*, 37(064009), 2009.
- [4] M. Anahid, M. K. Samal, and S. Ghosh. Dwell fatigue crack nucleation model based on crystal plasticity finite element simulations of polycrystalline Titanium alloys. *Jour. Mech. Phys. Solids*, 59(10):2157–2176, 2011.
- [5] L. Anand and M. Kothari. A computational procedure for rate-independent crystal plasticity. *Jour. Mech. Phys. Solids*, 44(4):525–558, 1996.
- [6] T. L. Anderson. *Fracture Mechanics: Fundamentals and Applications*. CRC Press, 2005.
- [7] M. F. Ashby. The deformation of plastically non-homogeneous materials. *Phil Mag.*, 21:399–424, 1970.
- [8] M. R. Bache. A review of dwell sensitive fatigue in titanium alloys: the role of microstructure, Texture and Operating Conditions. *Int. J. Fatigue*, 25:1079–1087, 2003.
- [9] M. R. Bache. A review of dwell sensitive fatigue in titanium alloys: the role of microstructure, texture and operating conditions. *Int. J. Fatigue*, 25:1079–1087, 2003.
- [10] M. R. Bache, M. Cope, H. M. Davies, E. J. Evans, and G. Harrison. Dwell sensitive fatigue in a near alpha titanium alloy at ambient temperature. *Int. J. Fatigue*, 19(93):83–88, 1997.
- [11] M. R. Bache, W. J. Evans, B. Suddell, and F. R. M. Herrouin. The effects of texture in titanium alloys for engineering components under fatigue. *Int. J. Fatigue*, 23:153–159, 2001.
- [12] S. Balasubramanian and L. Anand. Elasto-viscoplastic constitutive equations for polycrystalline fcc materials at low homologous temperatures. *Jour. Mech. Phys. Solids*, 50(1):101–126, 2002.
- [13] V. P. Bennett and D. L. McDowell. Polycrystal orientation distribution effects on microslip in high cycle fatigue. *Int. J. Fatigue*, 25:27–39, 2003.
- [14] V.P. Bennett and D.L. McDowell. Polycrystal orientation distribution effects on microslip in high cycle fatigue. *Int. Jour. Fatigue*, 25:27–39, 2003.
- [15] S.P. Bhat and M.E. Fine. Fatigue crack nucleation in iron and a high strength low alloy steel. *Materials Science and Engineering A*, 314:9096, 2001.
- [16] I. I. Blekhman. *Vibrational mechanics*. World Scientific, 2000.
- [17] T. Bohlke, G. Risý, and A. Bertram. Finite element simulation of metal forming operations with texture based material models. *Model. Simul. Mater. Sci. Engng.*, 14:365–387, 2006.
- [18] F. Bridiera, D. L. McDowell, P. Villechaisea, and J. Mendeza. Crystal plasticity modeling of slip activity in Ti-6Al-4V under high cycle fatigue loading. *Int. J. Plasticity*, 25:1066–1082, 2009.

- [19] O. Cazacu and F. Barlat. Generalization of druckers yield criterion to orthotropy. *Math. Mech. Solids*, 6:613–630, 2001.
- [20] O. Cazacu and F. Barlat. Application of representation theory to describe yielding of anisotropic aluminum alloys. *Int. Jour. Eng. Sci.*, 41:13671385, 2003.
- [21] O. Cazacu and F. Barlat. A criterion for description of anisotropy and yield differential effects in pressure-insensitive metals. *Int. Jour. Plast.*, 20:2027–2045, 2004.
- [22] P. Chakraborty, D. S. Joseph, and S. Ghosh. Wavelet transformation based multi-time scale crystal plasticity FEM for cyclic deformation in titanium alloys under dwell load. *Fin. Elem. Ana. Des.*, 47:610–618, 2011.
- [23] R.Q. Chu, Z. Cai, S.X. Li, and Z.G. Wang. Fatigue crack initiation and propagation in an a-iron polycrystals. *Mater. Sci. Engng.*, 313:61–68, 2001.
- [24] L. F. Coffin. Fatigue. *Ann. Rev. Matls. Sci.*, 2:313–348, 1973.
- [25] A. H. Cottrell. Theory of brittle fracture in steel and similar metals. *Trans. Met. Soc. AIME*, 212:192–203, 1958.
- [26] D. L. Davidson and D. Eylon. Titanium alloy fatigue fracture facet investigation by selected area electron channeling. *Mat. Trans. A*, 11A:837–843, 1980.
- [27] P.R. Dawson. Computational crystal plasticity. *Inter. Jour. Sol. Struct.*, 37:115–130, 2000.
- [28] D. Deka, D. S. Joseph, S. Ghosh, and M. J. Mills. Crystal plasticity modeling of deformation and creep in polycrystalline Ti-6242. *Metall. Trans. A.*, 37A(5):1371–1388, 2006.
- [29] D. Deka, D. S. Joseph, S. Ghosh, and M. J. Mills. Crystal plasticity modeling of deformation and creep in polycrystalline Ti-6242. *Metall. Trans. A.*, 37(5):1371–1388, 2006.
- [30] F.P.E. Dunne and D. Rugg. On the mechanisms of fatigue facet nucleation in titanium alloys. *Fatigue Fract. Engng. Mater. Struct.*, 31:949–958, 2008.
- [31] R. A. B. Engelen, M. G. D. Geers, and Baaijens F. P. T. Nonlocal implicit gradient-enhanced elasto-plasticity for the modeling of softening behavior. *Int. Jour. Plasticity*, 19:403–433, 2003.
- [32] W. J. Evans. Optimising mechanical properties in alpha + beta titanium alloys. *Mat. Sc. Engg. A*, 243:89–96, 1998.
- [33] D. Eylon and J. A. Hall. Fatigue behavior of beta processed titanium alloy imi 685. *Met. Trans. A*, 8A:981–990, 1977.
- [34] F. Feyel and J. Chaboche. Fe2 multiscale approach for modelling the elastoviscoplastic behaviour of long fiber sic/ti composite materials. *Comput. Meth. Appl. Mech. Engrg*, 183:309–330, 2000.
- [35] M.E. Fine and R.O. Ritchie. *Fatigue and Microstructure*. American Society for Metals, Metals Park, OH, 1979.
- [36] N. A. Fleck, K. J. Kang, and M. F. Ashby. The cyclic properties of engineering materials. *Acta Metall. Mater.*, 42:365–381, 1994.
- [37] S. Ghosh, M. Anahid, and P. Chakraborty. Modeling fatigue crack nucleation using crystal plasticity finite element simulations and multi-time scaling. In S. Ghosh and D. Dimiduk, editors, *Computational Methods for Microstructure-Property Relationships*, pages 497–554. Springer, New York, Dordrecht, Heidelberg, London, 2010.
- [38] S. Ghosh, J. Bai, and D. Paquet. Homogenization-based continuum plasticity-damage model for ductile failure of materials containing heterogeneities. *Jour. Mech. Physics Solids*, 57:1017–1044, 2009.
- [39] S. Ghosh, Y. Bhandari, and M. Groeber. Cad-based reconstructed 3D polycrystalline alloy microstructures from fib generated serial sections. *Comp. Aided Des.*, 40:293–310, 2008.
- [40] S. Ghosh, Y. Bhandari, and M. Groeber. CAD based reconstruction of three dimensional polycrystalline microstructures from FIB generated serial sections. *Jour. Comp. Aid. Des.*, 40(3):293–310, 2008.
- [41] S. Ghosh and N. Kikuchi. An arbitrary LagrangianEulerian finite element method for large deformation analysis of elastic-viscoplastic solids. *Comput. Methods Appl. Mech. Eng.*, 86:127–188, 1991.

- [42] S. Ghosh, K. Lee, and P. Raghavan. A multi-level computational model for multi-scale damage analysis in composite and porous materials. *Int. Jour. Solids Struct.*, 38:2335–2385, 2001.
- [43] C. H. Goh, R. W. Neu, and D. L. McDowell. Crystallographic plasticity in fretting of ti-6al-4v. *Int. Jour. Plast.*, 19:1627–1650, 2003.
- [44] C. H. Goh, J. M. Wallace, R. W. Neu, and D. L. McDowell. Polycrystal plasticity simulations of fretting fatigue. *Int. J. Fatigue*, 23:5423–5435, 2001.
- [45] C.H. Goh, D.L. McDowell, and R.W. Neu. Plasticity in polycrystalline fretting fatigue contacts. *Jour. Mech. Physics Solids*, 54:340–367, 2006.
- [46] C.H. Goh, R.W. Neu, and D.L. McDowell. Crystallographic plasticity in fretting of ti-6al-4v. *Int. Jour. Plasticity*, 19:1627–1650, 2003.
- [47] M. Groeber, S. Ghosh, M. D. Uchic, and D. M. Dimiduk. A framework for automated analysis and representation of 3D polycrystalline microstructures, part 1: statistical characterization. *Acta. Mater.*, 56(6):1257–1273, 2008.
- [48] M. Groeber, S. Ghosh, M. D. Uchic, and D. M. Dimiduk. A framework for automated analysis and representation of 3D polycrystalline microstructures, part 2: synthetic structure generation. *Acta. Mater.*, 56(6):1274–1287, 2008.
- [49] M. Groeber, S. Ghosh, M. D. Uchic, and D. M. Dimiduk. A framework for automated analysis and simulation of 3d polycrystalline microstructures. Part 1: Statistical characterization. *Acta. Mat.*, 56:1257–1273, 2008.
- [50] M. Groeber, S. Ghosh, M. D. Uchic, and D. M. Dimiduk. A framework for automated analysis and simulation of 3d polycrystalline microstructures. Part 2: Synthetic structure generation. *Acta. Mat.*, 56:1274–1287, 2008.
- [51] T. M. Hashimoto and M. S. Pereira. Fatigue life studies in carbon dual-phase steels. *Int. Jour. Fatigue*, 18(8):529–533, 1996.
- [52] V. Hasija, S. Ghosh, M. J. Mills, and D. S. Joseph. Modeling deformation and creep in Ti-6Al alloys with experimental validation. *Acta Mater.*, 51:4533–4549, 2003.
- [53] V. Hasija, S. Ghosh, M. J. Mills, and D. S. Joseph. Modeling deformation and creep in Ti-6Al alloys with experimental validation. *Acta Mater.*, 51:4533–4549, 2003.
- [54] A. Heinz and P. Neumann. Crack initiation during high cycle fatigue of an austenitic steel. *Acta Metallurgica et Materialia*, 38(10):1933–1940, 1990.
- [55] R. Hill. A theory of the yielding and plastic flow of anisotropic metals. *Proc. R. Soc. London, Ser. A*, 193:281–297, 1948.
- [56] W. F. Hosford. Texture strengthening. *Met. Eng. Q.*, 6:13–19, 1966.
- [57] M. A. Imam and C. M. Gilmore. Room temperature creep of Ti-6Al-4V. *Metall. Trans. A.*, 10A:419–425, 1979.
- [58] J. R. Jain and S. Ghosh. A 3d continuum damage mechanics model from micromechanical analysis of fiber reinforced composites with interfacial damage. *ASME Jour. Appl. Mech.*, 75(3):031011–1–031011–15, 2008.
- [59] D. S. Joseph, P. Chakraborty, and S. Ghosh. Wavelet transformation based multi-time scaling for crystal plasticity FE simulations under cyclic loading. *Comp. Meth. App. Mech. Engg.*, 199:2177–2194, 2010.
- [60] S. R. Kalidindi, C. A. Bronkhorst, and L. Anand. Crystallographic texture evolution in bulk deformation processing of fcc metals. *Jour. Mech. Phys. Solids*, 40:537–569, 1992.
- [61] A. S. Khan, R. Kazmi, and B. Farrokh. Multiaxial and non-proportional loading responses, anisotropy and modeling of Ti-6Al-4V titanium alloy over wide ranges of strain rates and temperatures. *Int. Jour. Plast.*, 23(6):931–950, 2007.
- [62] A. S. Khan, Y. S. Suh, and R. Kazmi. Quasi-static and dynamic loading responses and constitutive modeling of titanium alloys. *Int. Jour. Plast.*, 20(12):2233–2248, 2004.
- [63] W.H. Kim and C. Laird. Crack nucleation and stage i propagation in high strain fatigue i. microscopy and interferometric observations. *Acta Metallurgica*, 26(5):777–787, 1978.

- [64] W.H. Kim and C. Laird. Crack nucleation and stage i propagation in high strain fatigue-ii. mechanism. *Acta Metallurgica*, 26(5):789–799, 1978.
- [65] K. Kirane and S. Ghosh. A cold dwell fatigue crack nucleation criterion for polycrystalline Ti-6242 using grain-level crystal plasticity FE model. *Inter. Jour. Fatigue*, 30:2127–2139, 2008.
- [66] K. Kirane, S. Ghosh, M. Groeber, and A. Bhattacharjee. Crystal plasticity finite element based grain level crack nucleation criterion for Ti-6242 alloys under dwell loading. *Jour. Engng. Mater. Tech. ASME*, 131:27–37, 2009.
- [67] V. Kouznetsova, W. Brekelmans, and F. Baaijens. An approach to micro-macro modeling of heterogeneous materials. *Comput. Mech.*, 27:37–48, 2001.
- [68] C. M. Laird. The fatigue limit of metals. *Mater. Sci. Engng.*, 22:231–236, 1976.
- [69] L.C. Lim. Surface intergranular cracking in large strain fatigue. *Acta Metallurgica*, 35(7):1653–1662, 1987.
- [70] M.R. Lin, M.E. Fine, and T. Mura. Fatigue crack initiation on slip bands: Theory and experiment. *Acta Metallurgica*, 34(4):619–628, 1986.
- [71] G. Lutjering and J. C. Williams. *Titanium*. Springer-Verlag, Berlin-Heidelberg, 2007.
- [72] S. Manchiraju, M. Asai, and S. Ghosh. A dual time scale finite element model for simulating cyclic deformation of polycrystalline alloys. *J. Strain Anal. Engg. Des.*, 42:183–200, 2007.
- [73] D. McDowell and F. P. E. Dunne. Microstructure-sensitive computational modeling of fatigue crack formation. *Int. J. Fatigue*, 32:1521–1542, 2010.
- [74] D.L. McDowell and F.P.E. Dunne. Microstructure-sensitive computational modeling of fatigue crack formation. *Int. Jour. Fatigue*, 32:1521–1542, 2010.
- [75] R. M. Miller, T. R. Bieler, and S. L. Semiatin. Flow softening during hot working of Ti-6Al-4V with a lamellar colony microstructure. *Scripta Mater.*, 40(12):1387–1393, 1999.
- [76] M. Mineur, P. Villechaise, and J. Mendez. Influence of the crystalline texture on the fatigue behavior of a 316L austenitic stainless steel. *Mater. Sci. Engng.*, A286:257–268, 2000.
- [77] R. Morrissey, C. H. Goh, and D. L. McDowell. Microstructure-scale modeling of hcf deformation. *Mech. Mater.*, 35:295–311, 2003.
- [78] R. Morrissey, C.H. Goh, and D.L. McDowell. Microstructure-scale modeling of hcf deformation. *Mech. Mater.*, 35:295–311, 2003.
- [79] R. J. Morrissey, D. L. McDowell, and T. Nicholas. Microplasticity in HCF of Ti-6Al-4V. *Int. J. Fatigue*, 23:S55–S64, 2001.
- [80] T. Neeraj, D. H. Hou, G. S. Daehn, and M. J. Mills. Phenomenological and microstructural analysis of room temperature creep in Titanium alloys. *Acta Mater.*, 48:1225–1238, 2000.
- [81] J. F. Nye. Some geometrical relations in dislocated crystals. *Acta Metall.*, 1:153–162, 1953.
- [82] G. B. Olson. Computational design of hierarchically structured materials. *Science*, 277:1237–1242, 1997.
- [83] C. Oskay and J. Fish. Fatigue life prediction using 2-scale temporal asymptotic homogenization. *Int. J. Num. Methods Engg.*, 61:329–359, 2004.
- [84] C. Oskay and J. Fish. Multiscale modeling of fatigue for ductile materials. *Int. J. Multiscale. Comput. Engg.*, 2:1–25, 2004.
- [85] P. C. Paris. *The fracture mechanics approach to fatigue, fatigue an interdisciplinary approach*. Syracuse University Press, Syracuse, 1964.
- [86] H. Parvatareddy and D. A. Dillard. Effect of mode-mixity on the fracture toughness of Ti-6Al-4V/FM-5 adhesive joints. *Int. Jour. Fracture*, 96:215–228, 1999.

- [87] P. Perzyna. Fundamental problems in viscoplasticity. *Adv. Appl. Mech.*, 9:243–377, 1966.
- [88] N. J. Petch. In B. L. Averbach, D. K. Felbeck, G. T. Hahn, and D. A. Thomas, editors, *Fracture*, page 54. John Wiley, New York, 1959.
- [89] D. Raabe and F. Roters. Using texture components in crystal plasticity finite element simulations. *Int. Jour. Plast.*, 20:339–361, 2004.
- [90] D. Raabe, Z. Zhao, and F. Roters. Study on the orientational stability of cube-oriented fcc crystals under plane strain by use of a texture component crystal plasticity finite element method. *Scripta Mater.*, 50:1085–1090, 2004.
- [91] J. R. Rice. A path independent integral and the approximate analysis of strain concentration by notches and cracks. *Jour. Appl. Mech.*, 35:379–386, 1968.
- [92] J.R. Rice and D.M. Tracey. On the ductile enlargement of voids in triaxial stress fields. *Journal of the Mechanics and Physics of Solids*, 17(3):201–217, 1969.
- [93] S. Rokhlin, J. Y. Kim, and B. Zoofan. *unpublished research*, The Ohio State University, 2005.
- [94] S. Rokhlin, J. Y. Kim, and B. Zoofan. *unpublished research*. The Ohio State University, Columbus, OH, 2005.
- [95] G. Ruiz, A. Pandolfi, and M. Ortiz. Three-dimensional cohesive modeling of dynamic mixed mode fracture. *Int. Jour. Numer. Meth. Engng.*, 52:97–120, 2001.
- [96] E.E. Sackett, L. Germain, and M.R. Bache. Crystal plasticity, fatigue crack initiation and fatigue performance of advanced titanium alloys. *Int. J. Fatigue*, 29:2015–2021, 2007.
- [97] S. L. Semiatin, F. Montheillet, G. Shen, and J. J. Jonas. Self-consistent modeling of the flow behavior of wrought alpha/beta titanium alloys under isothermal and nonisothermal hot-working conditions. *Metall. Trans. A.*, 33(8):2719–2727, 2002.
- [98] S. Sinha and S. Ghosh. Modeling cyclic ratcheting based fatigue life of hsla steels using crystal plasticity fem simulations and experiments. *Int. Jour. Fatigue*, 28:1690–1704, 2006.
- [99] V. Sinha, M. J. Mills, and J. C. Williams. Understanding the contributions of normal-fatigue and static loading to the dwell fatigue in a near-alpha titanium alloy. *Metall. Mat. Trans. A*, 35:3141–3148, 2004.
- [100] V. Sinha, M. J. Mills, and J. C. Williams. Crystallography of fracture facets in a near alpha titanium alloy. *Metall. Trans. A.*, 37 A:2015–2026, 2006.
- [101] V. Sinha, M. J. Mills, and J. C. Williams. Crystallography of fracture facets in a near-alpha titanium alloy. *Metall. Mat. Trans. A*, 37:2015–2026, 2006.
- [102] V. Sinha, J. E. Spowart, M. J. Mills, and J. C. Williams. Observations on the faceted initiation site in dwell-fatigue tested Ti-6242 alloy: Crystallographic orientation and size effects. *Metall. Mat. Trans. A*, 37:1507–1518, 2006.
- [103] V. Sinha, J. E. Spowart, M. J. Mills, and J. C. Williams. Observations on the faceted initiation site in the dwell-fatigue tested Ti-6242 alloy: Crystallographic orientation and size effects. *Metall. Trans. A.*, 37 A:1507–1518, 2006.
- [104] E. Smith. The formation of a cleavage crack in a crystalline solid-I. *Acta Metal.*, 14:985–989, 1966.
- [105] E. Smith. Dislocations and cracks. In F. R. N. Nabarro, editor, *Dislocations in Solids*, volume 4, pages 363–449. North Holland Amsterdam, The Netherlands, 1979.
- [106] G. Strang and T. Nguyen. *Wavelets and filter banks*. Wellesley College, 1996.
- [107] A. N. Stroh. The formation of cracks as a result of plastic flow. *Proc. R. Soc. London, Ser. A*, 223:404–414, 1954.
- [108] A. N. Stroh. The formation of cracks as a result of plastic flow. *Proc. R. Soc. London, Ser. A.*, 223:404–414, 1954.
- [109] S. Suresh. *Fatigue of Materials*. Cambridge University Press, Cambridge, 1998.
- [110] K. Terada and N. Kikuchi. A class of general algorithm for multi-scale analysis of heterogeneous media. *Comput. Meth. Appl. Mech. Engrg*, 190:5427–5464, 2001.

- [111] J. J. Thomsen. *Vibrations and stability: theory, analysis and tools*. Springer-Verlag, Berlin, second edition, 2004.
- [112] C. N. Tome, P. J. Maudlin, R. A. Lebensohn, and G. C. Kaschner. Mechanical response of zirconium-i. derivation of a polycrystal constitutive law and finite element analysis. *Acta Mater.*, 49:3085–3096, 2001.
- [113] H. S. Turkmen, R. E. Loge, P. R. Dawson, and M. Miller. On the mechanical behavior of aa 7075-t6 during cyclic loading. *Int. J. Fatigue*, 25:267–281, 2003.
- [114] H.S. Turkmen, R.E. Loge, P.R. Dawson, and M. Miller. On the mechanical behavior of aa 7075-t6 during cyclic loading. *Int. J. Fatigue*, 25:267–281, 2003.
- [115] G. Venkataramani, S. Ghosh, and M. J. Mills. A size dependent crystal plasticity finite element model for creep and load-shedding in polycrystalline Titanium alloys. *Acta Mater.*, 55:3971–3986, 2007.
- [116] G. Venkataramani, K. Kirane, and S. Ghosh. Microstructural parameters affecting creep induced load shedding in Ti-6242 by a size dependent crystal plasticity FE model. *Int. Jour. Plas.*, 24:428–454, 2008.
- [117] G. Venkatramani, D. Deka, and S. Ghosh. Crystal plasticity based FE model for understanding microstructural effects on creep and dwell fatigue in Ti-6242. *ASME Jour. Engng. Mater. Tech.*, 128(3):356–365, 2006.
- [118] G. Venkatramani, D. Deka, and S. Ghosh. Crystal plasticity based fe model for understanding microstructural effects on creep and dwell fatigue in Ti-6242. *ASME J. Engg. Mater. Tech.*, 128(3):356–365, 2006.
- [119] G. Venkatramani, S. Ghosh, and M. J. Mills. A size dependent crystal plasticity finite element model for creep and load-shedding in polycrystalline Titanium alloys. *Acta Mater.*, 55:3971–3986, 2007.
- [120] J.S. Walker. *A primer on wavelets and their scientific applications*. CRC Press, 1999.
- [121] J. C. Williams. The evaluation of cold dwell fatigue in Ti-6242. FAA report summary, The Ohio State University, 2006.
- [122] X. Wu, S. R. Kalidindi, C. Necker, and A. Salum. Prediction of crystallographic texture evolution and anisotropic stress-strain curves during large plastic strains in high purity α titanium using a taylor-type crystal plasticity model. *Acta Mater.*, 55:423–432, 2007.
- [123] C.L. Xie, S. Ghosh, and M. Groeber. Modeling cyclic deformation of hsla steels using crystal plasticity. *ASME Jour. Engng. Mater. Tech.*, 126:339–352, 2004.
- [124] Y. Yao, M.E. Fine, and L.M. Keer. An energy approach to predict fatigue crack propagation in metals and alloys. *International J. of Fracture*, 146:149158, 2007.
- [125] Q. Yu and J. Fish. Temporal homogenization of viscoelastic and viscoplastic solids subjected to locally periodic loading. *Comput. Mech.*, 29:199–211, 2002.
- [126] Z.F. Zhang and Z.G. Wang. Dependence of intergranular fatigue cracking on the interactions of persistent slip bands with grain boundaries. *Acta Materialia*, 51(2):347–364, 2003.

Appendix B

Task 2: Multi-Scale Sensing & Evaluation Framework for Fatigue Life Prediction

Abstract

This appendix reports a detailed description of the second task of the project. In this task a comprehensive experimental methodology and inverse models are developed for structural health monitoring and noninvasive assessment of fatigue sensitive microstructures in Ti alloys. The aim is to provide realistic data input for computational predictive models under development in this project. *First* we describe the method for ultrasonically-monitored initiation and evolution of fatigue cracks in forged titanium alloy samples during fatigue testing. An in-situ surface wave acoustic method is applied during fatigue with an overlaid small low-frequency periodic loading, resulting in nonlinear modulation of the reflected ultrasonic pulses. The material is characterised by strong microstructure-induced ultrasonic scattering. To improve the signal-to-noise ratio a post-processing subtraction technique is introduced to enhance initiated crack detectability. The method is suitable for identification of small initiated and gradually-evolving fatigue crack features and is suitable for integration of microstructure-based fatigue life prognosis and multi-scale sensing. *Second* we describe a novel approach for ultrasonic imaging of damage precursors as anomalous plastic microstrain: ultrasonic microtexture backscattering as strain markers. It aims to detect anomalous local strain increase as fatigue crack precursors. The preliminary experimental data from fatigue experiments performed in this work on titanium samples have demonstrated and highlighted the precursors of crack initiation. The strain and the change in ultrasonic signals are linked dynamically as synchronized elasto-plastic strain variation due to fatigue loading. *Finally*, we describe experimental methodology and inverse models for ultrasonic volumetric assessment of fatigue sensitive microstructures in Ti alloys which are characterized by the presence of large microtextured regions (MTRs). A general model for elongated duplex microstructures is proposed for modeling scattering-induced ultrasonic longitudinal attenuation and backscattering in hexagonal polycrystals for application to titanium alloys. The material system consists of microtextured regions (MTRs) which are formed by much smaller α crystallites with preferred orientations. Their preferred orientation is represented by a modified Gaussian orientation distribution function. Scattering induced by MTRs and by crystallites is added to obtain ultrasonic attenuation in the medium. The effective elastic properties of MTRs are determined and used to obtain the scattering-induced MTR attenuation and backscattering. Crystallite attenuation is estimated by the untextured attenuation coefficient factored by a texture transition function. The total attenuation and backscattering are obtained by combining solutions for microtextured region attenuation and crystallite attenuation. Spectroscopic attenuation and backscattering measurements are performed on forged samples of titanium alloy. Reasonable agreement is found between experiment and the model predictions with a given texture parameter.

Chapter 1

Relevant Information

1.1 Personnel Supported

1. Stanislav Rokhlin, PI
2. Jia Li, Ph.D. Student, Graduate Research Associate, partially supported
3. G. D. Connolly, Post-Doctoral Researcher, partially supported; Now at Electric Power Research Institute (EPRI), Charlotte NC
4. L. Yang, Post-Doctoral Researcher, partially supported

1.2 Refereed Journal Publications

1. G. D. Connolly, J. Li and S. I. Rokhlin “Fatigue crack monitoring in titanium alloy by dynamic subtraction of modulated surface acoustic wave” NDT&E International (submitted)
2. Yang and S. I. Rokhlin “Ultrasonic scattering in polycrystals with ellipsoidal orientation clusters of orthorhombic crystallites” Wave Motion (submitted).
3. L. Yang and S. I. Rokhlin “Ultrasonic backscattering in cubic polycrystals with ellipsoidal grains and texture” J. Nondestruct. Eval. (submitted)
4. L. Yang, O. I. Lobkis and S. I. Rokhlin “Shape effect of elongated grains on ultrasonic attenuation in polycrystalline materials” Ultrasonics 51(6) 697-708 (2011)
5. O.I. Lobkis, L. Yang, J. Li and S. I. Rokhlin “Ultrasonic backscattering in polycrystals with elongated single phase and duplex microstructures” Ultrasonics 52(6), 694-705 (2012)
6. L. Yang, O. I. Lobkis and S. I. Rokhlin “Integrated model for ultrasonic wave propagation and scattering in polycrystalline medium with elongated hexagonal grains” Wave Motion 49(5), 544-560 (2012)
7. G. D. Connolly and S. I. Rokhlin “Enhancement of fatigue crack monitoring by surface acoustic wave reflection and modulation in a space-cycle-load domain: an imaging approach” Struct. Health Monit. 11 (2), 187-196 (2012)
8. L. Yang, J. Li, O.I. Lobkis, and S.I. Rokhlin “Ultrasonic propagation and scattering in duplex microstructures with application to titanium alloys” J. Nondestruct. Eval. 31(3), 270-283 (2012)
9. L. Yang, O. I. Lobkis and S. I. Rokhlin “Shape effect of elongated grains on ultrasonic attenuation in polycrystalline materials” Ultrasonics 51(6) 697-708 (2011)

10. O. I. Lobkis and S.I. Rokhlin “Characterization of polycrystals with elongated duplex microstructure by inversion of ultrasonic backscattering data” Appl. Phys. Lett. 96 (16) Arti.161905-1-3 (2010)

1.3 Proceedings Publications

1. G. D. Connolly and S. I. Rokhlin “Quantitative Enhancement of Fatigue Crack Monitoring by Imaging Surface Acoustic Wave Reflection in a Space-Cycle-Stress Domain” Review of Progress in Quantitative NDE, Thompson, D. O. and Chimenti, D. E. eds., American Institute of Physics, New York, AIP Conf. Proc. 1335, pp. 1499-1506, (2011)
2. O. I. Lobkis, L. Yang, J. Li, and S. I. Rokhlin “Directional Ultrasonic Backscattering in Polycrystals with Elongated Grains” Review of Progress in QNDE Vol 31, Thompson, D. O. and Chimenti, D. E. eds., American Institute of Physics 1430, pp. 1389-1396;, New York, AIP Conf. Proc. doi.org/10.1063/1.4716380, (2012)
3. J. Li , O. I. Lobkis, L. Yang and S. I. Rokhlin “Integrated Method of Ultrasonic Attenuation and Backscattering for Characterization of microstructures in Polycrystals” Review of Progress in QNDE, Thompson, D. O. and Chimenti, D. E. eds., American Institute of Physics, New York, AIP Conf. Proc. 1430, pp. 1397-1404, doi.org/10.1063/1.4716380, (2012)

1.4 Invited Lectures at Conferences

S.I Rokhlin, J.Li, O.I Lobkis, L. Yang and A.L Pilchak “Characterization of Elongated Microtextures in Ti Alloys by Ultrasonic Backscattering” 2012 TMS Annual Meeting & Exhibition, Orlando, FL, March ,2012 (Invited)

Chapter 2

Introduction

In this task the PI (S. I. Rokhlin) and his coworkers have developed a comprehensive experimental methodology and inverse models for structural health monitoring and noninvasive assessment of fatigue sensitive microstructures in Ti alloys. The aim is to provide realistic data input for computational predictive models under development in this project.

The research performed is summarized below and detailed in Chapters 3-5.

2.1 Dynamic Load-Lock-In Processing for Visualisation of Small Fatigue Crack Initiation and Evolution

For practical application of robust fatigue analysis and structural health monitoring (SHM) methods leading to life prediction of aerospace materials and structures it is important to develop nondestructive capabilities in multi-scale sensing of damage evolution. A novel structural health monitoring (SHM) methodology is developed in this project, which utilize nonlinear-structural-load-modulated guided ultrasonic waves for real-time monitoring of damage initiation and evolution. The dynamic load-induced change of the crack opening/closure state modulates the sensor signature.

The difficulty of small crack detection and localization in Ti alloys is due to the presence of strong backscattering noise in titanium alloys as has been described in earlier studies. In contrast to the previous work, the principal thrust of this study is tackling the difficulty in extracting meaningful information from the noise. This was achieved with the use of a novel subtraction technique applied to ultrasonic backscattering signatures that is dynamically synchronized with the applied cyclic load. Also, application of the dynamic subtraction method to data acquired during the modulation regime has resulted in a significant increase in crack SNR, improving crack detection and localization. It was shown to be effective in identifying just-formed fatigue cracks and as such, is particularly suited to online SHM for real-time monitoring.

The developed method for continuous ultrasonic monitoring of fatigue crack initiation, evolution and localization uses a novel multidimensional image representation of the large amounts of data collected in our methodology during fatigue testing. Image representation allows an extrapolation of identified patterns which is useful for distinguishing the crack from noise even at low signal-to-noise ratios. It has been shown that different cross-sections of the data representation provide continuous image patterns that facilitate the identification of reflected signals from the initiated damage. Measurement of the time differences between certain reflected signals can be used to quantify the evolution of the crack. Time domain subtraction at the same load level has been applied to improve the signal-to-noise ratio. Such a visualisation approach allows greater understanding of crack initiation and evolution. Dynamic time domain subtraction results in 20 times signal-to-noise ratio improvement.

In addition to the linear monitoring method the imaging modulation method has been developed and has been shown to allow earlier detection of the crack at early stages of the fatigue experiment, which is particularly relevant in health monitoring applications. This was achieved using a time domain subtraction method in conjunction with the modulation method, yielding great potential for improvements in early crack detection.

2.2 Imaging of Damage Precursors as Anomalous Plastic-Microstrain: Ultrasonic Microtexture Backscattering as Strain Markers

Standard NDT or health monitoring techniques are able to detect fatigue cracks only in the latest stages of fatigue life of engine grade Ti alloys. The challenge of nondestructive detection of fatigue crack initiation, or more accurately small fatigue cracks, is addressed in item 2.1. An even more difficult problem, the solution of which is not available, is determination of fatigue damage precursors: i.e. such micro-regions of the sample where the initiation of a fatigue crack will occur with the highest probability. In this work we propose a method for dwell and cyclic fatigue damage precursor visualisation based on backscatter signal (noise) variation with the applied fatigue load. We will illustrate this idea by preliminary experimental data, demonstrating such precursors appearing before and in the vicinity of the initiated fatigue crack in the titanium alloy sample studied.

To achieve the objective and the realization of the method to identify the damage precursors this work focused on the relative increase of plastic microstrains and thus dislocation build-up.

Recent research has shown that one main reason for early failure under dwell fatigue conditions in Ti alloys was the presence of large micro-textured regions (MTRs). In particular, it was shown that the crystallographic orientation and size of the MTRs are associated with facet-initiation sites of fatigue cracks. Physically, the MTRs are formed as regions of hexagonal α -phase crystallites with a common crystallographic orientation such that the combined MTR size noticeably outstrips the size of the primary α grains. Those MTRs can be considered as large grains with effective elastic properties that produce significant quantifiable ultrasonic scatter. It was observed in this study that the scattering noise is significantly affected by fatigue loading not only for the results shown, but for a number of our earlier fatigue experiments for this alloy (those earlier digital ultrasonic data, that were analyzed in this study, were collected in our earlier fatigue experiments on Ti6242). The scattering amplitude variation is not systematic from sample to sample but the time stretching of the scattering signal is very consistent.

From our perspective, large local plastic deformations occur and accumulate prior to crack initiation. This local elasto-plastic strain variation is synchronized and associated with fatigue load, leading to excessive grain size stretching and local variations of the ultrasonic scattering. At the frequencies studied, the random ultrasonic scattering signal is a result of interference of the scattering from grain boundaries of different grains. Large microplastic deformation changes this scatter interference and results in stretching of the backscatter signal in this microregion.

A peak-tracking (and, equally, trough-tracking) algorithm of ultrasonic backscattering noise evolution during fatigue cycling has been developed. It was applied to the shifts in the backscatter time signals in the data generated from fatigue experiments. This allows the measurement of the absolute time, and therefore of the time shift, of every backscatter signal peak and trough during the applied fatigue load cycles. The most important point from our objective is the observation of persistent high local strain at early stages of the experiment at the future crack location. This is an indication of excessive plastic strain in that part of the grain structure, increasing susceptibility to crack formation under cyclic loading.

2.3 Experimental Methodology and Inverse Models for Ultrasonic Volumetric Assessment of Fatigue Sensitive Microstructure

Recent research in cyclic and dwell fatigue behavior of engine grade near-alpha titanium alloys have demonstrated that one of the main reasons for early fatigue damage initiation is the presence of large microtextured regions (MTRs) in these alloys. In general, MTRs (also known as macrozones) are formed as orientation clusters of a large number of small alpha crystallites with a common crystallographic

orientation. Due to the detrimental effect of such microtextures on the dwell and cyclic fatigue properties it is highly desirable to determine the possible microtexture existence in manufactured parts and to characterize them nondestructively. Ultrasonic characterization using wave attenuation and backscattering may provide nondestructive methods to determine the presence of fatigue sensitive microtexture and its morphology.

We have developed ultrasonic backscattering and attenuation models for scattering in Ti alloys to understand the relationship between ultrasonic scattering and the elongated microtextured microstructures. The microtexture is characterized by two size scales. The larger phase r is composed of elongated microtextured regions (MTRs) which by themselves are formed by smaller size hexagonal primary α crystallites (small phase α) with their preferred common orientation in the MTRs. The preferred orientation is not necessarily along the elongation direction of the MTRs. The model assumes that the directions of preferred orientation of crystallites in different MTRs are not correlated and their distribution is homogeneous; i.e. the medium is macroscopically isotropic (untextured). The material model explicitly describes the orientation distribution function of crystallites in MTRs with use of a modified Gaussian orientation distribution function. The ensemble elastic properties in MTRs are characterized by the effective stiffness using an average over the MTR region of the elastic properties of hexagonal crystallites with the specified orientation distribution function. The total attenuation and backscattering are considered as a sum of scattering by MTRs with effective elastic properties and additional scattering due to crystallites.

The experimental theoretical framework was developed to assess microstructural material characteristics using ultrasonic backscattering and for grading the size of microtexture from ultrasonic measurements. This was accomplished by developing an inverse experimental methodology for data processing usable by the inverse model developed in this research. Ultrasonic attenuation and backscattering measurements on the forged Ti-6242 alloy samples were conducted and microtexture characteristics were obtained with the developed models.

Inverse experimental methodologies have been developed that have been applied together with our inverse models to assess microstructural material characteristics using ultrasonic backscattering and attenuation. We have determined that our effective model of the elastic properties and texture of the MTRs provides a consistent simulation framework to predict two independently measured ultrasonic characteristics of the same sample: attenuation and backscattering. We also have evaluated a sensitivity to microtexture parameters in the inversion model and have demonstrated the method's applicability for unique recovery of microtexture properties. Reasonable agreement was found between the experiment and the model predictions and direct comparison with orientation image microscopy (OIM) measurements of microtexture on the same samples.

2.4 Organization of Appendix B

The details of Task 2 activities are described in this Appendix. It is divided into three subsequent chapters. In chapter 3, the developed methodology for dynamic load-lock-in processing for visualisation of small fatigue crack initiation and evolution is described. Imaging of damage precursors based on ultrasonic microtexture backscattering is given in Chapter 4. Experimental methodology and inverse models for ultrasonic volumetric assessment of fatigue sensitive microstructure of Ti Alloys are provided in Chapter 5.

Chapter 3

Fatigue Crack Monitoring in Engine-Grade Titanium Alloy by Dynamic Subtraction of Surface Acoustic Wave Modulation

3.1 Introduction

Surface acoustic waves have been demonstrated to be a particularly useful for the purposes of monitoring small fatigue crack initiation and evolution [3.1-3.3]. The nature of the fatigue-induced crack closure has been investigated by measuring ultrasonic reflectivity in-situ during fatigue by quasi-static [3.4] and modulation (dynamic) [3.5] techniques. It was demonstrated that applying low frequency thermal [3.6] or mechanical [3.5] modulation that periodically changes crack closure may significantly enhance earlier detection of fatigue cracks. Nonlinear methods are used [3.7, 3.8] because interaction of surfaces of partially closed crack generate significantly larger nonlinearity than that of bulk solid. In the modulation method an externally-applied modulating load is used as the ultrasonic data are collected in order to closely monitor the crack-closure behaviour [3.5], a process that can also be potentially useful for the monitoring of general nonlinear scatterers [3.9], given that crack closure has strong effects on modulation [3.3]. On a similar note, a study of ultrasonic nonlinear effects due to fatigue-induced dislocation density variations [3.10] has demonstrated the possibility of the identification of earlier fatigue damage precursors by such nonlinear ultrasonic measurements.

The work presented in this chapter builds upon the authors' previous study, which concentrated on the initiation and evolution of fatigue cracks initiated from surface damage in samples composed of an aluminium alloy [3.11]. It was proposed in that study that multidimensional image representation of experimental fatigue data, collected in the form of ultrasonic time signals, could aid characterization of early fatigue crack initiation and evolution. These dimensions are:

1. the number of fatigue cycles to which the specimen has been exposed;
2. the level of load in the cycle applied to the specimen; and
3. the time of flight.

The key objectives of this chapter are twofold: firstly, to demonstrate the application of this multidimensional image methodology to ultrasonic data acquired from fatigue testing of a different material (titanium alloy), where the background structural noise is of a magnitude comparable to those of the useful reflected ultrasonic signals; and secondly, to propose and discuss the possibility of a microscopic plastic grain level strain assessment, based upon the grain scattering of the material; an idea that could be used to identify anomalously high local plastic strain leading to crack initiation, i.e, to identify the fatigue damage precursors.

The difficulty of small crack detection and localization due to backscattering noise in titanium alloys has been described in our earlier work [3.12]. In contrast to the previous work, the principal thrust of this study is tackling the difficulty in extracting meaningful information from the noise. Also, no initial surface

damage (stress raiser) was induced on the sample surface and thus the location of crack initiation is not predetermined as was the case in our preliminary work [3.11].

Using multidimensional visualisation, the authors will demonstrate a time-domain subtraction method to improve the signal-to-noise ratio to vastly improve the early detection of just-formed fatigue cracks, which is a promising structural health monitoring application. A great deal of work has already been performed on the application of time-domain subtraction to structural health monitoring and guided waves [3.13] with interest across a swathe of disciplines from the aerospace industry [3.14] to civil engineering [3.15].

This chapter describes a novel subtraction method that is uniquely synchronised with the fatigue cycling and the modulation loads, and performed at specifically pre-determined levels of loading bias. This is required for optimum accuracy of computation due to the dynamically-changing signal at different static bias loading levels as the experiment progresses. In such implementation the modulation method presented is also potentially able to be applied in real-time online structural health monitoring.

The next section explains the experimental procedure and how the data were collected. Section 3 will explore the application of the quasi-static results to monitor the crack. The modulation method and results are presented and discussed in section 4, and section 5, explores the possibility of fatigue damage precursor visualisation based on the fatigue load induced backscatter noise change.

3.2 Experiment

3.2.1 Samples

In this chapter, the fatigue samples used were prepared from a large forging of the titanium alloy Ti-6Al-2Sn-4Zr-2Mo-0.2%Si (referred to hereafter as Ti-6242) in the shape of flat dog-bone specimens of thickness 1.905mm. This material has a yield stress of around 940MPa and an ultimate tensile strength of around 1050MPa. The specimens were machined and surface polished by Metcut Research (Cincinnati OH) to a shape slightly modified from ASTM E466-96 to increase its gauge length. The total length of the specimen is 190mm; it has a gauge width of 6.6mm and a gauge length of 12.8mm. After preparation, the specimen surfaces were polished to 812nm, except in the gauge area, where the surface finish was 203nm. The assumption is made that there is no initial defect of significance, due to the quality of preparation of the sample and since it originated from a well-characterized sample.

3.2.2 Experiment and Data Acquisition

Ultrasonic guided waves were excited in the fatigue specimen in order to collect reflectional information of the specimen structure during fatigue. A longitudinal wave transducer of centre frequency 5.0MHz and a wedge composed of polystyrene were attached to one end of the gauge length to generate surface waves for the relevant frequency-thickness product. On the opposite side of the gauge length was mounted a wedge reflector (see figure 3.1(a)) to monitor the double-through-transmitted signal through the sample gauge area. This setup is similar to that in previous experiments carried out by the authors [3.12], a study with a different aim: to size and locate internal microcracks in fatigue samples.

The specimen was loaded into an 810 Material Test System (MTS). The complete ultrasonic data acquisition setup is shown in figure 3.1(b). The software to control the applied fatigue load and to manage the acquired data was developed in-house. The ultrasonic data acquisition is performed after amplification using a 12bit, 125MHz digitising board.

The fatigue loading sequence and in-situ ultrasonic data acquisition is divided into segments, whose composition is shown in figure 3.2, to allow the recording of both modulated and non-modulated signals over the duration of the experiment. Each segment is composed of two regimes: a fatigue regime and a modulation (to distinguish it from fatigue) regime. The full range of fatigue load is applied during the fatigue regime over 25 cycles. The load was applied at a frequency of 10Hz with a range of 1.8kN to 10.9kN 1.8kN (400lb to 2450lb), such that the stress ratio was in the region of 0.15 and the stress range was around 8.9kN (2000lb). As the applied fatigue load is in progress, ultrasonic pulses are exited in the specimen at various recording points during the loading cycle. Since an ultrasonic event occurs during a very short time period and the event can be considered to be quasi-static, though in this chapter, these data are referred to as fatigue regime signals (to differentiate them from the modulation regime signals) and the regime in which they occur is referred to as the fatigue regime.

Following the fatigue regime is the modulation regime (see also figure 3.2), where a sinusoidal modulation vibration of 10Hz with an amplitude of $\pm 133\text{N}$ ($\pm 30\text{lb}$) is superimposed upon a static bias loading at various levels. Time signals are recorded at a rate of 300Hz (i.e., 30 records per cycle) for 50 cycles at each level of applied static bias load. Three static bias loading levels were used: a high level of a similar load to the maximum fatigue load; a medium load and a very low level of loading. The number of levels was kept to a minimum to avoid a dwell fatigue effect that could complicate interpretation of results [3.12]. Other experimental parameters were chosen so as to be similar to those in work previously carried out by this research group, useful for future comparison to earlier experiments should the need arise.

After acquisition, the acquired pulses were treated by a low-pass filter of cut-off frequency 5MHz. Measurements have been repeated on other samples composed of titanium and aluminium, and consistent results have been observed. In each recorded ultrasonic pulse, two reference signals were used to define the area of interest. They were (as shown in figure 3.1):

- R1 the reflection from the corner of the polystyrene transducer wedge; and
- R2 the reflection from the wedge reflector.

The subsequent sections deal with the nature of the post-processing of the data contained within the area of interest.

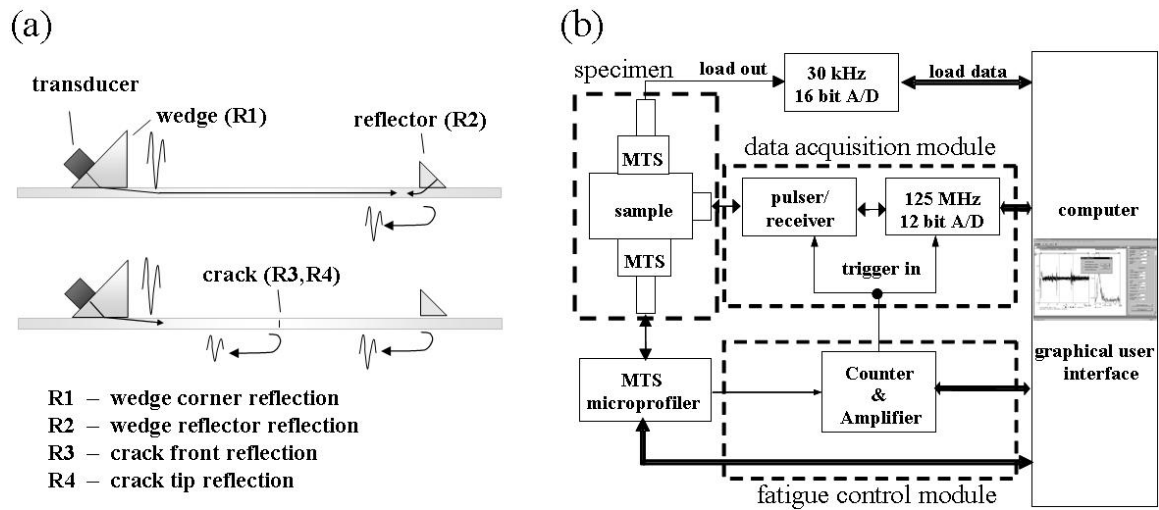


Figure 3.1: (a) Setup for in-situ ultrasonic experiment during fatigue tests and (b) schematic of data acquisition and fatigue control system.

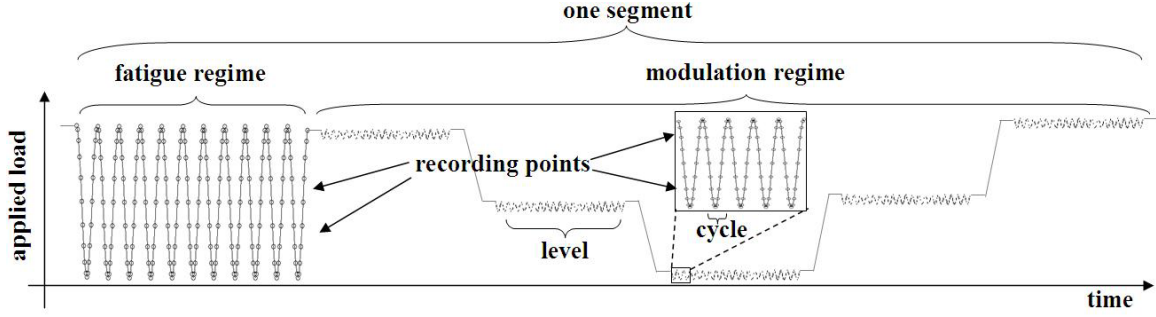


Figure 3.2: Structure of each fatigue test segment as a function of applied load versus time.

3.3 Fatigue Regime Results: Application to Crack-Sizing

3.3.1 The Subtraction Method

At the start of the experiment, it was determined that no defects are present in the specimen. In the area of interest, only the background noise is present, the strong attenuation and complex scattering a result of the elongated grain structure (with a shorter dimension in the order of $1\mu\text{m}$ and the longer dimension is $10\mu\text{m}$) of the material.

The ultrasonic time data in the fatigue regime consists of a collection of time traces that we could write as $u^f(t)$, that could be considered as a single function $u^f(L, C, t)$; the other variables being the applied fatigue load L (N), the fatigue cycle number C and with the superscript f to indicate that the data are those of the fatigue regime.

Previous work [3.11] carried out by the authors on aluminium samples took advantage of a method involving subtracting the time signal of the first cycle from all subsequent cycles in order to remove the effects of reflection from the initial surface damage (ISD), thus facilitating the process of identifying the ultrasonic reflection from a fatigue crack initiated from the ISD. This process can be expressed as

$$u_s^f(L, C, t) = u^f(L, C, t) - u^f(L, 1, t) \text{ for } C = 2, 3, \dots n_C \quad (3.1)$$

for a given fatigue load L with the total number of cycles n_C . However; in [3.11], where work was performed on aluminium, the ultrasonic microstructural noise is small. The objective of the current experiment is to identify a small ultrasonic reflection in the predominating background microstructural noise and this particular method of subtraction (1) performs relatively poorly when applied to the results acquired from samples subjected to lower fatigue loads and under variable strain due to minor translations in time of the recorded ultrasonic signals (due to minor temperature instabilities and fatigue induced plastic deformation of the sample). Though a time signal was recorded for every cycle C , this report only shows time signals for selected cycles at regular intervals for conciseness. This is due to the great quantity of data that were recorded (it also is the intention of the authors that the data will be analyzed more thoroughly and in different techniques in future work); tens of gigabytes of binary data were typical even for the shortest experiments.

In this chapter, an alternative method of time-domain subtraction is proposed, and is expressed as

$$u_{ss}^f(L, C, t) = u^f(L, C, t) - u^f(L, C-1, t) \text{ for } C = 2, 3, \dots n_C, \quad (3.2)$$

that is to say that the time signal of the previous cycle is subtracted from that of the current cycle, provided that the difference is taken between two time signals acquired at the same level of fatigue loading.

3.3.2 Discussion of Fatigue Regime Results

In this section, a qualitative analysis of the acquired fatigue results is presented. A typical reflected signal for the evolving crack is shown in figure 3.3(a). A gate is placed around the reflected crack signal. The peak amplitude of the signal increases as the crack grows due to the increasing strength of the reflection from the crack. As this happens, the strength of the reflection from the back-wedge reflector (R2 in figure 3.1(a)) diminishes accordingly.

For about three quarters of the life of the specimen, before the initiation of the crack, the peak amplitude is nonzero due to background noise. After the crack begins to form, there is a sharp increase in the peak amplitude since the open crack starts to increase the coefficient of reflection in this part of the time signal. In figure 3.3(b), the peak amplitude of the signal within the gate at cycle A_C is plotted against cycle number having been normalized against the peak amplitude within the gate at the first cycle A_1 (essentially backscattering noise), a process that can be represented by the following expression:

$$\frac{\max\{u^f(L, C, t)\}_{t=35.5\mu s}^{t=37.5\mu s}}{\max\{u^f(L, 1, t)\}_{t=35.5\mu s}^{t=37.5\mu s}} \text{ for } C = 1, 2, \dots, n_C. \quad (3.3)$$

The change in the peak amplitude is first observed at the highest fatigue load level at around 18250 cycles, then at around 18500 cycles at the medium load and finally an increase in peak amplitude is not visible at the lowest fatigue load until around 19250 cycles. The general physical interpretation is that the higher applied loads will open the crack more fully, and thus a greater area of a free surface at the crack position will reflect a greater proportion of ultrasonic energy.

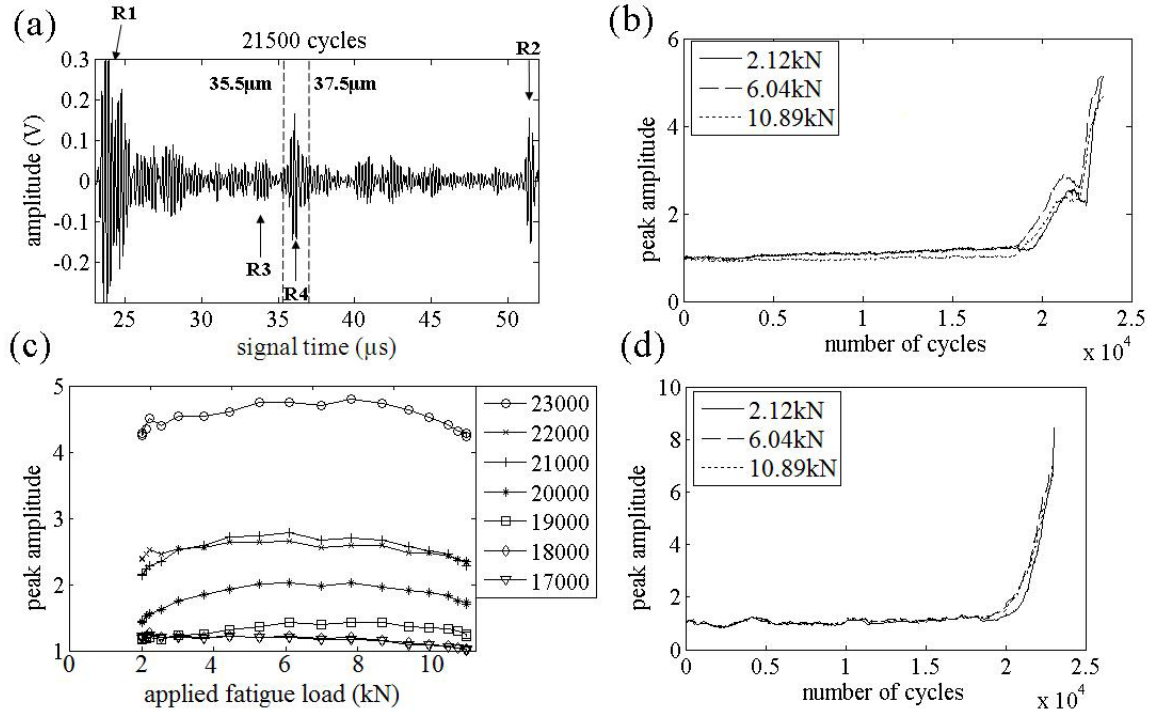


Figure 3.3: (a) A typical acquired reflected ultrasonic signal, showing the signal time from which are plotted: (b) the normalised peak amplitude against number of cycles; (c) the normalised peak amplitude against applied fatigue load and (d) the subtracted and normalised peak amplitude against number of cycles.

In figure 3.3(c), the peak amplitude is plotted versus applied fatigue load. The graph shows that above 20000 cycles, the dependence of the peak amplitude upon the applied fatigue load is not particularly strong, in stark contrast to the results observed in previous studies [3.4, 3.11, 3.16]. The difference is explained by the fact that in prior experiments, the crack was initiated in the plastic zone generated by the small pit, whose purpose was to simulate ISD and to act as a stress-raiser.

Here a possible change of interpretation is offered. In our previous study [3.11], decreases in signal amplitude were observed even as cracks were growing. The interference between the omnipresent background noise and the signals of the multiple growing cracks signal is complicated and it is conceivable that if the two signals are out of phase, then growing crack signals will result in a decrease of peak amplitude within the gate. As the nature of the interference changes. This would explain the dips in peak amplitude strength in figure 3.3(b) at around 21000-22500 cycles. Although the general trend is very clear, the interference of signals makes very complicated the explanation of specific phenomena.

The amplitude data of figure 3.3(b) are subtracted according to process of equation (3.2), normalized and then smoothed using a moving average window of a semi-width of 25 data out of a total of 938 data. In figure 3.3(d), the resulting subtracted data are plotted versus number of cycles, a process that can be represented by the following expression:

$$\frac{\max\{u_{ss}^f(L, C, t)\}_{t=35.5 \mu s}^{t=37.5 \mu s}}{\max\{u_{ss}^f(L, 2, t)\}_{t=35.5 \mu s}^{t=37.5 \mu s}} \text{ for } C = 2, 3, \dots, n_C. \quad (3.4)$$

This subtraction method produces the incremental difference in the time signals accruing at the same cycle load from one cycle to the next due to crack evolution. Since the backscattering microstructural noise is not changing significantly at these conditions, most of the effect due to the noise is removed (except the effect of interference between the noise and the signal).

In this figure, it is seen that the dip visible in figure 3.3(b) is removed at all applied loads. A possible interpretation for the dip and its removal is presented. There may have been two cracks present: a first crack and a second crack. It is suggested here that the first crack grew from 18000 cycles, causing the initial increase in the reflected peak amplitude. At some point before 21000 cycles, the first crack is arrested and that the subsequent dip in amplitude at 22000 cycles and the following increase in amplitude is caused by the formation and growth of a second crack, which eventually brakes the specimen (similar phenomena have been observed in the authors' earlier work [3.12]). The subtraction removes the dip because this method is sensitive only to incremental changes and hence did not respond to the first crack after it was arrested, but was only sensitive to the second, growing crack. By contrast, the raw data were affected by the presence of the first crack even after it was arrested.

3.3.3 Visualisation of Fatigue Regime Data

At the level of fatigue load in figure 3.3(d), the smoothed peak amplitudes initially begin to show an increase in the region of 18250 cycles. This is the same point of the experiment that an increase in peak amplitude was first observed for the original data without subtraction. Although the subtraction method may not reveal the presence of the evolving crack earlier in the experimental life of the specimen, the strength of the subtraction method is in the improvement of the signal-to-noise ratio (SNR) in real-time acquisition of crack-reflected ultrasonic signal, once the crack has formed during fatigue, and thus its real-time detectability.

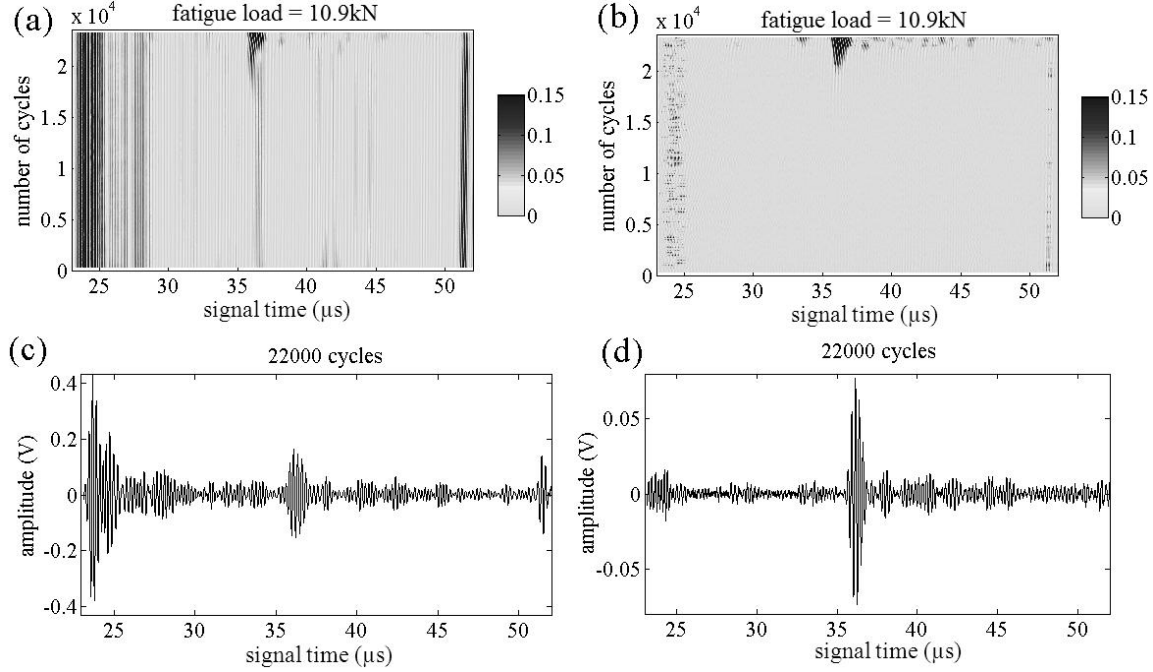


Figure 3.4: Normalised reflected ultrasonic signal amplitude is plotted for a range of numbers of cycles in (a) the original form and (b) the subtracted form. The acquired reflected ultrasonic signal is plotted at 22000 cycles in (c) the original form and (d) the subtracted form.

The data can be visualised in two-dimensions since the time signal is a function of amplitude with respect to position along the specimen and applied load. Thus, for a given load, $u^f(L, C, t)$ or $u_{ss}^f(L, C, t)$ can be plotted for $C = 2, 3, 4, \dots, n_C$ and for $t_{wc} < t < t_{wr}$ where t_{wc} is the time index for the reflection from the transducer wedge corner and t_{wr} is the time of the reflection from the wedge reflector. Example of the plots of such data are shown in figure 3.4(a) and figure 3.4(b) for original and subtracted data respectively for the same applied load and for the same time range. In figure 3.4(b), the crack signal is much more easily identifiable and the signals due to the two reflections are reduced from the graph.

The time signals used to compose the visualisations at 22000 cycles (chosen as an example; the data from other cycles illustrate the same point) are extracted and plotted in figure 3.4(c), where $SNR=9.51dB$, and figure 3.4(d), where $SNR=16.83dB$. These values were calculated by dividing the mean rectified value of the time signal between $t=35.5\mu m$ and $t=37.0\mu m$ by the mean value of the time signal between $t=37.0\mu m$ and $t=50.5\mu m$ (the times were chosen empirically but are held constant in the SNR calculations for both the static and the modulation data). The subtraction method is seen to powerfully enhance crack SNR, thus aiding crack detection and identification.

3.3.4 Crack Evolution and Ultrasonic Signals

In this section, the relationship between the evolution of the crack within the fatigue specimen and the evolving ultrasonic signals is discussed. The crack was measured to be 7mm from the tip of transducer wedge, a point labeled "w" in figure 3.5. A specular reflection from the crack is predicted due to wave interaction with the crack. The reflected signals vary in strength and position as the experiment progresses and could potentially yield information about crack initiation and evolution of size. Previous work on crack

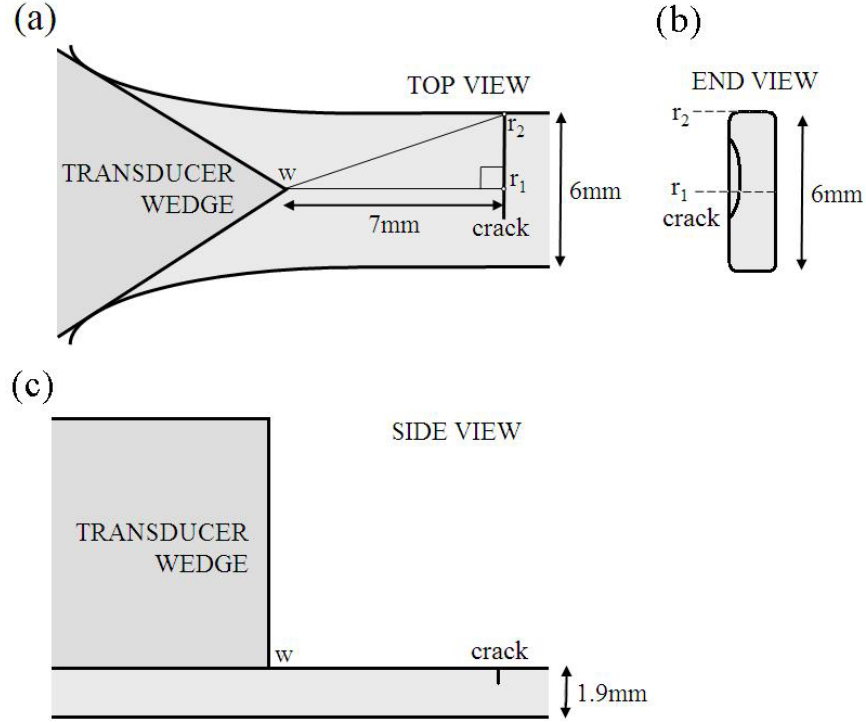


Figure 3.5: The model of the crack within the specimen used in this work: (a) a top view; (b) an end view and (c) a side view.

sizing has related the amplitude of the signal reflected from the crack to the depth of the crack [3.12, 3.16], assuming that the closed portion of the crack is a perfect transmitter of ultrasonic waves and that the open portion of the crack is a perfect reflector. For a discussion of the fatigue crack closure phenomenon, the reader is referred to [3.17, 3.4]. In this chapter, we investigate the interpretation and the evolution of the relevant peak due to crack reflection.

In figure 3.4(a), at the point of crack initiation (for this specimen, assumed to be at 18250 cycles), several ultrasonic peaks, associated with reflection R4, which becomes dominant towards the conclusion of the experiment, begin to develop. As the experiment progresses, not only does the reflected signal become stronger but the peaks begin to shift from its original position, as illustrated in figure 3.6(a). The dominant reflection and its associated ultrasonic peaks gradually take longer to arrive back to the transducer location. This chapter concentrates on peak shifts as its metric.

Let the time shift between the initial position of a prominent ultrasonic peak generated by the wave reflection from the crack and its current position be defined as Δt . In order to measure the peak position, a two-stage procedure was used:

1. the time signal was smoothed by a moving average window, 25 data in width;
2. then a parabola-fitting technique was applied to the peak datum and the two data on either side to return an interpolated peak position.

The time difference is plotted in figure 3.6(b) with respect to number of cycles and in figure 3.6(c) with respect to applied load.

To better understand the signal gating process, figure 3.7 shows (a) the schematic of the sample and the ultrasonic transducer and reflector wedge arrangement and (b) an example of the ultrasonic time trace of backscattering signal. It shows that prior to application of the signal subtraction algorithm the signal from an initiated small fatigue crack in Ti 6242 is completely embedded in the microstructure scattering noise.

A fractography analysis of the failed sample cross-section show that in addition to the main crack also a secondary is initiated and hence due to reflected signals interference the dips in signal amplitude in figure 3.3(b) as discussed earlier in section 3.2. The interpretation offered here is that at early stages of crack evolution, the bulk of the crack, and thus the source of reflection, was towards the centreline of the sample, indicated by the label r_1 . As the crack propagated, and as the secondary crack began to generate and evolve, the dominant source of reflection began to shift towards the right side of the specimen cross-section, indicated by the label r_2 . Finally, at sample failure, the crack has grown to almost the full depth of the specimen at position r_2 .

These two labels are also present in the model of the crack presented in figure 3.6(a). At early stages of crack growth, the bulk of the reflected energy takes the path $w-r_1$ (the path along the centreline). This distance was measured after specimen failure as 7mm. Towards the end of the experiment, it is assumed that the bulk of the reflected energy takes the path $w-r_2$. The difference in travel distance is $616\mu\text{m}$. The Rayleigh wave velocity is taken to be 2900ms^{-1} for this material, using the method adopted by Viktorov [3.18], and thus the difference in travel time would be 212ns.

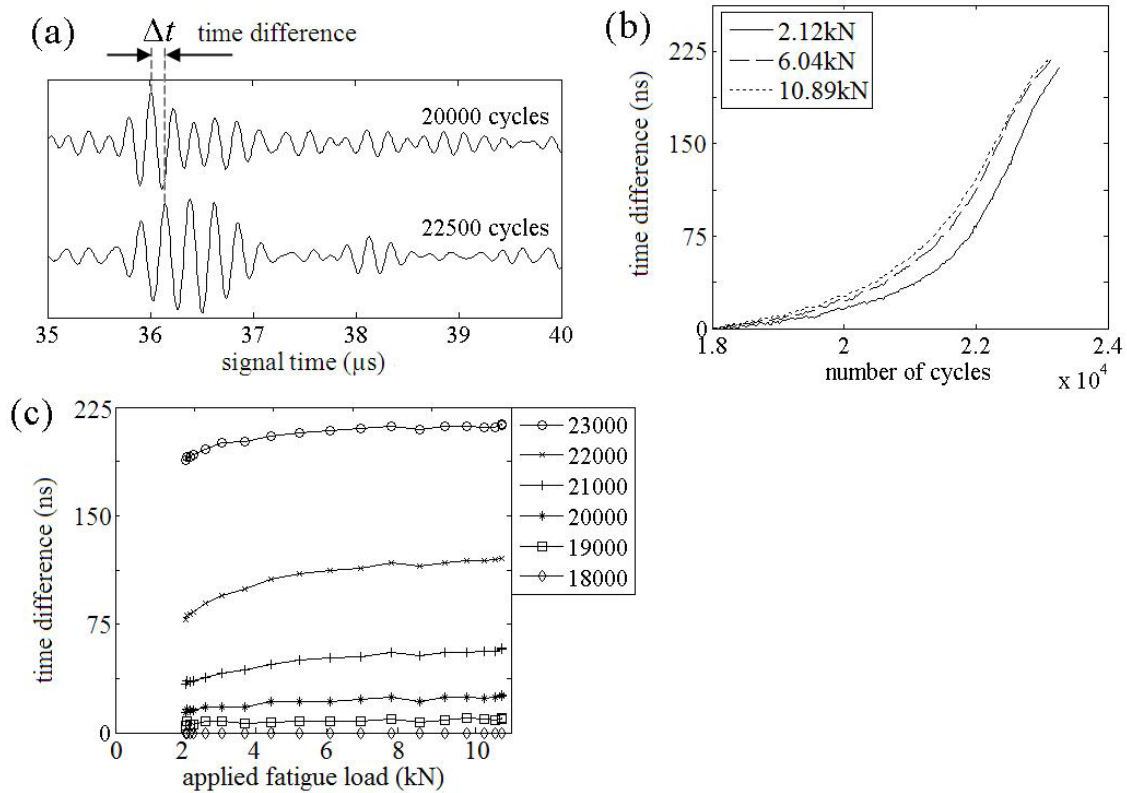


Figure 3.6: (a) An example of the acquired ultrasonic crack signal showing peak shifting; (b) time difference due to peak shifting plotted against number of cycles and (c) plotted versus applied fatigue load.

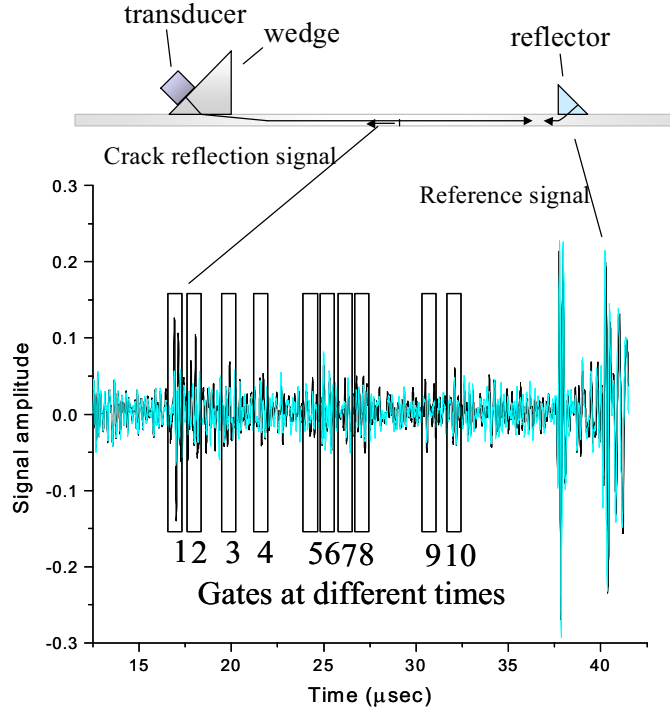


Figure 3.7: Real time monitoring of small fatigue crack in Ti 6242: (a) the schematic of the sample and the ultrasonic transducer and reflector wedge arrangement and (b) an example of the ultrasonic time trace of backscattering signal. It shows that prior to application of the signal subtraction algorithm the signal from an initiated small fatigue crack in Ti 6242 is completely embedded in the microstructure scattering noise.

The time differences seen in figure 3.6(b) and figure 3.6(c) tend to be in the range of 0-215ns and thus are well supported by the evidence provided in the cross-sectional image. A slight interference with the measurement of the peak position is as a result of the background noise due to the grain scattering. More experimentation will be required to make a more consistent interpretation of the data collected and presented in this chapter. It is the intention of the authors to collect further data from other specimens and to formulate a consistent relationship between the evolution of the crack and the time shifting of the dominant peak of the reflected signals.

3.4 Modulation Regime Results and Discussion

3.4.1 Modulation Overview

A qualitative analysis for the modulation data, equivalent to the fatigue data analysis presented in the previous section, is shown here. Work involving modulation analysis has previously been carried out by the authors [3.11] and has been demonstrated that the earlier detection of just-formed fatigue cracks from stress-raiser is possible many cycles earlier when modulation data are taken into account.

This is a method that can be applied to online real-time monitoring (with strong SHM application) because it is applied to data collected at specific modulation load biases. This takes advantage of the nonlinearity of

the crack behaviour at modulation, and uses the data collected at different modulation load biases to interpret the current condition of the crack. Although for practical reasons it is not done in this work, it is possible for this procedure to be implemented online in real-time, after the acquisition of each segment of modulation data.

The objective of this section is to demonstrate that the subtraction method introduced earlier is just as applicable to modulation data and may potentially be useful in enhancing crack signals. The significant difference from our prior implementation of this method is utilization of a novel subtraction method and the way it synchronised with the modulation load at specifically pre-determined levels of loading bias.

As for the fatigue data, the data collected during the modulation regime can also be considered as a single function $u^m(L, C, m, t)$; where m is the index of the point of data acquisition in the modulation cycle (50 modulation cycles per level of static bias loading and 10 acquisitions per cycle, hence 500 points per level) and the superscript m to indicate that the data are those of the modulation regime. The data are processed, for a given value of L , C and t to extract the first harmonic of modulation, h^1 at 10Hz, the modulation frequency, from the spectrum defined as

$$h^1(L, C, t) = \text{abs}(F\{u^m(L, C, m, t)\}) \text{ at 10Hz for } m = 1, 2, \dots, 500 \quad (3.5)$$

with $\text{abs}\{\}$ indicating that the magnitude of the expression is used. The extraction of any number of harmonics is possible, yielding potentially useful information [3.19, 3.5], but fall outside the scope of this work. Future work of the authors may cover discussion of the conclusions that might be gleaned from analysis of the second harmonic.

3.4.2 Modulation and Subtraction

Subtraction can be used in conjunction with modulation data. In this case, the subtracted data would be defined as

$$h_s^1(L, C, t) = F\{u^m(L, C, m, t) - u^m(L, 1, m, t)\} \text{ for } m = 1, 2, \dots, 500 \text{ and } C = 2, 3, \dots, n_C \quad (3.6)$$

if only the data of the first segment are subtracted, or

$$h_{ss}^1(L, C, t) = F\{u^m(L, C, m, t) - u^m(L, C-1, m, t)\} \text{ for } m = 1, 2, \dots, 500 \text{ and } C = 2, 3, \dots, n_C \quad (3.7)$$

if the data of the previous segment are subtracted. As an example, the data of u^m would look much like those acquired during the fatigue regime (see figure 3.3(a)), a typical frequency spectrum $F\{u^m\}$ of such a signal is shown in figure 3.8(a), with the extracted value of h^1 indicated in the figure, and a typical plot of $h^1(t)$ is shown in figure 3.8(b).

The amplitude of the first harmonic of modulation within the gate shown in figure 3.3(a) is plotted versus number of cycles in figure 3.9(a). An increase in the reflected energy from the growing crack coincides with an increase in the level of modulation. The corresponding plot of the modulation amplitude versus number of cycles for the subtracted data is shown in figure 3.9(b). In both cases, the modulation amplitude is fairly constant until the initiation of the crack, where the index suddenly begins to increase with increasing crack size due to the greater variation in reflected signal strength as the open segment of the crack becomes larger.

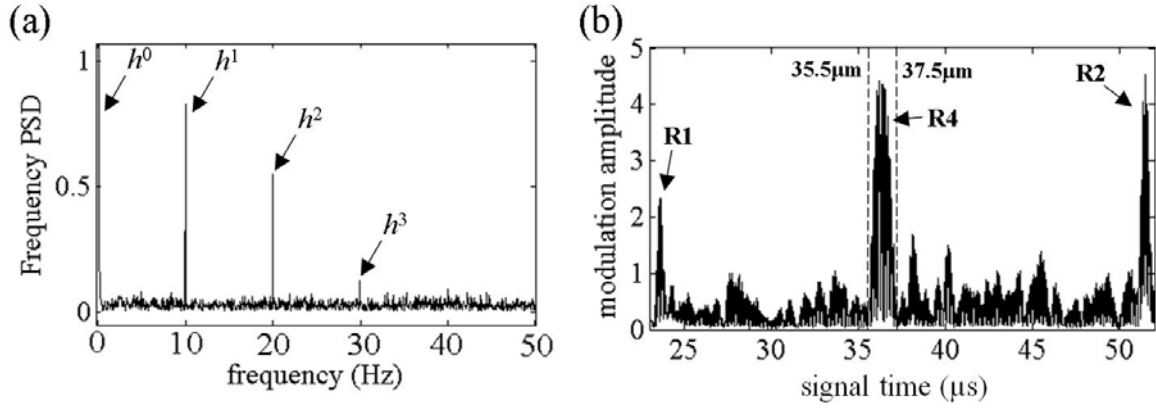


Figure 3.8: (a) A typical frequency spectrum acquired from the modulation data in the modulation regime and (b) a typical plot of the amplitude of the first harmonic of modulation plotted versus signal time (to be compared to a typical acquired reflected ultrasonic signal in figure 3.3(a)).

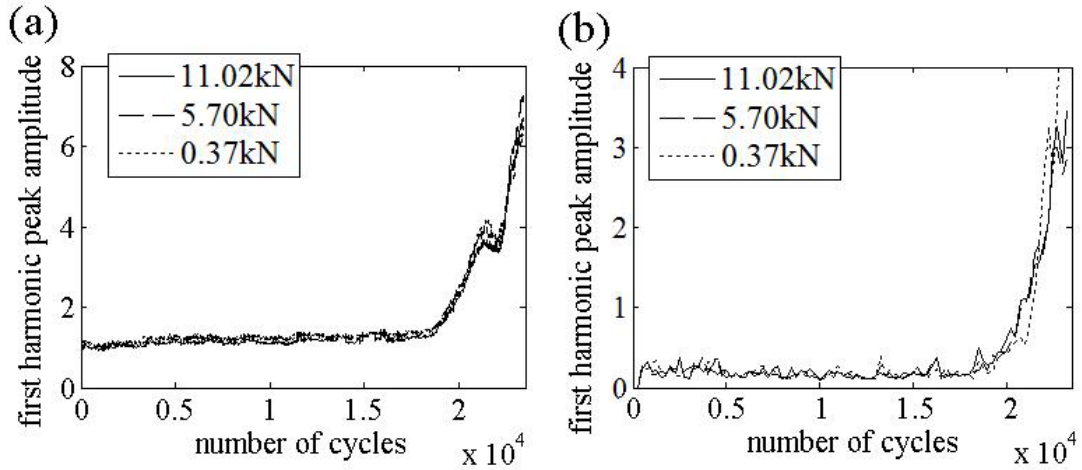


Figure 3.9: (a) The peak amplitude of the first harmonic of modulation plotted against number of cycles and (b) the modulation index plotted against number of cycles.

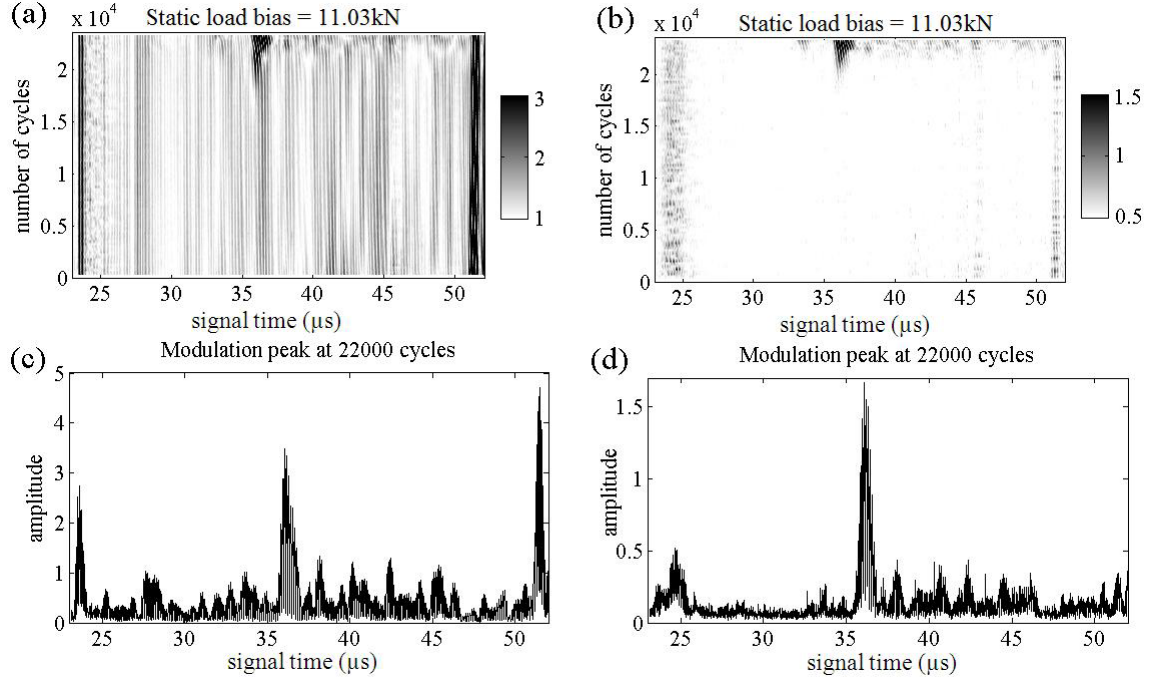


Figure 3.10: Modulation data of the ultrasonic signal amplitude reflected from the crack are plotted for a range of numbers of cycles in (a) the original form and (b) the subtracted form. The amplitude of the first harmonic of modulation is plotted against signal time at 22000 cycles in (c) the original form and (d) the subtracted form.

Here it is demonstrated that subtraction can be applied to modulation, resulting in a similar enhancement of the crack SNR. In figure 3.10(a), $h^1(L, C, t)$ is plotted for $C = 1, 2, \dots, n_C$ and for $t_{wc} < t < t_{wr}$. The subtracted equivalent, $h_{ss}^1(L, C, t)$, is plotted in figure 3.10(b). The values of the first harmonic of modulation that were used to compose the visualisations at 22000 cycles are extracted and plotted in figure 3.10(c), where $\text{SNR}=11.62\text{dB}$, and figure 3.10(d), where $\text{SNR}=14.63\text{dB}$. A method equivalent to that of section 3.3 was used here; the SNR was computed by dividing the mean modulation in the range $t=35.5\mu\text{m}$ to $t=37.0\mu\text{m}$ by the mean modulation in the range $t=37.0\mu\text{m}$ to $t=50.5\mu\text{m}$.

As in the fatigue case, the SNR is enhanced through the subtraction method. However, the improvement is not quite as strong as in the quasi-static measurements of the quasi-static fatigue case described in section 3. A possible explanation offered here is that the magnitude of the first harmonic was starker in contrast to the surrounding noise to begin with. Another possibility is that modulation measurements are greater in number; the procedure for the calculation of the magnitude of the modulation is of greater complexity and there is a greater influence of experimental noise.

It has thus been demonstrated that the subtraction method has a powerful effect of improvement upon the visualised time-space-cycle domain images of the modulation data. The subtraction method excels at removing background noise due to both the complex grain structure and the reflection from the wedge corner at $24\mu\text{s}$, leaving us with just the crack reflection as the main signal at $36\mu\text{s}$.

3.5 Conclusion

This chapter has presented the results of an investigation of the in-situ ultrasonic monitoring of fatigue crack initiation and evolution. Time domain subtraction has been applied to the acquired time signal data from the fatigue regime and it has been demonstrated that an increase of crack SNR can be achieved in both the static loading domain (figure 3.4) and the modulation domain (figure 3.10). The space-cycle-loading imaging has been useful in visualising these improvements.

The application of the subtraction method to data acquired during the modulation regime has been explored and discussed. A similar increase in crack SNR has resulted, presenting the possibility for improvements in crack detection and localisation. In addition, a novel subtraction technique applied to these dynamic signals and synchronized with the applied modulation static loading level, was shown to be effective in identifying just-formed fatigue cracks and as such, is particularly suited to online SHM for real-time monitoring.

It is well known that changes in environmental or operating conditions may render the baseline subtraction technique less reliable. The subtraction technique of (2) may be less susceptible to changes in ambient conditions as long as they are changing at a slow rate. Nevertheless, it is possible that theoretical time shifts due to loading changes or temperature changes could be applied [3.20] to improve the effectiveness of the subtraction method.

Further experimentation to improve the interpretation of both the changes in amplitude and time position of the reflected signals due to the growing crack is desirable. While much difficulty has been encountered due to the scattering and attenuative nature of the complex grain structure, it is our view that the subtraction and modulation techniques are promising in mitigating the scattering noise problem and the difficulties of earlier real-time detection of small fatigue cracks.

Chapter 4

Imaging of Damage Precursors as Anomalous Plastic-Microstrain: Ultrasonic Microtexture Backscattering as Strain Markers

4.1 Background and Method Formulation

In this chapter we propose a method for dwell and cyclic fatigue damage precursor visualisation based on backscatter signal (noise) variation with the applied fatigue load. We will illustrate this idea by preliminary experimental data, demonstrating such precursors appearing before and in the vicinity of the initiated fatigue crack in the titanium alloy sample studied.

A general use of backscatter noise for strain gauging has already been developed and demonstrated elsewhere. Elastographic methods [4.1] operate along similar principles in the medical literature, where they have been used effectively to track soft tissue displacement. Scattering noise has also been used by other authors in the form of speckle-tracking [4.2, 4.3] in medical imaging and for internal strain measurements [4.4] in structures. Our objective and the realization of the method are different since we do not aim at accurate macrostrain measurement but focus instead on the relative increase of plastic microstrains to identify the damage precursors.

Recent research has shown that one main reason for early failure under dwell fatigue conditions in Ti alloys was the presence of large micro-textured regions (MTRs) [4.4, 4.5]. In particular, it was shown that the crystallographic orientation and size of the MTRs are associated with facet-initiation sites of fatigue cracks. Physically, the MTRs are formed as regions of hexagonal α -phase crystallites with a common crystallographic orientation such that the combined MTR size noticeably outstrips the size of the primary α grains [4.4-4.7]. Those MTRs can be considered as large grains with effective elastic properties that produce significant quantifiable ultrasonic scatter [4.8, 4.9]. It was observed in this study that the scattering noise is significantly affected by fatigue loading not only for the results shown, but for a number of our earlier fatigue experiments for this alloy (those earlier digital ultrasonic data, that were analyzed in this study, were collected in our earlier fatigue experiments on Ti6242). The scattering amplitude variation is not systematic from sample to sample but the time stretching of the scattering signal is very consistent.

In titanium alloys, the dwell fatigue crack initiation mechanism is attributed to the inhomogeneous stress distribution [4.10-4.12] in polycrystalline material due to grain anisotropy. It is suggested in those studies that crack initiation may occur in the “hard grain” which is surrounded by “soft” grains that are favourably oriented for slip; thus large plastic grain deformations occur in this locality that are eventually followed by crack initiation. From our perspective, large local plastic deformations occur and accumulate prior to crack initiation. This local elasto-plastic strain variation is synchronized and associated with fatigue load, leading to excessive grain size stretching and local variations of the ultrasonic scattering. At the frequencies studied, the random ultrasonic scattering signal is a result of interference of the scattering from grain boundaries of different grains. Large microplastic deformation changes this scatter interference and results in stretching of the backscatter signal in this microregion.

4.2 Approach and Results

4.2.1 Samples and Data Acquisition

The data acquisition and Ti-6242 fatigue samples were described in Chapter 3. The data analyses reported here has been performed on the data set described in that chapter.

4.2.2 Results

It is assumed that the background noise corresponds to certain features within the titanium sample, and that when the sample is strained, the grains and their boundaries stretch accordingly. The signals associated with this stretch manifest themselves as time shifts in the time signal with respect to the applied load (as is illustrated for crack initiation and evolution in figure 3.6(b) and figure 3.6(c) of Chapter 3).

A peak-tracking (and, equally, trough-tracking) algorithm directly applicable to the data generated from these experiments was developed in-house and applied to the shifts in the time signal, allowing the measurement of the absolute time, and therefore of time shift, of every peak and trough as the applied static load was adjusted. In figure 4.1(a), an example of the output of peak-tracking is illustrated. In the top plot, the time trace output at the highest static loading level (10.9kN; 2443lb) is plotted as a continuous line and that the lowest static loading level (2.12kN; 475lb) is plotted as a dotted line. In the lower plot, the positions of the peaks are drawn as a continuous line and those of the troughs as dotted lines, but both peaks and troughs are processed in exactly the same manner. The figure shows the absolute time of each peak or trough. Using the lowest time (i.e. the time at the lowest loading level) as the reference baseline, the time shift is calculated for every level of applied load, with the shift defined as zero for the lowest loading level.

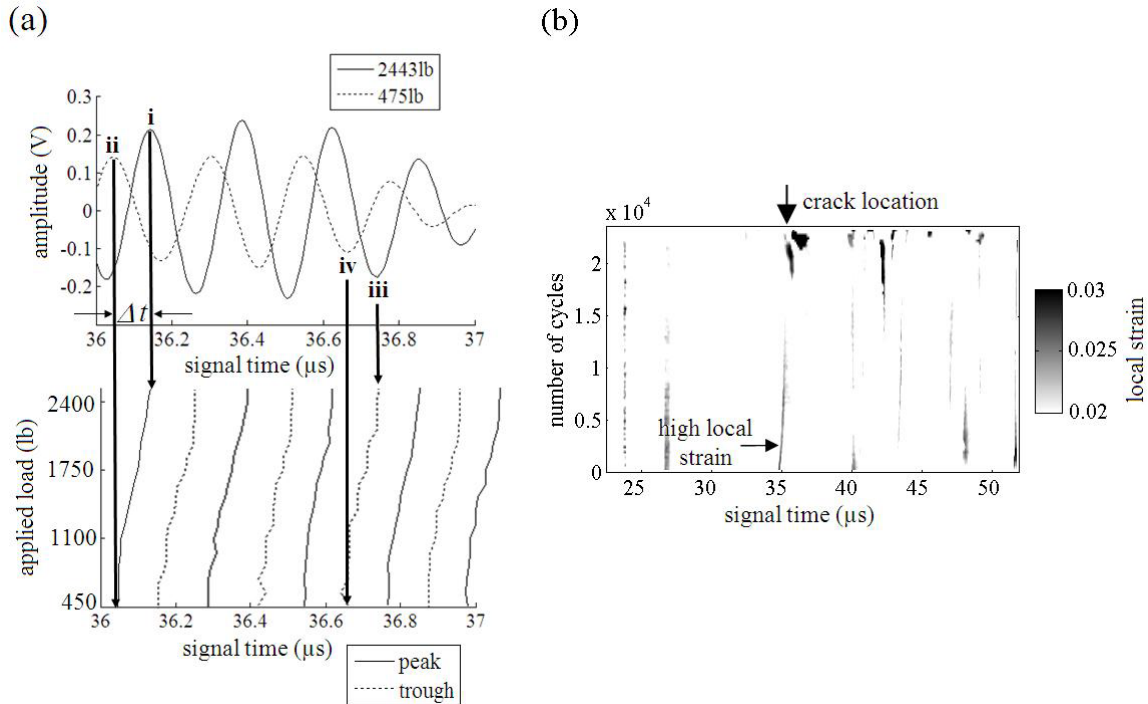


Figure 4.1: (a) Time shifting plotted versus signal time and (b) local strain plotted versus signal time.

As an example, the peak occupying position **i** in the upper plot at the highest static loading level but shifts to position **ii** as the load is decreased, hence the slant of the continuous line in the lower plot. Similarly, the trough occupying position **iii** shifts to position **iv** as the applied static load is decreased, thus resulting in a slanted dotted line in the lower plot. Though not explicitly shown here due to scale, it is generally noted that the time shifts generally become larger as with each peak and trough as we move farther from the transducer; this is to be expected since the time is being measured from the transducer receiver itself.

Let us also define the time shift between the minimum and the maximum applied static loads as $\Delta t(C, \tau)$ at cycle C , and where time τ represents the local position of the peak or trough along the specimen at the lowest loading level in seconds (e.g. at positions **i** or **iii** in figure 4.1(a)). In figure 4.1(b), the local strain is plotted, defined as

$$\varepsilon(C, \tau) = \frac{\Delta t(C, \tau)}{\tau}. \quad (4.1)$$

This figure clearly shows high straining around the crack position as it initiates and grows. It is important that persistent high local strain can also be seen at early stages of the experiment at the future crack position. This, as we have discussed in the previous section, is an indication of excessive plastic strain in that part of the grain structure, increasing susceptibility to crack formation under cyclic loading. The strain in cycle C for the entire specimen within the gauge area is expressed as

$$\varepsilon = \frac{\Delta t_2^C}{\Delta t_2^1}, \quad (4.2)$$

where the time difference Δt_2 , between the reference signals R1 and R2, is proportional to the extension of the sample gauge length.

The result defined by equation (4.2) is a total "ultrasonic macro strain". Prior work has demonstrated that the acousto-elastic effect [4.4] that is attributable to the change in strain-dependent sound velocity affects this total strain. However, large plastic local strains, which provide significant increase of local scatter, are above the average ultrasonic strain and the corresponding excess of scatter is clearly observed in figure 4.1 (b). These serve as potential indicators of crack precursors. Identification of such precursors may allow monitoring and inspection to focus on these weaker areas of a specimen where higher straining is measured at early stages. This topic will be tackled in future work by the authors.

4.3 Conclusion

A new ultrasonic microstrain-gauging backscattering technique is proposed. It focuses on visualising excess localized plastic grain strain. The preliminary experimental data obtained during fatigue of titanium samples has demonstrated and highlighted the precursor of crack initiation. The strain and the change in ultrasonic signals are linked dynamically as synchronized elasto-plastic strain variation due to fatigue loading.

Chapter 5

Inverse Models and Experimental Methodology for Ultrasonic Volumetric Assessment of Fatigue Sensitive Microstructure

5.1 Introduction

Dwell fatigue is known to cause significant reduction in fatigue life of near- α titanium alloys that are broadly used in aircraft engine compressor rotors. Recent research showed that one main reason for early failure under dwell fatigue conditions was the presence of large microtextured regions (MTRs) [5.1, 5.2]. In particular, Sinha et al. [5.1] showed that the crystallographic orientation and size of the MTRs are associated with facet-initiation sites of fatigue cracks. Physically the MTRs are formed as regions of hexagonal α -phase crystallites with a common crystallographic orientation such that the combined MTR size noticeably outstrips the size of the primary α grains [5.3, 5.4]. Due to the detrimental effect of such microtextures on the fatigue properties it is highly desirable to determine the possible microtexture existence in the forgings and to characterize them nondestructively. Ultrasonic attenuation at high frequencies is dependent on the length scale of the grains as discussed in [5.4, 5.5], so ultrasonic characterization may potentially provide nondestructive means to determine the microtexture presence and its morphology.

Most past studies of ultrasonic scattering in polycrystals have been related to the understanding and prediction of scattering-induced attenuation as a function of frequency and microstructure [5.5-5.16]. Hirsekorn has considered attenuation in cubic equiaxed randomly oriented polycrystals [5.6] as well as in materials with texture [5.7, 5.8]. She has also studied multiphase materials with orthorhombic crystallites [5.9]. Stanke and Kino [5.10] and Weaver [5.11] have developed general methods to model attenuation in polycrystals with equiaxial grains and applied them to materials of cubic symmetry. Yang et al. [5.12] have considered attenuation in texture materials with equiaxial grains of hexagonal symmetry. Attenuation in materials with cubic elongated grains has been investigated by Ahmed and Thompson [5.14] by numerical implementation of Stanke and Kino's [5.10] method and Yang et al. [5.5] by using Weaver's [5.11] model. Application of an exact ray tracing model to assess attenuation in the geometrical acoustics region has been reported by Rokhlin et al. [5.15].

Studies of backscattering in duplex Ti microstructures were presented by Han and Thompson [5.17], Panetta et al. [5.16], Lobkis and Rokhlin [5.18] and Lobkis et al. [5.19]. Hassan and Nagy [5.20] have developed an interferometric method for ultrasonic scattering detection in Ti and Blodgett and Eylon [5.21] have studied attenuation and backscattering in Ti alloys with special attention to the material texture. Han and Thompson [5.17] and Panetta et al. [5.16], who have examined experimentally the backscattering and attenuation for duplex microstructures, described in [5.17], mainly focused on arrangements of a second phase (they call it colony) in the large macrograins (prime β grains of cubic symmetry). While Lobkis and Rokhlin [5.18] and Lobkis et al. [5.19] have considered microtextural regions (MTRs) (colonies in the Han and Thompson terminology) as the largest size phase which is formed by a secondary (small size phase) of

prime α crystallites as shown in figure 5.1(a), the contribution of those crystallites to ultrasonic backscattering was neglected in [5.17].

In this chapter, an ultrasonic attenuation model for application to Ti alloys is proposed to investigate the relationship between ultrasonic attenuation and the elongated duplex microtexture/microstructure. The duplex microtexture is characterized by two size scales figure 5.1(a). The larger phase r is composed of elongated microtextured regions (MTRs) which by themselves are formed by smaller size hexagonal primary α crystallites (small phase α) with their preferred common orientation in the MTRs. The preferred orientation is not necessarily along the elongation direction of the MTRs. A detailed characterization of microstructure and microtexture of the Ti alloy samples used in this work was described in reference [5.4]. The model assumes that the directions of preferred orientation of crystallites in different MTRs are not correlated and their distribution is homogeneous; i.e. the medium is macroscopically isotropic (untextured). We have recently provided a backscattering model for characterizing such duplex microstructure of Ti alloys [5.18, 5.19]. In this work the material model is further generalized by explicitly describing the orientation distribution function of crystallites in MTRs with use of a modified Gaussian orientation distribution function [5.22]. The ensemble elastic properties in MTRs are characterized by the effective stiffness [5.23, 5.12] using an average over the MTR region of the elastic properties of hexagonal crystallites with the specified orientation distribution function. The total attenuation is considered as a sum of the attenuation due to scattering by MTRs with effective elastic properties and additional attenuation due to scattering by crystallites calculated using the model of [5.13] factored by a single texture function (as we will see this crystallite-induced attenuation is small).

We describe ultrasonic attenuation and backscattering measurements on the Ti alloy sample, whose microstructure was studied in [5.4]. Reasonable agreement was found between the experiment and the model predictions given a particular texture parameter for the sample. The objective of this work is to provide better understanding of ultrasonic interaction with the duplex microstructure and to serve our eventual goal of ultrasonic nondestructive characterization of Ti alloy microstructure/microtexture.

5.2 Model with Duplex Microstructure

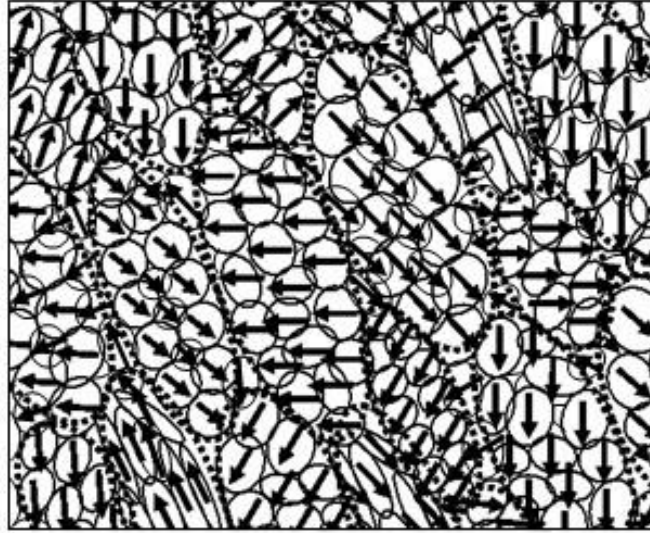
5.2.1 General Model Description

The geometry of a general ellipsoidal MTR or crystallite is shown in figure 5.1(b) with wave propagation and scattering directions. The wave propagation direction is arbitrarily related to the ellipsoid radii or the crystallographic orientation of the grains. A physical model of the duplex microstructures, as is applicable to forged Ti alloys, is needed for meaningful theoretical analysis of ultrasonic attenuation in those alloys. The duplex microtexture consists of the large phase r in the form of elongated microtextured regions (MTRs) [5.4, 5.18, 5.19], which are formed by smaller size hexagonal primary α crystallites (phase α) with preferred orientation in this region. The preferred orientation is not necessarily along the elongation direction of the MTRs.

A simplified duplex microstructure of the forged near- α Ti alloy, proposed in [5.18, 5.19] and which we generalize here to explicitly include the orientation distribution function (ODF) of the crystallites and use to develop our ultrasonic attenuation model, is shown schematically in figure 5.1(a). A material volume is completely filled with α crystallites which are grouped in elongated regions of common crystallite orientation, microtextured regions. The preferred directions of crystallite texture in different MTRs are oriented randomly to each other and the macroscopic medium is elastically isotropic. The MTRs are approximated by ellipsoids; they are indicated in figure 5.1(a) as dashed ellipses (in the volume of the sample we model these regions as arbitrary ellipsoids). Due to plastic processing of the material the MTR shapes (ellipsoids) are preferentially oriented in the sample and the wave propagation is assumed arbitrary to this preferred orientation, figure 5.1(b). Thus, we define two phases: the larger phase r of elongated microtextured regions (MTRs) and a smaller phase of Ti hexagonal primary α crystallites (phase α),

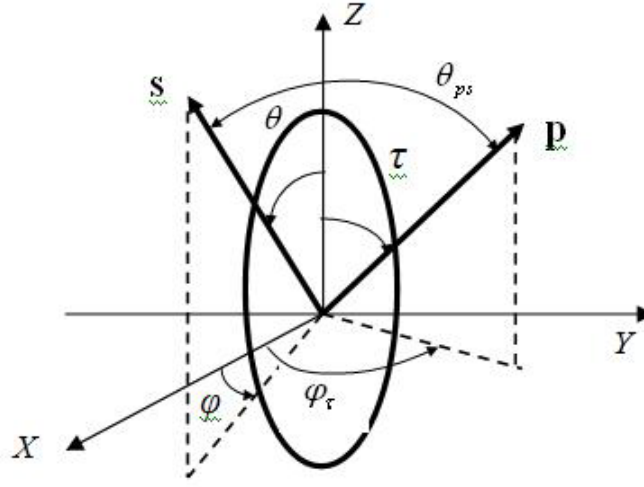
which form the MTRs and have a preferred orientation in those regions characterized by their orientation distribution function (ODF) which is specified by its width. The α crystallites are shown for simplicity as circles or ellipses in figure 5.1(a); arrows indicate their mean crystallographic (c-axis) orientation (those crystallites could be of a general ellipsoidal shape). Examples of actual microtextures of forged Ti samples studied in this work are given in reference [5.4]. It will be discussed below how the degree of the misorientation of crystallites in the MTRs is described in our model.

Consider an elastic wave propagating in a polycrystalline medium with elasticity of grains described by the elastic tensor c_{ijkl} . As the wave propagates it scatters due to change of the crystallographic orientation of the grains. This change of grain orientations is described by small random variations $\delta c_{ijkl}(\mathbf{X})$ of the elastic tensor $c_{ijkl}(\mathbf{X}) = \langle c_{ijkl} \rangle + \delta c_{ijkl}(\mathbf{X})$ as functions of the spatial coordinate \mathbf{X} ; the brackets $\langle \bullet \rangle$ indicate an ensemble average; $\langle c_{ijkl} \rangle = c_{ijkl}^0$ is the macroscopic elastic tensor of the homogenized, textured, polycrystalline medium and $\langle \delta c_{ijkl} \rangle = 0$. Stochastic wave propagation in a polycrystalline medium is a complex wave phenomenon. It depends on material microstructure which, as a random inhomogeneous medium, can be described by a hierarchy of point correlation functions. The two-point or pair correlation function (PCF) $\langle \delta c_{ijkl}(\mathbf{X}) \delta c_{\alpha\beta\gamma\delta}(\mathbf{X}') \rangle$ for the elastic tensor fluctuations δc_{ijkl} is a probability density for having two crystallographic orientations of grains specified by points \mathbf{X}, \mathbf{X}' . Since the PCF depends on grain size and morphology it affects the scattering at grain boundaries and it naturally appears in the ultrasonic scattering models [5.10, 5.11].



(a)

Figure 5.1: (a) Schematics of the model microstructure showing α – Ti crystallites as circles and ellipses which completely fill the material volume. Regions of the microstructure with a common crystallographic orientation of crystallites are called microtextural regions (MTR); those regions are approximated by ellipsoids as indicated by dashed ellipses. Those ellipsoidal shapes are preferentially oriented in the sample. The orientation of crystallites in the MTR is described by the orientation distribution function with the width varying from sample to sample. Arrows in the crystallites indicate their preferred (mean) crystallographic orientation of the anisotropy axis c ; those preferred crystallographic orientations in different MTRs are not correlated and the material is assumed to have elastic isotropy macroscopically.



(b)

Figure 5.1: (b) Geometry of ellipsoidal grains with the axes a_x, a_y, a_z and wave propagation p and scattering s directions. The ellipsoid radii enter the formalism solely through the spatial correlation function equation (A1) that can be interpreted as the correlation lengths [5.10, 5.11]. The wave propagation direction is arbitrary to the preferred orientation of ellipsoids in (a).

First we factorize the covariance on the tensorial and spatial parts [5.10, 5.11] $\langle \delta c_{ijkl}(\mathbf{X}) \delta c_{\alpha\beta\gamma\delta}(\mathbf{X}') \rangle = \langle \delta c_{ijkl} \delta c_{\alpha\beta\gamma\delta} \rangle w(\mathbf{X} - \mathbf{X}')$, where $w(\mathbf{X} - \mathbf{X}')$ is a geometrical two-point correlation function. Next we assume that every microtextured region (r) is significantly larger than the crystallite and contains many smaller crystallites (α) (figure 5.1(a)), therefore the length scales of the geometrical two-point correlation functions w_r for the MTRs and w_α for the crystallites are very different. It was proposed by Lobkis and Rokhlin [5.18] and Lobkis et al. [5.19], to represent the total covariance function of the two-point correlation functions for Ti duplex microstructures $\langle \delta c_{ijkl}(\mathbf{X}) \delta c_{\alpha\beta\gamma\delta}(\mathbf{X}') \rangle$ as a sum of two terms with the phenomenological ODF factors $(1 - M)$ and M :

$$\begin{aligned} \langle \delta c_{ijkl}(\mathbf{X}) \delta c_{\alpha\beta\gamma\delta}(\mathbf{X}') \rangle &= (1 - M) \langle \delta c_{ijkl} \delta c_{\alpha\beta\gamma\delta} \rangle_r w_r(\mathbf{X} - \mathbf{X}') \\ &+ M \langle \delta c_{ijkl} \delta c_{\alpha\beta\gamma\delta} \rangle_\alpha w_\alpha(\mathbf{X} - \mathbf{X}') \end{aligned} \quad (5.1)$$

The first term with sub-index r represents the covariance for the microtextural region and the second term, α , that for the crystallites; w_r, w_α are geometrical two-point correlation functions: w_r is the probability for two points \mathbf{X}, \mathbf{X}' to fall in the phase r (MTR) and w_α is that for the crystallites. The parameter M is a phenomenological parameter introduced in [5.18, 5.19] to account for the ODF: when $M = 1$ the crystallites are randomly oriented with a homogeneous distribution and MTRs are absent (the first term in equation (5.1) is zero); when $M = 0$ the MTRs are single crystal grains and scattering by crystallites is absent (the second term in equation (5.1) is zero). In references [5.18, 5.19] the parameters $(1 - M)$ and M were not explicitly related to the crystallites ODF; however, they were related to the measured ultrasonic backscattering amplitudes. In this work we will generalize equation (5.1) by explicitly considering an orientation distribution function potentially obtainable from orientation image microscopy experiments [5.22].

In the new model we take into account the preferred orientation of crystallites in the MTRs explicitly by an orientation distribution function (ODF) $F(\beta, \alpha, \gamma)$ in Euler space. The ODF is the probability density function [5.24] for the crystallite to have orientation β, α, γ in the polycrystalline aggregate. The limiting cases are a homogeneous random distribution (no texture) and a perfect alignment of the crystallites (single crystal). The ODF is normalized so integration over the space gives unity. This will allow us to represent the effective elastic tensor of MTR $C_{ijkl}(\sigma)$ (see next section) as a function of the texture parameter σ which governs the texture in the MTR, it emphasizes the dependence on the ODF in the form of a modified Gaussian distribution function [5.22] as discussed below (more specifically it is a width of the Gaussian ODF distribution). We redefine equation (5.1) for the total covariance function with the use of the geometrical two-point correlation functions for both phases as

$$\begin{aligned} \langle \delta C_{ijkl}(\mathbf{X}) \delta C_{\alpha\beta\gamma\delta}(\mathbf{X}') \rangle &= \langle \delta C_{ijkl}(\sigma) \delta C_{\alpha\beta\gamma\delta}(\sigma) \rangle_r w_r(\mathbf{X} - \mathbf{X}') \\ &+ M(\sigma) \langle \delta c_{ijkl} \delta c_{\alpha\beta\gamma\delta} \rangle_\alpha w_\alpha(\mathbf{X} - \mathbf{X}') \end{aligned} \quad (5.2)$$

where $\langle \delta C_{ijkl}(\sigma) \delta C_{\alpha\beta\gamma\delta}(\sigma) \rangle_r$ is the covariance of the effective elastic tensor variations $\delta C_{ijkl}(\sigma)$ of the MTR. In this representation the MTRs are considered as single crystal grains with effective elastic properties using which the covariance of and scattering from the MTRs will be determined. The representation (5.2) also elucidates the meaning of the factor $(1-M)$ in equation (5.1) as the ratio $\langle \delta C_{ijkl}(\sigma) \delta C_{\alpha\beta\gamma\delta}(\sigma) \rangle_r / \langle \delta c_{ijkl} \delta c_{\alpha\beta\gamma\delta} \rangle_\alpha$. The crystallite scattering is described by the second term in equation (5.2). In this term the parameter $M(\sigma)$ is a generalization of the parameter M in equation (5.1) implying its dependence on the ODF. c_{ijkl} is the elastic tensor of α -Ti crystallites; the covariance $\langle \delta c_{ijkl} \delta c_{\alpha\beta\gamma\delta} \rangle_\alpha$ describes uncorrelated (untextured) orientations of crystallites to each other, while the microtexture of crystallites in the MTR is taken care of by the factor $M(\sigma)$.

5.2.2 Effective Elastic Property of Mictotextured Region (MTR)

As was described above the MTRs are formed by small primary α crystallites characterized by their orientation distribution function in those regions. We will treat each MTR as an elastically equivalent, bigger elongated single crystal grain of hexagonal macroscopic symmetry with effective elastic properties $C_{ijkl}(\sigma)$; this is similar to a macroscopic treatment of a textured polycrystalline medium as a homogeneous anisotropic medium. This implies a quasi-static description of scattering on those microtextured regions (first term in equation (5.2)). This is justified since for those materials experiment is done at frequencies below 20MHz and the longitudinal wave length is above 200 μm . This is much larger than the crystallite size (about 10 μm), thus when considering wave interaction with the MTRs we neglect their crystallite scale microstructures replacing their effect by the effective elastic properties of the MTRs. However, we independently account for the ultrasonic scattering by crystallites by the second term in equation (5.2).

The effective elastic properties $C_{ijkl}(\sigma)$ of the crystallite ensemble in the MTR can be obtained by averaging the elastic tensor c_{ijkl} for a single hexagonal crystallite weighted by the crystallite orientation distribution function over the entire MTR. For hexagonal crystallites, the elastic modulus tensor for a crystallite is given by

$$\begin{aligned} c_{ijkl} &= \lambda \delta_{ij} \delta_{kl} + \mu (\delta_{ik} \delta_{jl} + \delta_{il} \delta_{jk}) + A (\delta_{ij} e_k e_l + \delta_{kl} e_i e_j) \\ &+ B (\delta_{ik} e_j e_l + \delta_{il} e_j e_k + \delta_{jk} e_i e_l + \delta_{jl} e_i e_k) + D e_i e_j e_k e_l, \end{aligned} \quad (5.3)$$

where the unit vector \mathbf{e} is defined as the symmetry axis of the hexagonal crystallites. The five coefficients are given in terms of single crystallite elastic constants $c_{11}, c_{33}, c_{44}, c_{12}, c_{13}$, and c_{66} as $\lambda = c_{12}$, $\mu = c_{66}$, $A = c_{13} - c_{12}$, $B = c_{44} - c_{66}$, and $D = c_{11} + c_{33} - 2c_{13} - 4c_{44}$.

The orientation volume average of the elastic tensor weighted by the ODF is given in general [5.25, 5.26] as

$$\langle Fc_{ijkl} \rangle = \frac{1}{8\pi^2} \int_0^\pi \int_0^{2\pi} \int_0^{2\pi} F(\beta, \alpha, \gamma) c_{ijkl} \sin(\beta) d\alpha d\gamma d\beta. \quad (5.4)$$

$F(\beta, \alpha, \gamma)$ is usually represented in the form of a series of generalized spherical harmonic functions with so-called texture coefficients W_{lmn} which can be determined using orientation image microscopy (OIM) [5.24]. This was done for example for textured steel [5.27] where excellent agreement was found between diffraction and ultrasonic measurements of macroscopic elastic constants and those obtained by Hill averaging crystallite moduli. In this work to simulate attenuation coefficients for different crystallite misorientation in MTRs it is convenient to approximate $F(\beta, \alpha, \gamma)$ analytically by the standard distribution functions [5.22, 5.23]. For the OIM data inversion and for modeling the ODF it is often represented [5.23] by a Gaussian-shape distribution as was suggested by Bunge [5.28]. However, it was later demonstrated [5.22] that the representation

$$F(\sigma, \theta) = F_0 \exp\left(\frac{\cos \theta}{2\sigma}\right) \quad (5.5)$$

is advantageous as a standard ODF representation to fit experimental OIMs. Here σ is the texture parameter governing the width of the ODF and θ is the angular distance between the texture “ideal” direction and the crystallite orientation state [5.22]; F_0 is a normalization factor such that

$$\frac{1}{2} \int_0^\pi F(\sigma, \theta) \sin \theta d\theta = 1 \quad (5.6)$$

and

$$F_0 = \frac{2S}{e^S - e^{-S}}, \quad (5.7)$$

where $S = 1/2\sigma$. The parameters σ and F_0 can be related to the average ODF of the sample, which could be measured from orientation image microscopy (OIM) scans by evaluating pole figures of electron backscatter diffraction spectra or other diffraction methods [5.22, 5.24, 5.4] (in reference [5.22] the parameters $\theta = \tilde{\omega}$ and full-width at half-maximum $b = 4 \arcsin \sqrt{\sigma \ln 2}$ were used for this purpose). In figure 5.2 the distribution function (5) is plotted versus angle θ for four texture parameters σ . The variable σ describes the degrees of the preferred orientation of the crystallites. For identical orientations of crystallites in the microtextural regions, $\sigma = 0$, the microtextured region behaves like a single crystal (perfectly identical orientation of crystallites in the dashed ellipsoid regions in figure 1(b)). For random (statistically isotropic), arbitrary orientation of the crystallites, $\sigma = \infty$, and thus MTRs are absent. The covariance function (2) for MTRs and crystallites includes effects of the orientation distribution function to account for this preferred orientation.

The effective elastic constants in matrix notation C_{ij} of a microtextured region (MTR) are obtained from equation (5.4) and may be expressed similarly to [5.12] as

$$\begin{aligned}
C_{11} &= \lambda + 2\mu + (2A + 4B)M_1 + 3DM_3, \\
C_{12} &= \lambda + 2AM_1 + DM_3, \\
C_{13} &= \lambda + A(2M_1 + M_2) + DM_4, \\
C_{44} &= \mu + B(2M_1 + M_2) + DM_4, \\
C_{33} &= \lambda + 2\mu + (2A + 4B)(M_1 + M_2) + DM_5, \\
C_{66} &= 1/2(C_{11} - C_{12}),
\end{aligned} \tag{5.8}$$

where M_i in equation (5.8) are expressed as

$$\begin{aligned}
M_1 &= \frac{1}{2}(I_\sigma^0 - I_\sigma^2), \quad M_2 = \frac{1}{2}(-I_\sigma^0 + 3I_\sigma^2), \quad M_3 = \frac{1}{8}(I_\sigma^0 - 2I_\sigma^2 + I_\sigma^4), \\
M_4 &= \frac{1}{2}(I_\sigma^2 - I_\sigma^4), \quad M_5 = I_\sigma^4, \\
I_\sigma^m &= \frac{1}{2} \int_0^\pi F(\sigma, \theta) \cos^m \theta \sin \theta d\theta = 1 - \frac{m}{S} \frac{(1 + e^{-2S})}{(1 - e^{-2S})} + \frac{m(m-1)}{S^2} I_\sigma^{m-2},
\end{aligned} \tag{5.9}$$

where $I_\sigma^0 = 1$ as follows from equation (5.6) and $m = 2, 4, 6$, and 8 . The effective elastic constants in equation (5.8) are assumed to be the new elastic property of a single MTR having transverse isotropy or hexagonal symmetry. They are used to obtain the MTR related scattering contribution to the total attenuation for duplex microstructures (as is shown in the attachment to this chapter). Now we can use equation (5.3) to calculate the effective elastic tensor C_{ijkl} of the MTR for use in the scattering model (instead of c_{ijkl} for crystallites); the coefficients λ, μ, A, B, D in equation (5.3) are replaced by the coefficients

$$\begin{aligned}
\lambda_{MTR} &= C_{12}, \quad \mu_{MTR} = C_{66}, \quad A_{MTR} = C_{13} - C_{12}, \\
B_{MTR} &= C_{44} - C_{66}, \quad D_{MTR} = C_{11} + C_{33} - 2C_{13} - 4C_{44},
\end{aligned} \tag{5.10}$$

where the index MTR indicates that the coefficients relate to the effective properties of the MTR. In figure 3 the effective elastic constants of MTRs C_{ij} are plotted as a function of texture parameter σ . For calculation we use the measured [5.29] elastic properties of hexagonal α Ti crystallites that are given in table 5.1. As is shown in figure 3 when σ is close to zero, the microstructure corresponds to a single MTR with crystallites having the same crystallographic orientation; as it increases above $\sigma > 0.2$ the microstructure becomes statistically isotropic. In this case, the MTRs are absent in the medium which is a single phase crystallite microstructure. Those effective elastic constants of a MTR are used to determine the attenuation coefficients contributed by MTRs.

For calculation of attenuation coefficients (see in the attachment) we use macroscopic velocities V_L, V_T of the homogenized medium, the velocities being obtained by Voigt averaging [5.10]. Since directions of preferred orientation of crystallites in different MTRs are not correlated the averaged macroscopic elastic properties are independent of σ (the Voigt averaging is insensitive to clustering) and equal to the macroscopic properties of a medium with homogeneous distribution orientation of α crystallites (a medium without microtexture, without MTRs). This is clear from the microtexture model depiction in figure 5.1(a): for a large sample including many MTRs the total α crystallite orientation becomes homogeneously distributed with the averaged macroscopic elastic moduli corresponding to that of the infinite σ (macroscopically isotropic).

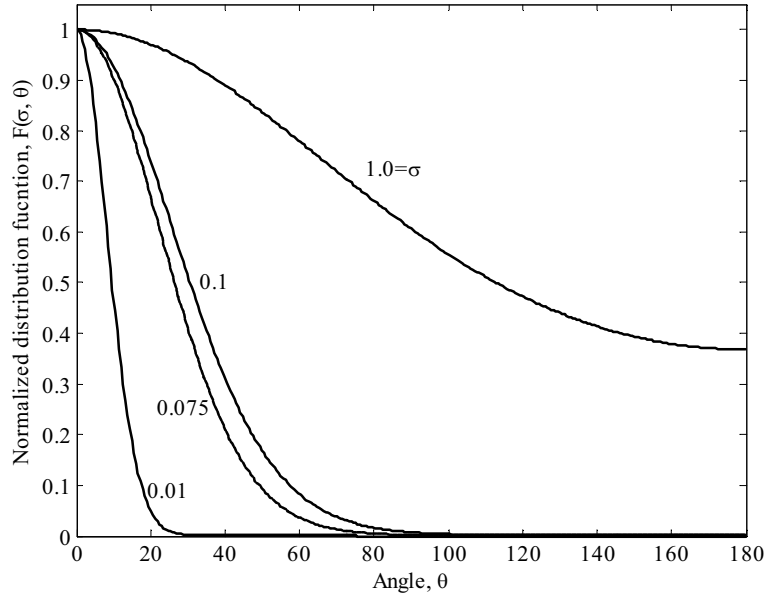


Figure 5.2: Normalized Gaussian orientation distribution function [5.22] $\exp(\cos \theta / 2\sigma) / \exp(1/2\sigma)$ versus distribution angle θ for different texture parameters σ .

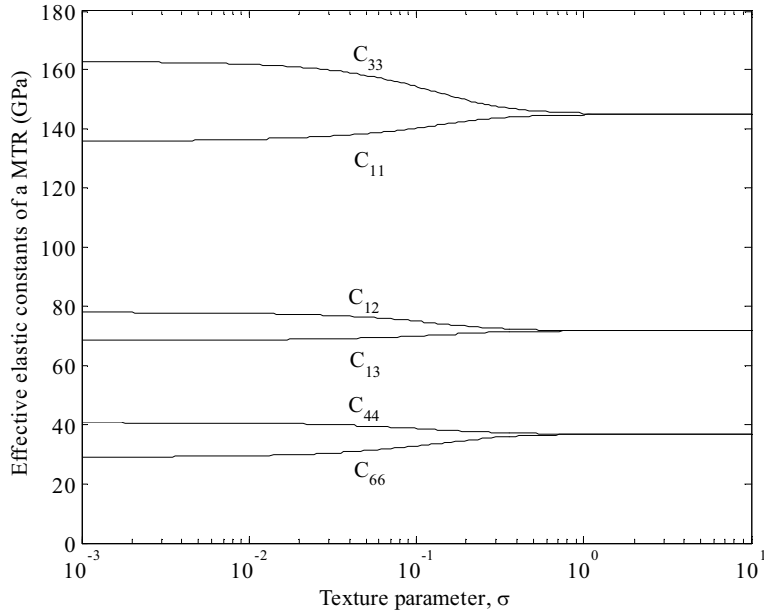


Figure 5.3: Effective elastic constants $C_{ij}(\sigma)$ (in the matrix form) of the MTRs for duplex microstructure versus microtexture parameter σ . At $\sigma = 0$ the effective elastic constants are equal to those of the α -Ti crystallites $C_{ij}(0) = c_{ij}$. As σ increase the material becomes isotropic with $2C_{44} = C_{11} - C_{12}$.

5.2.3 Attenuation in Duplex Microstructures

As represented by the total covariance function in equation (5.2), the attenuation for polycrystalline aggregates with duplex microstructures is determined by adding two independent components, the attenuation contributed by MTRs and by crystallites

$$\alpha_{Total} = \alpha_{MTR} + \alpha_{Crystallites} \quad (5.11)$$

The formulation (5.11) assumes independence of scattering by the MTRs and crystallites due to their different length scales.

For scatter and attenuation due to MTRs, the texture parameter σ enters the calculation only through the effective elastic constants of the MTRs. The MTRs are assumed to have uncorrelated crystallographic orientations of the related effective crystals with the same effective constants for all MTRs (physically the average effective elastic constants are assigned to the MTRs). Once those stiffness constants are determined, they are used in the model described in the attachment for determining the covariance (and attenuation/backscatter) of collections of ellipsoidal, single phase, hexagonal crystals having randomly-oriented lattice directions relative to each other (see also ref.[5.30] for detailed model description). Our attenuation model is based on the Born approximation [5.11, 5.13], the applicability of which is supported in our frequency range by comparison with the high order theory [5.10, 5.30]. The Born approximation assumes that elastic perturbations from MTR to MTR are small and the wave field in the MTR is that of the incident wave. The attenuation term α_{MTR} in equation (5.11) is obtained by substituting the effective elastic constants given by equation (5.10) into equation (A6) of the attachment and then using equations. (A3-A4).

When the propagating wave enters the MTR it independently scatters on crystallites (the scales are such that each MTR contains thousands of crystallites). We make the approximation that crystallite scattering in the MTR occurs, due to its relative size, as in the unbounded textured medium. The attenuation term $\alpha_{Crystallites}$ is small (due to the relative size of the crystallites). In a textured medium ultrasonic attenuation depends on the direction of wave propagation. In our case the ultrasonic wave propagates through different MTRs with different preferred directions of crystallite texture, that are randomly oriented to each other and thus to the direction of wave propagation. Therefore, the crystallite scatter should be averaged over the propagation direction relative to the different preferred texture directions. Such averaging produces a smooth function reminiscent of the behavior of the covariance of the elastic modulus $\Xi_{1111}^{1111} = \langle \delta c_{1111} \delta c_{1111} \rangle$ which is responsible for forward scattering. For this reason we approximate the average crystallite attenuation, while wave propagates through many MTRs, by using the untextured isotropic attenuation as described in the attachment and factoring it by the texture covariance function $\langle \delta c_{1111} \delta c_{1111} \rangle$ which will provide the transition function from small to large σ . The resulting approximate crystallite attenuation is

$$\alpha_{Crystallites} = \alpha_{untextured} \langle \delta c_{1111} \delta c_{1111} \rangle, \quad (5.12)$$

where $\langle \delta c_{1111} \delta c_{1111} \rangle$ is a texture transitional function. The covariance of the elastic modulus $\Xi_{1111}^{1111} = \langle \delta c_{1111} \delta c_{1111} \rangle$ is taken from Yang et al. [5.12]:

$$\begin{aligned} \langle \delta c_{1111} \delta c_{1111} \rangle &= \langle c_{1111} c_{1111} \rangle - \langle c_{1111} \rangle^2 \\ &= 3(2A + 4B)^2 M_3 + 30D(2A + 4B)M_6 + 105D^2 M_7 \\ &\quad - [(2A + 4B)M_1 + 3DM_3]^2 \end{aligned} \quad (5.13)$$

and

$$\begin{aligned}
M_6 &= \frac{1}{48} (I_\sigma^0 - 3I_\sigma^2 + 3I_\sigma^4 - I_\sigma^6), \\
M_7 &= \frac{1}{384} (I_\sigma^0 - 4I_\sigma^2 + 6I_\sigma^4 - 4I_\sigma^6 + I_\sigma^8),
\end{aligned} \tag{5.14}$$

where σ is the texture parameter of the MTR and M_1, M_3 and I_σ^m are given in equation (5.5). This approximation for $\alpha_{Crystallites}$ becomes nearly exact for $\sigma > 0.2$ when the crystallites are almost randomly oriented; in this case $\alpha_{Crystallites} > \alpha_{MTR}$. For smaller σ , it is unnecessary for our analysis to account for the exact texture since the effect of crystallite scattering is then very small.

Figure 5.4 shows the total attenuation (solid lines) for a longitudinal wave propagating in the z axis direction in a material with duplex microstructures versus the texture parameter σ at frequencies of 5, 10 and 15 MHz. The elastic constants of the hexagonal crystallites and MTRs, the MTR radii and density used are given in table 5.1; the crystallites are assumed to be equiaxed grains and $a_x = a_y = a_z = 0.005$ mm. Each MTR includes roughly 24,000 crystallites. In addition to the total attenuation, figure 5.4 shows for frequency 15 MHz two attenuation components (equation (5.11)): α_{MTR} is shown by the dashed-dotted line and $\alpha_{Crystallites}$ by the dashed line. As one can see from the curves for 15 MHz in figure 5.4, the total attenuation is almost entirely contributed by the MTRs for small σ where the texture is moderately strong. As σ increases, the MTR related attenuation decreases and the total attenuation is contributed mostly by the $\alpha_{Crystallites}$ at $\sigma > 0.2$ crystallites since the MTRs vanish in the medium (figure 5.3) and the medium becomes a single phase medium with a small crystallite size. However, for strong texture (small σ) the MTR acts nearly as a single crystal and the crystallite scattering is negligible.

The total longitudinal wave attenuation versus frequency with different texture parameters σ of 0.01, 0.1 and 1 is presented in figure 5.5. The crystallite sizes are the same as for figure 5.4. As one can see from the figure, the total attenuation is greatest for the smallest σ (solid line); for this case the MTR behaves similarly to an α Ti single crystal (elastic constants at $\sigma=0$ in figure 5.3). The dotted line shows attenuation at $\sigma=1$ (essentially absence of the microtextured regions) and scattering is due to α Ti crystallites; it is much lower than the solid curve due to scatterer size reduction (from MTR to crystallite). The dashed line $\sigma=0.1$ shows an intermediate case.

One should note that the difference between the two curves for $\sigma=0.01$ and $\sigma=0.1$ is due to the MTR elasticity change. The MTR size is the same and, as one can see, the frequency behavior of the attenuation coefficients is very similar, preserving the same smooth transition from fourth, in the Rayleigh regime, to second power frequency dependence in the stochastic region (high frequency). In the transition range the frequency dependence deviates significantly from the Rayleigh or stochastic behavior where the longitudinal wave attenuation is characterized by a hump. For the dotted curve $\sigma=1$ the Rayleigh range is significantly extended and the transition range shifts significantly toward high frequency. In summary, the results show that the attenuation changed dramatically for different texture parameters due to significant differences in MTR and crystallite sizes and the reduction of the effective MTR stiffness in the intermediate cases.

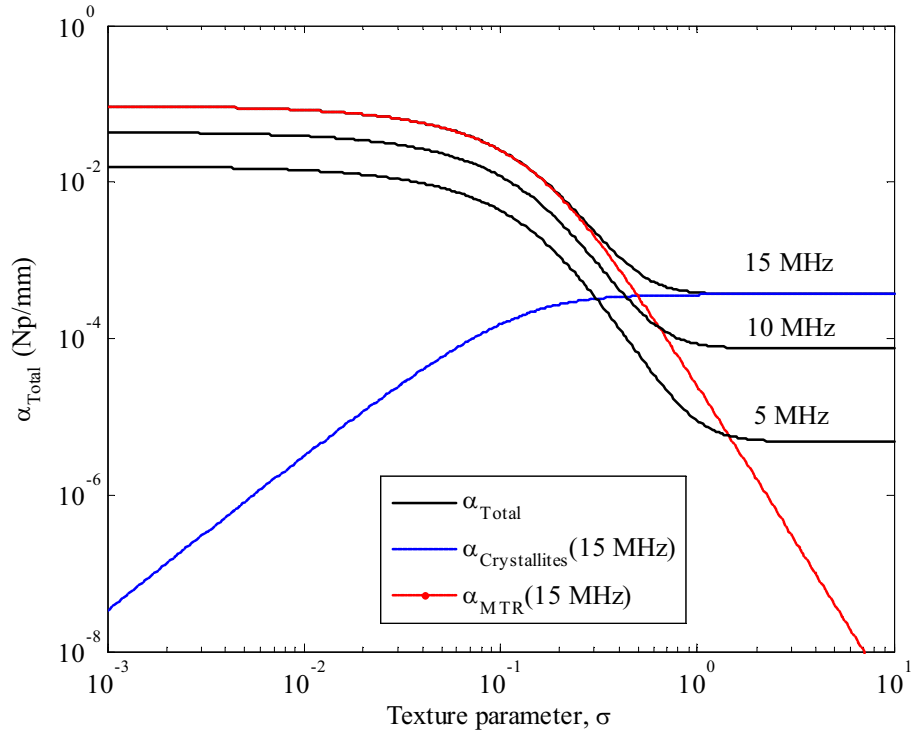


Figure 5.4: The total attenuation coefficients (solid lines) versus the texture parameter σ at three frequencies of 5, 10 and 15 MHz; longitudinal wave propagates in the z axis direction. Also shown for 15 MHz are the MTR and crystallite components of attenuation; α_{MTR} is dashed-dotted line and $\alpha_{Crystallites}$ is dashed line. The MTR radii are $a_x = 0.2$ mm, $a_y = 0.3$ mm and $a_z = 0.5$ mm and the radius of crystallites is 0.005mm.

Table 5.1: Elastic constants for crystallites and effective elastic constants and radii of MTRs.

Elastic constants α Ti [29] (GPa)					MTR effective elastic constants (GPa, $\sigma=0.075$)					MTR main radii (mm)			Density (g/cm ³)
c_{11}	c_{12}	c_{13}	c_{33}	c_{44}	C_{11}	C_{12}	C_{13}	C_{33}	C_{44}	a_x	a_y	a_z	ρ
136	78	68.5	163	40.6	139	76	70	156	39	0.16	0.19	0.29	4.54

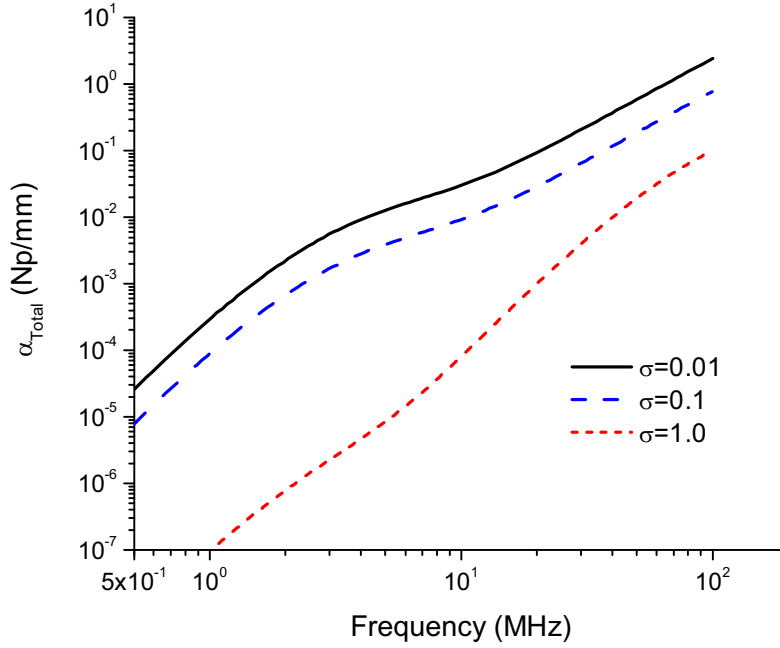


Figure 5.5: The total attenuation for longitudinal wave versus frequency with three texture parameters σ of 0.01, 0.1 and 1.0 when wave propagates in the z axis direction. The MTR radii is $a_x = 0.16$ mm , $a_y = 0.19$ mm and $a_z = 0.29$ mm and the radius of crystallites is 0.005mm.

In the next section we will compare our MTR model with ultrasonic attenuation and backscattering measurements. Accounting for the MTR scattering only, the backscattering coefficient in the medium formed by elongated MTRs is calculated using the method of [5.18, 5.19]:

$$\eta(\mathbf{k}) = \frac{Q_r V k^4}{(1 + k^2 l^2)^2}, \quad (5.15)$$

where $k = \sqrt{k_x^2 + k_y^2 + k_z^2}$ and $V = 8\pi a_x a_y a_z$ is the effective volume of the MTR; $l = 2\sqrt{n_x^2 a_x^2 + n_y^2 a_y^2 + n_z^2 a_z^2}$ is the interaction length [5.19] and \mathbf{n} is the wavenormal vector. The normalized elastic covariance for the MTR is denoted as $Q_r = BS_h / (16\pi^2 \rho^2 V_L^4)$ and the notation BS_h is defined as

$$BS_h = \frac{112}{1575} A_1^2 + \frac{48}{1575} A_2^2 + \frac{32}{1575} A_1 A_2, \quad (5.16)$$

where $A_1 = C_{33} - C_{11}$ and $A_2 = -C_{11} + C_{13} + 2C_{44}$. The effective elastic constants C_{ij} are given by equation (5.8) and are dependent on the texture parameter σ . Once we know the texture parameter σ , the MTR backscattering coefficient is obtained by equation (5.15) for arbitrary wave propagation direction. The value $\sqrt{\eta(k)}$ is proportional to the spectral amplitude of the root mean square (RMS) of the

backscattering signal and is used to compare with experiment. The scattering effect of the second phase (crystallites) is discussed in references [5.18, 5.19].

5.3 Ultrasonic Measurements and Comparison with the Model

In this section we report attenuation and backscattering measurements and comparison with the model. We use those independent measurements to demonstrate a reasonable consistency of the model to simulate ultrasonic wave interaction with the complex microstructure of the Ti alloy discussed in this work.

5.3.1 Near α -Ti Sample

Ultrasonic measurements have been performed in three orthogonal directions on one engine-graded near α -Ti alloy sample, Ti-6Al-2Sn-4Zr-2Mo (Ti-6242), and compared with the model. The 30 x 30 x 60 mm³ rectangle sample has been cut from the original Ti alloy forging. The sample microtexture/microstructure is reported in Ref. [5.4] (sample #2). The crystallites in the sample are nearly equiaxed primary α grains and the MTR have elongated shapes which we approximate by a general ellipsoid. Due to forging the shapes of the MTRs are preferably oriented in the sample. The averaged MTR radii in the direction of wave propagation were determined for this sample by the directional ultrasonic backscattering measurements described in ref. [5.19] and supported by the results of ref. [5.4]. The MTR orientation relative to the laboratory coordinate system was also determined [5.31] by the directional ultrasonic backscattering measurements. The angle of the averaged MTR ellipsoid orientation relative to the axial direction of the sample in the axial and hoop plane is $\theta = 73^\circ$ (see insert in figure 5.6); this allows us to determine the main radii of the MTR (they are listed in table 5.1). The elastic properties of α crystallites are also listed in table 5.1 together with the computed averaged effective properties for the MTR; the elastic properties of α crystallites used are those measured experimentally for Ti-6%Al α single crystal [5.29] (one should note that in the second column of table 5.1 of reference [5.29] is a misprint in the elastic constant legend listed as C_{22} , it should be read C_{33} as is listed in table 5.1 of the current work; they were correctly listed in ref. [5.4]). Those elastic properties are more suitable than elastic constants for pure α Ti used by us in reference [5.13].

To estimate macroscopic texture longitudinal ultrasonic velocity has been measured in three orthogonal directions of the sample. We found that the velocity deviation from an average (isotropy) is within $\pm 0.3\%$, which is comparable to the possible error due to geometry imperfections of our sample. In any case it is much smaller than the texture-induced 2% longitudinal velocity difference [5.21] measured in Ti-6Al-4V alloy along and perpendicular to the texture direction. Thus we conclude that our sample is sufficiently macroscopically isotropic for an application of our model which assumes that the polycrystalline medium is macroscopically untextured.

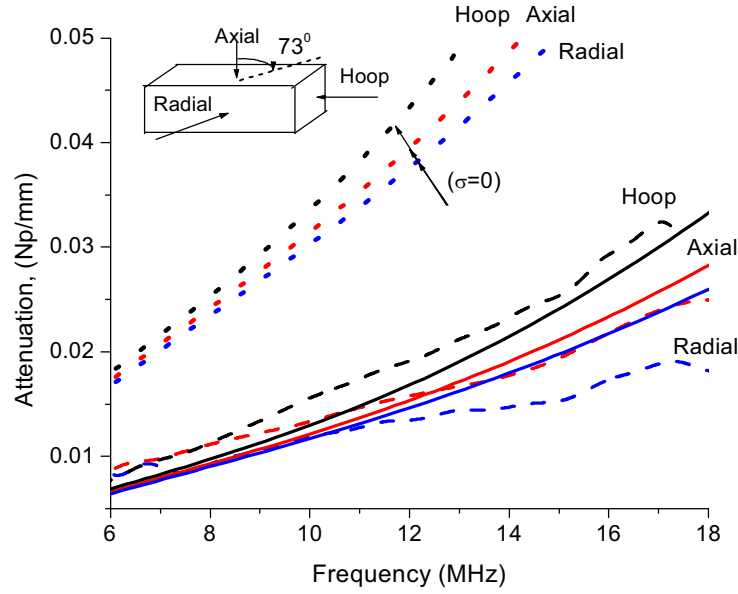


Figure 5.6: Longitudinal wave attenuation coefficients versus frequency in three orthogonal directions of titanium alloy sample. Dashed lines represent measurement and solid lines are analytical model; the texture parameter is $\sigma = 0.075$; the average MTR radii are as in table 5.1. The orientation angle of the averaged MTR ellipsoid is $\theta = 73^\circ$ relative to the axial direction of the sample in the axial and hoop plane. The top dotted lines are provided for comparison; they are calculated for the same geometrical parameters of the MTR as the actual one except the MTR elastic properties are for a single α Ti (table 5.1) crystal ($\sigma = 0$). The texture parameter $\sigma = 0.075$ is obtained by shift of the dotted curves to match the experimental data.

5.3.2 Attenuation and Backscattering Measurements

The attenuation measurements were conducted by the pulse-echo immersion technique at normal incidence in three orthogonal directions (axial, radial and hoop). Ultrasonic signals were excited and received by a pulser/receiver (Panametrics, USA) operating in pulse-echo mode. The ultrasonic signals have been acquired and digitized, using a 12-bit, 125MHz digitizing board, for later processing. A 12 mm diameter plane ultrasonic transducer with 10 MHz central frequency was used for measurement. The transducer was positioned about 21mm away from the sample top surface and carefully aligned for normal incidence. The transducer beam diffraction correction has been accounted for and the data processing procedure is as described in [5.4]. The digitized waveforms were gated for the Fast Fourier Transform (FFT) and then the frequency spectra were processed and analyzed. Front surface echo and first and second back wall reflections were generally used for analysis. Frequency dependences of the attenuation coefficients were obtained by accounting for the ultrasonic diffraction correction and taking ratios of the frequency responses of consecutive pulse reflections. The measurements were performed in multiple sample locations and averaged. Automated scanning measurements of attenuation were also performed and resulted in similar averaged results.

Absolute backscattering measurements were also performed in three orthogonal directions of the sample with a 15-MHz 12-mm-diameter plane ultrasonic transducer. The rms of the backscattering signal normalized on the transducer frequency response is proportional to the square root of the backscattering coefficient $\sqrt{\eta(f)}$ [5.32, 5.19] obtained in our analysis. The details of our backscattering measurement

methodology and data processing were described in [5.19]. The difference is that the measurements in [5.19] were focused on relative directional backscattering data processing which is not affected by crystallites ODF in the MTRs since the elastic factor in the BS coefficient is purposely excluded in directional measurements. In this work our interest is in the MTRs elastic factor and thus absolute backscattering measurements.

Samples were scanned over each of the six faces with 1 mm steps and signals from 656 positions were acquired on radial and axial faces and from 336 positions on hoop faces. Digitized signals were time averaged for every spatial position and acquired at about 40 μ s duration; the first 6 μ s of the signal inside the sample were gated for backscattering RMS calculation (this corresponds to the 18 mm propagation length in the sample). To eliminate the pulse generator and transducer tail [5.32] subtraction of the spatially averaged backscattering signal from the averaged RMS was applied prior to deconvolution. For the deconvolution we have used the sample front reflection spectrum normalized by the theoretical diffraction correction in water. The backscattering signal attenuation is small in this sample and its correction produces negligible results on the data. The effect of processing was compared with and without the diffraction correction and backscattering attenuation in the sample: the difference was not more than 3% at 10 MHz (the backscattering attenuation should be distinguished from the apparent attenuation partly related to the received signal interference on the receiver [5.33]). Next, in order to obtain the absolute backscattering coefficient, the backscattering RMS was deconvolved with the front reflected signal and then normalized as discussed in [5.32] with modification needed for the near field of the transducer [5.31].

5.3.3 Measurement Results

The measured attenuation coefficients are shown by dashed lines in figure 5.6 and the measured backscattering signal RMS are shown by dashed lines in figure 5.7. Both attenuation and backscattering data are in three orthogonal directions of the sample: axial, radial and hoop. For the backscattering only (useful) data uncorrupted by deconvolution are presented (dashed lines from 5 to 18 MHz). The frequency range that was selected as acceptable for the backscattering spectrum is nearly the same frequency range that is meaningful for the attenuation coefficients shown in figure 5.6. It is well known that deconvolution increases the noise effect; one needs to be especially careful in this regard in deconvolution of BS data due to a several-orders-of-magnitude difference in the backscattering and front wall signal with which the BS signal is deconvolved (the raw spectrum has larger bandwidth compared to that deconvolved by the front echo signal spectrum [5.19]).

In this frequency range (5 to 20 MHz) the experimental backscattering data is nearly independent of frequency with only slight bending-up toward high frequency which is attributed to the crystallite scattering [5.19]; the crystallite effect on the backscattering is small and is not considered in this work (for discussion of the crystallite scattering effect see ref. [5.19]). The dependence on the MTR size in the usable frequency range, figure 5.7, mainly displays itself in the backscattering RMS level. The backscattering data shown in figure 5.7 is the same data set that was used in [5.19] for the backscattering coefficient ratios but in a wider frequency range since the deconvolution by the front echo was not used in [5.19] and thus the usable signal bandwidth is significantly larger. Due to the use of the wider frequency range those backscattering ratios exhibit much stronger frequency dependences [5.19] which are affected at high frequency by crystallite scattering.

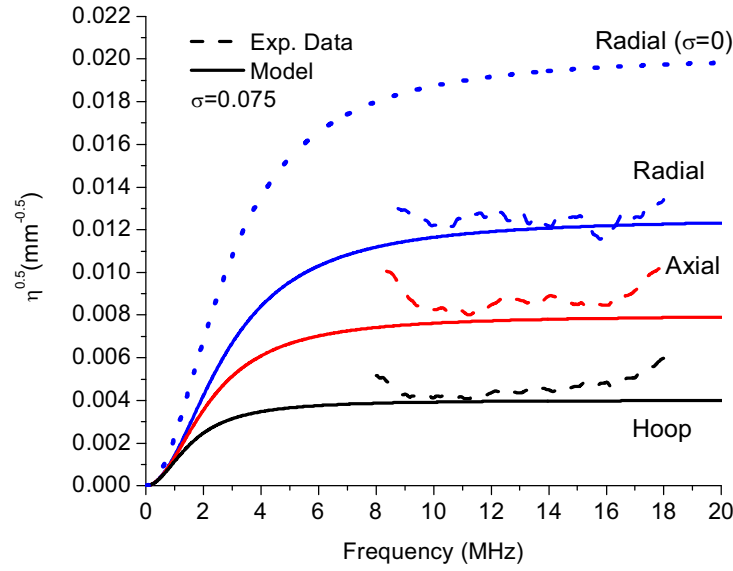


Figure 5.7: Backscattering coefficient for the MTRs versus frequency in the axial, radial and hoop directions. The irregular dashed lines are experimental data and solid lines are the theoretical model; the texture parameter is $\sigma = 0.075$; the average MTR radii and orientation as in figure 5.6. The top dotted line is provided for comparison; it is for the backscattering amplitude in the radial direction for an artificial material with the same parameters as the actual one except the MTR elastic properties are for a single α Ti (table 5.1) crystal ($\sigma = 0$).

5.3.4 Comparison with the Model and Discussion

The measured attenuation coefficients are shown by dashed lines in figure 5.6 in three orthogonal directions of the sample: axial, radial and hoop. The theoretical attenuation coefficients are shown versus frequency (dotted and solid lines) together with experiment in figure 5.6; the averaged MTR parameters used for calculations are as those discussed in the previous sections. Dotted lines show simulated attenuation for the MTRs with perfect orientation of crystallites ($\sigma = 0$, MTR is a single α -Ti crystal); they display significantly higher attenuation than measured values. The microtexture parameter σ was used as an adjustable parameter in the model to shift the theoretical curves to the experimental attenuation curves. This resulted in the averaged microtextural parameter $\sigma = 0.075$ and the calculated effective elastic properties used for the MTR listed in table 5.1; they were obtained as described in Section 2.2. The attenuation coefficient curves for $\sigma = 0.075$ are shown in figure 5.6 by solid curves. The value of the texture parameter σ obtained indicates moderate misorientation of crystallites in the MTR (figures 5.2, 5.3). In the frequency range of the measurements the contribution of the crystallite scattering to total attenuation is small (figure 5.4) and can be neglected.

The attenuation measurements are in the Rayleigh-to-stochastic transition range which is characterized by the transition from fourth, in the Rayleigh regime, to second power frequency dependence in the stochastic region. The transition range for longitudinal wave attenuation is characterized by a hump [5.10, 5.13], which is physically explained by a transition of the scattering mechanism: from longitudinal-to-transverse wave scattering in the Rayleigh region to longitudinal-to-longitudinal in the stochastic region. The existence of the hump complicates frequency behavior and interpretation of the attenuation experimental data especially in the narrow frequency range in our experiments. The attenuation model agrees reasonably with the measurements. The possible errors are in part due to the approximate estimation of the average

MTR radii and simplified assumptions of the model, in particular the approximation of the two-point correlation function. Even for well characterized single phase equiaxed microstructures [5.34] there is some discrepancy between the measured attenuation and the model as was discussed in [5.35].

To further support the model and illustrate its consistency figure 5.7 compares the measured (irregular dashed lines) and simulated backscattering amplitudes $\sqrt{\eta(k)}$ in the three orthogonal directions of the sample (the MTR parameters are the same as those used for figure 5.6; $\sigma = 0.075$). To illustrate the effect of σ figure 5.7 shows by a dotted line the backscattering amplitude for the MTRs with perfect orientation of crystallites, $\sigma = 0$, indicating a significant difference. Note from figures 5.6, 5.7 that backscattering and attenuation have opposite behaviors with the ellipsoid radii: in the axial direction (the largest MTR size in this propagation direction) the backscattering is smallest while the attenuation is largest; in the radial direction (the smallest MTR size in this propagation direction) the backscattering is largest and the attenuation is smallest. Such an opposite behavior of the backscattering and attenuation on size is consistent with similar observations by others [5.21, 5.32] and our model predictions (for discussion see [5.5, 5.19]).

5.4 Further Discussion and Sensitivity to Parameter Uncertainty

5.4.1 Discussion and Sensitivity to Parameter Uncertainty

This section does not describe the inverse problem, i.e. determination of all microstructure parameters from ultrasonic measurements. The inverse problem of determination of the average radii of the ellipsoidal MTRs was addressed by us in [5.18, 5.19], using the ratio of backscattering coefficients in different directions, and in [5.31], using the backscattering/attenuation coefficients ratio. In both those methods the elastic (tensorial) factor is cancelled thus reducing the number of parameters to be determined. Also, in the backscattering ratio method [5.18, 5.19], the system parameters are excluded without deconvolution by the reference signal allowing one to increase the frequency bandwidth of the method [5.19]. We are aiming to show that the introduced microtexture model and microtexture parameter σ provide a consistent way to describe and simulate experimental ultrasonic attenuation and backscattering if the average radii in the geometrical correlation function w_r , equation (A1), for the microtextured regions are known.

In this section we pose the question if our effective model of the elastic properties and texture of the MTRs provides a consistent simulation framework to predict two independently measured ultrasonic characteristics of the same sample: attenuation and backscattering. The main radii for the MTR correlation function are taken from our previous backscattering ratio measurements [5.19]. However, if those radii are uncertain and because the MTR scattering change due to radii change may be potentially compensated by the microtexture change, the question may be raised if a different MTR texture parameter exists for the different set of radii that equally well match the experimental data. Thus the question is the sensitivity to and the uniqueness of the obtained parameter set. Below, without introducing rigor estimates, we will illustrate the sensitivity to the parameter set and show that the original parameter set provides significantly better visual matching with the experimental backscattering data; a complete investigation of those issues is beyond the scope of this work.

Let us first assume that the averaged MTR radii are increased by 50% which leads to increase of simulated ultrasonic attenuation. By increasing the parameter σ , similarly as described in the previous section and shown in figure 5.6, we find that a new parameter $\sigma = 0.092$ provides reasonable visual overlap between simulated and measured attenuation coefficients (recall that increase of the parameter σ corresponds to microtexture decrease). The comparison of new simulated attenuation and measurements is not shown since the resulting behavior is similar to that shown in figure 5.6. Next for this new parameter σ and 50% increase of the averaged MTR radii we calculate the backscattering amplitude in all three propagation directions. The calculated backscattering results for the new sizes and $\sigma = 0.092$ are shown by dotted lines

in figure 5.8 together with the measurements (irregular dashed lines from figure 5.7); also for comparison the simulated results from figure 5.7 (for the original MTR parameters) are also shown by solid lines. It is clear that the new MTR parameters do not provide good agreement with the measured backscattering amplitude.

Next the average MTR size was changed by $\pm 25\%$ and the same approach as above is used to obtain the two texture parameters σ by visual best fit of the experimental attenuation coefficients. Then, with the new texture and radii parameters, backscattering amplitudes $\sqrt{\eta(k)}$ are computed and then compared to those measured; they are shown in figure 5.9: i. -25% decrease in size and $\sigma = 0.067$, dashed-dotted lines; ii. 25% size increase and $\sigma = 0.084$, dotted lines. The experimental backscattering data, dashed irregular curves, are bounded by the simulated $\pm 25\%$ curves. Also the simulated data with the original parameters (solid curves in figures 5.7, 5.8) are bounded by these curves; recall that the original averaged MTR radii used here were determined by optimization data inversion from the three directional backscattering ratios [5.19] and no attempt is made to obtain them in this work.

In our frequency range and MTR sizes if one arbitrarily deviates the MTR radii from the actual value and correspondingly changes σ to fit the experimental attenuation coefficients, the backscattering coefficient will shift in the opposite direction deviating from the experiments (while both attenuation and backscattering synchronously depend on increase or decrease of σ , in this frequency range they depend oppositely with the MTR size: the attenuation increase but the backscattering decreases ([5.19], figure 5.4). Thus, this analysis indicates that there exists a particular single set of model parameters (MTR size and texture) best predicting both attenuation and backscattering coefficients.

There are other uncertainties in model assumptions when applied to predict measured results. In particular, we use elastic constants measured [5.29] on a single $\alpha - \text{Ti}$ crystal (they are listed in table 5.1). However, the alloy composition for forgings of different manufactures, even for similarly specified alloys, can be different and thus the elastic constants for $\alpha - \text{Ti}$ crystallites in our samples are not known exactly. Also in addition to $\alpha - \text{Ti}$ crystallite, 26% of the secondary alpha (small size α / β colonies) exists in our sample [5.4] that has a different set of effective elastic constants of low symmetry [5.29]. These factors result in some deviation of the determined microtexture parameter σ from the actual averaged microtexture of the MTRs. A quantitative measurement of the ODF distribution of the crystallites in the MTRs for comparison with ultrasonic measurements requires special MTR segmentation in the OIM data; those activities are a part of the current cooperative effort in the extension of the study [5.4] and will be addressed elsewhere.

The specimen used for study in this work is one of several jet-engine titanium-alloy specimens characterized in Ref [5.4] (sample#2). It is the best characterized sample that was used in our follow-up experimental studies, and is for this reason selected for this work. However, we have applied the same methodology to sample#1 of Ref. [5.4]. It has larger MTRs, which result in larger attenuation; it also has a lower percentage of secondary alpha phase. The complete methodology of this work was applied to this sample too. The comparison of the model prediction and the experiment for this sample shows very similar quality of results as those described above. The obtained texture parameter for sample#1 is $\sigma = 0.03$; it is smaller than $\sigma = 0.075$ obtained for sample#2 studied in this work. This indicates stronger microtexture in sample#1 which is consistent with the OIM images [5.4] showing for sample#1 a narrower color range for crystallite orientations in the MTRs.

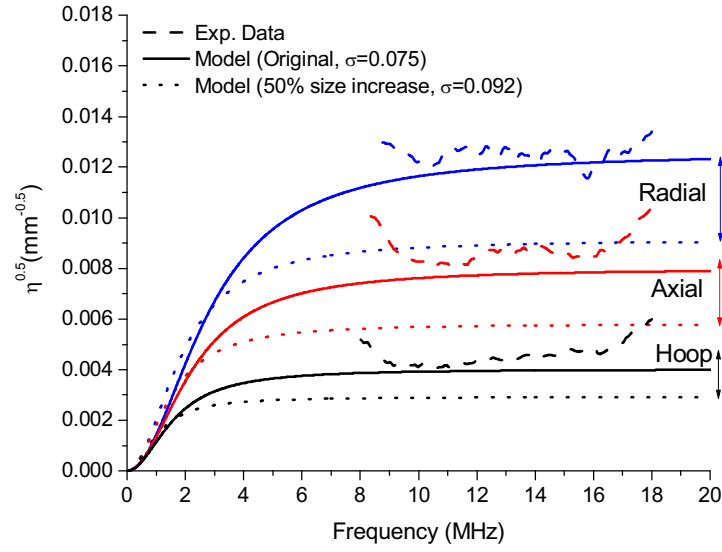


Figure 5.8: Calculated backscattering amplitude (dotted lines) with 50% increase of average MTR ellipsoid radii; the texture parameter is also increased to $\sigma = 0.092$ to match the attenuation data (the MTR texture decreases with the texture parameter increase). The irregular dashed lines are measurements. The calculated backscattering curves for the original radii and texture parameters as in figure 5.7 are also shown for comparison by solid lines.

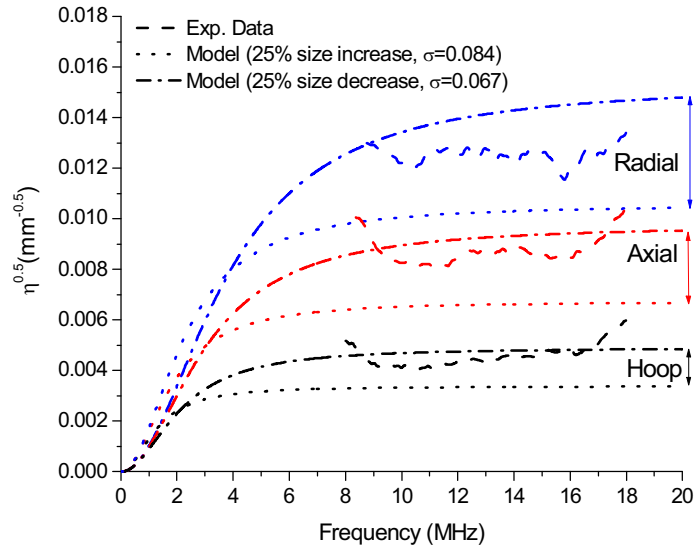


Figure 5.9: The same as in figure 5.7 where dashed lines represent backscattering measurement. Calculations are for the average MTR radii proportionally increased by 25% with the texture parameter $\sigma = 0.084$ (dotted lines) or decreased by 25% with the texture parameter $\sigma = 0.067$ (dashed-dotted lines); the parameters σ were obtained by match with the attenuation curves. The measured values are bounded between the calculations for the increased and decreased MTR radii.

5.4.2 Orthotropic Crystallites and 3-D Texture

A phenomenological ultrasonic backscattering model described above for microtextured explicitly accounts for preferred orientation in the MTRs of hexagonal alpha crystallites. It is in a reasonable agreement with experiment and has reasonable predictive capabilities of the model with proper selection of a single averaged microtexture parameter. It assumes hexagonal symmetry of crystallites and the effective elastic tensor of the resulting clusters (MTRs) and explicitly accounted for only hexagonal alpha phase crystallites in the clusters. However, about 10-50% of secondary alpha (alpha-beta phase) may exist in these alloys [5.4]; it has comparable size to and is intermixed with the primary alpha crystallites. The secondary alpha-beta phase has lower than hexagonal symmetry [5.29], thus the combined elastic behavior of crystallites forming the MTR may deviate from that of the hexagonal. Also, if clusters have a 3D microtexture they should be considered elastically orthotropic. This model was generalized in this work by assuming [5.36] orthotropic symmetry of the crystallites and the resulting MTRs and to provide better understanding of ultrasonic wave interaction with orthotropic orientation clusters.

Microtextured regions (MTRs) are described by a generalized orientation distribution function (GODF) in terms of three texture parameters; the attenuation and backscattering coefficient for such duplex microstructures are obtained. The MTRs are formed by orientation clustering of a large number of small orthorhombic crystallites with a preferred orientation in the MTR; those MTRs behave as large orthorhombic elastic scatterers with effective elastic properties depending on three texture parameters.

The ensemble elastic properties in MTRs are characterized by the effective stiffness by averaging elastic properties of orthorhombic crystallites weighted by the generalized orientation distribution function within the MTR region. This means that, at the large (MTR) scale, all MTRs are described as orthorhombic ellipsoidal regions having the same ellipsoid axis directions and the same (average) effective elastic constants with random crystallographic orientations of MTRs relative to each other. The total ultrasonic attenuation and backscattering in the polycrystalline medium are considered as a sum of scattering by MTRs, with effective elastic properties, and additional scattering by orthorhombic crystallites within the MTRs.

The resulting wave scattering model for MTR is quasi-static in the sense that the MTRs in the scattering model are considered as ellipsoidal single crystals with effective elastic properties and the scattering by crystallites, inside the MTRs, is considered separately as an additive scattering term. Therefore, the total attenuation and backscattering coefficients are determined by adding together both the MTR and crystallite attenuation/backscattering. The numerical attenuation results have shown that for relatively weak microtexture (larger σ) the MTR scattering is small and the crystallite attenuation makes a major contribution even though the crystallites are of significantly smaller size. For strong microtexture (small σ) the MTR attenuation term is dominant. For certain texture parameters two characteristic humps are observed due to the contribution of both attenuation components (the lower frequency hump for MTR scattering and the high frequency hump for the crystallites). The backscattering result has shown that it is the highest when the wave propagates in the direction of the smallest ellipsoid radius, and it is the lowest in the direction of the largest radius. The crystallite backscattering is included at higher frequencies.

5.5 Conclusions

We have introduced an approximate attenuation and backscattering models for duplex microstructures with elongated microtextured regions (MTRs) which is particularly applicable to forged Ti alloys. The MTRs are formed by a large number of small crystallites with a preferred orientation in the MTR. We approximate the crystallite ODF in the MTR by a Gaussian distribution function characterized by its width σ and determine the homogenized effective elastic properties of MTRs, which depend on σ . The resulting wave scattering model for MTR is quasi-static in the sense that the MTRs in the scattering model are considered as ellipsoidal single crystals with effective elastic properties and the scattering by crystallites, inside the MTRs, is considered separately as an additive attenuation term. Thus the total longitudinal attenuation coefficient is obtained by adding together both the MTR attenuation and crystallite attenuation. The results have shown that for strong microtexture (small σ) the MTR attenuation term is dominant, for relatively weak microtexture (large σ) the MTR scattering is small and the crystallite attenuation makes a major contribution even though it is significantly lower due to the smaller size of the crystallites.

Examples of attenuation and backscattering measurements are described and compared with the model. The average MTR sizes and crystallite elastic constants are obtained inversion of our directional backscattering measurements. Once the ODF parameter σ is selected the model predicts reasonably well both attenuation and backscattering in the different directions of the sample. This indicates the consistency of the model and the measurements.

Also, generalized model was developed [5.36] in this project; it in this assumes orthotropic symmetry of the crystallites and the resulting MTRs and provides better understanding of ultrasonic wave interaction with orthotropic orientation clusters.

Attachment: Attenuation Coefficients for Hexagonal Elongated Grains

In this attachment we briefly describe the computation algorithm for the attenuation coefficients of the medium with hexagonal elongated grains. Given the geometrical two point correlation function of ellipsoidal [5.5, 5.14, 5.17-5.19] grains as a generalized exponential function in terms of three effective ellipsoid radii in the form

$$w(x, y, z) = \exp \left(- \sqrt{\frac{x^2}{a_x^2} + \frac{y^2}{a_y^2} + \frac{z^2}{a_z^2}} \right), \quad (\text{A1})$$

where a_x, a_y and a_z are the effective ellipsoid radii for three major axes corresponding to x, y and z coordinates (figure 5.1(b)) , the nondimensional attenuation coefficients for hexagonal and elongated crystallites are expressed as

$$\begin{aligned} \alpha_L &= \alpha_{LL} + \alpha_{LT}, \\ \alpha_T &= \alpha_{TT} + \alpha_{TL}, \end{aligned} \quad (\text{A2})$$

where α_{QM} are attenuation coefficient components due to scattering of wave mode Q to wave mode M . As described in detail in [5.30] and similar to the approach developed for cubic elongated crystallites [5.5], we obtain for each attenuation component α_{QM}

$$\begin{aligned} \alpha_{LL} a_x &= \frac{x_L^4 R_0 R_1}{4\pi V_L^4 \rho^2} \int_0^{2\pi} \int_0^\pi \frac{I_{LL}(\theta, \varphi)}{[1 + S_{LL}^0 + S_{LL}^1 + S_{LL}^2]^2} \sin \theta d\theta d\varphi, \\ \alpha_{LT} a_x &= \frac{x_T^4 R_0 R_1}{4\pi V_L^3 V_T \rho^2} \int_0^{2\pi} \int_0^\pi \frac{I_{LT}(\theta, \varphi)}{[1 + S_{LT}^0 + S_{LT}^1 + S_{LT}^2]^2} \sin \theta d\theta d\varphi, \\ \alpha_{TL} a_x &= \frac{1}{2} \left(\frac{V_T}{V_L} \right)^2 \alpha_{LT} a_x, \\ \alpha_{TT} a_x &= \frac{x_T^4 R_0 R_1}{8\pi V_T^4 \rho^2} \int_0^{2\pi} \int_0^\pi \frac{I_{TT}(\theta, \varphi)}{[1 + S_{TT}^0 + S_{TT}^1 + S_{TT}^2]^2} \sin \theta d\theta d\varphi, \end{aligned} \quad (\text{A3})$$

where S_{QM}^0, S_{QM}^1 and S_{QM}^2 were given as

$$\begin{aligned} S_{QM}^0 &= x_Q^2 + x_M^2 - 2x_Q x_M (\mathbf{p} \cdot \mathbf{s}) \\ S_{QM}^1 &= (R_0^2 - 1) (x_Q \cos \tau - x_M \cos \theta)^2 \\ S_{QM}^2 &= (R_1^2 - 1) (x_Q \sin \tau \sin \varphi_\tau - x_M \sin \theta \sin \varphi)^2 \end{aligned} \quad (\text{A4})$$

and

$$\begin{aligned} x_L &= \omega a_x / V_L = k_l a_x, & x_T &= \omega a_x / V_T = k_t a_x \\ X &= \mathbf{p} \cdot \mathbf{s} = \cos \theta_{ps}, & R_0 &= a_z / a_x & R_1 &= a_y / a_x \end{aligned}$$

V_L , V_T are macroscopic velocities obtained by Voigt averaging [5.10] (for MTRs they are obtained from the effective elastic constants); it is important to note that as a result of averaging those velocities are independent of the parameter σ and are thus equal to those used for the second phase (crystallites).

Using the analysis of [5.13] for the hexagonal crystallites the inner products are written in the form

$$\begin{aligned} I_{LL}(X) &= A_{LL} + B_{LL}X^2 + C_{LL}X^4, \\ I_{LT}(X) &= A_{LT} + B_{LT}X^2 + C_{LT}X^4, \\ I_{TT}(X) &= A_{TT} + B_{TT}X^2 + C_{TT}X^4, \end{aligned} \quad (A5)$$

where the coefficients A_{QM} , B_{QM} , and C_{QM} were expressed in terms of A , B and D in the following:

$$\begin{aligned} A_{LL} &= \frac{4}{45}A^2 + \frac{8}{1575}D^2 + \frac{8}{315}AD, \\ B_{LL} &= \frac{4}{15}A^2 + \frac{16}{15}B^2 + \frac{92}{1575}D^2 + \frac{64}{45}AB + \frac{32}{63}BD + \frac{88}{315}AD, \\ C_{LL} = C_{TT} = -C_{LT} &= \frac{16}{45}B^2 + \frac{4}{525}D^2 + \frac{32}{315}BD, \\ A_{LT} &= \frac{2}{15}A^2 + \frac{4}{15}B^2 + \frac{2}{105}D^2 + \frac{4}{15}AB + \frac{4}{35}BD + \frac{8}{105}AD, \\ B_{LT} &= \frac{28}{45}B^2 + \frac{32}{1575}D^2 + \frac{4}{15}AB + \frac{68}{315}BD + \frac{4}{105}AD, \\ A_{TT} &= \frac{13}{45}B^2 + \frac{23}{1575}D^2 + \frac{26}{315}BD, \\ B_{TT} &= -\frac{1}{3}B^2 - \frac{1}{175}D^2 - \frac{2}{21}BD. \end{aligned} \quad (A6)$$

and

$$X = \hat{\mathbf{p}} \cdot \hat{\mathbf{s}} = \cos(\phi - \phi_r) \sin \theta \sin \tau + \cos \theta \cos \tau. \quad (A7)$$

The wave propagation and scattering directions are defined in the coordinate system as shown in figure 5.1(b) by

$$\begin{aligned} \mathbf{p} &= (\sin \tau \cos \varphi_r, \sin \tau \sin \varphi_r, \cos \tau), \\ \mathbf{s} &= (\sin \theta \cos \varphi, \sin \theta \sin \varphi, \cos \theta). \end{aligned}$$

For the attenuation term α_{MTR} in equation (5.11) the coefficients $A = A_{MTR}$, $B = B_{MTR}$, $D = D_{MTR}$ in equation (A6) are obtained from equation (5.10).

Bibliography

Chapter 3

- 3.1 H. H. Yuce, D. V. Nelson and M. T. Resch. The use of surface acoustic waves to study small fatigue cracks in 7075-T651 aluminum and 4340 steel. *Rev Prog Q*, 3A: 105-113, 1985.
- 3.2 M. T. Resch and D. V. Nelson. An ultrasonic method for measurement of size and opening behavior of small fatigue cracks Small-crack test methods. *ASTM STP* 1149: 169-196, 1992.
- 3.3 J.-Y. Kim and S.I. Rokhlin. Surface acoustic wave measurements of small fatigue cracks initiated from a surface cavity. *Int. J. Solids Struct.*, 39: 1487-1504, 2002.
- 3.4 S.I. Rokhlin and J.-Y. Kim. In-situ ultrasonic measurement of crack closure. *Int. J. Fatigue*, 25: 51-58, 2003.
- 3.5 J.-Y. Kim, V. A. Yakovlev and S. I. Rokhlin. Surface acoustic wave modulation on a partially closed fatigue crack, *J. Acoust. Soc. Am.*, 115(5): 1961-1973, 2004.
- 3.6 H. Xiao and P.B. Nagy. Enhanced ultrasonic detection of fatigue cracks by laser-induced crack closure. *J. Appl. Phys.*, 83: 7453-7460, 1998.
- 3.7 D. Donskoy, A. Sutin and A. Ekimov. Nonlinear acoustic interaction on contact interfaces and its use for nondestructive testing. *NDT&E Int.* 34: 231-238, 2001.
- 3.8 I.Y. Solodov. Ultrasonics of nonlinear contacts: Propagation, reflections and NDE applications. *Ultrasonics*, 36: 383-390, 1998.
- 3.9 J.P. Jiao, B.W. Drinkwater, S.A. Nield and P.D. Wilcox. Low-frequency vibration modulation of guided waves to image nonlinear scatterers for structural health monitoring. *Smart Mater. Struct.*, 18 065006 (8pp), 2009.
- 3.10 J.H. Cantrell and W.T. Yost. Nonlinear ultrasonic characterisation of fatigue microstructures. *Int. J. Fatigue*, 23: 487-490, 2001.
- 3.11 G.D. Connolly and S.I. Rokhlin. Enhancement of fatigue crack monitoring by surface acoustic wave reflection and modulation in a space-cycle-load domain: an imaging approach. *J. SHM*, 11(2): 187-196, 2011.
- 3.12 S.I. Rokhlin, J.-Y. Kim, B. Xie and B. Zoofan. Nondestructive sizing and localization of internal microcracks in fatigue samples. *NDT&E Int.* 40: 462-470, 2007.
- 3.13 A.J. Croxford, P.D. Wilcox, B.W. Drinkwater and G. Konstantinidis. Strategies for guided-wave structural health monitoring. *Proc. Royal Soc. A*, 463: 2961-2981, 2007.
- 3.14 A. Raghavan and C.E.S. Cesnik. Review of guided-wave structural health monitoring. *Shock & Vibration Digest*, 39(2): 91-114, 2007.
- 3.15 J.P. Lynch and K.J.Loh. A summary review of wireless sensors and sensor networks for structural health monitoring. *Shock & Vibration Digest*, 38(2): 91-128, 2006.
- 3.16 S.I. Rokhlin and J.-Y. Kim. In-situ ultrasonic monitoring of surface fatigue crack initiation and growth from surface cavity. *Int. J. Fatigue*, 25: 41-49, 2003.

- 3.17 S. Suresh. *Fatigue of Materials* 2nd Ed. Cambridge University Press, 1998.
- 3.18 I.A. Viktorov. *Rayleigh and Lamb Waves: physical theory and applications*. Pub. Plenum Press, 1967.
- 3.19 O. Buck, W.L. Morris and J.M. Richardson. Acoustic harmonic generation at unbonded interfaces and fatigue cracks. *Appl. Phys. Letters*, 33: 317-373, 1978.
- 3.20 Mi, J.E. Michaels and T.E. Michaels. An ultrasonic method for dynamic monitoring of fatigue crack initiation and growth. *J. Acoust. Soc. Am.*, 119(1): 74-85, 2005.

Chapter 4

- 4.1 L. Sandrin, M. Tanter, J.-L. Gennisson, S. Catheline and M. Fink. Shear elasticity probe for soft tissues with 1-D transient elastography. *IEEE T. Ultrason. Ferr.*, 49(4): 436-446, 2002.
- 4.2 M.A. Lubinski, S.Y. Emelianov and M. O'Donnell. Speckle tracking methods for ultrasonic elasticity imaging using short-time correlation. *IEEE T. Ultrason. Ferr.*, 46(1): 82-96, 1999.
- 4.3 A.R. Skovoroda, S.Y. Emelianov, M.A. Lubinski, A.P. Sarvazyan and M. O'Donnell. Theoretical analysis and verification of ultrasound displacement and strain imaging. *IEEE T. Ultrason. Ferr.*, 41(5): 302-313, 1994.
- 4.4 A.I. Bowler, B.W. Drinkwater and P.D. Wilcox. An investigation into the feasibility of internal strain measurement in solids by correlation of ultrasonic images. *Proc. Royal Soc. A*, 467: 2247-227, 2011.
- 4.5 V. Sinha, J. E. Spowart, M. J. Mills and J. C. Williams. Observations on the faceted initiation site in the dwell-fatigue tested Ti-6242 alloy: Crystallographic orientation and size effects. *Metall. Mater. Trans. A*, 37: 1507-1518, 2006.
- 4.6 A.L. Pilchak and J. C. Williams. Observation of facet formation in near- α titanium and comments on the role of hydrogen. *Metall. Mater. Trans. A*, 42(4): 1000-1027, 2010.
- 4.7 A. Bhattacharjee, A.L. Pilchak, O.I. Lobkis, J.W. Foltz, S.I. Rokhlin and J.C. Williams. Correlating ultrasonic attenuation and microtexture in a near alpha titanium alloy. *Metall. Mater. Trans. A*, 42(8): 2358-2372, 2011.
- 4.8 O.I. Lobkis and S. I. Rokhlin. Characterization of polycrystals with elongated duplex microstructure by inversion of ultrasonic backscattering data. *Appl. Phys. Lett.*, 96 (16): Art.161905-1-3, 2010.
- 4.9 O. Lobkis, L. Yang, J. Li and S. I. Rokhlin. Ultrasonic backscattering in polycrystals with elongated single phase and duplex microstructure. *Ultrasonics*, 52(6): 694-705, 2012.
- 4.10 Deka, D. S. Joseph, S. Ghosh and M. J. Mills. Crystal plasticity modeling of deformation and creep in polycrystalline Ti-6242. *Metal. Mater. Trans.*, 37A: 1371-1388, 2006.
- 4.11 Venkatramani, S. Ghosh and M. Mills. A size-dependent crystal plasticity finite-element model for creep and load shedding in polycrystalline titanium alloy. *Acta Materialia*, 55: 3971-3986, 2007.
- 4.12 Kirane and S. Ghosh. A cold dwell fatigue crack nucleation criterion for polycrystalline Ti-6242 using grain-level crystal plasticity FE Model. *Int. J. Fatigue*, 30: 2127-2139, 2008.

Chapter 5

- 5.1 V. Sinha, J. E. Spowart, M. J. Mills and J. C. Williams. Observations on the faceted initiation site in the dwell-fatigue tested Ti-6242 alloy: Crystallographic orientation and size effects. *Metall. Mater. Trans. A*, 37A: 1507-1518, 2006.
- 5.2 F. P. E. Dunne, A. Walker and D. Rugg. A system study hcp crystal orientation and morphology effects in polycrystal deformation and fatigues. *Proc. R. Soc. A*, 463: 1467-1489, 2007.
- 5.3 G. Lütjering and J.C. Williams. *Titanium*. Springer-Verlag, 2003.
- 5.4 A. Bhattacharjee, A.L. Pilchak, O.I. Lobkis, J.W. Foltz, S.I. Rokhlin and J.C. Williams. Correlating ultrasonic attenuation and microtexture in a near alpha titanium alloy. *Metall. Mater. Trans. A*, 42 (8): 2358-2372, 2011.
- 5.5 L. Yang, O. I. Lokis and S. I. Rokhlin. Shape effect of elongated grains on ultrasonic attenuation in polycrystalline materials. *Ultrasonics*, 51(6): 697-708, 2011.
- 5.6 S. Hirsekorn. The scattering of ultrasonic waves by polycrystals. *J. Acoust. Soc. Am.* 72: 1021, 1982.
- 5.7 S. Hirsekorn. The scattering of ultrasonic waves in polycrystalline materials with texture. *J. Acoust. Soc. Am.*, 77: 832-843, 1985.
- 5.8 S. Hirsekorn. Directional dependence of ultrasonic propagation in textured poly-crystals. *J. Acoust. Soc. Am.*, 79: 1269-1279, 1986.
- 5.9 S. Hirsekorn. The scattering of ultrasonic waves by multi-phase polycrystals. *J. Acoust. Soc. Am.*, 83: 1231-1242, 1988.
- 5.10 F. E. Stanke and G. S. Kino. A unified theory for elastic wave propagation in polycrystalline materials. *J. Acoust. Soc. Am.* 75: 665-681, 1984.
- 5.11 R.L. Weaver. Diffusivity of ultrasound in polycrystals. *J. Mech. Phys. Solids*, 38: 55-86, 1990.
- 5.12 L. Yang, J. A. Turner and Z. Li. Ultrasonic characterization of microstructure evolution during processing. *J. Acoust. Soc. Am.*, 121: 50-59, 2007.
- 5.13 L. Yang, O. I. Lobkis and S. I. Rokhlin. Explicit model for ultrasonic attenuation in equiaxial hexagonal polycrystalline materials. *Ultrasonics*, 51: 303-309, 2011.
- 5.14 S. Ahmed and R. B. Thompson. Attenuation of ultrasonic waves in cubic metals having elongated, oriented grains. *Nondestr. Test. Eval.*, 8-9: 525-531, 1992.
- 5.15 S. I. Rokhlin, T. K. Bolland and L. Adler. High frequency ultrasonic wave propagation in polycrystalline materials. *J. Acoust. Soc. Am.* 91: 151-165, 1992.
- 5.16 P.D. Panetta, R.B. Thompson and F.J. Margetan. Use of electron backscattering diffraction in understanding texture and the mechanism of backscattered noise generation in titanium alloys. *Rev. Prog. Q.*, 17A: 89-96, 1998.
- 5.17 Y.K. Han and R.B. Thompson. Ultrasonic backscattering in duplex microstructures: theory and application to titanium alloys. *Metall. Mater. Trans. A*, 28A: 91-104, 1997.
- 5.18 O. I. Lobkis and S. I. Rokhlin. Characterization of polycrystals with elongated duplex microstructure by inversion of ultrasonic backscattering data. *Appl. Phys. Lett.*, 96 (16): Art.161905-1-3, 2010.

- 5.19 O. I. Lobkis, L. Yang, J. Li and S. I. Rokhlin. Ultrasonic backscattering in polycrystals with elongated single phase and duplex microstructure. *Ultrasonics* (published on line Dec 2011).
- 5.20 W. Hassan and P. B. Nagy. Experimental investigation of the grain noise in interferometric detection of ultrasonic waves. *J. Nondestr. Eval.* 18 (4): 139-147, 1999.
- 5.21 M.P. Blodgett and D. Eylon. The influence of texture and phase distortion on ultrasonic attenuation in Ti-6Al-4V. *J. Nondestr. Eval.* 20 (1): 1-16, 2001.
- 5.22 J. H. Cho, A. D. Rollett, and K. H. OH. Determination of volume fractions of texture components with standard distributions in Euler space. *Metall. Mater. Trans. A.* 35A: 1075-1086, 2004.
- 5.23 J.Y. Li. The effective electroelastic moduli of textured piezoelectric polycrystalline aggregates. *J. Mech. Phys Sol.*, 48: 529-552, 2000.
- 5.24 U.F. Kocks, C. N. Tomé, H.-R. Wenk, A. J. Beaudoin, H. Mecking. *Texture and Anisotropy*, Cambridge University Press, 2000.
- 5.25 C. M. Sayers, Ultrasonic velocities in anisotropic polycrystalline aggregates. *J. Phys. D: Appl. Phys.* 15: 2157-2167, 1982.
- 5.26 Y. Li and R. B. Thompson. Relations between elastic constants C_{ij} and texture parameters for hexagonal materials. *J. Appl. Phys.* 67: 2663-2666, 1990.
- 5.27 P. Spalthoff, W. Wunniike, C. Nauer-Gerhard, H.J. Bunge and E. Schneider. Determination of the elastic tensor of a low-carbon steel. *Textures and Microstruct.* 21: 3-16, 1993.
- 5.28 H.J. Bunge. *Texture analysis in materials science*. Butterworth and Co., 1982.
- 5.29 J.-Y Kim and S. I. Rokhlin. Determination of elastic constants of generally anisotropic inclined lamellar structure using line-focus acoustic microscopy. *J. Acoust. Soc. Am.* 126: 2998-3007, 2009.
- 5.30 L. Yang, O. I. Lobkis and S. I. Rokhlin. Integrated model for ultrasonic wave propagation and scattering in polycrystalline medium with elongated hexagonal grains. *Wave Motion*, 49(5): 544-560, 2012.
- 5.31 J. Li, O. I. Lobkis, L. Yang and S. I. Rokhlin. Integrated method of ultrasonic attenuation and backscattering for characterization of microstructure in polycrystals. *Rev. Prog. Q.*, (in press 2012)
- 5.32 F. J. Margetan, R.B. Thompson, and I. Yalda-Mooshabad. Backscattered microstructural noise in ultrasonic toneburst measurements. *J. Nondestr. Eval.*, 13 (3): 111-136, 1994.
- 5.33 R.B. Thompson, F.J. Margetan, P. Haldipur, L.Yu, A. Li, P. Panetta and H. Wasan. Scattering of elastic waves in simple and complex polycrystals. *Wave Motion*, 45: 655-674, 2008.
- 5.34 F. Zeng, S. R. Agnew, B. Raeisnia, and G. R. Myneni. Ultrasonic attenuation due to grain scattering in pure niobium. *J. Nondestr. Eval.*, 29: 93-103, 2010.
- 5.35 L. Yang and S. I. Rokhlin. On comparison of experiment and theory for ultrasonic attenuation in polycrystalline niobium. *J. Nondestr. Eval.* 31 (1): 77-79, 2012.
- 5.36 L. Yang and S. I. Rokhlin, Ultrasonic scattering in polycrystals with ellipsoidal orientation clusters of orthorhombic crystallites, *Wave Motion* (submitted).